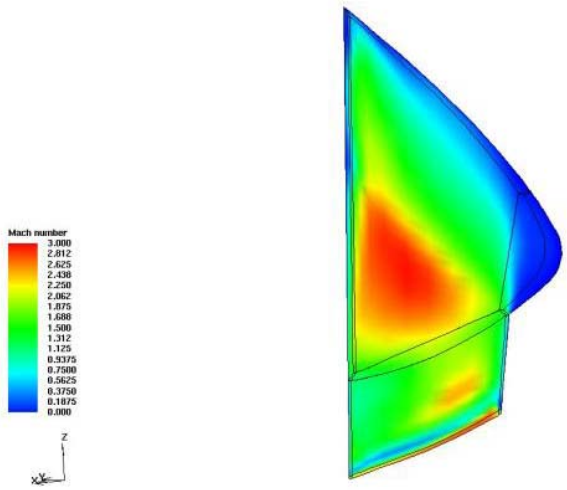

Figure 5.3.6-138 Mach Contours from Panel 8/9 T-Seal Damage Coupled External/Internal Flow Simulation (15 million-cell Model; Postprocessed using every other points)

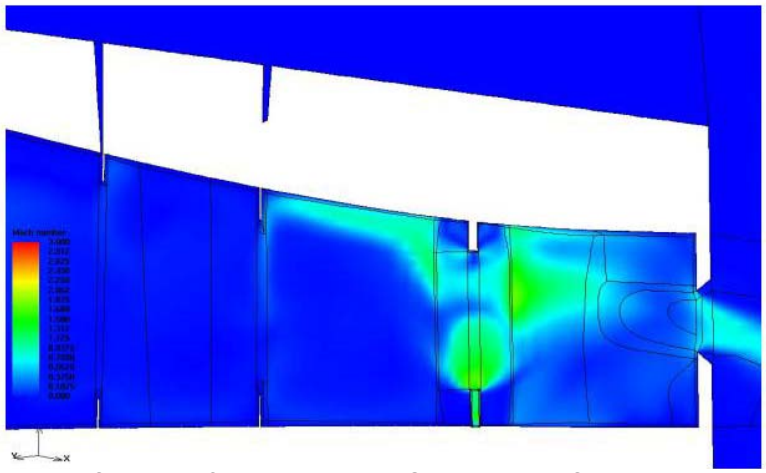

Figure 5.3.6-139 Mach Contours from Panel 8/9 T-Seal Damage Coupled External/Internal Flow Simulation (15 million-cell Model; Postprocessed using every other points)

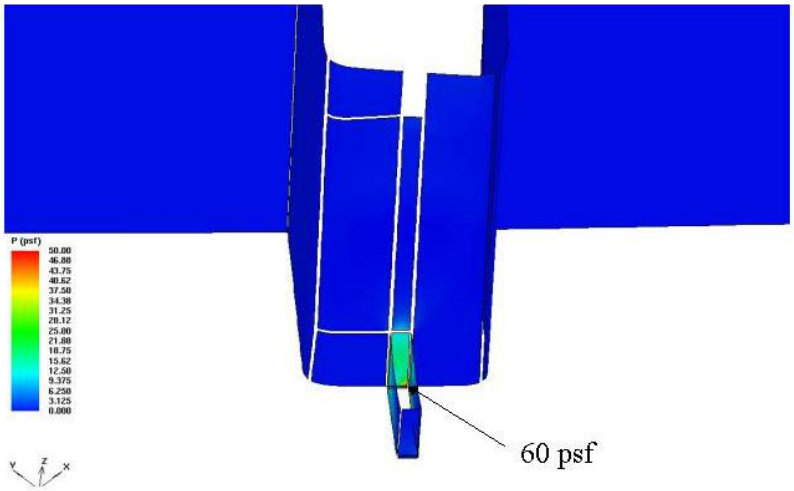

Figure 5.3.6-140 Pressure Contours on Earmuff Insulation and Rib Channel from Panel 8/9 T-Seal Damage Coupled External/Internal Flow Simulation (2 million-cell Model)

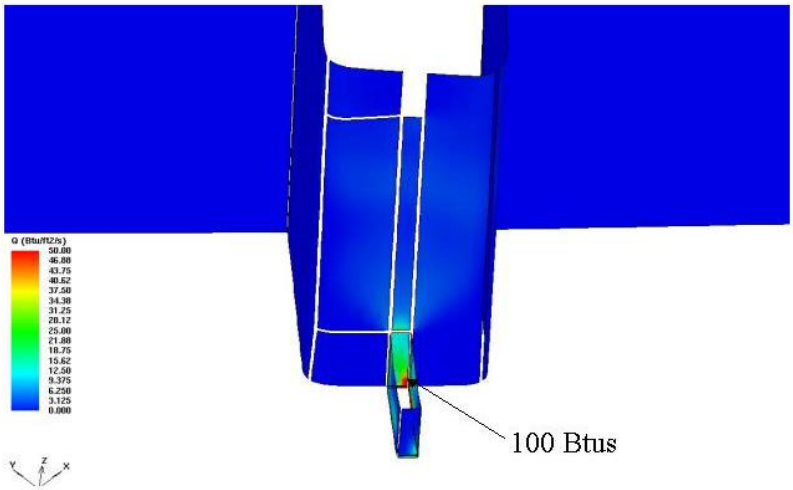

Figure 5.3.6-141 Heating Contours on Earmuff Insulation and Rib Channel from Panel 8/9 T-Seal Damage Coupled External/Internal Flow Simulation (2 million-cell Model)

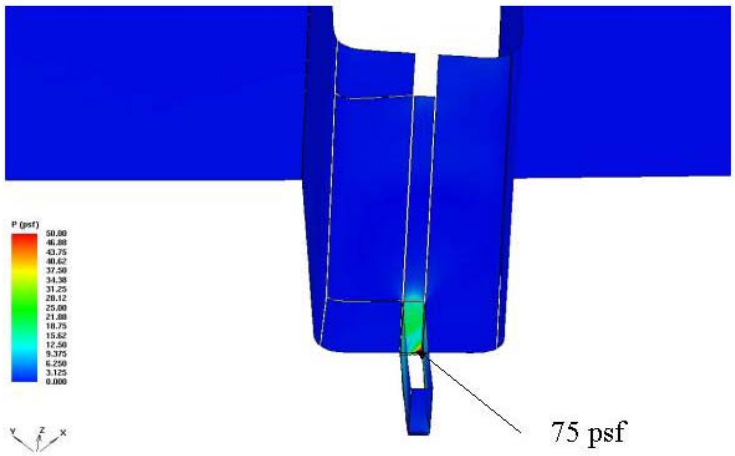

Figure 5.3.6-142 Pressure Contours on Earmuff Insulation and Rib Channel from Panel 8/9 T-Seal Damage Coupled External/Internal Flow Simulation (15 million-cell Model)

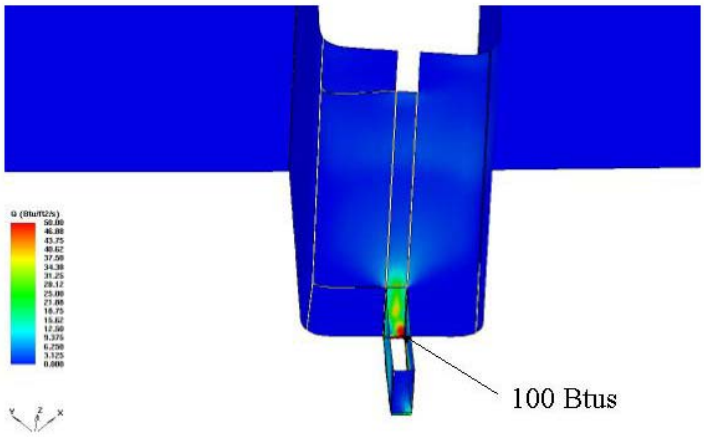

Figure 5.3.6-143 Heating Contours on Earmuff Insulation and Rib Channel from Panel 8/9 T-Seal Damage Coupled External/Internal Flow Simulation (15 million-cell Model)

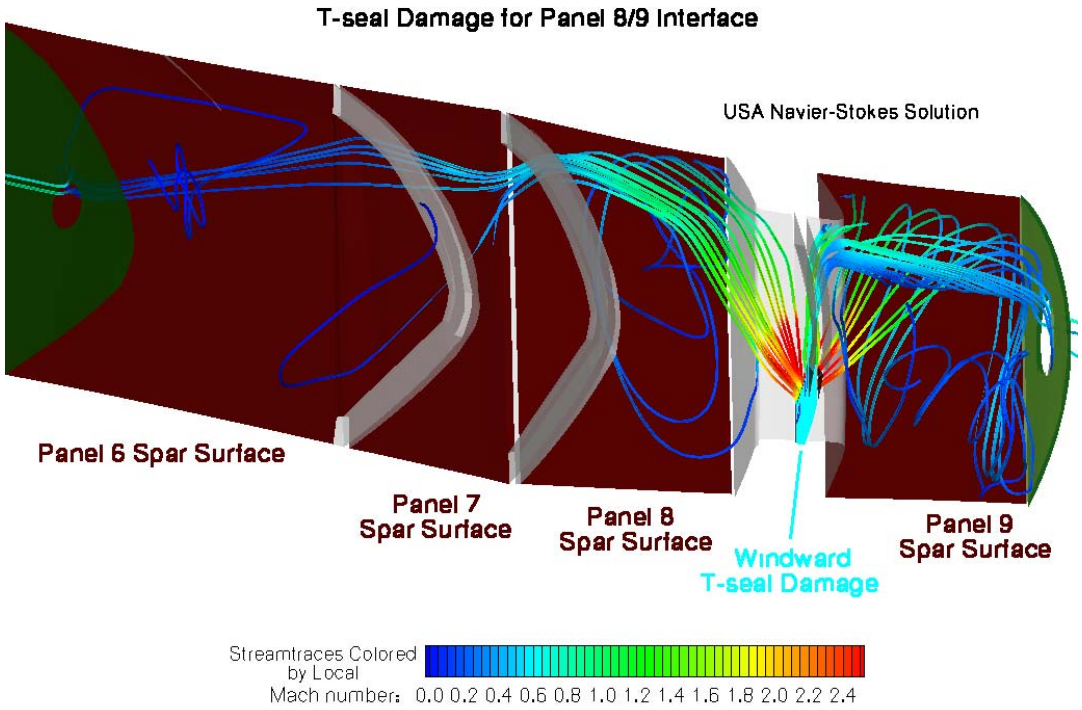

Figure 5.3.6-144 BHB Panel8/9 T-seal Damage Internal Streamtraces

5.3.6.2.4 BRPP 3-D Panel 8/9 Damaged T-Seal Solution

5.3.6.2.4.1 Case Description

The first objective of this effort was to compute convective heating rates on key surfaces of the Leading Edge Structural Subsystem (LESS) for the scenario of a damaged T-Seal in the RCC 8/9 location. These included:

- RCC T-Seal
  - Cavity
  - Rib channel
- Internal insulation units:
  - Forward spar insulator units (hot tubs)
  - Spanner Beam Insulator units (earmuffs)

The T-Seal damage was assumed to be a piece missing from the intersection of the T-Seal and the lower edge of the earmuff to the geometric leading edge as shown in Figure 5.3.6-145.

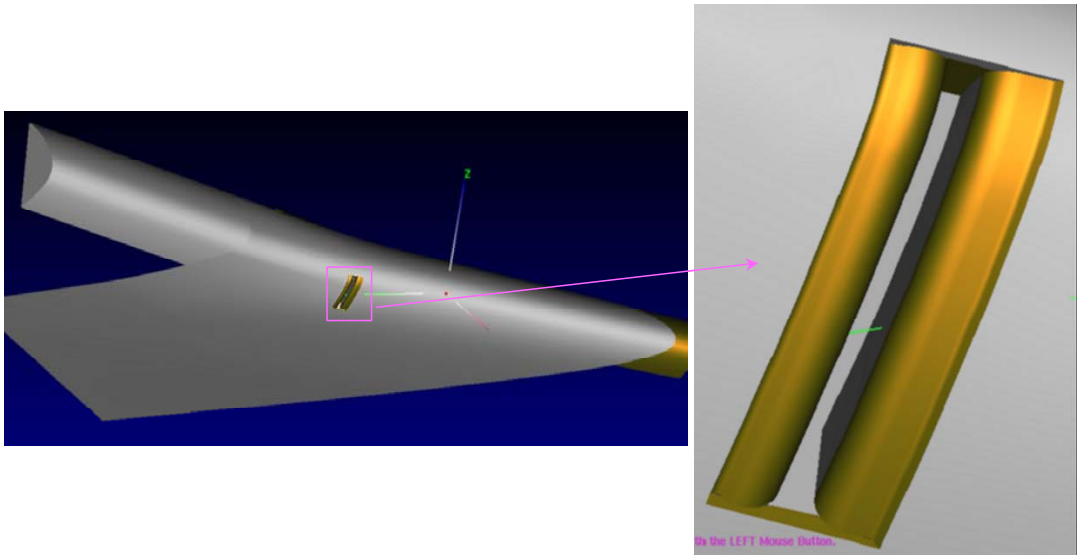

Figure 5.3.6-145 – Damaged T-Seal Geometry

The intended application of the data was to enhance the engineering heat transfer models and to improve understanding of this flow field structure. The second objective of this effort was to construct an accurate CAD model of the LESS components that would serve as a universal model usable for all types of multidimensional analysis via IGES export. This would possess clean, "watertight", trimmed surfaces for import to modeling software.

5.3.6.2.4.2 Grid/Solution Development

The universal CAD model was constructed with the Pro/Engineer parametric CAD system. Sources for geometry included imported CAD models for the RCC panels, forward wing spar, and RCC attachment brackets. Design specifications combined with photographs were used for the earmuffs, hot tubs, and wick insulators. No detailed drawings for the latter three components have been located to date. The model has been completed however issues precluded its use for CFD grid generation. The imported RCC parts were too complex for analysis use. They contained over 1,000 surfaces per RCC panel as well as duplicate surfaces. In addition, the model architecture requires a large amount of prep work prior to export for analysis grid generation due to the grouping of surfaces with solids. It was anticipated that an additional 1-2 weeks would be required to complete this task. A fallback plan was implemented in which development of the universal CAD model would continue, while the NASA JSC-based model for internal region used in for the 10" Leading Edge Breach would be modified for use in this analysis. The T-Seal channel geometry was extracted from the Pro/E CAD model and integrated into the JSC model (Figure 5.3.6-145). As discussed in Section 5.3.6.1.4, the JSC model included the RCC 7/8, 8/9, 9/10 earmuffs and the hot tubs in between them. The negative aspect of this model was that all of the edges were sharp, which conflicted with other models and photographs. Dimensions of key components, such as the earmuffs and hot tubs, were also somewhat uncertain since the JSC dimensions conflicted with a model used by Boeing Huntington Beach and some photographs.

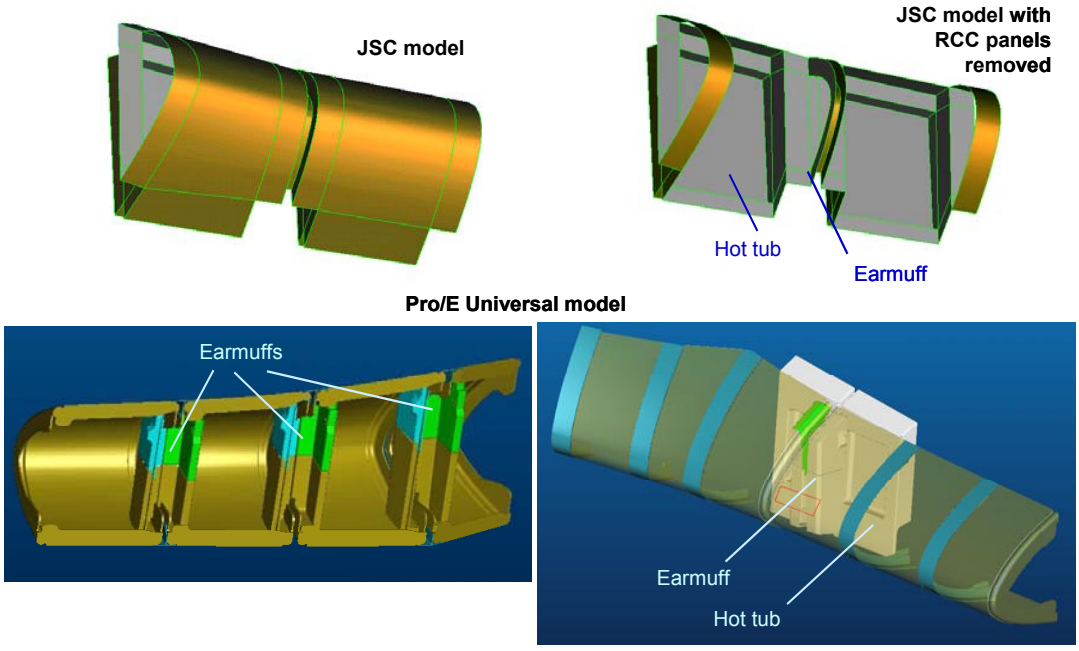

Figure 5.3.6-146 – Internal Region Geometry Models

The JSC and the Pro/E Universal model are compared in Figure 5.3.6-146. Extruded "dump" regions were added on either side of RCC 8 and 9 to enable the application of constant pressure outflow boundary conditions. The dimensions of these regions were based on the results of the 2-D T-Seal analysis of Sec.5.3.6.2.2.

Previous analyses had shown that a high degree of coupling existed between the internal and external flow fields. A NASA LaRC LAURA external flow solution was used to provide the necessary coupling, but only a small three-zone portion of it. This was carefully selected to reduce the size of the model while preserving the external solution in the region of interest (Figure 5.3.6-147). Not all of Zone 36 was required so it was sectioned with a cutting-plane interpolation.

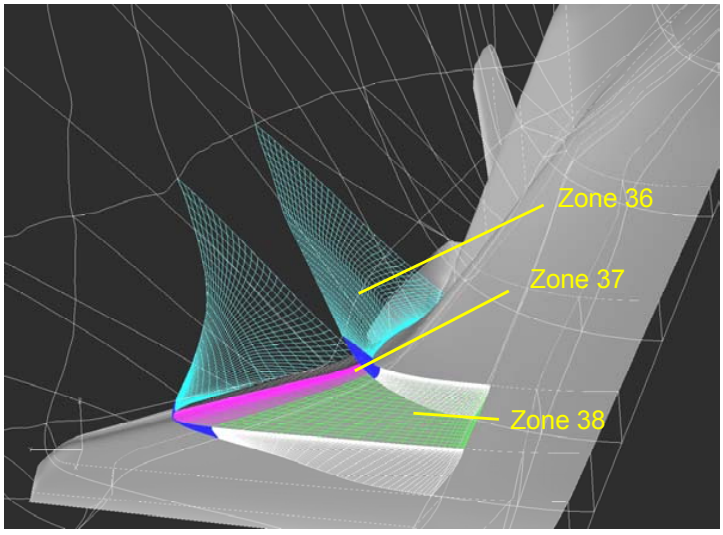

Figure 5.3.6-147 - LAURA Solution Zones Used as External Domain

The Boeing APPT system was used to generate the hybrid viscous unstructured computational grid. The unstructured approach greatly reduces the time required to generate the grid and eliminates wasted clustering cells in complex internal regions. After a number of revisions, final grids (Figure 5.3.6-148) were produced containing 4.1M elements with a wall spacing of $1.0e^{-4}$ inches, and 5.7M elements with a wall spacing of $1.0e^{-5}$ inches. Results from the 2-D T-Seal analysis (Sec. 5.3.6.2.2) along with a cardboard model and discussion among compressible flow experts were used to determine the clustering of elements in the internal region.

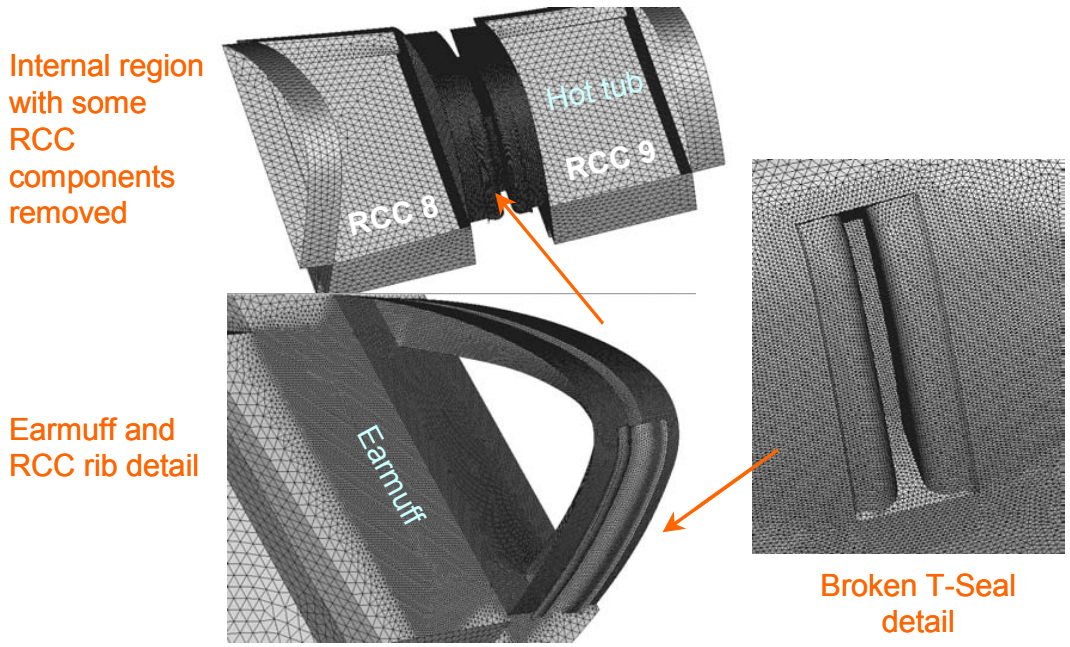

Figure 5.3.6-148 – Hybrid Viscous Unstructured Grid

The solutions were obtained using the Boeing ICAT code. Fully laminar flow was assumed based on the extremely low Reynolds numbers present. Liu-Vinokur equilibrium air thermochemistry and Tannehill transport properties were used. The convergence criteria were to drive net fluxes to an initial steady-state and also to drive integrated heat load in key areas to steady-state. Contours of heat flux in key areas were also plotted at different time steps.

The CFD Condition 1 trajectory point was used to define the freestream conditions. All wall temperatures were set to 3,000º R. This corresponds to the melting temperature for the Inconel 601 outer layer of the Dynaflex surfaces such as the earmuffs and hot tubs. The pressure on the cavity outflow surfaces was set according to Table 5.3.6.1-1. These values were established from venting analysis. Note that the values have evolved over time as has the venting analysis. The current level of 10.8 psf (517 Pa) is the result of the 2-D T-Seal computations being fed back into the venting analysis.

5.3.6.2.4.3 Results

5.3.6.2.4.4 Major flow structure comments

Figure 5.3.6-149 shows the flow inside the LESS cavity. The walls are colored by static pressure, and the streamlines are colored by Mach number and are launched from the center of rib channel. Subsonic flow is observed exiting the rib channel into the LESS cavity. This is due to the high cavity backpressure of .075 psia vs. ~.060 psia at the rib channel exit. The latter number comes from examination of the T-Seal 2-D solutions (Sec. 5.3.6.2.2) and represents the rib channel exit pressure without the influence of backpressure. Overexpanded laminar flow, such as this, easily separates, and normal shock structures reduce the flow to subsonic and also reduce total pressure. Both of these effects reduce the capability of the flow to generate heat flux on impingement surfaces. The majority of the LESS cavity flow is large-scale subsonic vortices.

Figure 5.3.6-150 shows the flow in the RCC rib channel. Again, the walls are colored by static pressure, and the streamlines are colored by Mach number, however this time they are launched from a boundary layer rake in the external flow. This flow field has features similar to the 2-D T-Seal solutions (Sec. 5.3.6.2.2). These include the aerodynamic throat, the upstream edge separation, and the downstream edge bow shock. Surface pressures are also close to the 2-D solutions.

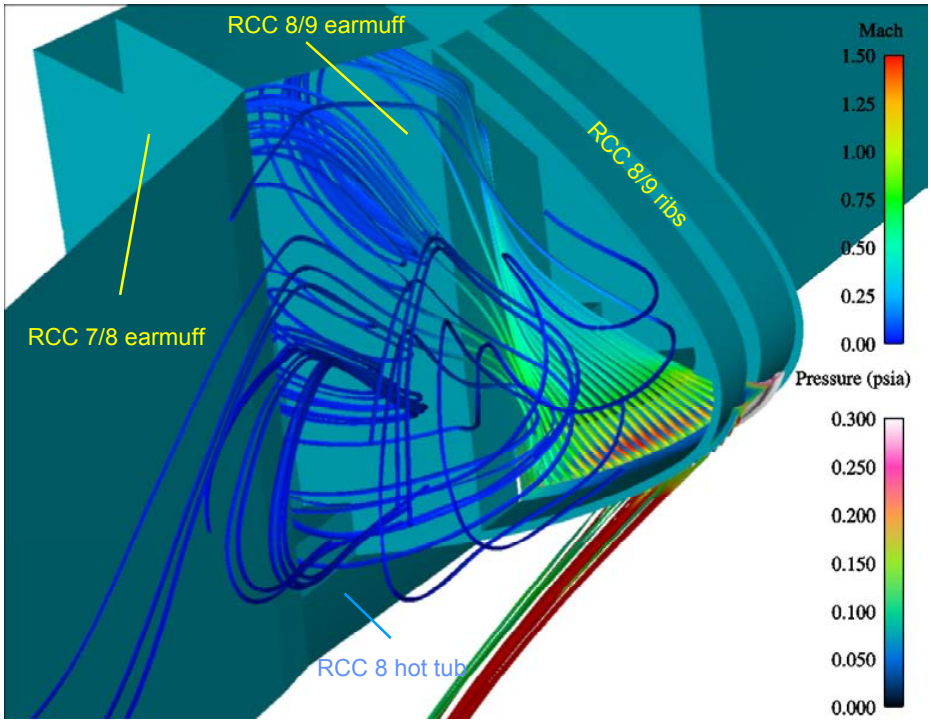

Figure 5.3.6-149 - Mach-colored Cutting Plane and Wall Static Pressure Detail View From in Front of Leading Edge

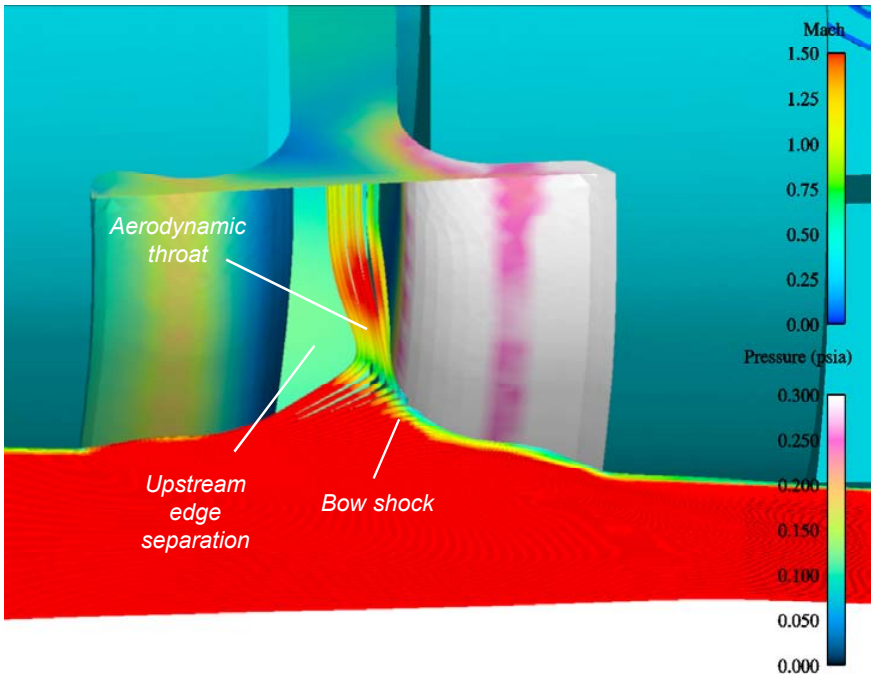

Figure 5.3.6-150 – View Into RCC Rib Channel

5.3.6.2.4.5 Surface heating and pressure comments

Figure 5.3.6-151 shows surface heat flux in the region where the RCC 8/9 earmuff and the RCC 8 hot tub intersect. This is the area of highest heating on the earmuff and hot tub surfaces, as would be expected based on the pressure and Mach fields observed. The levels are low compared to the peaks observed for the 2-D T-seal solution (Sec. 5.3.6.2.2) where supersonic flow is impinging on the earmuff. Heat fluxes in the rib channel closely match the USA 2-D T-Seal solutions (Sec. 5.3.6.2.2). The medium grid solution was run a total of 28,000 time steps. The solution was monitored periodically using flow visualization. No indication of unsteady flow was found, however there is still a possibility that this could occur. Many more time steps would be needed to be certain.

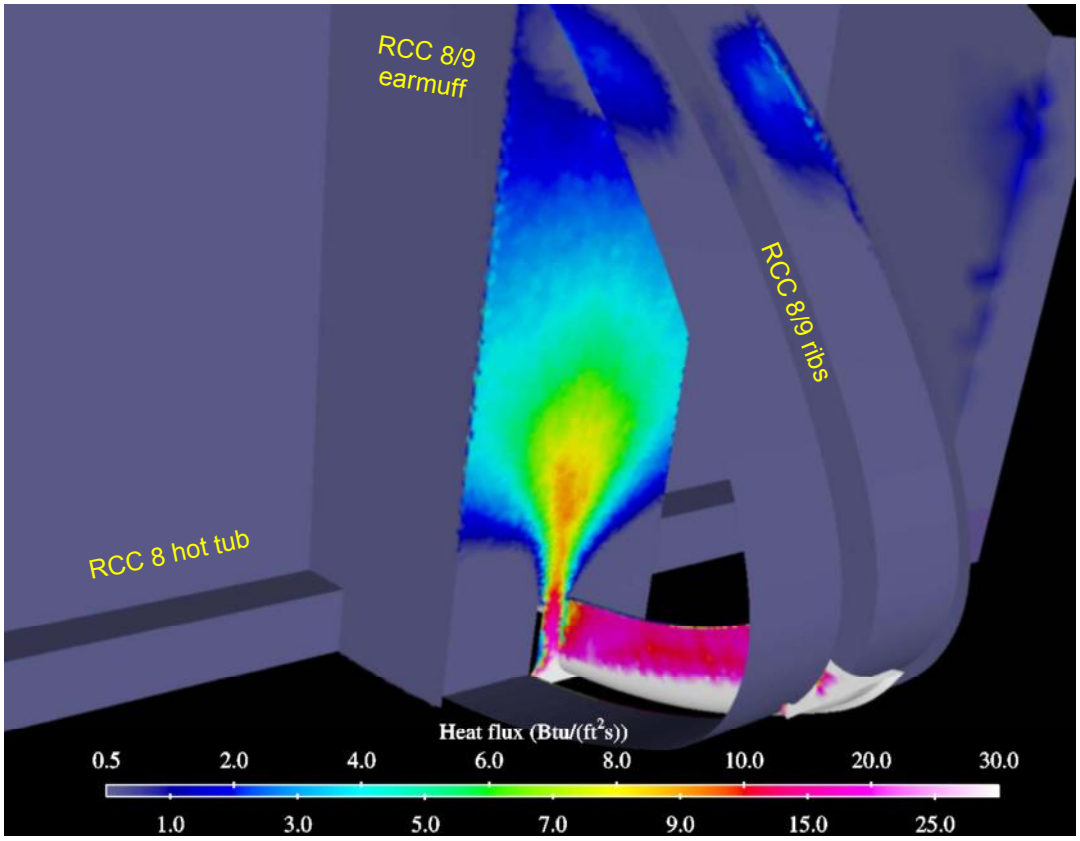

Figure 5.3.6-151 - Surface Heat Flux Detail View From in Front of Leading Edge

5.3.6.3 CFD of Simplified Internal Wing Geometry

5.3.6.3.1 Methodology and Philosophy of "Insight CFD"
CFD was used not only to help characterize fine details in the flow field with large, detailed CFD models, but also to help understand some of the larger scale flow phenomenon. For this purpose a few large scale, simplified models were created to understand the flow patterns once a breach of the internal wing cavity was initiated. These models were primarily used to visualize flow patterns within the wing cavity. They were not relied upon for detailed information such as wall heat fluxes, heat transfer coefficients, surface temperatures, or transient calculations.

Two simplified models were created. The first was a simplified model of the entire left wing aft of the 1040 wing spar and without the wheel well cavity. Wing spar designations are shown in Figure 5.3.6-153 for reference. This model did not include the RCC cavity along the wing leading edge. The purpose of this model was to visualize the flow field within the wing cavity immediately after the leading edge spar breach. This model assumed that the flow coming onto the wing cavity was normal to the spar. The second "insight" CFD model was a 2-D model of the left wing cavity and the RCC cavity. This model was used to visualize the flow through the RCC breach, through the wing spar breach, then into the wing cavity directly outboard of the wheel well. The purpose of this model was to verify whether or not it was possible for the flow to come into the wing cavity normal to the leading edge spar or not.

Models are "simplified" in the sense that only the necessary surfaces needed to characterize the flow field satisfactorily are included. The 3-D wing model has none of the internal circular struts connecting the upper and lower wing surfaces. Only the internal spars and spar vents and the wing upper and lower surfaces are included. The wing upper and lower surfaces were generated based solely on the spar outlines; therefore some of the finer details in the wing curvature were not captured in the models. All walls within the models are smooth walls, which in reality is not the case, particularly in the area of the wheel well walls.

FLUENT 6.1 was the CFD code used to model these simplified geometries. FLUENT 6.1 is a commercial Navier-Stokes solver for unstructured meshes. It is a cell-centered, finite-volume code. FLUENT's three solvers can be used to compute the flow and heat transfer for all flow regimes, from low subsonic via transonic and supersonic to hypersonic. The unstructured grid capability in FLUENT allows for modeling of complex geometries similar to the geometry found in the wing and wheel well areas of Columbia. A more detailed description of FLUENT can be found in the Appendix and in [1].

5.3.6.3.2 3-D Solution Cases

5.3.6.3.2.1 <u>3-D Wing Model, 6 inch and 10 inch Spar Breach</u>
The purpose of the analysis was to determine the flow path of the plume entering the wing through the wing leading edge spar. A steady state analysis was done using boundary conditions corresponding to the time immediately following the wing spar breach, approximately 490 seconds after entry interface.

A simplified model of the left wing of Columbia was created, Figure 5.3.6-152, and shows the outer wall boundaries of the model including the wing upper and lower surfaces and the leading edge spar. A circular breach hole was located in the wing spar leading edge at the intersection of RCC panels 8 and 9. Two different spar breach hole diameters were modeled - circular breach sizes of 6 inches and 10 inches diameter were chosen based upon other analyses performed as part of the investigation. An assumption was made that the flow coming into the wing area would be normal to the spar.

Figure 5.3.6-153 shows the internal spars and vents not visible in Figure 5.3.6-152. Three flow exit areas are included in the wing model and are shown in Figure 5.3.6-153. A rectangular vent area of 180 in^2 is located in the 1040 wing spar. The internal wing volume forward of the 1040 spar was not included in the model, instead pressures obtained from the MSFC analyses outlined in Section 5.3.5.7 were used to set the conditions at that interface. The other two flow exits are located at the rear of the model at the 1365 spar location. These vents are located at the approximate locations where the inboard and outboard elevons penetrate the 1365 spar. Vent areas were 2.55 in^2 and 5.5 in^2 for the inboard and outboard

elevons, respectively. Four internal vents allow for flow between the various internal wing compartments and are shown along with their areas in Figure 5.3.6-153.

The wing geometry was simplified in order to reduce the computational expense of the model. None of the tubular struts supporting the upper and lower wing surfaces were included in the model. As mentioned previously, the wing volume forward of the 1040 spar was not included. The wheel well volume was not included due to the complex geometry in the wheel well and because the primary focus of the analysis was flow paths within the wing, not the wheel well area. Another area of simplification was the wing surfaces. These were not imported directly from CAD geometry, but were created within the FLUENT geometry generation program. This means that there may be subtle differences between the FLUENT wing surfaces and the actual wing surface geometry, however due to the overall size of the model it is not anticipated that this difference would have a significant effect on the results. The size of the 3D wing model computational domain was approximately 340,000 cells.

Boundary conditions for the 3-D model are shown in Figure 5.3.6-154 for the 6-inch breach case and in Figure 5.3.6-155 for the 10-inch breach case. Pressure boundary conditions were applied at the breach hole and three flow exit boundaries. These pressure values were obtained from the MSFC venting model discussed in Section 5.3.5.7. The pressures correspond to the boundary pressures at 500 seconds after entry interface. This time is 10 seconds after the estimated spar breach time of 490 seconds.

The standard k-e turbulence model available in FLUENT was activated for all of the 3-D and 2-D analyses. The working fluid was air modeled as an ideal gas. No attempt was made to model the chemical reactions occurring within the gas at these elevated temperatures using FLUENT. A correlation for determining the specific heat of air as a function of temperature from 495 ^{o}R to 10400 ^{o}R was used in the all of the 2-D and 3-D FLUENT models due to the large variation of specific heat over this temperature range. This correlation was input into FLUENT as a piecewise-polynomial function, and a plot of this correlation versus the data used to generate it can be found in Figure 5.3.6-156. The models were run until convergence was met on the net mass flow in and out of the domain, and pressures reached a steady state value.

5.3.6.3.2.2 Results – 3D Model, 6 inch Breach hole

Results of the 3-D internal wing flow case with a 6-inch diameter spar leading edge breach are shown in Figure 5.3.6-157 through Figure 5.3.6-161. Figure 5.3.6-157 is a contour plot of velocity magnitude on a plane cut horizontally through the entire wing. The plot shows that the flow does not penetrate significantly beyond the 1191 spar, and that it tends to circulate within the cavity outboard of the wheel well and exit through the 1040 spar vent. Some flow does penetrate all the way to the rear elevon vents, and Figure 5.3.6-158 shows this with a velocity contour plot with a different scale.

Mass flow rates and Mach numbers for the flow inlet and three flow exits are shown in Table 5.3.6.3-1. The mass flow rates indicate that 78% of the incoming gas exits the wing cavity through the 1040 spar vent.

Table 5.3.6.3-1 6-inch Breach Hole Mass Flow Rates and Mach Numbers

Vent	Mass Flow Lb/min	Flow direction	Mach Number
6” Dia breach Hole	0.686	In	1.06
1040 Spar Vent	0.535	Out	0.105
Inboard elevon	0.0667	Out	0.83
Outboard elevon	0.0835	Out	0.39

Figure 5.3.6-159 shows pathlines (colored by velocity magnitude) to indicate the flow paths of hot gas entering the wing cavity. The pathlines begin at the breach hole location. The flow impinges directly on the outboard wheel well wall then turns 180 degrees and the majority of the flow exits through the 1040 vent hole. A small percentage of the flow does penetrate all the way to the rear of the wing but at a much slower velocity than seen in the cavity outboard of the wheel well.

Figure 5.3.6-160 shows a contour of static pressure within the wing. The figure indicates that the pressure at the 1040 spar vent drives the resulting static pressure. This is due to the large size of that vent in relation to the two smaller rear vents. Figure 5.3.6-161 shows a contour plot of static temperature within the wing.

5.3.6.3.2.3 3D Model, 10 inch Breach hole

Results of the 3-D internal wing flow case with a 10-inch diameter spar leading edge breach are shown in Figure 5.3.6-162 through Figure 5.3.6-166. Figure 5.3.6-162 and Figure 5.3.6-163 are contour plots of velocity magnitude on a plane cut horizontally through the entire wing using two different scales to help visualize both the higher speed flow outboard of the wheel well and the low speed flow rear of the 1191 spar. The plots shows that even with the higher energy flow coming in the breach, the flow still does not penetrate significantly beyond the 1191 spar. Table 5.3.6.3-2 lists the mass flow rates and Mach numbers that again indicate that the majority of the flow (87%) entering the wing exits forward through the 1040 spar vent.

Table 5.3.6.3-2 10-inch Breach Hole Mass Flow Rates & Mach Numbers

Vent	Mass Flow Lb/min	Flow direction	Mach Number
6” Dia breach Hole	7.13	In	1.06
1040 Spar Vent	6.19	Out	0.75
Inboard elevon	0.29	Out	0.95
Outboard elevon	0.65	Out	0.95

Figure 5.3.6-164 shows pathlines (colored by velocity magnitude) to indicate the flow paths of hot gas entering the wing cavity. The flow impinges directly on the outboard wheel well and exits primarily through the 1040 vent hole, similar to the 6-inch breach case. As in the 6-inch breach case some flow penetrates the cavity aft of the 1191spar. Figure 5.3.6-165 shows a contour of static pressure within the wing. Figure 5.3.6-166 shows a contour plot of static temperature within the wing. Comparing the temperature contour plots between the 6-inch breach (Figure 5.3.6-161) and the 10-inch breach case (Figure 5.3.6-166), the area behind the 1191 spar is much warmer in the 10-inch case. The larger breach hole size is able to push more flow beyond the 1191 spar vent into this region.

5.3.6.3.3 2-D Simplified Wing Model Solutions

The purpose of the analysis was to trace the flow path of the plume as it enters the RCC cavity and impinges on the RCC attach hardware, then passes through a breach hole in the wing spar. It was assumed that the plume would be deflected by the RCC attach hardware and burn a hole through the spar, entering the wing cavity in the direction approximately normal to the spar. The analysis is an attempt to support the 3-D model assumption that flow is entering the wing cavity normal to the spar. A steady state analysis was done using boundary conditions corresponding to the time immediately following the wing spar leading edge breach, approximately 490 seconds after entry interface.

A simplified 2-D model of the left wing of Columbia was created and is shown in Figure 5.3.6-167. The view is looking up from below the left wing. The model consists of the wing cavity bounded by the wheel well outer wall, the 1040 spar, the 1191 spar, and the leading edge spar. This wing geometry was derived from the 3-D model. A section representing the RCC cavity was added along the length of the wing leading edge spar. The 2-D RCC cavity geometry was approximated with a 29-inch deep channel. A 10-inch diameter hole was located on the leading edge of the RCC cavity in the approximate location of panel 8. The green lines shown in Figure 5.3.6-167 represent interior zones in the domain and are not hard walls.

Four flow exit areas are included in the wing model. A pressure outlet is located in the 1040 wing spar, and another pressure outlet represents the vent in the 1191 spar that allows flow to pass to the rear cavities of the wing. The RCC cavity has two pressure outlets located at either end of the RCC cavity. These openings were sized based upon leakage areas obtained from the MSFC venting model discussed in Section 5.3.5.7

Figure 5.3.6-167 also shows the simplified RCC attach hardware used in the model. The attach hardware (representing the spanner beam insulation) in the model represents the hardware associated with RCC panel #8, and the breach hole in the spar is located directly adjacent to this attach hardware.

Boundary conditions for the 6 inch and 10 inch breach hole 2-D models are shown in Table 5.3.6.3-3. Static pressure boundary conditions were applied at the four flow exit boundaries. These pressure values were obtained from the MSFC venting model discussed in section 5.3.5.7. The pressures correspond to the boundary pressures at 500 seconds after entry interface.

Table 5.3.6.3-3 2-D Model Boundary Conditions

RCC Leading Edge Breach	Breach Pressure Lb/ft^2	Breach Temperature ^oR	1040 Spar Vent Lb/ft^2	1191 Spar Vent Lb/ft^2	RCC Fwd Vent Lb/ft^2	RCC Rear Vent Lb/ft^2
6 inches	37	6000	0.92	1.04	13.2	13.2
10 inches	37	6000	8.6	9.65	13.2	13.2

The flow entering the RCC cavity was redirected to impinge directly at the corner of the RCC attach hardware. This assumption was supported by other coupled external/internal CFD analyses which show the RCC inlet plume impinging directly on the corner of the attach hardware. All walls of the domain were set at a constant temperature of 50 ^oF, and the same turbulence models and specific heat correlations were used as in the 3-D models.

5.3.6.3.3.1 2-D Results - 6 inch Spar Breach

Results of the 2-D internal wing flow case are shown in Figure 5.3.6-168 and Figure 5.3.6-169. The velocity contour plot of Figure 5.3.6-168 shows the flow does penetrate the spar approximately normal to the spar. This figure as well as the pathlines of Figure 5.3.6-169.shows how the spanner beam insulation hardware turns the flow. Both plots support the assumption made in the 3-D model that initially the flow coming into the wing cavity was normal to the spar. There are some differences in the flow patterns compared with the 3-D model results, and this is likely due to the restrictions on the flow imposed by the 2-D geometry. In the 3-D case the flow can circulate around the wing cavity by splitting and traveling over and under the incoming jet, while in the 2-D model the flow is blocked from doing this by the incoming jet. The flow direction into the wing cavity at a later time would depend upon the length of time that the RCC attach hardware remained in place.

5.3.6.3.3.2 2-D Results - 10 inch Spar Breach

Results of the 2-D internal wing flow case are shown in Figure 5.3.6-170 and Figure 5.3.6-171. As in the 6-inch wing spar breach case, the velocity contour plot of Figure 5.3.6-170 shows the spanner beam insulation hardware turns the flow so it enters the wing approximately normal to the spar. This is also indicated in the pathline plot of Figure 5.3.6-171. Both plots support the assumption made in the 3-D model that initially the flow coming into the wing cavity was normal to the spar.

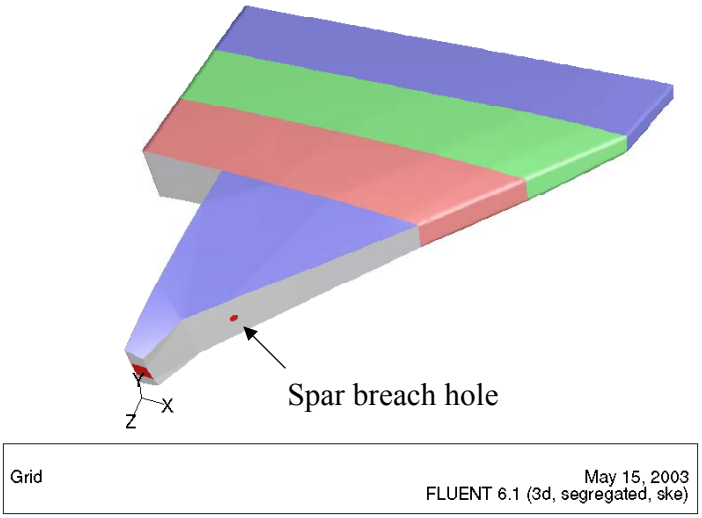

Figure 5.3.6-152 3-D Simplified Wing Geometry

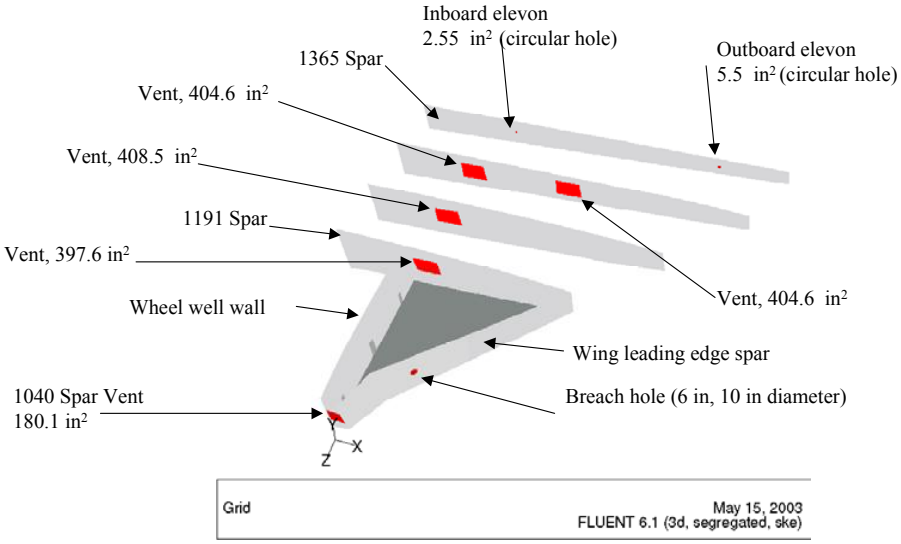

Figure 5.3.6-153 3-D Model Vent sizes

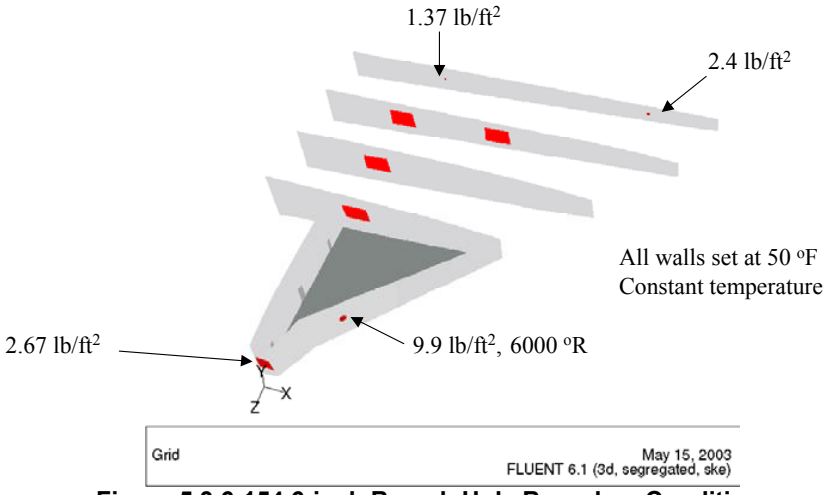

Figure 5.3.6-154 6-inch Breach Hole Boundary Conditions

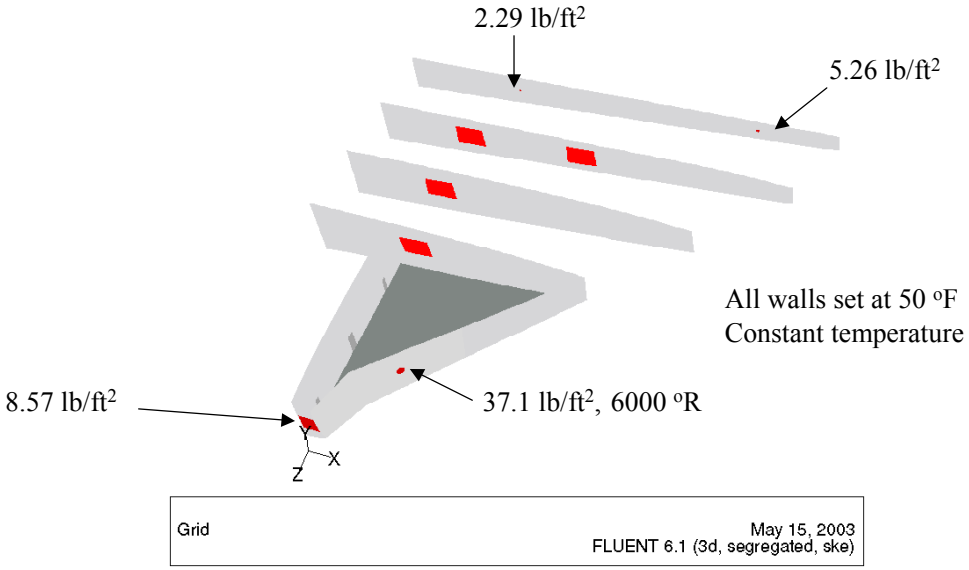

Figure 5.3.6-155 10-inch Breach Hole Boundary Conditions

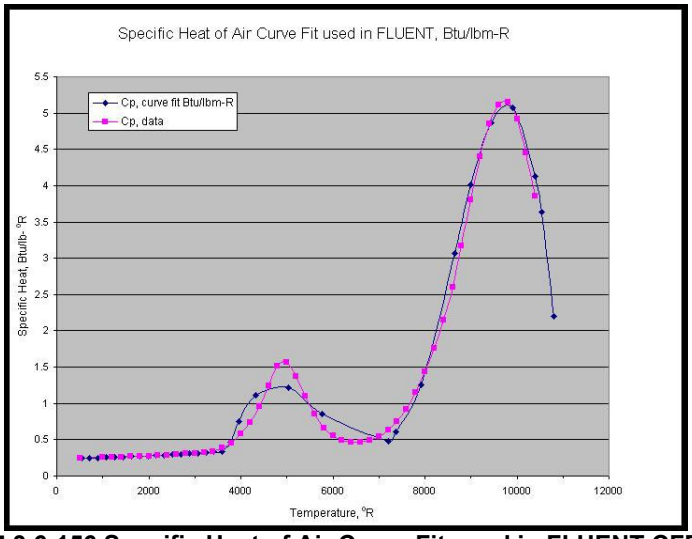

Figure 5.3.6-156 Specific Heat of Air Curve Fit used in FLUENT CFD Cases

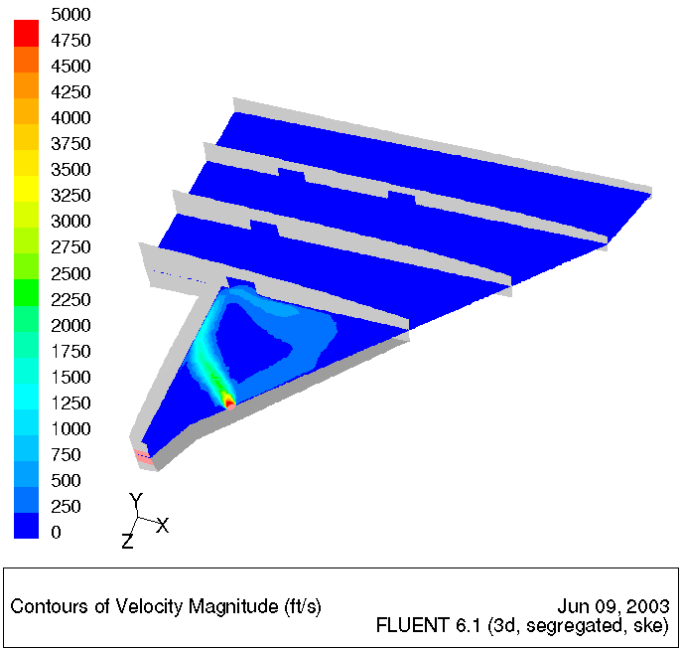

Figure 5.3.6-157 6-inch Breach hole, Velocity Contour Plot

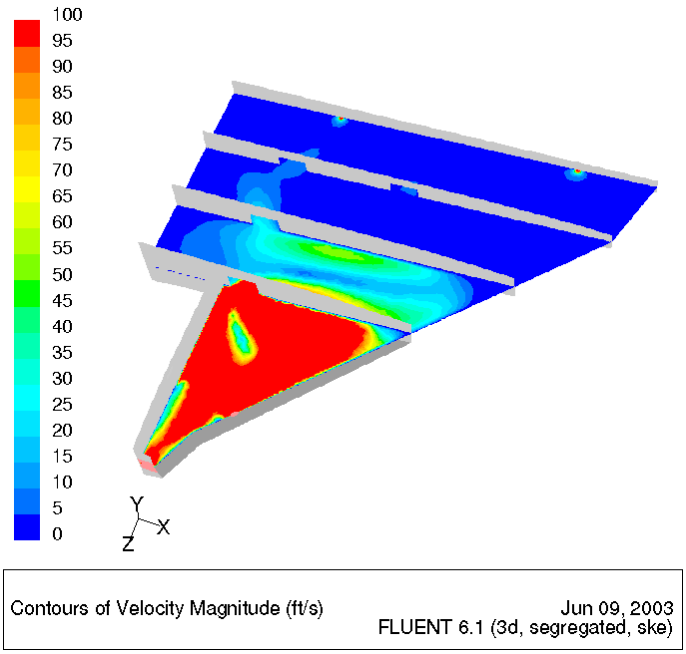

Figure 5.3.6-158 6-inch Breach Hole, Velocity Contour Plot

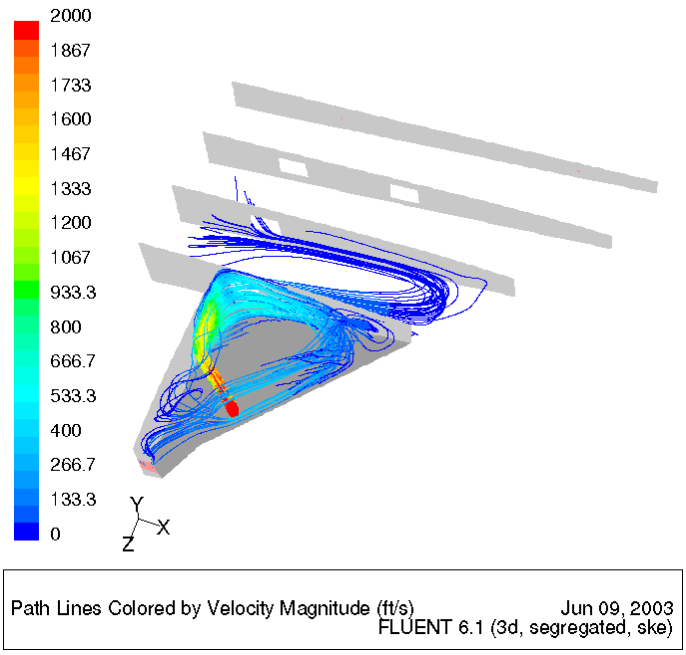

Figure 5.3.6-159 6-inch Breach Hole, Pathlines

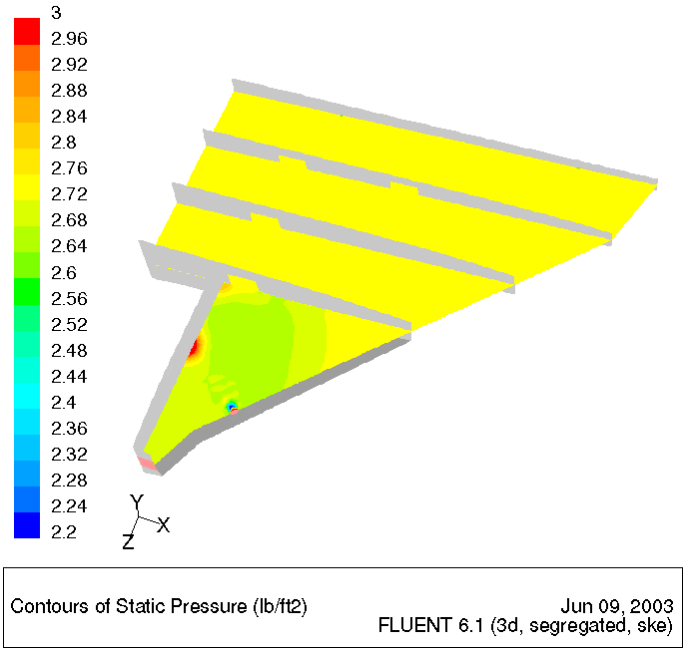

Figure 5.3.6-160 6-inch Breach Hole, Static Pressure

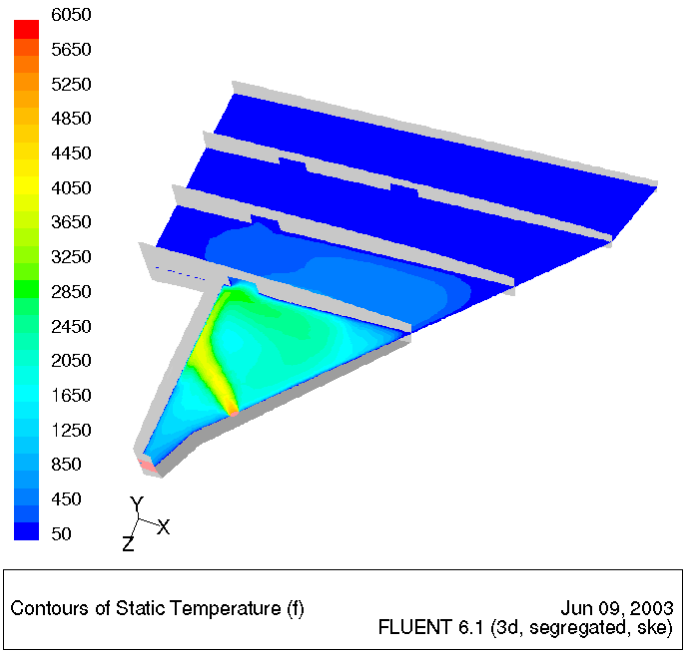

Figure 5.3.6-161 6-inch Breach Hole, Static Temperature

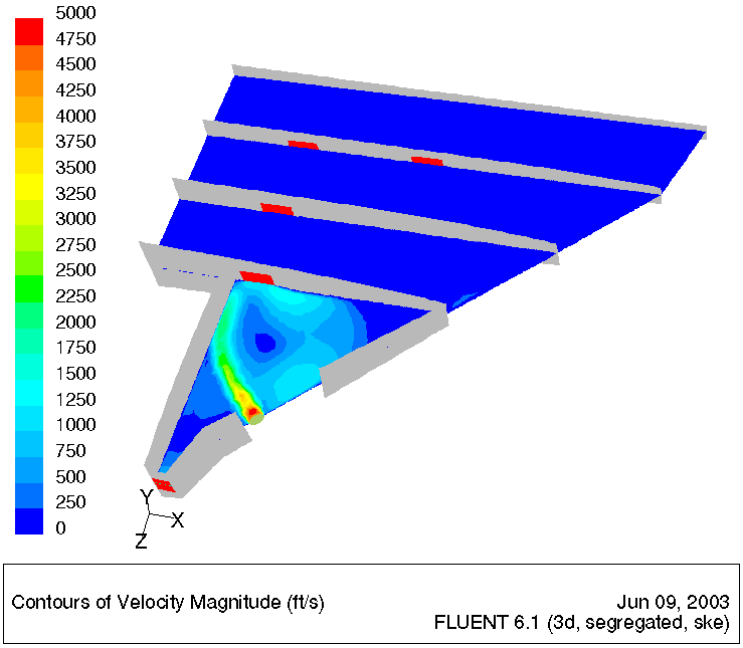

Figure 5.3.6-162 10-inch Breach Hole Velocity Contours

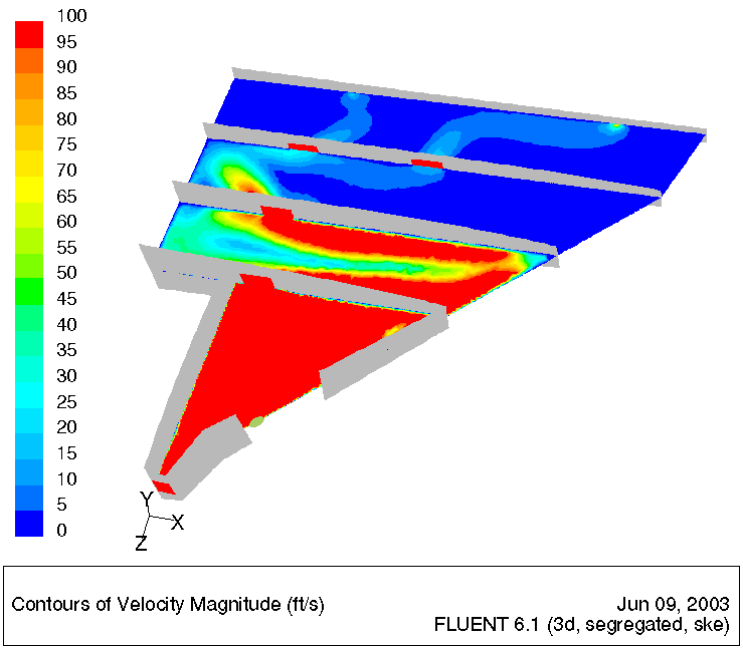

Figure 5.3.6-163 10-inch Breach Hole Velocity

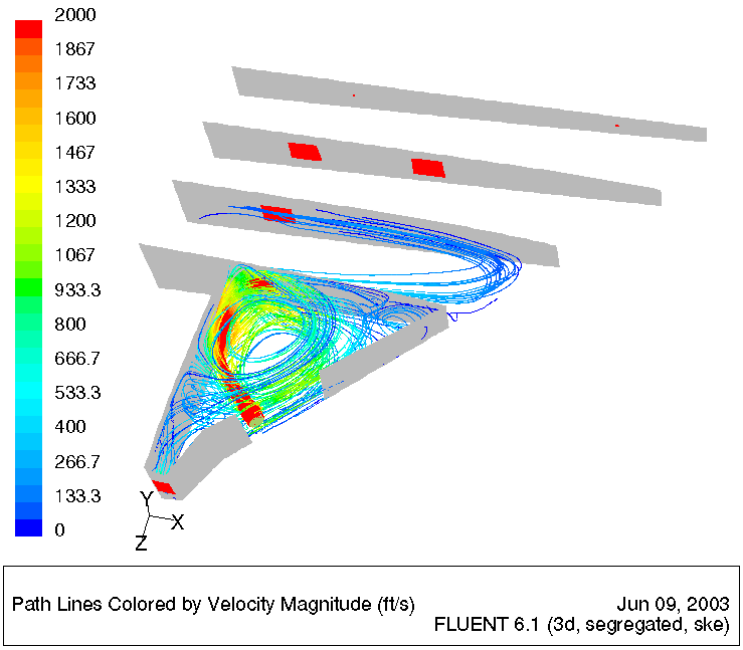

Figure 5.3.6-164 10-inch Breach Hole, Pathlines

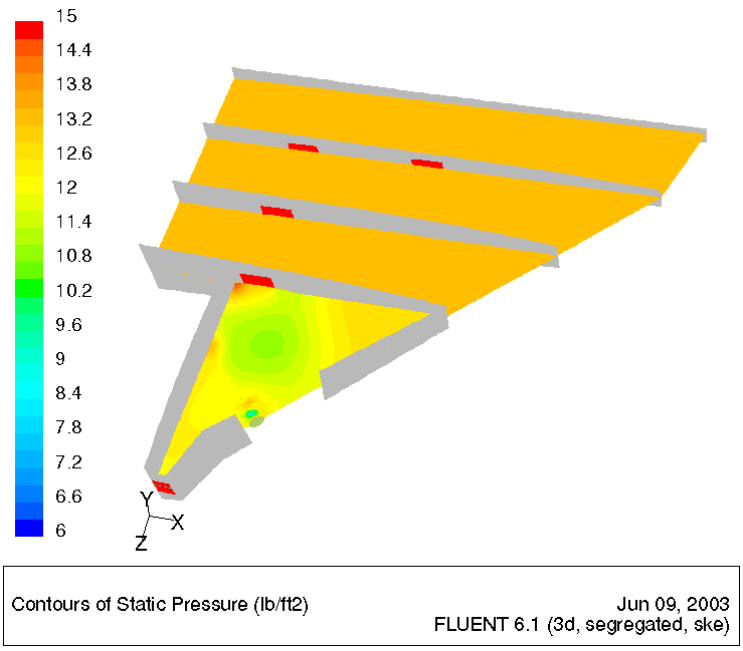

Figure 5.3.6-165 10-inch Breach Hole, Static pressure Contours

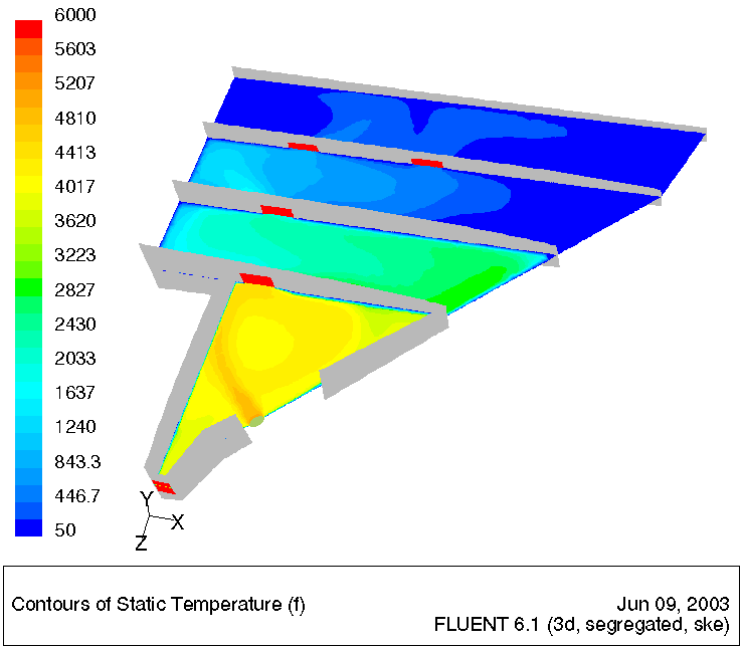

Figure 5.3.6-166 10-inch Breach Hole, Static Temperature Contours

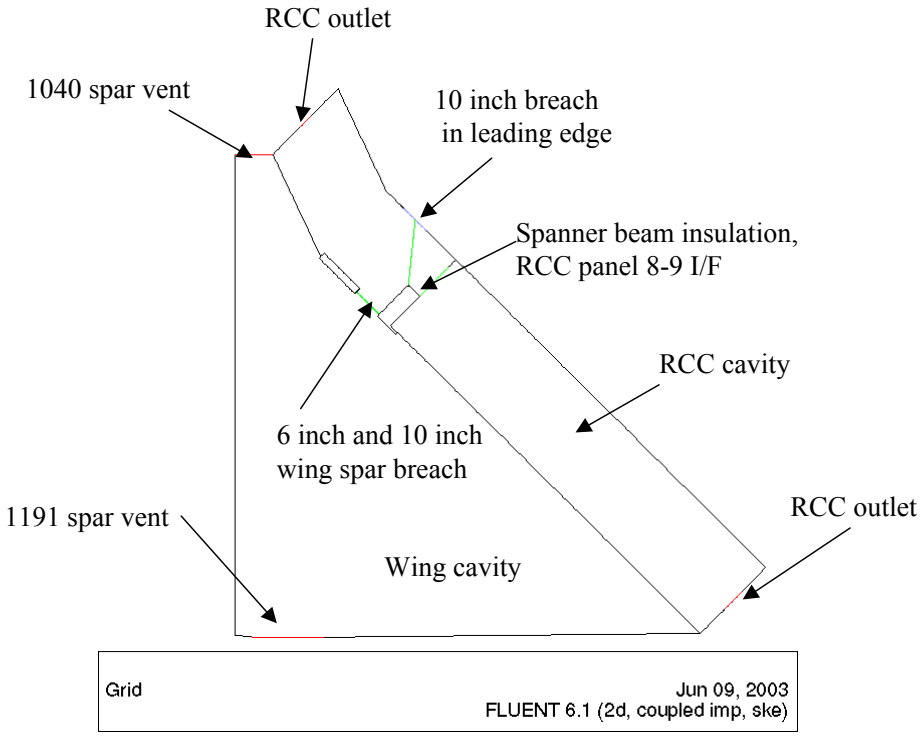

Figure 5.3.6-167 2-D Model Geometry – 10 inch Breach in RCC Leading Edge, 6 and 10-in Spar Breach

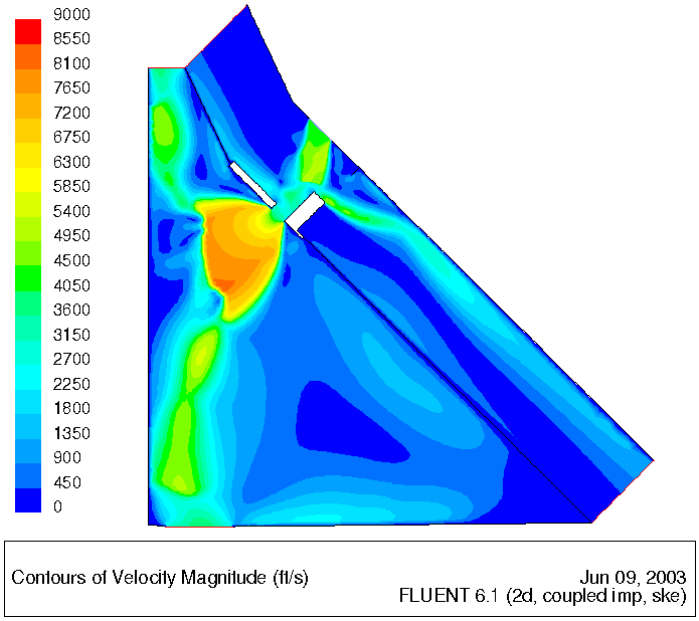

Figure 5.3.6-168 2-D Model, 6-inch Breach in Wing Spar, Velocity Contours

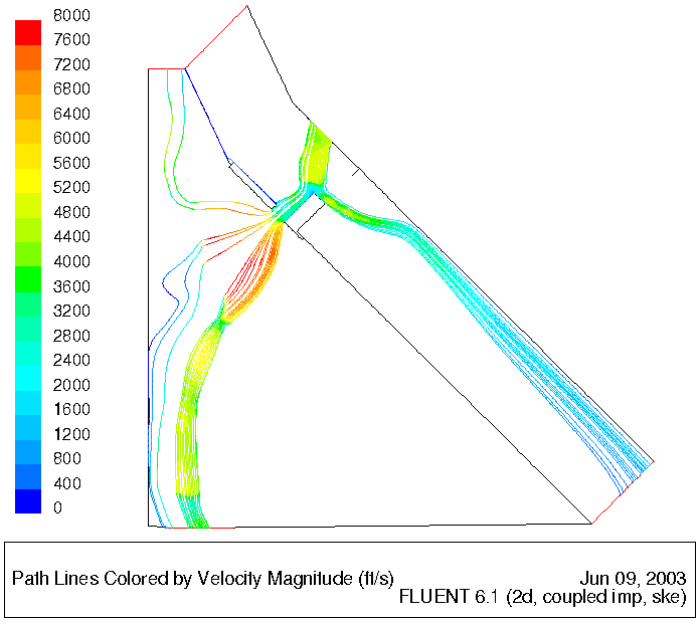

Figure 5.3.6-169 2-D Model, 6-inch Breach in Wing Spar, Pathlines

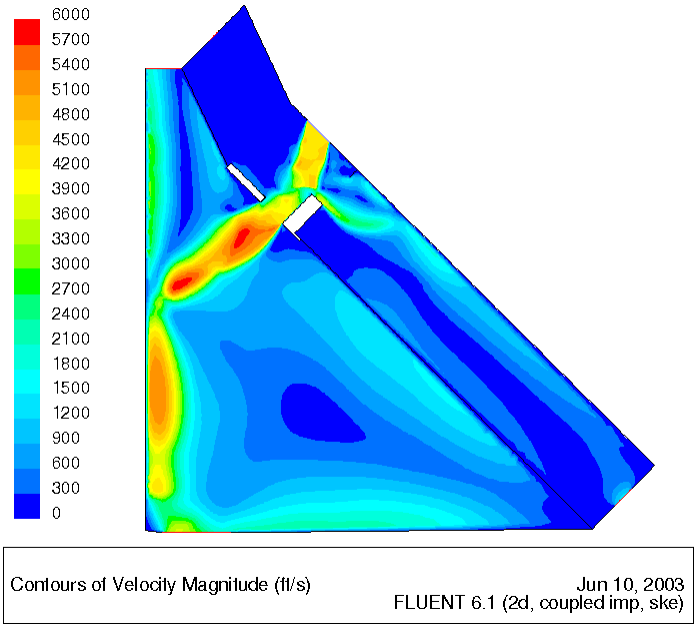

Figure 5.3.6-170 2-D Model, 10-inch Breach in Wing Spar, Velocity Contour

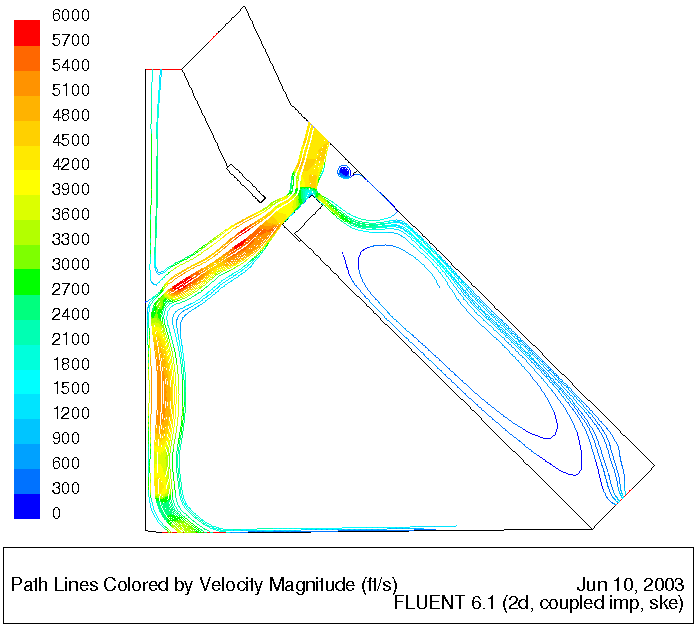

Figure 5.3.6-171 2-D Model, 10-inch Breach in Wing Spar Pathlines

5.3.7 Application of Data to the Working Scenario

5.3.7.1 Plume impingement angle in WLE

The insight provided by the CFD results for RCC penetrations with coupled flow fields allowed the adjustment of the assumed jet internal direction from normal to the interior surface to an angle reflective of the transverse momentum ingested into the RCC penetration. Figure 5.3.7-1 displays the two-inch penetration solution in RCC panel 6 by Peter Gnoffo. The streamlines turn into the hole initially at a 20-degree angle, that then interacts with the downstream lip shock resulting in a final flow turning angle of 41 degrees. It is desired to take advantage of this solution to generalize the internal jet direction to any penetration location. In doing so, the panel 6 results are assessed for a simple correlating parameter. A

local velocity based coordinate system is defined, as shown in Figure 5.3.7-1, with one component aligned with the velocity vector at the boundary layer edge and the other along the inward normal to the surface. Directional components were then assigned to the vectors. Many combinations of momentum components were tried, but with the uncertain impact of the lip shock, a simple correlation of boundary layer edge dynamic pressure (q_e) and surface static pressure (p_e) was chosen. The initial 20-degree flow turning angle was well reproduced with the ratio of static pressure over average ingested dynamic pressure. Boundary-layer edge properties are used to simplify the application to the entire wing. Figure 5.3.7-2 shows the process used to derive the correlation parameter, ***C***, to apply to the edge properties in establishing the flow turning into a penetration. Therefore, once the local coordinates are established, the predicted internal jet direction can be calculated as

$$\vec{J} = \left(0.176 \times \bar{q}_e\right)\vec{V} + p_e\vec{P}$$

With this definition established, a series of points along the projected debris path were chosen as illustrated in Figure 5.3.7-3 with the symbols. The ***J*** vectors are represented in three dimensions in the accompanying views of Figure 5.3.7-3, with the view from inboard on top and the view looking down on the RCC outlines on the bottom. Due to the double delta shape of the Orbiter wing, and the projected impact path at the juncture, the vectors primarily point to the spar region behind panel 8.In Figure 5.3.7-4 a representation of the RCC insulation system has been added in investigating the impact points of the selected jet penetrations. Due to the vector alignment and insulation configuration the conclusion is that the most likely primary impingement location for an RCC penetration along the predicted foam path is the spar region behind panel 8 or the earmuff region between panels 8 and 9. Table 5.3.7.1-1 provides the selected penetrations and the associated jet direction unit vectors.

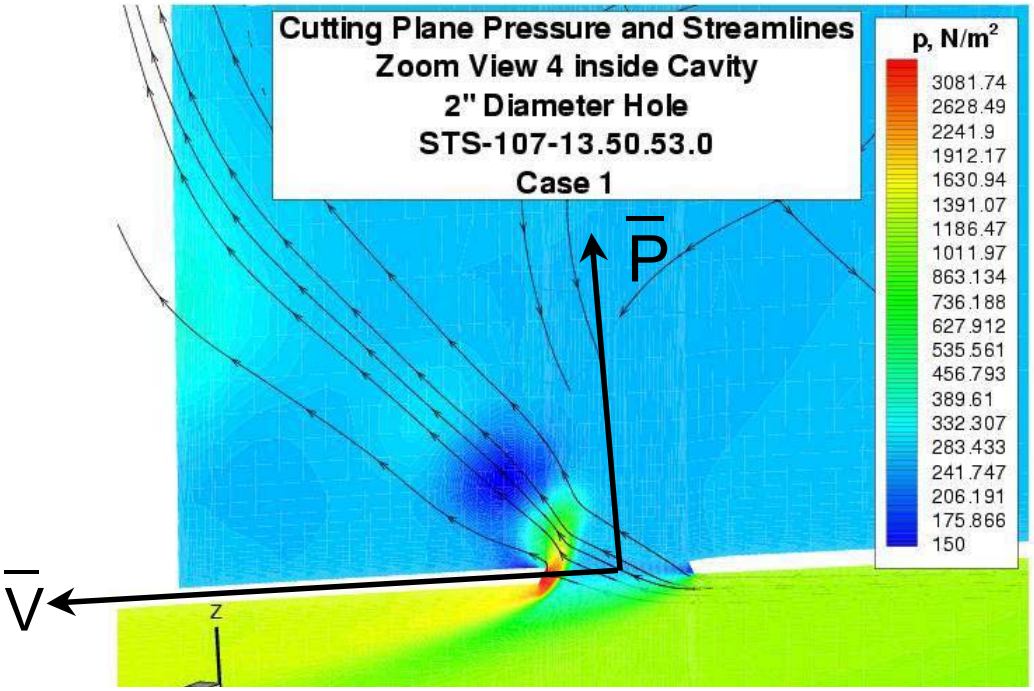

Figure 5.3.7-1 Panel 6 penetration and Jet direction coordinate system.

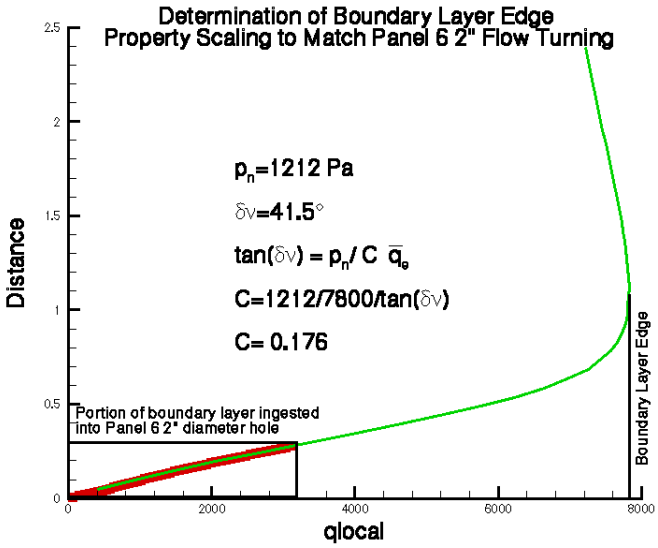

Figure 5.3.7-2 Jet direction correlation parameter derivation

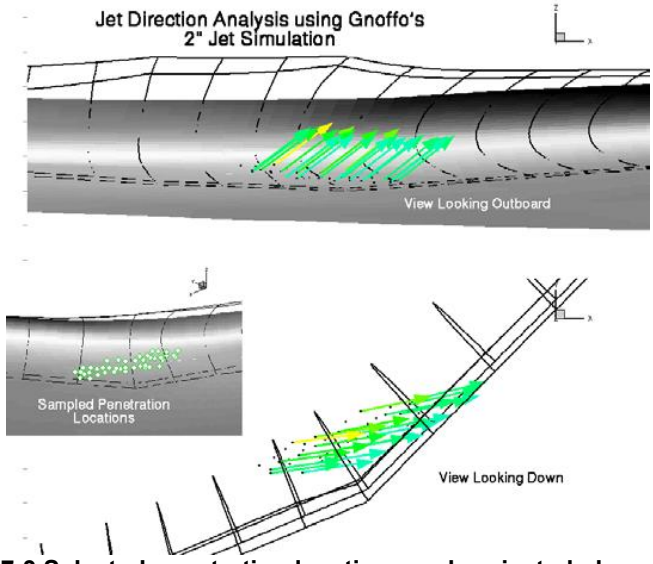

Figure 5.3.7-3 Selected penetration locations and projected plume directions

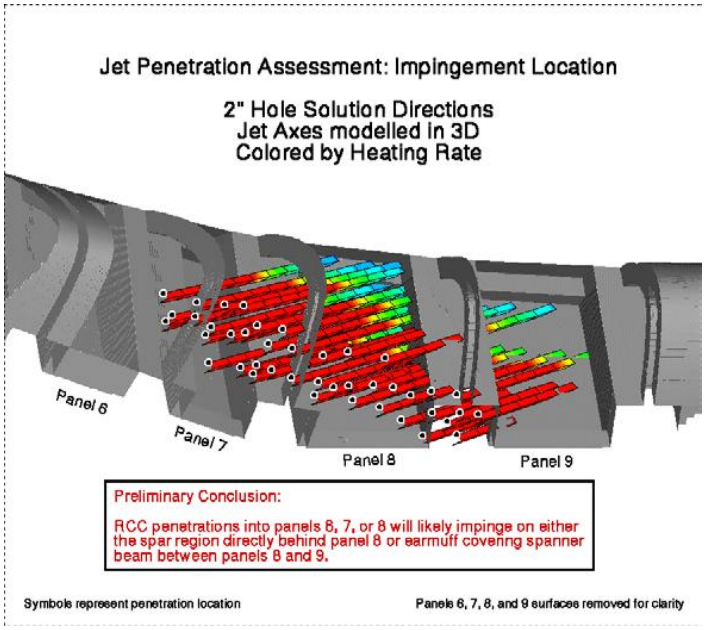

Figure 5.3.7-4 Jet penetration assessment

X	Y	Z	JetX	JetY	JetZ
1087.40	226.40	283.69	0.773	0.185	0.607
1088.09	221.74	282.61	0.775	0.173	0.608
1085.12	224.67	283.66	0.775	0.178	0.606
1082.34	226.31	284.54	0.776	0.179	0.605
1085.03	222.34	283.15	0.776	0.173	0.607
1084.47	218.03	282.33	0.777	0.165	0.607
1082.20	221.60	283.44	0.778	0.169	0.605
1079.10	223.87	284.55	0.779	0.169	0.603
1077.42	221.25	284.19	0.780	0.164	0.604
1079.82	217.54	282.90	0.780	0.159	0.605
1075.67	216.60	283.35	0.782	0.156	0.604
1074.39	220.23	284.52	0.783	0.157	0.602
1069.58	222.38	286.20	0.778	0.164	0.606
1071.82	218.29	284.50	0.784	0.151	0.602
1071.67	214.38	283.50	0.784	0.149	0.603
1067.86	213.76	284.04	0.786	0.145	0.601
1069.25	215.53	284.25	0.785	0.147	0.601
1064.78	218.99	286.31	0.785	0.149	0.601
1062.50	215.94	285.84	0.785	0.149	0.602
1065.37	212.72	284.25	0.788	0.141	0.600
1061.87	210.19	284.23	0.790	0.137	0.598
1058.09	213.32	286.04	0.792	0.135	0.596
1066.90	210.78	283.45	0.787	0.142	0.601
1058.65	208.86	284.49	0.792	0.134	0.596
1054.96	211.26	286.07	0.794	0.129	0.594
1051.40	211.92	287.24	0.797	0.121	0.592
1054.82	214.19	287.20	0.796	0.124	0.592
1050.94	209.88	286.56	0.797	0.122	0.591
1054.97	205.85	284.35	0.794	0.130	0.594
1057.20	206.49	284.10	0.793	0.132	0.595
1049.54	208.27	286.30	0.798	0.121	0.591
1045.30	210.44	288.34	0.801	0.104	0.590
1047.57	212.37	288.55	0.803	0.102	0.588
1046.34	206.93	286.58	0.798	0.119	0.590
1043.32	206.24	287.06	0.800	0.114	0.589
1041.77	207.76	288.11	0.806	0.104	0.583
1040.48	202.72	286.38	0.802	0.107	0.588
1036.79	205.16	288.31	0.810	0.087	0.581
1040.43	203.92	286.85	0.801	0.108	0.589
1046.73	205.56	285.99	0.797	0.119	0.591
1050.73	202.89	284.32	0.795	0.126	0.593
1056.37	207.78	284.63	0.793	0.132	0.595

Table 5.3.7.1-1Jet penetration directions

5.3.7.2 Plume heating distribution

As the investigation team narrowed in on a preferred working scenario, the internal flow team was asked to pull together internal heating distributions for assumed penetration locations that incorporate not only the primary impingement heating, like that described in 5.3.3.2, but also convective heating rates to the

surrounding internal TPS surfaces. Based on an assumed hole location and size, internal plume impingement environments were created that incorporate heating distributions for the panel 8/9 region based on assumed internal direction (5.3.7.1), degree of secondary splash heating, and geometric flow shadowing effects. Full 3-D CFD results for panel 7/8 penetrations were not yet complete, so the best fully coupled CFD solution with internal heating was used as a basis. Given the degree of engineering involved in producing the environments, uncertainty values of +/- 50% were applied to the final results and additional comparisons to higher fidelity CFD results were pursued to provide independent assessment of the expected internal heating.

5.3.7.2.1 Selection of assumed hole location

The present working scenario includes penetration of RCC from panels 6-9 with subsequent spar breach at 488 seconds from entry interface. The team chose a single penetration location for complete analysis in order to ballpark the hole size required to match the flight data for the panel 9 spar and clevis temperature measurements and the spar breach time of 488 seconds from E.I. Given similar heating analysis completed early in the investigation using the basic MMOD plume model, 5.3.3.2, hole sizes of 4, 6, and 10 inches in diameter were chosen and anticipated to bound the data. Hole location was chosen to maximize the predicted primary impingement heating rate, based on the internal flow direction analysis of 5.3.7.1. Using the simple 1-D plume heating model, the plume vectors of Table 5.3.7.1-1 were assessed and vector # 18 chosen and colored red in Figure 5.3.7-5. The anticipated heating rates at the primary impingement point are increased both by the short distance to the earmuff and the small radius of curvature on the TPS edge. The coordinates of the assumed penetration are X=1065 in, y=-219 in, and z= 286.3 in.

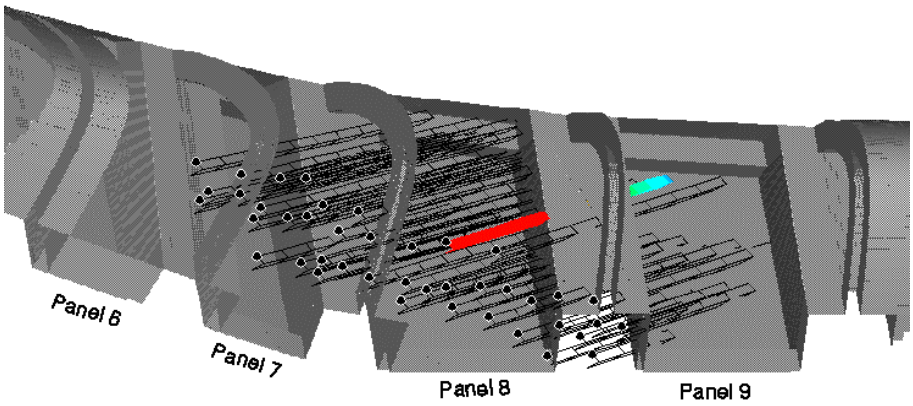

Figure 5.3.7-5 Panel 8 lower surface penetration location

5.3.7.2.2 Distribution methodology

Internal heating distributions are based on a modification of the baseline engineering methodology for holes as outlined Section 5.3.3.3 and take advantage of ingested flow enthalpy calculates using the methodology in Section 5.3.2 and a computed internal pressure using the methodology of Section 5.3.5. The local axis of the plume is assumed to align along the predicted direction of 5.3.7.1, independent of the hole diameter. This assumption was made due to the lack of available internal CFD at the time. (In truth, the larger holes will allow more transverse momentum to enter the hole and cause the jet to hug the interior RCC surface more than the present methodology based on 2" diameter hole results, but the heating distribution will only be shifted in space with little impact on peak heating values.) The radial position correction of the baseline methodology is replaced with computed three-dimensional factors as a function of hole size, which are presented in the results section below. Trajectory corrections remain the same, resulting in a final equation of

$$\dot{q}(x,y,z,t,d_{hole}) = \dot{q} \Big/ \dot{q}_{plate}(x,y,z,d_{hole}) \times \frac{\bar{q}_{\infty}(t)}{\bar{q}_{\infty}(488)} \times \frac{V_{\infty}^{2}(t)}{V^{2}{}_{\infty}(488)} \times \dot{q}_{plate}(d_{hole})$$

The baseline heating values, q_{plate}, are given for each hole size, computed for a trajectory time of 488 seconds from E.I., in Table 5.3.7.2-1.

10” Hole	55.9 Btu/ft^{2}sec for plate
6” Hole	30.1 Btu/ft^{2}sec for plate
4” Hole	27.1 Btu/ft^{2}sec for plate

Table 5.3.7.2-1 Panel 8 penetration heating values

5.3.7.2.3 Correlation and geometry correction factors

The methodology was adjusted based on the LAURA 2” diameter hole panel 6 penetration calculation of Section 5.3.6.1.4.1. Interior surface heating rates are extracted for the primary impingement region and the secondary splash surface. Corrections to the baseline model are made to bring the results into line with the CFD results. Comparison lead to a narrowing of the distribution by raising the values of Table 5.3.3.3-1 to the 1.6 power (also indicated by the comparisons in Figure 5.3.3-7) and the development of a splash heating approach to account for flow turning and secondary stagnation flows anticipated in the RCC cavity. Examination of the LAURA results indicated flow physics similar to a forward-facing step. Forward-facing step amplifications of 3.5 times the undisturbed value are appropriate for the observed internal Mach numbers and produced a good comparison on the splash surface of Figure 5.3.7-6. Secondary stagnation values are within 20% and the engineering methodology remains conservative as the flow moves down the surface.

In addition to secondary splash factors, other corrections to the baseline methodology are applied to account for “shadowing,” where the flow cannot directly impinge on the surface, local surface radius of curvature effects to earmuff edges and a general convective heating equal to three percent of peak values. The final geometry corrections are presented in Figure 5.3.7-7. Spar and carrier panel surfaces behind panel 8 are assumed to be secondary splash surfaces with a preference for the flow to splash on the upper surface and hence have amplification factors from 1 to 3.5. The edge of the panel 8/9 earmuff facing the assumed breach location shows high amplification factors to correct for local radius of curvature effects. The region behind panel 9 cannot be directly impinged upon from the assumed location and therefore has shadowing corrections that decrease the heating.

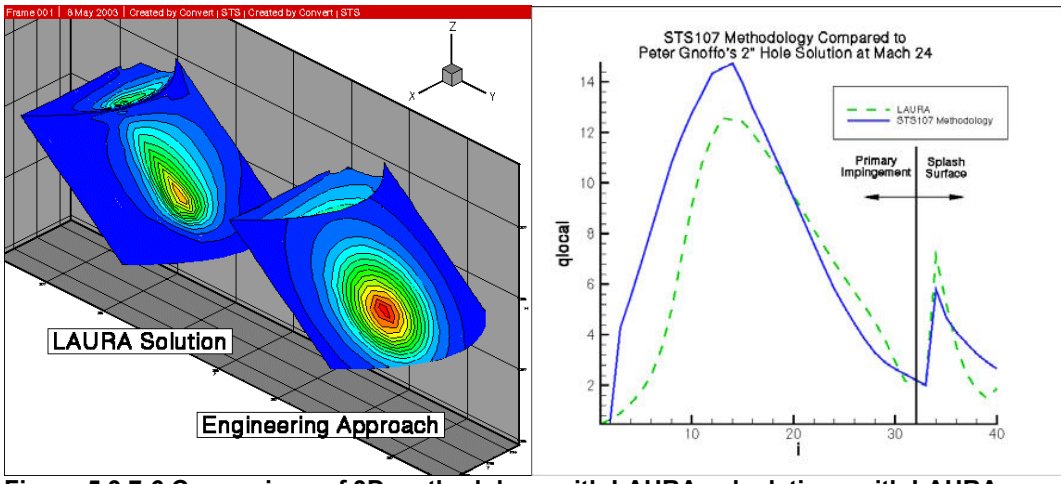

Figure 5.3.7-6 Comparison of 3D methodology with LAURA calculations with LAURA

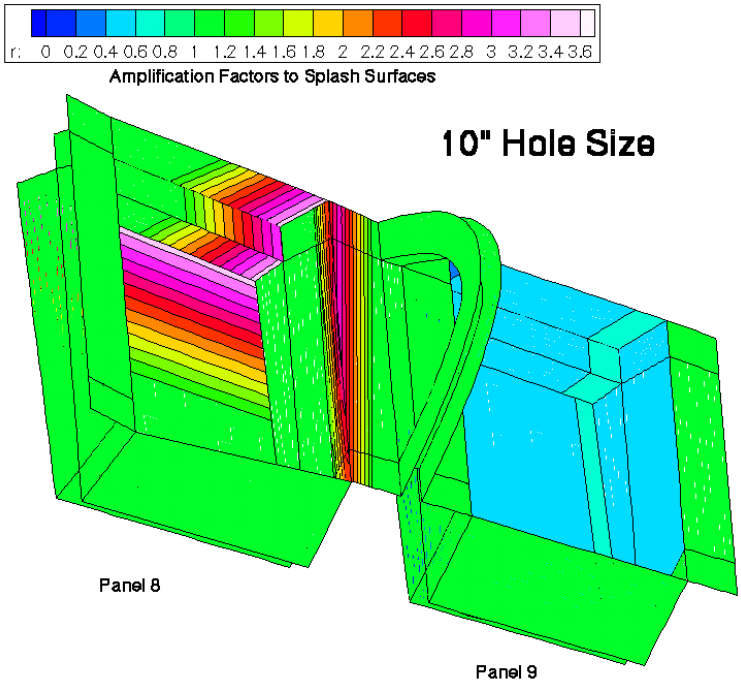

- Corrections given on a zone by zone basis to partially account for
  1. Secondary splash surface (based on forward facing step and panel 6 hole comparisons)
  2. Radius of curvature corrections to modeled geometry (Spanner beam insulation modeled with square corners, corrected to 1" radius heating)
  3. Line of sight shadowing and separation (panel 9 spar heating)
  4. Background heating values of 3% assumed on backward facing surfaces (on par with panel 6 and T-seal simulations)

Figure 5.3.7-7 Geometry correction for heating

5.3.7.2.4 Resulting Distributions

Engineering predicted heating distribution factors are presented in Figure 5.3.7-8 through Figure 5.3.7-10. All cases show a peak heating point on the earmuff between panels 8 and 9 at the edge of the TPS along the jet axis. By comparison, as the hole grows larger, so does the high heating region, with higher splash heating factors to secondary surfaces. Peak amplification factors do not change since the driving factor on the earmuff edge is local curvature, which is consistent between predictions. Keeping the previous equation and Table 5.3.7.2-1 in mind, however, shows that while the geometry amplification factors are the same, the 10" hole will experience significantly higher heating to the entire internal geometry.

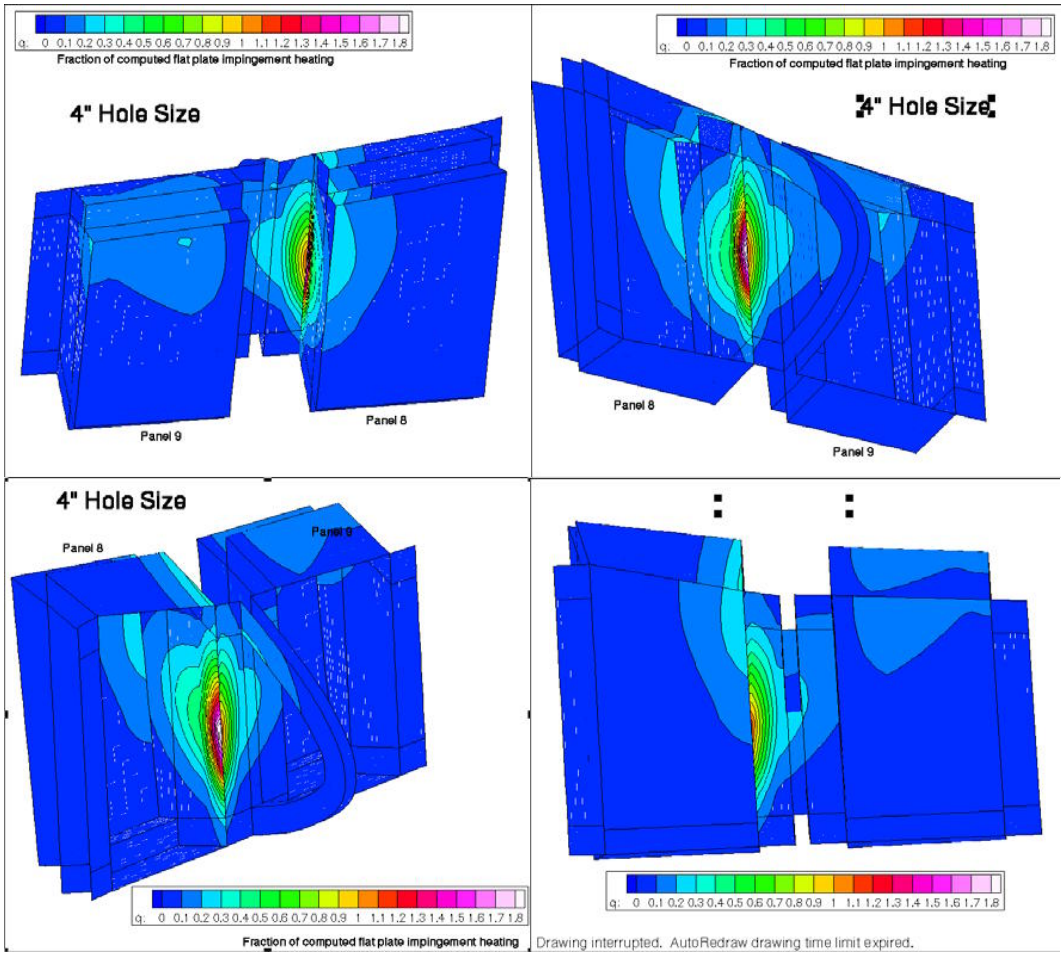

Figure 5.3.7-8 Heating factors for a 4" diameter hole in panel 8 lower surface

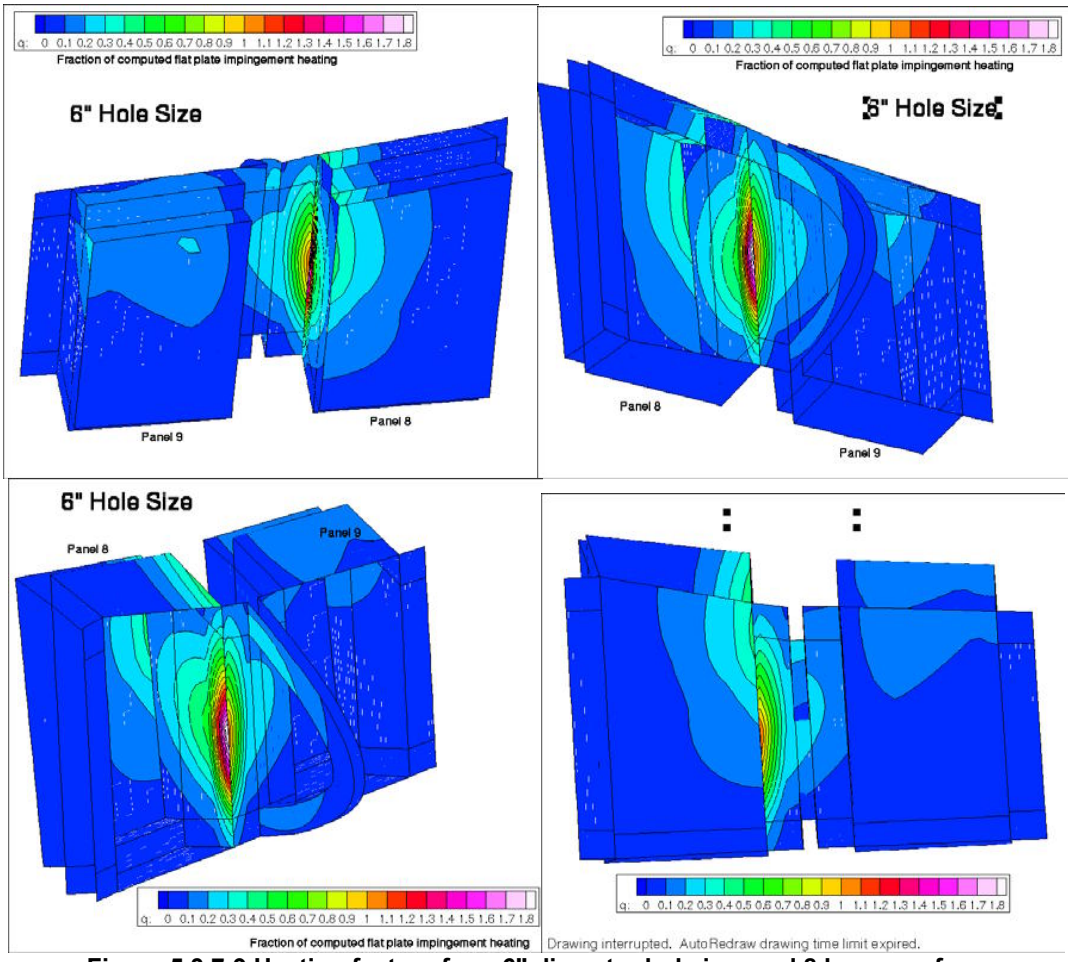

Figure 5.3.7-9 Heating factors for a 6" diameter hole in panel 8 lower surface

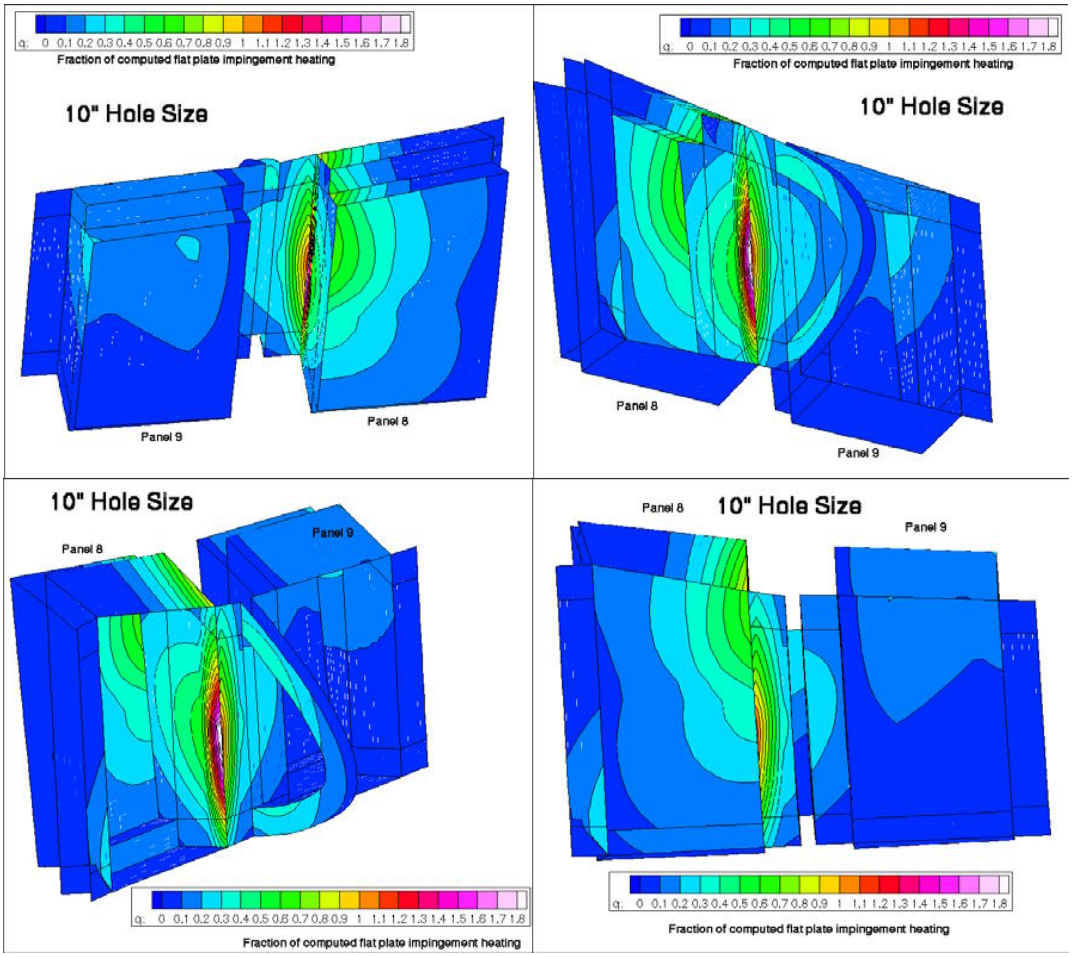

Figure 5.3.7-10 Heating factors for a 10" diameter hole in panel 8 lower surface

5.3.7.2.5 Comparison with 3D CFD/DSMC

The final STS-107 3-D plume heating methodology was developed based on very limited CFD results and represented a "highly engineered" environment for thermal analysis. It was desired to compare the engineering methodology to high fidelity CFD results for STS-107 type of geometries and assess the quality of the engineering predictions used for the subsequent thermal analysis. Given the complexity of the problem, the comparisons represent more of an independent assessment than a validation of the methodology, primarily since time did not allow a second loop through the process incorporating CFD lessons learned. Rather, the comparisons focused on gross fluid dynamic features and qualitative assessments. Comparisons with previously presented CFD results are given in Figure 5.3.7-11 through Figure 5.3.7-14.

Two types of comparisons with the DSMC results of 5.3.6.1.5 are displayed in Figure 5.3.7-11. On the left of the figure, both sets of data have been normalized by the peak impingement heating values on the panel 8/9 earmuff. The DSMC results fully couple the internal and external flow fields and provide additional support for the predicted internal jet direction since both methodologies predict peak heating values in the same location. DSMC results also provide an independent source for secondary splash heating to the spar region behind panel 8, again inline with the engineering methodology. Shadowing of the panel 9 spar region and some enhanced heating to the panel 9/10 earmuff are also predicted by the DSMC results inline with engineering assumptions. The right side of the figure provides a comparison of predicted heating magnitudes with the STS-107 engineering methodology. The engineering method predicts higher heating by roughly a factor of two. However, the engineering methodology is based on continuum assumptions and the calculations are made at rarefied condition so the conservatism is not surprising. Furthermore, the engineering method heat flux scaling appears to represent the physics well, given the two order of magnitude change in dynamic pressure.

Application of the engineering approach to the uncoupled panel 7 6" hole case, section 5.3.6.1.1, is displayed in Figure 5.3.7-12. Adjustments to the engineering methodology were made to account for the normal flow through the penetration, due to the uncoupled nature of the solution, and correction for total enthalpy variance. Comparison with two levels of grid refinement highlights a couple of conclusions. First, the STS-107 engineering methodology achieves qualitative agreement in terms of the size of the impinging jet, matching the spreading as the jet expands into the interior of the RCC. Peak heating values achieve excellent match with the medium grid results on the left. However, as more flow structure is captured with mesh refinement, the jet peak heating region changes shape and amplitude due to secondary flow patterns acting to self-focus the jet, enhancing peak heat transfer rates. While there remains a moderate level of unsteadiness in the results, as much as a factor of two increase over the engineering methodology is indicated. This phenomenon is independently predicted in the panel 8 results of section 5.3.6.1.4.2. The engineering methodology does not account for these flow interactions.

Figure 5.3.7-13 points out the dramatic change in internal heating distribution due to the external flow coupling. Here the same hole location produces a very concentrated, high enthalpy flow impingement on the interior rib surface of panel 7 just downstream of the hole. Examination of the engineering methodology indicates that the jet would, indeed, impact the rib, there is no automatic correction applied to account for it. The flow that strikes the rib has all of its downstream momentum arrested and winds up producing only moderate heating to the spar behind panel 7 while the STS-107 methodology shows a panel 8 spar impingement with elevated heating rates. Figure 5.3.7-14 shows the impact of local geometry changes to the distribution once more, as the earmuff between panels 7/8 is added and greatly changes the result. Fortunately, the additional interaction of the rib splash flow with the earmuff geometry produces heating distributions and magnitudes in line with the engineering methodology. While this is clearly a case of two wrongs make a right, it lends support to the use of the engineering approach for thermal analysis and does not negate the resulting outcome the thermal analysis to the panel 8 and 9 spar surfaces. RCC rib heating is handled by a separate modeling approach; section 5.3.3.6.5.

Overall, thermal analysis performed with the provided internal heat flux distributions will produce results consistent with CFD results, given the high levels of uncertainty applied to the approach. Final results may slightly change the hole size or hole location, but not invalidate the scenario.

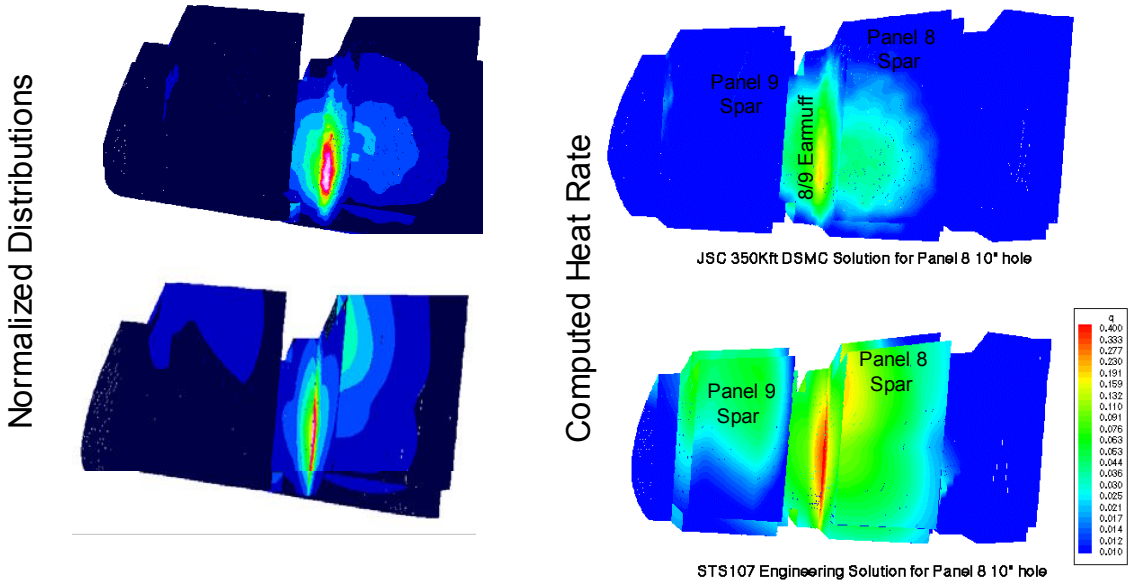

Figure 5.3.7-11 Comparison of engineering methodology with DSMC calculations at 350,000 feet

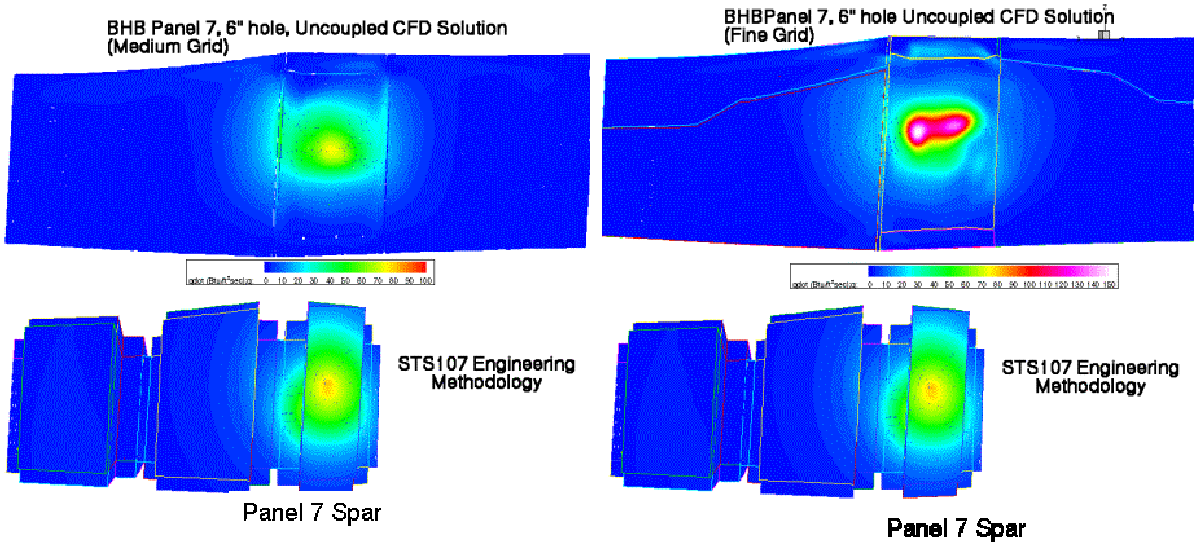

Figure 5.3.7-12 Comparison of STS107 methodology with panel 7 6” uncoupled CFD

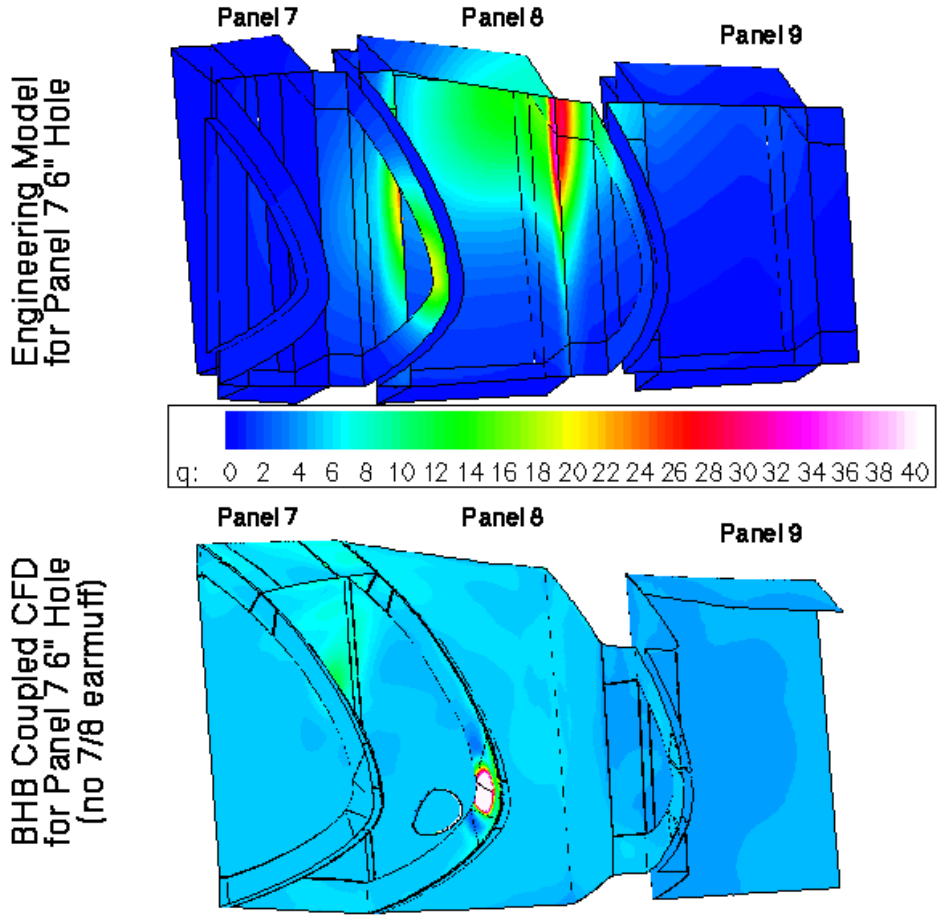

Figure 5.3.7-13 Comparison of STS107 methodology with panel 7 6” coupled CFD

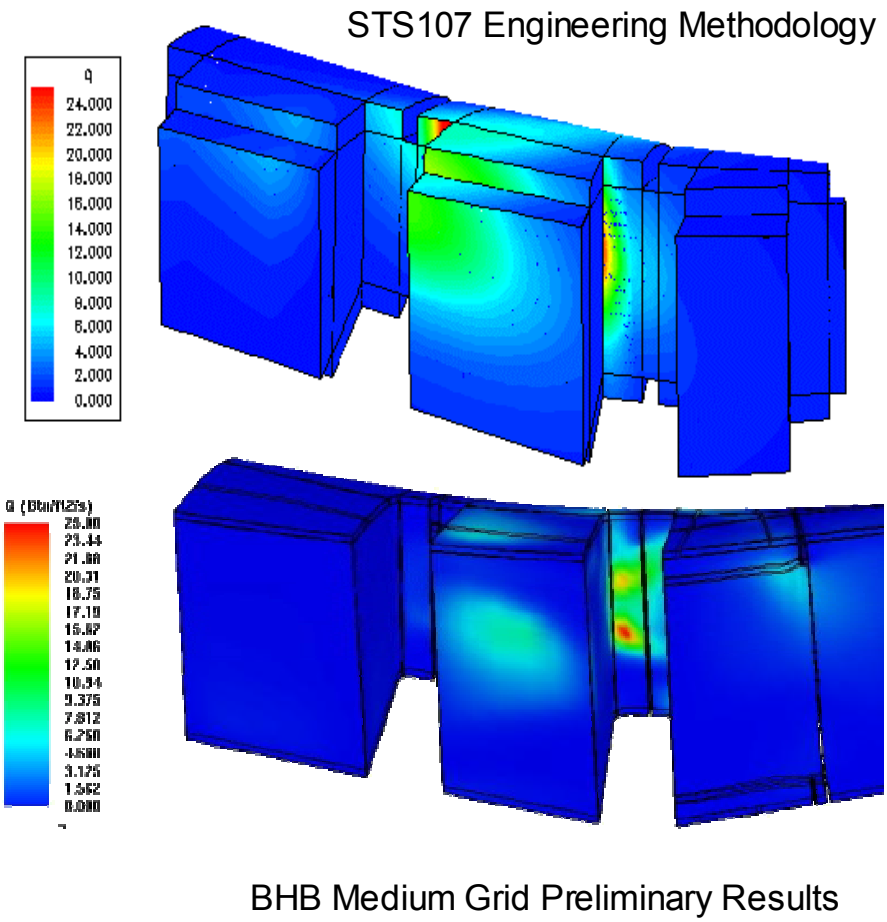

Figure 5.3.7-14 Comparison of STS107 methodology with panel 7 6" coupled CFD with earmuff

5.3.7.3 Assessment of Secondary Plume/Spar Breach

Thermal analysts keyed into wire burn-through times early in the investigation as a piece of known information that may be use to identify breach time, location, and size. The plume methodology of section 5.3.3.3 has been utilized in such assessment with one large, early assumption: that the plume enters through the spar normal to the surface. Early investigation activities, in fact, depended on the direction assumption with no conflicting information until the first coupled CFD results came out of Langley (5.3.6.1.4.1). With the additional knowledge that a significant fraction of transverse momentum is carried through the RCC breach, the question was raised about the secondary breach direction.

Secondary breach fluid dynamics are significantly different than RCC penetration for several reasons: 1) the internal RCC cavity geometry offers many surfaces to arrest momentum, 2) the highest heating point to the spar insulation is likely in a stagnant flow, high pressure region, 3) internal shock structures absorb significant portions of available flow energy, and 4) the flow must turn through several inches of structure and insulation rather than just 0.25 inches of RCC. With this information in hand, investigative activities continued assuming normal jet penetration. Final CFD calculations have continued to support the conclusion that the jet, at least initially, penetrated the spar normal to the surface.

Figure 5.3.7-15 represents the insight CFD results where the jet penetration direction was assumed normal to the spar. In the solution the jet structure remains coherent and impinges on the wheel well wall before being turned downstream and circulating through the mid wing volume. Figure 5.3.7-16 displays similar fluids dynamics from a two dimensional CFD solution where the flow initially carries streamwise momentum through the RCC breach and impacts internal geometry in the region where a hole is placed in the spar. This computed internal flow direction and mid wing fluid dynamic structure match the Figure 5.3.7-15 results quite well. While the two dimensional results modeled a large structural interference, the

BHB results of Figure 5.3.7-17 illustrate that even a relatively small geometric feature, in this case an RCC rib, can sufficiently absorb momentum to cause the jet to change direction completely. Any secondary burn-through of the spar in this case would clearly produce a normal jet through the breach.

In providing this assessment, however, the best that can be said is that **initially** the jet was certainly produced normal to the secondary breach surface. Given heating rates many times external values, eventually the primary impingement zone will be completely melted to the dimensions of the jet and there is then nothing to inhibit the free flow of the jet into the mid wing volume with full momentum. The time required to achieve such a state is entirely dependent on the initial damage and the TPS surface that is directly impinged.

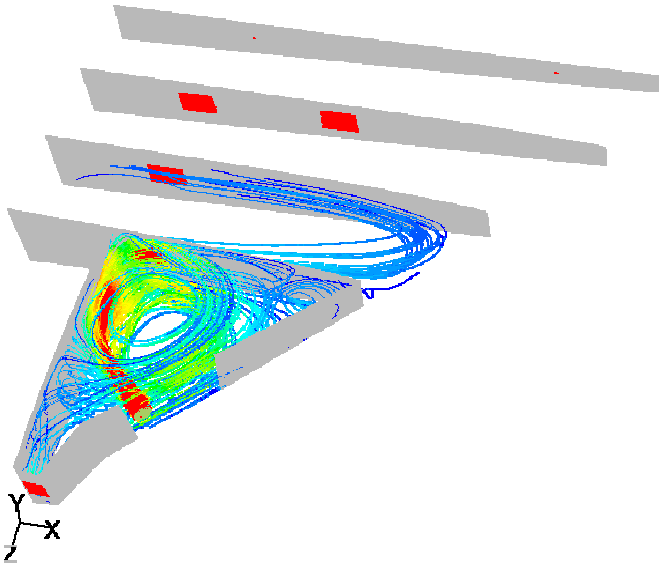

Figure 5.3.7-15 Assumed normal direction flow field

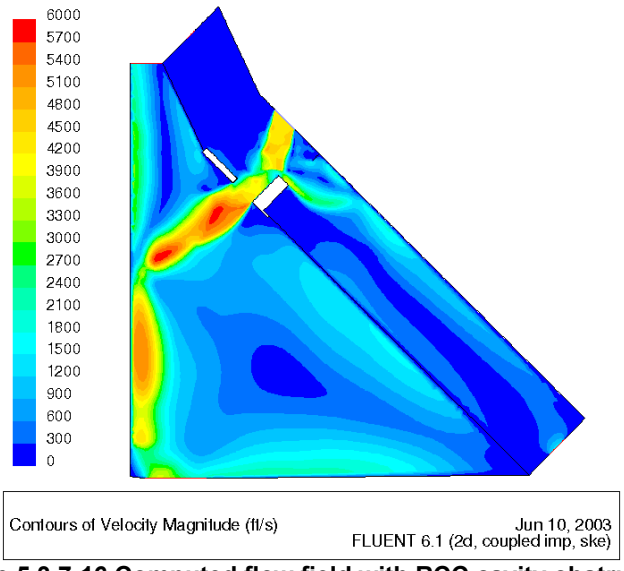

Figure 5.3.7-16 Computed flow field with RCC cavity obstruction

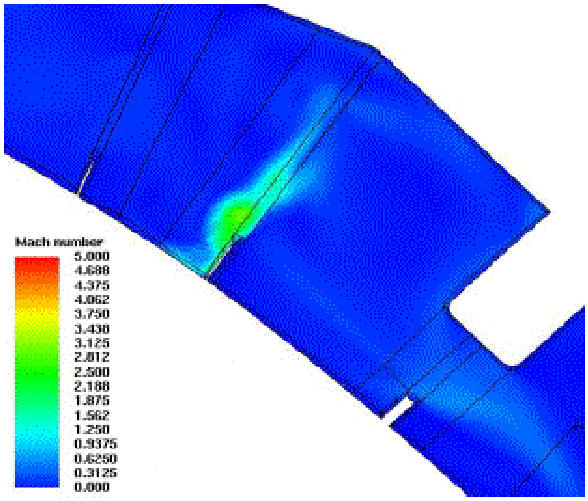

Figure 5.3.7-17 BHB Panel 7, 6" hole coupled internal flow field

5.3.7.4 Panel 8 penetration fluid dynamics and forensic evidence

Full three-dimensional CFD solutions for the panel 8 penetration provide invaluable insight into the flow inside the RCC that led to the eventual demise of the wing structure. Examination of the fluid dynamics and flowfield properties provides an explanation for, and independent verification of, hardware forensic evidence of a panel 8 breach. Figure 5.3.7-18 displays the internal streamline patterns for a 10" breach into the lower panel 8 surface. A supersonic stream of high-energy flow enters and directly impinges on the 8/9 earmuff, producing locally high pressures and heat rates. The flow re-expands and creates a supersonic "splash" flow that jets inward and upward into the panel 8 spar region before recirculating around to the panel 8 upper RCC inner surface and eventually exiting through the vents. This resultant flow field directly explains four key forensic features seen in the debris.

5.3.7.4.1 Inconel deposits on panel 8 inner surface

The initial deposits on the backside of the surviving panel 8 RCC have been analyzed and identified as Inconel nodules. The flow field predicted by BRPP provides the transport mechanism for the Inconel deposits. Initially high speed, high temperature flows impinge on the Dynaflex insulation, melting the outer Inconel surface. The melted/vaporized Inconel is deposited to the back of the panel as the supersonic tail jets scrub the panel 8 spar insulation and then the back side of panel 8.

5.3.7.4.2 Panel 8 and 9 rib erosion (knife-edging)

The BHB panel 7 CFD solution predicted heating rates over 200 Btu/ft^2-sec to the panel 7 interior rib surface in the primary jet impingement zone. BRPP results to the 8/9 earmuff are also over 200 Btu/ft^2-sec for the panel 8 penetration. Examination of Figure 5.3.7-18 shows how a slight adjustment of hole location would place the primary jet impingement heating region directly on the RCC rib. The directional aspect of the knife-edging observed in the debris can only be explained with a jet flowing internally from panel 8.

5.3.7.4.3 Erosion of panel 9 lower carrier panel tiles

Examination of panel carrier panel tiles shows clear indications of flow out from the corner of RCC panel 8, through the horse-collar seal and out and over the panel 9 lower carrier panel with significant erosion patterns. In order to produce such a flow, the internal pressure must be significantly higher than the lower surface pressure. In addition that erosion pattern indicates a coherent jet. Figure 5.3.7-19 shows the local pressure field for the panel 8 breach in the outboard lower panel 8 corner. Pressure values of 0.3 psia are greater than 2.5 times the external surface pressure at the same location on the lower surface of the Orbiter, more than sufficient to drive highly energetic flow out through the horse-collar. Of great significance is the localized aspect of the distribution: regions merely inches from the secondary stagnation point in the corner of the panel do not possess sufficient pressure to drive flow out onto the lower surface.

5.3.7.4.4 Panel 8 upper carrier panel "chimney" tile

Preferential jet splash patterns off of the earmuff surface and up and into the panel 8 spar region focus high temperature gases directly into the RCC leeside vents at the upper carrier panel. With the poor

radiation relief of tile to RCC, enhanced heating will quickly elevate the tile surface above the slump temperature and open the vent even more. Debris forensic evidence contains a panel 8 upper carrier panel tile with deposit buildup consistent with the internal insulation materials over 0.4" thick. Examination of Figure 5.3.7-20 shows the jet shape as it comes off the earmuff clearly heading directly into the region where the tile would be located, carrying with it any melted/vaporized material for deposit to the relatively cooler surface of the tile.

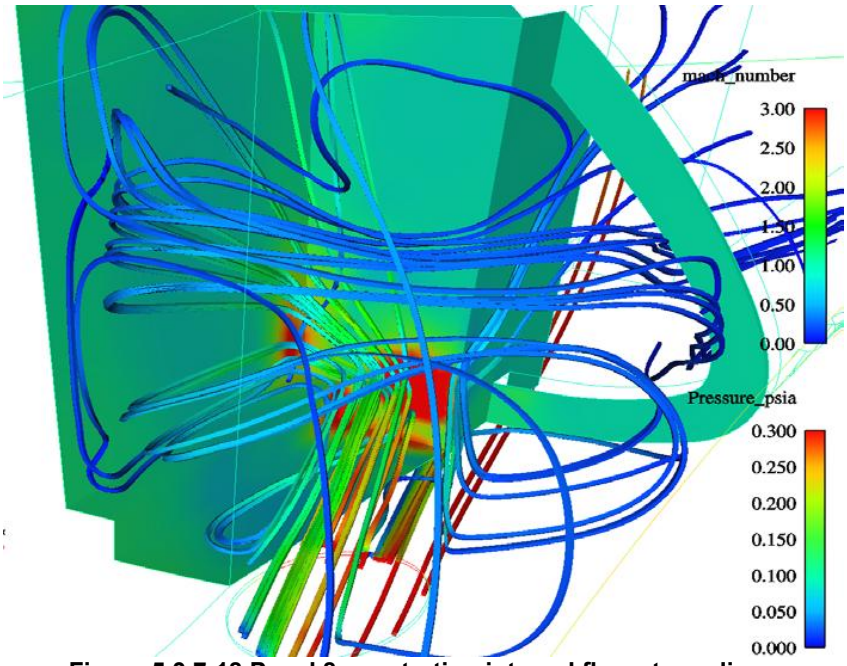

Figure 5.3.7-18 Panel 8 penetration internal flow streamlines

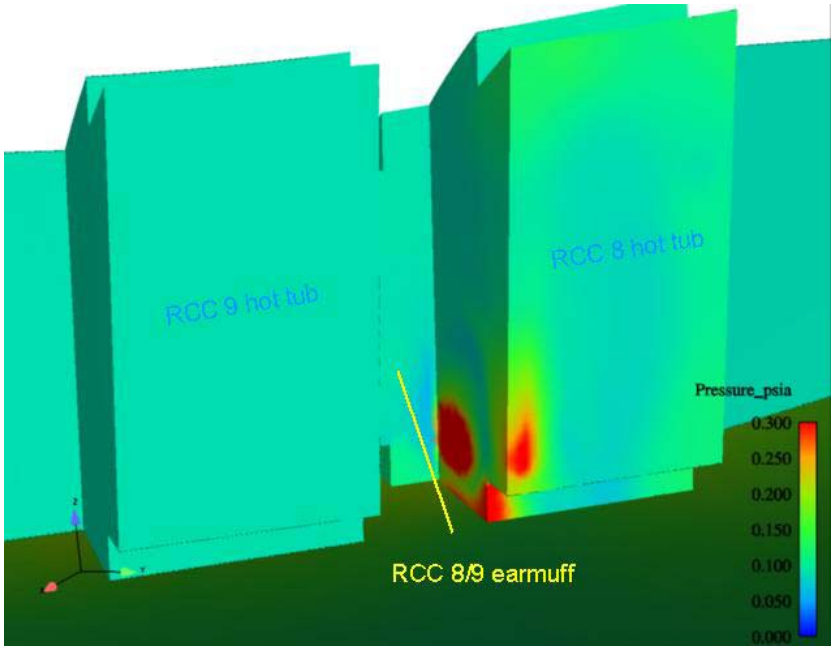

Figure 5.3.7-19 Panel 8 penetration internal stagnation pressures

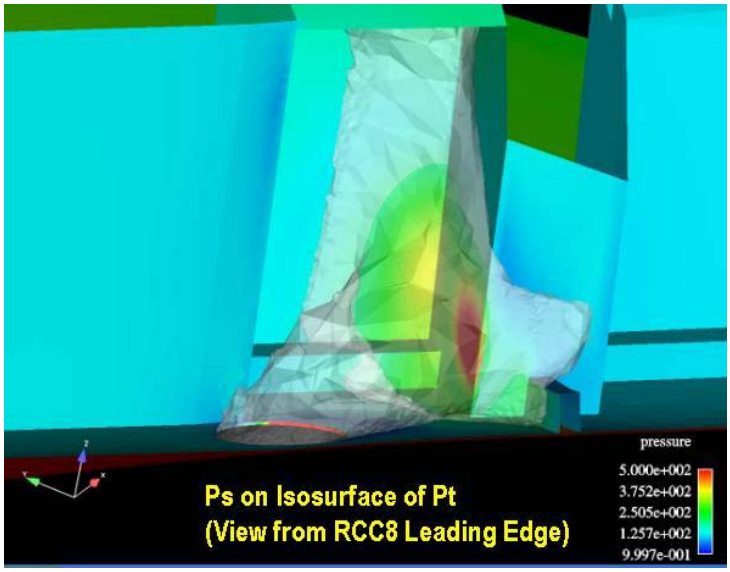

Figure 5.3.7-20 Panel 8 penetration internal jet shape

5.4 Aerothermodynamic Environments Summary

Aerothermodynamic analysis and testing has been conducted in support of the STS-107 Columbia accident investigation. The work presented above (in sections 5.1 – 5.3) explored various off-nominal external and internal aerothermodynamic events experienced by STS-107. The external aerothermodynamic analysis examined changes to the external Orbiter environment that result from a large matrix of possible damage types and locations. The internal aerothermodynamic analysis examined environments due to high temperature gas ingestion from the varying extent, location and type of damage. These analyses and test data were used to provide substantiating evidence in support of the Working Scenario: Damage to RCC Panels 5 through 9. In order to be considered as substantiating, the aerothermodynamic data had to be, (1) consistent with the results of data provided by the other technical disciplines and reported in this document, (2) consistent with evidence gathered through the recovered Columbia debris and data mapping, and (3) consistent with any other relevant evidence that became available during the investigation. Particularly important in this process of substantiating the aerothermodynamic data was correlating the aerothermodynamic team's analysis results with the data obtained from the STS-107flight instrumentation. Since the exact size, shape, and location of the damage was unknown, the process taken was to assume a damage configuration and evaluate the results on the aerothermodynamic environment. This was done by comparing the analysis or test results with the available flight data, as in the case of the surface thermocouples, or by providing the environments for thermal analysis to determine if the provided heating environment, coupled with the thermal model, was consistent with other data from the Orbiter.

Investigations of changes to the external environments through wind tunnel and numerical analyses have yielded much critical information. Although the chin panel and vent nozzle data could not be explained by these results, the side fuselage and OMS pod surface temperature and skin temperature responses were shown to be consistent with progressive wing leading edge damage. The extensive amount of wind tunnel test data obtained at Mach 6 Air and CF_4 facilities was mostly qualitative; however, the testing methods allowed for the rapid evaluation of multiple damage configurations and guided the focusing of the damage scenarios that were examined with computational analysis. High quality numerical simulations of the Orbiter with wing leading edge damage provided engineering information on leeside flow field features and surface heating. The combined efforts of numerical analyses and wind tunnel testing demonstrate that the reduced heating effect seen from the early part (< EI + 480 sec.) of the STS-107 flight instrumentation was caused by high pressure flow entering a hole on the windward side of the left wing leading edge and exiting to the lee side either through the leeside RCC channel vents or in combination with some localized leeside RCC/upper carrier panel breach. Analysis of the mass flow rates exiting the tested vent area

indicate that a hole size on the WLE windward side on the order of 80 square inches at flight scale was required to provide sufficient flow to affect leeside surface heating in a way that was consistent with flight data. The test and analyses data also showed that the increased leeside heating (side of fuselage and OMS pod) that occurred after EI + 480 seconds had to be associated with a significantly damaged leading edge; either severely damaged or missing upper carrier panels (more than one), the loss of significant portions of upper RCC panel(s), or even upper wing skin just aft of the WLE.

Supporting evidence for these damage geometries was generated with CFD tools, providing critical information at flight conditions. These CFD simulations represent a substantial effort, but they succeed in identifying the source of increased side fuselage heating as a jet emanating from a damaged RCC leading edge. This jet convects high-temperature/high-pressure gas onto the Orbiter leeside where, in sufficient strength, it both severely perturbs the leeside vortex flow field and impinges directly on the side fuselage. This side fuselage jet impingement was demonstrated to generate surface heating increases of more than a factor of ten. Damage configurations involving mass and energy convection to the Orbiter lee side, with less strength due to smaller leeside damage area, lack the strong coherent jet that impinges on the side fuselage. However, this weaker leeside flow disturbance still generates perturbations to the leeside vortex structure leading to movement of the wing strake vortices and the heating footprints associated with their flow structures. The identification of leeside surface heating differences was critical to interpreting these two classes of STS-107 flight data. The first being the early decrease in OMS pod and side fuselage heating, and the second being a substantially increased side fuselage heating together with moderate OMS pod heating increases.

The accuracy of leeside flow field computational simulations remains a concern for several reasons: (1) A comprehensive effort to validate leeside heating predictions has never been attempted. (2) The actual shape, location of the damage will never be known. (3) The progressive nature of the damage and the complicated mixed internal/external flows implies rapidly changing time dependent phenomena and hence unsteady solutions. (4) Details of modeling the proper internal cavity geometry and surface boundary conditions (both within the cavity and on the lee side) are beyond the scope of the currently available CFD methods. Nevertheless, the CFD simulations provided critical flow field information at flight conditions that allowed for an engineering perspective to draw the previously discussed conclusions. Similarly, questions remain about whether the Mach 6 air or Mach 6 CF_4 facility provide a more accurate representation of the high Mach number re-entry conditions of the Orbiter leeside flow field. However, these questions are less critical when considering the data in an engineering context and noting that the computational techniques are solving the equations for the conservation of mass, momentum, and energy and that both facilities reproduce the same basic physics of hypersonic flow.

In order to provide the internal heating environments in support of thermal analysis, new tools and techniques were developed. These included a process for the calibration and verification of the plume heating model, the development of a coupled equilibrium air venting and thermal model of the entire left wing, and the application of available CFD and DSMC computational tools on internal flows with complex geometry. As was discussed, the heating to an object is a function of its geometry. This problem is made even more difficult when the size, shape, and location of the original penetration is unknown, the internal configuration is complex and not designed for a convective environment, and the configuration is changing over the period in question. Thus, in order to provide internal heating environments, a static geometry strategy was pursued. For cases where a penetration in RCC panel acreage was assumed, a round hole was evaluated for simplicity. The area of the hole was the more critical factor because it determined the amount of energy ingested.

The engineering plume heating model used in the investigation had been previously applied for evaluation of micro-meteoroid penetrations of 0.25” to 1.0 “. For this work, holes as large as 10” in diameter were assessed. Experimental data for impinging plumes in a relevant environment were not readily available. This demanded that a process be developed to verify the applicability of the model to these larger diameter penetrations. The first step in the process was to analyze a series of relevant plume flows with two CFD codes. As there were no experimental data available, the CFD analysis relied on current best practices to estimate heat rates due to impinging plumes. Two CFD codes were run independently to develop confidence in the plume heating results. With confidence in the CFD established, the CFD results were compared to the engineering plume model at the same conditions. The engineering plume heating model was shown to compare to within +/- 30% of the CFD solutions. This plume model was used to evaluate plume heating on the wire bundles, wheel well wall, and the interior of the upper wing skin, as well as the

primary penetration in the WLE cavity. Arc jet tests were pursued to provide another source of verification of the plume model, the results of which are currently being evaluated.

An equilibrium air coupled venting and thermal model of the entire left wing of the Orbiter was developed principally to provide the best assessment possible of where the mass and energy of the high temperature gas was propagating within the wing outside of the direct plume impingement zone. This allowed for the evaluation of various penetration sizes and their effect on the interior surfaces and mass and energy distribution. This tool showed the internal compartment pressure and temperature effect that result from primary and secondary penetrations on the WLE, as discussed above, and a penetration of the wing spar. For the case of a 10" diameter hole in the wing spar behind RCC panel 8, it was shown that there was sufficient energy ingested to result in significant thermal damage to the interior of the intermediate wing prior to LOS. The case was used as substantiation for the configurations that were assessed for structural deformation. It also showed that the majority of the high temperature gas would flow towards the wing glove payload bay vent. These results provided the boundary conditions for CFD analysis of the interior wing volume.

CFD analysis was performed on the flow of the wing interior to provide insight into how the high temperature gases entering the wing from a breach of the spar behind RCC panel 8 would behave. The results of these analysis showed that a plume would remain coherent until impacting the wheel well wall and a majority of the flow would circulate back towards the 1040 spar vent as discussed above. The data from this analysis were used to update the heat transfer coefficients in the coupled vent / thermal analysis tool. Also, the analysis was used to assess whether or not an obstruction in the WLE cavity would be enough to redirect the flow such that it would enter into the wing interior normal to the spar. This assessment is important in that it would dictate the size of hole necessary to burn the wire bundle at the observed rate because of the distance involved in reaching the bundle from the WLE spar. The results indicated that any hardware impinged upon by the primary plume would be enough to arrest the momentum and redirect the flow. Since the interior geometry of the WLE cavity and the exact location, size, and shape of the WLE damage location remain unknown, it is likely that the plume entering the WLE did come in normal to the spar even if the flow entered the WLE cavity with some momentum.

Another concern of the internal heating group was the additional energy produced by the combustion of the aluminum that makes up the structure of the Orbiter. There was some concern that the combustion of aluminum could provide more than twice the energy available from only the ingested high temperature gas. Although more applicable to oxygen rich atmospheres, an analysis was performed to provide an estimate of the additional energy available at the high altitudes where the Orbiter was flying prior to breakup. The results showed that prior to EI+600 seconds only 30% additional energy could be released due to aluminum combustion and that variations in the breach hole size would result in larger changes in the total energy ingested. Given the uncertainty in the breach hole size, and therefore, the energy of the reentry-gas ingested, and the uncertainty in the predicted heating rates to the internal structures, the additional heating due to aluminum combustion was enveloped by these uncertainties.

In order to evaluate various size damage configurations of the WLE in support of the working scenario, an engineering heating distribution model of the internal WLE cavity was developed. This was needed not only to assess the direct plume impingement heating but also to provide secondary plume heating or "splash" effects. These "splash" environments were required in order to assess the thermal response of the RCC panel 9 clevis and spar temperature gauges, and again to establish consistency of the assumed damage size and location. But prior to this model's development, the question of, given a large enough hole, how does the external environment couple into the internal WLE cavity environment (i.e., does the plume come in normal to the penetration surface or does it flow in with momentum), had to be understood. The first ever coupled external / internal CFD analysis of the Orbiter was performed having only a simple one-foot vented cube as the interior volume. The results showed that for hole sizes 2" in diameter and greater, the majority of the upstream boundary layer was ingested into the interior volume. This result meant that the gases outside of the shock layer, at > 10,000° F, were being pulled into the WLE cavity. It also showed that the flow coming in carried with it its momentum and thus the plume no longer came in normal to the surface. This was critical for determining the location of plume impingement from a penetration in the acreage of an RCC panel. The initial engineering model was checked against these initial CFD solutions and provided to the thermal group for use in their analysis.

Additional CFD and DSMC analysis of the interior of the WLE was pursued to confirm the engineering model further and to include various degrees of complexity in the interior geometry of the WLE cavity. These involved holes in RCC panels 7 and 8 with and without the complex interior geometry and also partially missing T-Seal cases. All involved coupling the external flow field to the WLE interior. Each case provided further insight into the flow field of the interior WLE cavity. Several significant items resulted from these cases: (1) the heating rate on the edge of the RCC hole was an order of magnitude greater than the peak heating on the exterior of the Orbiter; (2) without a structural obstruction, the interior plume heating rate was an order of magnitude greater than the peak heating on the exterior of the Orbiter; (3) if obstructed, the momentum of the incoming gas would be arrested and redirected towards the spanner beam and spar insulation; (4) the heating distributions from the DSMC and CFD cases with obstructions agreed well with the engineering model; and (5) the heating from a partially missing T-Seal would be enough to burn through the spanner beam insulation but rapidly drops off as the flow reaches the spar. The latter indicated that although there was enough energy to get through the spar in the time required, there was not enough energy available to burn a wire bundle at the observed rate. Thus, the damage site was more likely either on the RCC panel acreage or a combination of panel acreage and T-Seal and less likely a partially missing T-Seal alone.

5.5 References

Bertin, John J. (1994), ”Hypersonic Aerothermodynamics,” American Institute of Aeronautics and Astronautics, Inc., Washington, DC.

Anderson Jr., John D. (1989), “Hypersonic and High Temperature Gas Dynamics,” McGraw-Hill, Inc., New York, NY.

NSTS-37384 Image Analysis Team Final Report projected completion date June 25, 2003

NSTS-37376 Data Review and Timeline Reconstruction Team Final Report in support of the Columbia Accident Investigation, June 3, 2003

NSTS-37379 Starfire Team Final Report in support of the Columbia Accident Investigation, June 3, 2003.

NSTS-37383 Vehicle Data Mapping Final Report in support of the Columbia Accident Investigation, June 18, 2003

NSTS-37385 Hardware Forensics Team Final Report in support of Columbia Accident Investigation projected completion, June 20, 2003

STS-107 Mishap Investigation – Combined Master Timeline, Revision 19.

NSTS-37397 Vehicle Reconstruction Team Final Report in support of the Columbia Accident Investigation, June 25, 2003

NSTS-60502 Columbia Working Scenario Final Report, projected completion date July 1, 2003

Chao, D. C. (2002), ”STS-107 Pre-Flight Aeroheating Report,” Boeing Technical Memorandum, Boeing NASA Systems – Houston, No. ATA-TM-02-0009.

Fay, J. A. (1958), and Riddell, F. R. “Theory of Stagnation Point Heat Transfer in Dissociated Air,” Journal of the Aeronautical Sciences, Vol. 25, No.2.

References for Section 5.2.2

“Orbiter Entry Heating Prediction Methods and Database,” Rockwell International Document STS 83-0948, Rev. 1, July 1988.

Fay, J.A. (1958) and Riddell, F.R., "Theory of Stagnation Point Heat Transfer in Dissociated Air," Journal of the Aeronautical Sciences, Vol. 25, No. 2, pp 73-85.

Beckwith, J.E. (1961), and Cohen, N.B., " Application of Similar Solutions to Calculation of Laminar Heat Transfer on Bodies with Yaw and Large Pressure Gradients in High Speed Flow," NASA TND-625.

Eckert, E.R.G. (1955), "Engineering Relations for Friction and Heat Transfer to Surfaces in High Velocity Flow," Journal of the Aeronautical Science, pp 585-587.

Spalding, D.G. (1964), and Chi, S.W., "The Drag of a Compressible Turbulent Boundary Layer on a Smooth Flat Plate with and without Heat Transfer," Journal of Fluid Mechanics, Vol. 18, pp 117-143.

Miller, B.A. (1984), "An Engineering Approach for Estimating Aeroheating to the Partially Catalytic STS Orbiter TPS Surface," Rockwell International Document STS 84-0015.

Holden, M.S. (????), "Boundary Layer Displacement and Leading Edge Bluntness Effects on Attached and Separated Laminar Boundary Layer in a Compressible Corner, Part I; Theoretical Study," AIAA Journal, Vol. 8, No. 12, pp 2179-2188, and "Part II: Experimental Study," AIAA Journal, Vol. 9, No. 1, pp 84-93.

Keys, J.W. (1973), and Hains, F.D., "Analytical and Experimental Studies of Shock Interference Heating in Hypersonic Flows," NASA TND-7139.

Bertin, J.J. (1975), Graumann, B.W. and Goodrich, W.D., "High Velocity and Real Gas Effects on Weak Two-Dimensional Shock Interaction Patterns," Journal of Spacecraft, Vol. 12, No. 3, pp 155-161.

Bertin, J.J. (1976), Mosso, S.J., Bacrette, D.W. and Goodrich, W.D., "Engineering Flowfields and Heating Rates for Highly Swept Wing Leading Edges," Journal of Spacecraft, Vol. 13, No. 9.

References for Section 5.2.3

Stone, David R. (1972), and Cary, Aubrey M. jr, "Discrete Sonic Jets Used as Boundary-Layer Trips at Mach Numbers of 6 and 8.5", NASA TN D-6802.

Zukoski, Edward E. (1964), and Spaid, Frank W., "Secondary Injection of Gases into a Supersonic Flow", AIAA J., vol. 2, no. 10, pp. 1689-1696.

References for Section 5.2.4

Steinbrenner, J. P. (1990), Chawner, J. R., and Fouts, C. L., "The GRIDGEN 3D Multiple Block Grid Generation System," WRDC-TR-90-3022, Wright Research and Development Center Report.

Alter, S.J. (1997), "The Volume Grid Manipulator (VGM): A Grid Reusability Tool," NASA CR-4772.

Sorenson, R.L. (1995), and Alter, S.J., "3DGRAPE/AL Users' Manual," NASA RP-1377, October 1995.

AMTEC Engineering Inc., (2002), "CFD Analyzer 3.0: User's Manual."

Olynick, D.D.R. (1996), "Importance of 3-D Grid Resolution and Structure for Calculating Reentry Heating Environments," AIAA Paper 96-1857.

Strang, W.Z. (1988), "QBERT: A Grid Evaluation Code," AFWAL Technical Memorandum 99-193, Wright Research and Development Center Report.

Thompson, J.F. (1985), Warsi, Z.U.A., and Mastin, C.W., *Numerical Grid Generation Foundations and Applications*, pp. 171-184, North-Holland, 1st ed.

Bird, G.A. (1976), Molecular Gas Dynamics, Clarendon Press, Oxford.

Boyles, K.A. (2003), LeBeau, G.J., Lumpkin, F.E., Wilmoth, R.G., "The Use of Virtual Sub-Cells in DSMC Analysis of Orbiter Aerodynamics at High Altitudes Upon Reentry", *41st AIAA Aerospace Sciences Meeting and Exhibit*, Reno, NV.

Stewart, D. (1997), "Surface Catalysis and Characterization of Proposed Candidate TPS for Access-to-Space Vehicles," NASA TM 112206.

DeVenezia, J. (1995), Wang, K.C., and Caram, J.M., "Space Shuttle Orbiter Wing Leading Edge Heating Predictions and Measurements," NASA CP 3248, Part 2, pp.741-809.

Baranowski, L. C. (1983), and Kipp, H. W., "A Study of Leeside Flow Field Heat Transfer On Shuttle Orbiter Configurations," NASA Contract NAS1-16839.

Berry, S.A. (2002), Hamilton, H.H., "Discrete Roughness Effects on Shuttle Orbiter at Mach 6," AIAA Paper 2002-2744.

Bouslog, S.A. (1995), An, M.Y., and Derry, S.M., "Orbiter Windward-Surface Boundary-Layer Transition Flight Data," Orbiter Experiments (OEX) Aerothermodynamics Symposium, NASA CP 3248, Part 2, pp. 703-740.

Brauckmann, G.J. (1995), Paulson, J.W., and Weilmuenster, J.K., "Experimental and Computational Analysis of Shuttle Orbiter Hypersonic Trim Anomaly," *Journal of Spacecraft and Rockets*, Vol. 32, No. 5, pp. 758-764.

Buck, G.M. (1989), "Automated Thermal Mapping Techniques Using Chromatic Image Analysis," NASA TM 101554.

Buck, G.M. (2000), "Rapid Model Fabrication and Testing for Aerospace Vehicles," AIAA Paper 2000-0826.

Buck, G.M. (1993), and Vasquez, P., "An Investment Ceramic Slip-Casting Technique for Net-Form, Precision, Detailed Casting of Ceramic Models," U. S. Patent 5,266,252.

Daryabeigi, K. (2003), Berry, S.A., Horvath, T. J., and Nowak, R. J., "Finite Volume Numerical Methods for Aeroheating Rate Calculations From Infrared Thermographic Data," AIAA Paper 2003-3634.

Fay, J.A. (1958), and Riddell, F.R., "Theory of Stagnation Point Heat Transfer in Dissociated Air," *Journal of Aeronautical Sciences*, Vol. 25, No. 2.

Haney, J.W. (1995), "Orbiter Pre STS-1 Aeroheating Design Data Base Development Methodology: Comparison of Wind Tunnel and Flight Test Data," Orbiter Experiments (OEX) Aerothermodynamics Symposium, NASA CP 3248, Part 2, pp. 607-676.

Joels, M.K. (1982), and Kennedy, G.P., "The Space Shuttle Operators Manual," Ballantine Books, New York.

Jones, R.A. (1969), and Hunt, J.L., "Use of Tetrafluoromethane to Simulate Real-Gas Effects on the Hypersonic Aerodynamics of Blunt Vehicles,", NASA TR 312.

Merski, N.R. (1998a), "Reduction and Analysis of Phosphor Thermography Data With the IHEAT Software Package," AIAA Paper 98-0712.

Merski, N.R. (1998b), "Global Aeroheating Wind-Tunnel Measurements Using Improved Two-Color Phosphor Thermography Method" *Journal of Spacecraft and Rockets*, Vol. 36, No. 2, pp. 160-170.

Miller, C.G. (1982), “Experimental Investigation of Gamma Effects on Heat Transfer to a 0.006 Scale Shuttle Orbiter at Mach 6,” AIAA Paper 82-0826.

Miller, C.G. (1999), “Development of X-33/X-34 Aerothermodynamic Data Bases: Lessons Learned and Future Enhancements,” NATO Research and Tech. Org., Applied Vehicle Technology Symposium Aerodynamic Design and Optimization of Flight Vehicles in a Concurrent Multi-Disciplinary Environment, paper no. 32.

Miller, C.G. (1990), “Langley Hypersonic Aerodynamic/Aerothermodynamic Testing Capabilities - Present and Future,” AIAA Paper 90-1376.

Throckmorton, D.A. (1995), “Orbiter Leeside Surface Aeroheating Environment Characterization,” Orbiter Experiments (OEX) Aerothermodynamics Symposium, NASA CP 3248, Part 2, pp. 811-822.

Hartung, L.C. (1988), and Throckmorton, D.A., “Space Shuttle Entry Heating Data Book: Volume I – STS-2,” NASA RP 1191.

Stewart, D., (1997), "Surface Catalysis and Characterization of Proposed Candidate TPS for Access-to-Space Vehicles", NASA TM 112206.

References for Section 5.3.2

Shapiro, A.H. (1953), “The Dynamics and Thermodynamics of Compressible Fluid Flow,” John Wiley & Sons, Inc.

References for Section 5.3.3

Hiester, N.K. (1966), and Clark, C.F., “Feasibility of Standard Evaluation Procedures for Ablating Materials,” NASA CR-379.

Kays, W.M. (1980), and Crawford, M.E., “Convective Heat and Mass Transfer”, McGraw-Hill Book Company, 2nd Edition.

Shapiro, A. (1958), "The Dynamics and Thermodynamics of Compressible Fluid FLow – Volume 1", 1953.
Moeckel, W. and Weston, K. "Composition and Thermodynamic Properties of Air in Chemical Equilibrium", NACA TN 4265.
Hrycak, P. (1970), et al., "Experimental Flow Characteristics of a Single Turbulent Jet Impinging on a Flat Plate", NASA TN D-5690.

Abramovich, (1963), "Theory of Turbulent Jets".

O'Connor, T. J. (1965), Comfort, E. H., and Cass, L. A. "Turbulent Mixing of Axisymmetric Jets of Partially Dissociated Nitrogen and Ambient Air", AVCO Corp Report RAD-TR-65-18.

Donaldson, C. DuP. (1971), and Snedeker, R. S. "A Study of Free Jet Impingements, Parts 1 & 2", J. Fluid Mechanics, Vol 45.

Rebrov, A.K. (1982), “Free Jet as an Object of Non-equilibrium Processes Investigation”, 13th International Symposium on Rarified Gas Dynamics, Vol II, pgs 849-864.

Chen, Y.-S. (1993), Liaw, P., Shang, H.-M. and Chen, C. P., “Numerical Analysis of Complex Internal and External Viscous Flows with a Second-Order Pressure-Based Method,” AIAA Paper 93-2966.

Roy, C. J. (2002), McWherter-Payne, M. A., and Oberkampf, W. L., “Verification and Validation for Laminar Hypersonic Flowfields Part 1: Verification,” manuscript submitted to the AIAA Journal.

References for Section 5.3.4

Gordon, S. (1994), and McBride, B.J., "Computer Program for Calculation of Complex Chemical Equilibrium Compositions and Applications," *NASA Reference Publication 1311*, National Aeronautics and Space Administration.
Glassman, I. (1977), "Combustion," Third Edition, Academic Press.

Werley, B. (1993), Barthelemy, H., Gates, R., Slusser, J.W., Wilson, K.B., and Zawierucha, R., "A Critical Review of Flammability Data for Aluminum," Flammability and Sensitivity of Materials in Oxygen-Enriched Environments, ASTM STP 1197, D.D. Janoff and J.M. Stoltzfus, Eds., American Society for Testing and Materials.

Newton, B. (2000), Hull, W., Stradling, J., "Failure Analysis of Aluminum-Bodied Medical Regulators," Flammability and Sensitivity of Materials in Oxygen-Enriched Environments, ASTM STP 1395, T.A. Steinberg, B.E. Newton, and H.D. Beeson, Eds., American Society for Testing and Materials.

References for Section 5.3.5

Fay, J.F. (1993), "Program CHCHVENT Version 5 User's Manual and Software Description." Sverdrup Technology/MSFC Group, Report 631-001-93-007.

Gnoffo, P.A. (1995), Weilmuenster, K.J., and Alter, S.J., "A Multiblock Analysis for Shuttle Orbiter Re-entry Heating from Mach 24 to Mach 12," NASA CP 3248.

Shapiro, A.H. (1953), The Dynamics and Thermodynamics of Compressible Fluid Flow, Volume 1, New York: John Wiley & Sons.

Haukohl, J. (1972), and Forkois, J.L. "Inflow Venting Orifice Efficiency Test Report." Lockheed Missiles & Space Company Report LMSC-HREC D225598, January.

Wong, LC. (1994), et al, "Orbiter Entry Venting Substantiation Report." Rockwell International Space Systems Division, SSD94D0275.

Cline, D.E. (2002), "As Built OV-102, Flight 27, STS-109 Integrated Vent Model," Boeing Company-Houston, DWC-2002-003.

Cline, D.E. (2003), and Torres, "Main Gear Wheel Well Leakage Mapping and Model," presentation to Aero-Thermal Mishap Investigation team, Boeing-PVD.

Hartung, L.C. (1988), Throckmorton, D.A., "Space Shuttle Entry Heating Data Book, Volume III – STS-5", NASA RP-1193.

Gong, L. (1984), Ko, W.L., Quinn, R.D., "Thermal Response of Space Shuttle Wing During Reentry Heating", NASA TM-85907, June 1984.
Thermal Protection Systems Expert and Material Property Database (TPSX), Web Edition Version 3, NASA Ames Research Center, 2003.

Incropera, F.P. (1985), Dewitt, D.P., "Fundamentals of Heat and Mass Transfer", Second Edition, John Wiley and Sons, Inc..

References for Section 5.3.6

Anon. (1976), U.S. Standard Atmosphere, 1976, National Oceanic and Atmospheric Administration, NASA, and U.S. Air Force.

"RCC 8-9 T-Seal Coupled Internal/External 2-D Bridging Phase II Results", Boeing Rocketdyne Propulsion and Power, CFDPUB00862.

"High Enthalpy Flow Benchmark Results", Boeing Rocketdyne Propulsion and Power, CFDPUB00822.

"High Enthalpy Flow Benchmark Extension Results", Boeing Rocketdyne Propulsion and Power, CFDPUB00865.

"Underexpanded Jet Benchmark Results", Boeing Rocketdyne Propulsion and Power, CFDPUB00866.

"RCC8 10in Leading Edge Breach Results", Boeing Rocketdyne Propulsion and Power, CFDPUB00867.

"Hybrid Viscous Unstructured CFD Mesh Technology", Boeing Rocketdyne Propulsion and Power, CFDPUB00756.

"Application of ICAT/BCFD in the Rocketdyne Design Environment", Boeing Rocketdyne Propulsion and Power, CFDPUB00752.

Goulard, R., "On Catalytic Recombination Rates in Hypersonic Stagnation Heat Transfer," Jet Propulsion, vol. 28, no. 11, 1958, pp. 737-745.

FLUENT 6.1 Users Guide, Volumes 1-24. Fluent Incorporated, 10 Cavendish Court, Centerra Resource Park, Lebanon, N.H. 03766.

References for Section 5.6.3

Gnoffo, P.A. (1989), Gupta, R.N., and Shinn, J., "Conservation Equations and Physical Models for Hypersonic Air Flows in Thermal and Chemical Nonequilibrium," NASA TP 2867.

Cheatwood, F.M. (1996), and Gnoffo, P.A. "Users Manual for the Langley Aerothermodynamic Upwind Relaxation Algorithm (LAURA)," NASA TM 4674.

Roe, P.L. (1981), "Approximate Riemann Solvers, Parameter Vectors, and Difference Schemes," Journal of Computational Physics, Vol.43, pp357-372.

Yee, H.C., (1986), "On Symmetric and Upwind TVD Schemes," NASA TM-88325.

Weilmuenster, K.J. (1994), Gnoffo, P.A., Greene, F.A., "Navier-Stokes Simulations of Orbiter Aerodynamic Characteristics Including Pitch Trim and Bodyflap," Journal of Spacecraft and Rockets, Vol. 31, No. 3, pp355-366.

Gnoffo, P.A. (1994), Weilmuenster, K.J., Alter, S.J., "Multiblock Analysis for Shuttle Orbiter Re-entry Heating from Mach 24 to Mach 12," Journal of Spacecraft and Rockets, Vol. 31, No. 3, pp367-377.

Kleb, W.L. (1994), Weilmuenster, K.J., "Characteristics of the Shuttle Orbiter Leeside Flow Dring a Re-Entry Condition," Journal of Spacecraft and Rockets, Vol. 31, No. 1, pp8-16.

Orbiter Experiments (OEX) Aerothermodynamics Symposium (1995), Edited by David Throckmorton, NASA Conference Publication 3248, Part I and II.

Wong, C.C. (1995), Soetrisno, M., Blottner, F.G., Imlay, S.T., and Payne, J.L., "PINCA:A ScalableParallel Program for Compressible Gas Dynamics with Nonequilibrium Chemistry," SAND 94-2436, Sandia National Laboratories, Albuquerque, NM.

Wong, C.C., Blottner (1995), F.G., Payne, J.L., and Soetrisno, M., "Implementation of a Parallel Algorithm for Thermo-Chemical Nonequilibrium Flow Solutions," AIAA Paper 95-0152.

Hassan, B. (1998), Kuntz, D.W., and Potter, D.L., "Coupled Fluid/Thermal Prediction of Ablating Hypersonic Vehicles," AIAA Paper 98-0168.

Kuntz, D.W. (1999), Hassan, B., and Potter, D.L., "An Iterative Approach for Coupling Fluid/Thermal Predictions of Ablating Hypersonic Vehicles," AIAA Paper 99-3460.

Yoon, S. (1988), and Jameson, A., "An LU-SSOR Scheme for the Euler and Navier Stokes Equa-tions," AIAA Paper 87-0600.

Peery, K.M. (1986), and Imlay, S.T., "An Efficient Implicit Method for Solving Viscous Multi-Stream Nozzle/Afterbody Flow Fields," AIAA Paper 86-1380, June 1986.

Steger, J.L. (1981), and Warming, R.F., "Flux Vector Splitting of the Inviscid Gasdynamic Equations with Applications to Finite Difference Methods," *Journal of Computational Physic*s, Vol. 40, pp. 263-293.

Van Leer, B. (1979), "Towards the Ultimate Conservative Difference Scheme. V. A Second Order Sequel to Godunov's Method," *Journal of Computational Physic*s, Vol. 32, No. 1, pp. 101-136.

Payne, J.L. (1999), and Hassan, B., "Massively Parallel Computational Fluid Dynamics Calculations for Aerodynamics and Aerothermodynamic Applications," Proceedings of the 1998 HPC-CP/CAS Workshop, NASA/CP 1999-208757, pp. 111-116.

Srinivasan, S. (1986), Tannehill, J.C., and Weilmuenster, K.J., "Simplified Curve Fits for the Thermodynamic Properties of Equilibrium Air," ISU-ERI-AMES-86041, Iowa State University.

Roy, C.J. (2000), McWherter-Payne, M.A., and Oberkampf, W.L., "Verification and Validation for Laminar Hypersonic Flowfields," AIAA Paper 2000-2550.

Roy, C.J. (2002), McWherter-Payne, M.A., and Oberkampf, W.L., "Verification and Validation for Laminar Hypersonic Flowfields Part 1: Verification," manuscript submitted to the *AIAA Journa*l.

Payne, J.L. (1995), and Walker, M.A., "Verification of Computational Aerodynamic Predictions for Complex Hypersonic Vehicles using the INCA TM Code," AIAA Paper 95-0762.

Roy, C.J. (2002), Gallis, M.A., Bartel, T.J., and Payne, J.L., "Navier-Stokes and DSMC Simulations for Hypersonic Laminar Shock-Shock Interaction Flows," AIAA Paper 2002-0737.

Roy, C.J. (2002), Gallis, M.A., Bartel, T.J., and Payne, J.L., "Navier-Stokes and DSMC Predictions for Laminar Hypersonic Shock-Induced Separation," manuscript to be submitted to the *AIAA Journa*l.

Alter, S.J. (1997), "The Volume Grid Manipulator (VGM): A Grid Reusability Tool," NASA CR-4772,.

Taubin, G. (1995), "A Signal Processing Approach to Fair Surface Design," SIGGRAPH.

Bartel, T.J. (2001), Plimpton, S.J., and Gallis, M.A., "Icarus: A 2-D Direct Simulation Monte Carlo (DSMC) Code for Multi-Processor Computers: User's Manual - v 10.0," Sandia Report SAND2001-2901, Sandia National Laboratories, Albuquerque, NM.

Bird, G.A. (1994), *Molecular Gas Dynamics and the Direct Simulation of Gas Flows*, Clarendon Press, Oxford.

Wagner, W. (1992), "A convergence proof for bird direct simulation Monte-Carlo method for the Boltzmann-equation," *J. Stat. Phys.*, **66**(3-4), pp.1011-1044.

Gallis, M.A. (2001), Torczynski, J.R., and Rader, D.J., "An approach for simulating the transport of spherical particles in a rarefied gas flow via the direct simulation Monte Carlo method," *Phys. Fluids*, **13**(11), pp.3482-3492.

Gallis, M.A. (2002), Torczynski, J.R., and Rader, D.J., "Calculations of the near-wall thermophoretic force in rarefied gas flow," *Phys. Fluids*, **14**(12), pp.4290-4301.

Torczynski, J.R. (2002), Gallis, M.A., and Piekos, E.S., “Comparison of methods for simulating gas forces on moving microbeams,” ASME Paper IMECE2002-33788.

Roy, C. J. (2002), Gallis, M. A., Bartel, T. J., and Payne, J. L., “Navier-Stokes and DSMC Simulations for Hypersonic Laminar Shock-Shock Interaction Flows,” AIAA Paper 2002-0737.

Roy, C. J. (2002), Gallis, M. A., Bartel, T. J., and Payne, J. L., “Navier-Stokes and DSMC Predictions for Laminar Hypersonic Shock-Induced Separation,” manuscript to be submitted to the *AIAA Journa*l.

Shufflebotham, P.K. (1995), Bartel, T.J., Berney, B., “Experimental validation of a direct simulation by Monte Carlo molecular gas flow model,” *J. Vac. Sci. Technol. B*, **13**(4), pp. 1862-1866.

Johannes, J.J. (1997), Bartel, T.J., Hebner, G.A., Woodworth, J., Economou, D.J., “Direct simulation Monte Carlo of inductively coupled plasma and comparison with experiments,” *J. Electrochem. Soc.*, **144**(7), pp. 2448-2455.

Gallis, M.A. (1999), and Bartel, T.J., “Direct simulation Monte Carlo modeling of viscous interactions,” AIAA Paper 99-3453.

Chakravarthy, S.R. (1985), and Osher, S., Computing With High-Resolution Upwind Schemes for Hyperbolic Equations, Proceedings of the 1983 AMS-SIAM Summer Seminar on Large-Scale Computations in Fluid Mechanics, published by American Mathematical Society in Lectures in Applied Mathematics, Vol. 22.

Rajagopal, K. (1997), Numerical Simulation of Flow Inside an Orbiter Wing Section during Entry through a Hole from a Possible On-Orbit Debris Impact Damage, AIAA Paper No. 97-2227.

Bird, G.A. (1976), *Molecular Gas Dynamics*, Clarendon Press, Oxford (1976).

Wilmoth, R.G. (1996), LeBeau, G.J. and Carlson, A.B., “DSMC Grid Methodologies for Computing Low-Density, Hypersonic Flows About Reusable Launch Vehicles”, AIAA Paper No. 96-1812.

LeBeau, G.J. (1999), "A Parallel Implementation of the Direct Simulation Monte Carlo Method", Computer Methods in Applied Mechanics and Engineering, Vol. 174, pp. 319-337.

LeBeau, G.J. (2001), and Lumpkin III, F.E., “Application highlights of the DSMC Analysis Code (DAC) software for simulating rarefied flows”, *Computer Methods in Applied Mechanics and Engineering*, Vol. 191, Issue 6-7, pp. 595-609.

References for Section 5.6.4

Steinbrenner, J.P. (1990), Chawner, J.R., and Fouts, C.L., “The GRIDGEN 3D Multiple Block Grid Generation System,” WRDC-TR-90-3022, Wright Research and Development Center Report.

Alter, S.J. (1997), “The Volume Grid Manipulator (VGM): A Grid Reusability Tool,” NASA CR-4772.

Sorenson, R.L. (1995), and Alter, S.J., “3DGRAPE/AL Users’ Manual,” NASA RP-1377

AMTEC Engineering Inc. (2002), “CFD Analyzer 3.0: User’s Manual.”

Olynick, D.D.R. (1996), “Importance of 3-D Grid Resolution and Structure for Calculating Reentry Heating Environments,” AIAA Paper 96-1857.

Strang, W.Z. (1988), “QBERT: A Grid Evaluation Code,” AFWAL Technical Memorandum 99-193, Wright Research and Development Center Report.

Thompson, J.F. (1985), Warsi, Z.U.A., and Mastin, C.W., *Numerical Grid Generation Foundations and Applications*, pp. 171-184, North-Holland, 1st ed.

Alter, S.J. (1997) "The Volume Grid Manipulator (VGM): A Grid Reusability Tool," NASA CR-4772.

Taubin, G. (1995), "A Signal Processing Approach to Fair Surface Design," SIGGRAPH.

5.6 Appendix for Aerothermodynamics

5.6.1 Engineering Tools

5.6.1.1 XF0002

XF0002/Exact Attitude Aerothermal Heating Computer Program is the main tool utilized for predicting re-entry heating of the Orbiter. The XF0002 Aeroheating Computer Program was formulated as a design tool for predicting ascent or re-entry heating to geometrically simple vehicle shapes. The program accurately predicts local properties and heat fluxes within the scope of the many user selected options. The options were obtained through the application of open literature publications on the subject and have been modified as required.

For re-entry, 2008 body points (aeroheating models) are used to cover the whole Orbiter body. The models are correlated with wind tunnel test data and the flight data from STS-1 through 5. The technical approaches and the body point heating methodology used in this program are described in Section 5.2.1.

XF0002 is under configuration control by Boeing Orbiter Vehicle Engineering Office.

5.6.2 Wind Tunnel Facilities & Measurement Techniques

The purpose of this section is to provide brief descriptions of the hypersonic aerothermodynamic wind-tunnel facilities and global heating measurement techniques at the NASA Langley Research Center utilized in support of the STS-107 accident investigation. Details regarding these facilities can be found in Miller (1990,1999).

5.6.2.1 Mach 6 Air

Heated, dried, and filtered air is used as the test gas. Typical operating conditions for the tunnel are: stagnation pressures ranging from 30 to 500 psia; stagnation temperatures from 760 deg to 1000 deg R; freestream unit Reynolds numbers from 0.5 to 8 million per ft., freestream and post normal shock gamma of 1.4, and a normal shock density ratio of 5.3. A two-dimensional, contoured nozzle is used to provide nominal freestream Mach numbers from 5.8 to 6.1. The test section is 20.5 by 20 in; the nozzle throat is 0.399 by 20.5 in. The test core varies from 12 to 14 inches depending on the operating condition. A floor-mounted model injection system can insert models from a sheltered position to the tunnel centerline in less than 0.5 s. For heat-transfer and flow visualization tests, the model residence time in the flow is only a few seconds; nominal run time for force & moment testing is approximately 60 to 120 s in this facility although longer run times are possible. Table 1 (sec 4.3.2) summarizes the nominal test conditions for the tests performed for this investigation.

5.6.2.2 Mach 6 CF4

Heated, dried, and filtered carbon tetrafluoride (CF_4 or Freon 14; molecular weight of 88 which is three times heavier than air) is used as the test gas. Typical operating conditions for the tunnel are: stagnation pressures ranging from 60 to 2000 psia, stagnation temperatures up to 1300 R, freestream unit Reynolds numbers from 0.01 to 0.55 million per ft., freestream gamma of 1.21 and a post normal shock gamma of 1.1, and a normal shock density ratio of 11.7. A contoured axisymmetric nozzle is used to provide a nominal freestream Mach numbers from 5.9 to 6.0. The nozzle exit diameter is 20 in with the flow exhausting into an open jet test section; the nozzle throat diameter is 0.466 in. The test core varies from 12 to 14 inches depending on the operating condition. A floor-mounted model injection system can inject models from a sheltered position to the tunnel centerline in less than 0.5 s. For heat-transfer and flow visualization tests, the model residence time in the flow is only a few seconds; nominal run time for force &

moment testing is approximately 20 s. Table 1 (sec 4.3.2) summarizes the nominal test conditions for the tests performed for this investigation.

5.6.2.3 IR Thermography

Model surface temperatures were measured using a FLIR SC2000 infrared imaging system having an un-cooled microbolometer-based focal plane array detector with 320 × 240 detector elements. The imager has a field of view of 24° × 18°, and is sensitive to infrared radiation in the 7–12 micrometer range of the electromagnetic spectrum. An eight-inch diameter zinc selenide window with a transmittance of 0.98 in the 7-14 micrometer spectral range was used for optical access to the test section. The measured infrared radiation was converted to actual surface temperatures using the emittance of a target, which for the phosphor-coated fused silica model was determined to be 0.906. The imager produces 30 frames of images per second, while the data acquisition hardware used with the infrared imaging system was only capable of real–time digital storage of approximately 6 frames per second. With temperature images acquired at different times during a wind-tunnel run, global heat-transfer images are computed assuming one-dimensional semi-infinite heat conduction formulation with convective boundary conditions. Details regarding the test methodology can be found in Daryabeigi, (2003).

5.6.2.4 Phosphor Thermography

With the two-color relative-intensity phosphor thermography technique (Buck, 1989; Merski, 1998a-b), ceramic wind-tunnel models are fabricated and coated with phosphors that fluoresce in two regions of the visible spectrum when illuminated with ultraviolet light. The fluorescence intensity is dependent upon the amount of incident ultraviolet light and the local surface temperature of the phosphors. By acquiring fluorescence intensity images with a color video camera of an illuminated phosphor model exposed to flow in a wind tunnel, surface temperature mappings can be calculated on the portions of the model that are in the field of view of the camera. A temperature calibration of the system conducted prior to the study provides tables used to convert the ratio of green and red intensity images to global temperature mappings. With temperature images acquired at different times during a wind-tunnel run, global heat-transfer images are computed assuming one-dimensional semi-infinite heat conduction. The primary advantage of the phosphor technique is the global resolution of the quantitative heat-transfer data. Such data can be used to identify the heating footprint of complex, three-dimensional flow phenomena (e.g., boundary layer transition locations, flow separation and reattachment locations, etc.) that are extremely difficult to resolve by discrete measurement techniques.

5.6.2.5 Flow Visualization

Flow visualization in the form of schlieren and oil-flow techniques was used to complement the surface heating and force & moment tests. The LaRC 20-Inch Mach 6 air and CF_4 Tunnels are equipped with a pulsed white-light, Z-pattern, single-pass schlieren system with a field of view encompassing the entire test core. Images were recorded on a high-resolution digital camera.

Surface streamline patterns were obtained using an oil-flow technique. Orbiter models were coated with a phosphorescent material dispersed in a thin layer of silicon oil. After the model surface was prepared, the model was injected into the airstream and the development of the surface streamlines was recorded with a conventional video camera. The model was retracted immediately following flow establishment and formation of streamline patterns, and post-run digital photographs were taken.

5.6.3 CFD/DSMC Tools

5.6.3.1 GASP (ARC)

The GASP Real-Gas Navier-Stokes code was the primary code for solutions accomplished at Ames Research Center. This code originated as a commercially available code developed at AeroSoft, Inc, but has been modified at ARC to enhance both capability and robustness specifically for hypersonic reentry applications.

The GASP Reynolds Averaged Navier-Stokes code is a three-dimensional (3D) finite-volume code. Upwind flux options exist for this code, but for the present solutions the Van Leer inviscid flux formulation was applied in all three directions. A formally 3rd order upwind-biased MUSCL scheme combined with min-mod limiter is selected to provide higher order accuracy. Experience at ARC with this code has indicated that wall normal spacing is sufficient to obtain accurate heat transfer with the Van Leer flux formulation and 3rd order accuracy provided the wall node Cell Reynolds number is kept below a value of 5. For most of the calculations provided in the present work the wall node Cell Reynolds number is approximately 1, which yields the best results in convergence and accuracy. Time advancement to steady state is accomplished with either a 2D Approximate Factorization, AF2, in the nominal cross-flow plane with planar relaxation in the streamwise direction, or, alternatively, with a point-Jacobi algorithm with inner iterations. Experience at ARC has shown that these two time-advancement schemes as implemented in GASP are nearly identical in convergence, robustness and speed.

The 5-species finite reaction rate model for dissociating air of Park was used in these calculations using GASP. In this chemistry model, air is composed primarily of molecular nitrogen, N2, and molecular oxygen, O2, with the possibility of dissociation at high temperature into atomic nitrogen, N, and atomic oxygen, O, followed by formation of NO. For the high Mach number, high altitude portion of a low Earth orbit reentry trajectory as considered herein, the molecular oxygen, O2, present in the atmosphere will almost entirely dissociate into atomic oxygen, O, upon encountering the bow shock. However, N2 will undergo but slight dissociation with lesser amounts of N and NO formed. The reaction rates are typically slow enough that little recombination occurs for hypersonic flows prior to the exit boundary except for that due to the catalytic effect of certain thermal protection surface materials.

The real-gas air chemistry has an important effect on the hypersonic flow about the orbiter by altering the shock location since energy is required to dissociate the molecular oxygen through the shock, the temperature and density rise through the shock are not as great as would otherwise occur for a perfect gas thereby reducing the effective gamma for the real gas in the shock relations. A further real-gas effect is that chemical energy is released at the shuttle surface due to recombination of O to O2 as a consequence of the catalytic behavior of the RCG shuttle tile material. This catalytic wall effect yields a higher heating rate to the wall than for non-catalytic materials. Species transport properties are calculated using Blottner relations with mixture properties calculated using Eucken relations.

Stewart characterized the surface catalytic recombination of air due to various thermal protection system insulation materials including RCG as used on the windward side of the shuttle orbiter. RCG and other catalytic materials act to enhance the rate of recombination of atomic oxygen into molecular oxygen and of atomic nitrogen into molecular nitrogen. Molecular NO is assumed to experience no catalytic effect. In the process, additional thermal energy is released to the wall due to the chemical reaction occurring at the surface.

The primary wall boundary condition used for these shuttle calculations is that of radiative equilibrium combined with the above RCG catalytic behavior. In this viscous wall boundary condition, there is an assumption that the radiative heat transfer from the wall exactly balances the thermal energy transfer to the wall due to convective heat transfer combined with energy release to the wall due to the surface catalytic chemical reaction. The radiative equilibrium boundary condition requires the simultaneous solution of 4 species equations (molecular NO is not considered catalytic) combined with an equation for the energy balance, all of which are written at the wall node. To then solve this wall boundary condition for each Navier-Stokes solver iteration, a Newton-Raphson method achieves quadratic convergence.

Additional boundary conditions used include conventional point-to-point zonal boundaries, adiabatic viscous wall, free-stream, and a specified back-pressure outflow boundary condition. Point-wise boundary conditions can be specified optionally for any of the 6 faces of each grid block and were used for the vented cavity panel 9 solutions.

Most of the solutions delivered were laminar throughout the solution domain. However, some eddy-viscosity turbulence models calculations were conducted to establish approximate turbulence heating enhancements and for validation purposes. Turbulence models implemented into this code include the Baldwin-Lomax algebraic model of Baldwin-Lomax and the 2-eq SST/K-Omega turbulence model of Menter. These models have compressibility corrections suitable for hypersonic flows and have been validated for heat transfer in hypersonic strong interactions as implemented in the ARC version of the GASP code. A means for specification of turbulence transition is implemented in the code, but is not used for the present work.

The GASP code was run initially on a serial processor computer (Intel 2 GHz XEON processor running RedHat Linux v 7.3). These early runs were for fully catalytic solid surface rather than RCG on grids of approximately 3/4 million grid points and took 96 hours. To improve throughput, subsequent work was moved to the NAS parallel-processing cluster, chapman, which is based on up to 1024 SGI Origin O3K cpus. For the parallel processor runs, the grids were decomposed into as many as 48 grid blocks each of which was then run on a separate SGI processor in the NAS chapman cluster. With grids of 1.9 million grid points, the chapman parallel processor runs took approximately 48 hours.

Convergence criterion was based on examination of residual history, temperature and pressure history for selected surface points during the entire iteration sequence, and when convergence was nearly complete examination of delta T and delta P surface plots separated by 50 to 200 iterations. Typically the L2 residual would drop by 5 orders of magnitude and the selected surface temperatures and pressures would become constant. The delta T and delta P surface plots were facilitated by the gasptools package written by D. Prabhu and M. Wright of Ames and which is based on perl scripts making use of the GASP print utility and the Tecplot plotting package. Typically the delta T surface plots were examined for constant temperature within 5 degrees over the entire shuttle surface. Some of the damage cases exhibited some oscillation of approximately a 10 degree K magnitude which was deemed acceptable inasmuch as there existed a physical basis.

5.6.3.2 LAURA (LaRC)

The Langley Aerothermodynamic Upwind Relaxation Algorithm (LAURA) was applied to external and internal flow simulations for the Columbia investigation. LAURA is a high fidelity analysis tool, specialized for hypersonic re-entry physics, utilizing state-of-art algorithms for computational fluid dynamic (CFD) simulations. Key elements of LAURA include Roe's averaging and Yee's Total Variation Diminishing (TVD) formulation of second-order, inviscid flux. Yee's TVD formulation has been found to be exceptionally robust and Courant-number-independent using point-implicit relaxation for hypersonic flow simulations. The TVD algorithm uses a non-linear, minmod function as a flux limiter that maintains second-order accuracy away from extrema but can admit limit cycles in the convergence process, particularly in the vicinity of captured shocks. This occurrence usually manifests itself as a stalling of convergence at a very low error norm, essentially a benign ringing in the solution at a level that has no impact on aerothermodynamic quantities. Viscous flux is computed using central differences.

Previous simulations of STS 1,2 and 5 with LAURA to resolve questions of a pitching moment anomaly (STS 1) and to validate heating predictions were published in the AIAA Journal of Spacecraft and Rockets in 1994. Some of this material was also presented in an ITAR restricted document with more detail and dimensions. All of the current simulations specify laminar flow of air in chemical nonequilibrium (N, O, N_2, O_2, NO) and thermal equilibrium. Only CFD point 1 is simulated for internal cavity flow simulations with freestream conditions: V_∞ = 7350.6 m/s, ρ_∞ = 3.9005 10^{-5} kg/m^3, T_∞ = 217.3 K, α = 40.1681 deg., and time = 13.50.53.0. The external flow simulations are implemented on the shared, baseline grid developed for the External Environments Team. The baseline grid has been modified to allow coupling of the external flow with flow through a breach in the wing entering a vented cavity.

5.6.3.3 SACCARA (SNL)

The Sandia Advanced Code for Compressible Aerothermodynamics Research and Analysis, SACCARA, was developed from a parallel distributed memory version of the INCA code, originally written by Amtec Engineering. SACCARA employs a massively parallel distributed memory architecture based on multi-block structured grids. The solver is a Lower-Upper Symmetric Gauss-Seidel scheme based on the works of Yoon et al., and also Peery and Imlay, which provides for excellent scalability up to thousands of processors.

For the current simulations, SACCARA was used to solve the Navier-Stokes equations for conservation of mass, momentum, and energy. The convective fluxes at the interface were calculated using the Steger and Warming flux vector splitting scheme. Second-order reconstructions of the interface fluxes were obtained via MUSCL extrapolation. A flux limiter was employed which reduces the spatial discretization to first order in regions of large second derivatives of pressure and temperature. This limiting process is used to prevent oscillations in the flow properties at shock waves. The use of flux limitiers results in a mixture of first- and second-order spatial accuracy. In this study three different equations of state were used depending on the physics that where being modeled.

The simulations for wind tunnel conditions assumed a perfect gas equation of state. The ratio of specific heat and the gas constant were specified and the remaining state variables were calculated. The viscosity was calculated using Keyes curve fit for air and conductivity was determined by assuming a constant Prandtl number. An iso-thermal, no-slip wall boundary condition was applied to the shuttle surface. This boundary condition enforces a zero velocity condition at the surface and keeps the wall temperature fixed at specified a value, while also assuming a zero pressure gradient at wall. The supersonic inflow boundary condition allows the user to specify inflow variables which remain fixed during the simulation. The outflow boundary condition assumes a zero order extrapolation.

A number of the simulations at flight conditions assumed equilibrium air. Tannehill's curve fits were used to determine the pressure and temperature from the known energy and density. The viscosity was calculated using Sutherland's law for air. The conductivity was calculated by assuming a constant Prandtl number. A radiative-equilibrium, no-slip wall boundary condition was applied to the shuttle surface. The wall temperature was calculated using an emissivity of 0.9. Remaining boundary conditions were as stated above.

The solutions were assumed to be converged when the residuals dropped by six or more orders of magnitude. The iteration histories of the quantities of interest were also carefully examined

A number of code verification studies provide confidence that the SACCARA code is free from coding errors. These studies included comparison to established numerical benchmark solutions as well as code-to-code comparisons with Navier-Stokes and Direct Simulation Monte Carlo approaches.

5.6.3.4 USA (BHB)

The unified solution algorithm (USA) code is a very versatile flow solver that can be used to compute numerical solutions to a large class of aerodynamic and aerothermodynamic problems by solving the Euler or Reynolds averaged Navier-Stokes (RANS) equations. The discretization is of TVD formulation using finite volume framework. Various Riemann solvers can be used with the preferred one being the modified Lax-Freidrichs scheme. A multizonal structural grid bookkeeping method facilitates the treatment of complex geometric topologies. A real gas approach based on a finite rate chemistry formulation can be coupled or uncoupled with the fluid dynamics to treat reacting and nonreacting gaseous species. Additional information on the USA code can be obtained in Chakravarthy (1985). In this work, the approximate factorization scheme using the implicit time marching option was used. The simulations discussed in Sections 5.3.6.1.1 and 5.3.6.2.2 modeled laminar flow conditions using equilibrium air chemistry model. The external flow surface had radiative equilibrium temperature boundary condition whereas the internal surfaces were kept at cold wall temperature of 0 degree F. The simulations were speeded up using grid-sequencing. The convergence of flow simulations were confirmed by monitoring the time history of surface heating results. An additional reference for the framework in which the USA code was applied can be found in Rajagopal (1997).

5.6.3.5 ICAT (B-RKDN)

ICAT is a general Navier-Stokes code that extends the well-validated numerical algorithms and physical models found in the structured USA code into an unstructured solver. ICAT can be used to compute a numerical solution to a large class of aerodynamic and aerothermodynamic problems by solving the Euler or Reynolds averaged Navier-Stokes (RANS) equations, and offers most of the chemistry, boundary condition and solver features of USA. However, the unstructured grid solver available in ICAT offers the advantage of being able to use hybrid viscous grids, which take an order of magnitude less time to create than structured grids, for complex geometries. The use of ICAT, along with Boeing grid generation tools, enabled the modeling and solution of complex orbiter wing and internal geometries in days, rather than in the weeks required for a comparable structured grid model and solution. The most important features of ICAT are currently being integrated into BCFD, Boeing's next generation structured/unstructured solver.

5.6.3.6 FLUENT (LMSC)

FLUENT 6.1 is a commercial Navier-Stokes solver for unstructured meshes. It is a cell-centered, finite-volume code. It is easy to use and the license entails full technical support, as well as two meshing programs called "Gambit" and "TGrid". Users can add their own functionality and models to FLUENT through the use of C-programs, with
Fluent providing a wide range of looping macros for accessing cell centers and face centers.

FLUENT's three solvers can be used to compute the flow and heat transfer for all flow regimes, from low subsonic via transonic and supersonic to hypersonic. The turbulence can be modeled by means of the Spalart-Allmaras model, the k-epsilon or k-omega families, the Reynolds Stress Model, the LES model, or the DES model. The software includes an integrated postprocessing suite.

FLUENT's broad range of physical models, designed to work on unstructured grids, is what differentiates it from other codes. The physical models include combustion models and associated multi-species capability, multiphase models, and radiation models. Finally, problems in which object boundaries move with respect to each other (e.g., stage
separation and store separation) are treated via FLUENT's moving-deforming mesh model.

Fluent Inc. also offers two finite-element solvers - FiDAP and PolyFlow
for engineers working with low-Reynolds number flows, i.e., materials
processing applications, viscoelastic flows, etc.

5.6.3.7 DAC (JSC)

DAC represents NASA's state-of-the-art implementation of the Direct Simulation Monte-Carlo (DSMC) method for simulating rarefied gas dynamic environments. Different than traditional CFD techniques, the DSMC method is a more direct physical simulation of a gas at the molecular level. Molecules are tracked as they move in space and time, colliding with surfaces and other molecules. The move and collision phases are decoupled, allowing molecules to move linearly a distance corresponding to the product of the molecule's velocity and the size of the time step, before collisions are considered. The microscopic quantities tracked during the simulation are converted to more familiar flowfield quantities of density, velocity and temperature by statistically sampling the ensemble of particles in the simulation. Although DSMC solutions are continuously unsteady, steady-state results are achieved by averaging an ensample of samples once a pseudo steady-state condition is achieved. Often, the cells of the grid used to group the molecules for collisions are also used as sampling zones for the flowfield quantities. This provides a distribution of the flowfield quantities throughout the computational domain. Likewise, the molecule-surface collisions simulated at the microscopic level are also converted macroscopic quantities by employing appropriate sampling techniques. For example, the pressure on a surface element is simply the time-rate-of-change of momentum for molecules impacting the surface element, divided by the area of the element. Similar techniques are used to obtain shear stress and heating on surface elements. Further details on the DSMC method can be found in the Reference section.

The DAC Series can simulate 2D, axi-symmetric and 3D problems using a handful of programs that perform specific tasks in the analysis process. The software employs a two level embedded Cartesian grid system that is used to both pair neighboring molecules, and for sampling of the macroscopic quantities. Embedded within the flowfield grid is the surface geometry. DAC represents the surface geometry as a collection of unstructured triangular elements, which also act as sampling zones for surface properties. Each triangle in the surface geometry may be assigned a specific boundary condition type. There are five types of boundary conditions: 1) a solid wall, 2) an outgassing wall, 3) an inflow boundary, 4) an outflow boundary, and 5) as a freestream. A solid wall means no molecules are produced at the wall and none pass through. An outgassing wall is the same as a solid wall, except molecules are created on the flowfield side of the triangle at a rate that matches the specified flux. An inflow boundary also creates molecules on the flowfield side of the triangle, but any molecules that hit that surface will disappear, as will those that hit an outflow boundary or a freestream boundary. Three types of boundary conditions can also be applied to edges of the computational domain: 1) vacuum, 2) freestream, and 3) a symmetry plane.

The rectangular bounding box for the computational domain is specified by the user, as is the discretization in each of the three Cartesian directions. The cells created by this uniform Cartesian grid are referred to as Level-I Cartesian cells – or simply Level-I cells. Each of these Level-I Cartesian cells can be further refined by its own embedded Cartesian grid. These embedded Cartesian grids allow varying degrees of refinement from one Level-I cell to the next as required by the local flowfield properties in that region of the computational domain. These embedded Cartesian grids form Level-II Cartesian cells – or simply Level-II cells. While the Level-II cells may be much smaller than their parent Level-I cell, they may be no larger than the parent Level-I cell, which would be the case if a Level-I cell was refined by a 1x1x1 Level-II grid.

The two-level embedded Cartesian grid system permits variable refinement throughout the computational domain, which is essential for meeting the local mean-free-path cell size requirement. The catch-22 here is that in order to create an appropriate grid, you need to know the local flowfield properties. But in order to accurately predict the flowfield properties, you have to have an appropriate grid. This issue is addressed in DAC through an adaptation process that allows the solution on one grid system to be used as the basis for the creation of a new more appropriate grid. This is an iterative process typically requiring one and sometimes two adaptations. Metrics provided by the post-processing software can be used to determine if additional adaptation in warranted. Figure 5.6.3-1 displays the ratio of the local mean-free-path to the flowfield cell size for the DSMC Point AA solution. As is shown in the figure, mean-free-path resolution was obtained near the body and greater-than-mean-free-path resolution was obtained everywhere else in the computational domain. Historically, solutions that have reached mean free path resolution in their flowfield grids have compared well with experimental data. It should be noted that for the DSMC Point A solution, the mean-free-path resolution requirement was approximated but not satisfied due to the excessive computational load that this would result in. Violation of this rule results in overestimation of the transport properties and the heat flux to the walls (the viscosity and heat conductivity of the flow is overestimated). Based on convergence analysis performed on these solutions the error should not exceed 10%, so the heat fluxes given Section 5.4 should be interpreted as maximum values.

In addition to controlling grid refinement, the adaptation process is also used to automatically specify other simulation parameters throughout the computational domain. The DSMC method also has very specific requirements for the size of the time step used in the simulation, and for having each cell be populated with an adequate number of simulated molecules. The DAC software efficiently addresses these requirements by allowing the time step and ratio of real-to-simulated molecules to be specified independently within each Level-I cell as needed.

In addition to the preprocessor (PREDAC) and the run code (DAC), the DAC Software also contains two post-processing codes, SLICE and SPROP, for viewing flowfield and surface properties, and a utility code, Surface Tools Plus (STP), which can be used for importing different file types, modifying boundary conditions, managing groups, manipulating geometry and performing diagnostic testing of the user created surface grids.

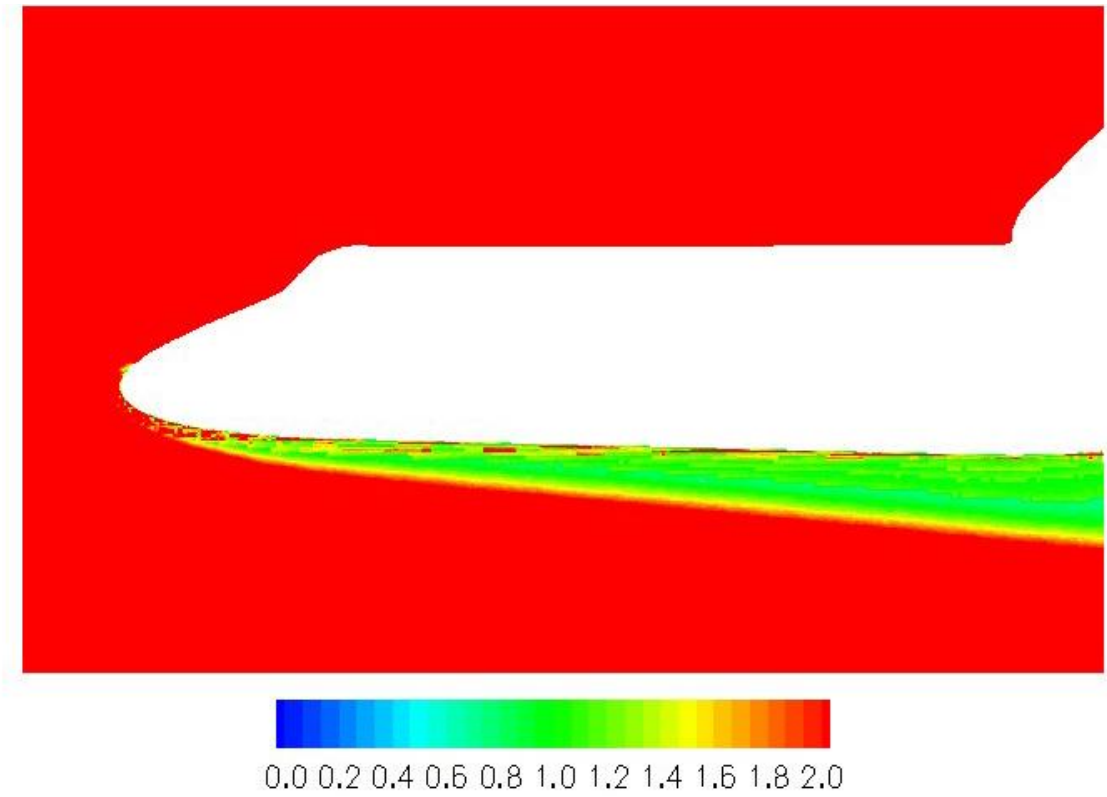

Figure 5.6.3-1 Ratio of Local Mean-Free-Path to Flowfield Cell Size for Nominal Orbiter Configuration DSMC Point AA.

5.6.3.8 ICARUS (SNL)

Icarus is a 2D gas dynamics code developed at Sandia by Bartel *et al.* based on the direct-simulation Monte Carlo (DSMC) method of Bird. It can model flowfields ranging from the continuum to the free molecular regime on Cartesian and axisymmetric grids. Icarus was optimized for a parallel computational environment with thousands of processors.

The DSMC method has been shown to approximate the Boltzmann equation. It employs computational particles that each represent a number of real molecules. During each time step, these particles undergo a deterministic move followed by a stochastic collision process. Collisions can involve multiple species, internal energy modes (rotation and vibration), and chemistry. Macroscale variables, such as temperature and velocity, are obtained by taking appropriate moments over the statistically-represented distribution functions.

The simulations of jet expansion were performed using both Cartesian and axisymmetric grids. The jet was modeled by introducing a constant flux of a given temperature, species mole fraction, and temperature. A vacuum condition was enforced at the outlet by deleting all particles that contact the boundary. The remaining boundaries were modeled as symmetry planes or solid surfaces, as the geometry required. Solid surfaces were treated as isothermal with full thermal accommodation.

The simulations of cavity flow were performed with Cartesian grids. A freestream boundary condition with a specified temperature, pressure, and velocity was enforced at the inflow edge. A vacuum was enforced at the outflow edge. Solid surfaces defining the wing and an open cavity were treated as isothermal with a specified thermal accommodation coefficient. In some calculations a vent was opened in the cavity with a specified outlet pressure.

The solutions were deemed steady-state when the total number of particles on the domain reached an asymptote. Statistical sampling then commenced and continued until the scatter was reduced to an acceptable level for all required quantities.

Extensive code verification studies have been performed on Icarus. These studies include comparison to data from analytic solutions, independent codes, and wind tunnel measurements.

5.6.3.9 VGM (LaRC)

The Volume Grid Manipulator (VGM) software was utilized on the Shuttle Orbiter Columbia Accident Investigation to modify, improve, refine, etc., structured surface and volume grids for viscous flow simulations. The software was developed in the late 1990's based on a set of existing grid manipulation tools. The suite of tools shared one specific drawback – they each required input and output which was the slowest part of operating on a grid. A grid manipulation language to couple the suite together was developed, and the VGM code was produced. Since its inception, the software has found application beyond its original intent, including the removal of negative celled volumes, feature based grid adaptation, and volume grid extrusion.

For the Columbia Accident Investigation, the VGM software was used to:

Correct negative celled volumes.

Transfer and adapt an existing solution to an entirely different topological grid.

Impose an orthogonal boundary condition on a block boundary attached to the wall of the shuttle orbiter.

Implement a C-II continuous matching block boundary condition in three dimensions.

Smooth surface and volume grids produced from adapting a grid to a specific solution.

Increase and decrease grid dimensionality to improve flow simulation accuracy without having to reconstruct the entire volume grid.

Expand existing volume grids to ensure outer bow-shock and entire flow field capture.

Reduce grid stretching and increase grid line intersection orthogonality to improve grid quality for flow simulations.

Smooth solution adapted grids through the implementation of method suggested by Taubin, but extended to fully three-dimensional problems.

The VGM language consists of 10 commands, where each command may have as many as 10 different options with up to 3 different settings for each option. Exercising each command with each option and setting produces a language with over 1000 individual operations. Coupling the individual operations enables the user to expand the capabilities of VGM to do extremely complex manipulations efficiently and with very few commands. Overall, the software provides a set of capabilities that do not exist in any other tool. As such, the user of this software can solve problems posed with structured grids that cannot be solved with any other grid generation software.

5.6.4 Hypersonic Boundary Layer Transition Effective Trip Height Calculation

The effective trip heights shown in Figure 5.2.5-15 were computed at Mach Numbers of 22.91 and 17.9 along the STS-107 flight path. The computations were based on a Euler/approximate boundary layer technique and on a Shuttle ground test boundary layer transition correlation (Berry,2002). Effective trip heights are defined in the study as the height required to move transition onset to the trip location. The transition correlation is presented by Berry as the momentum thickness Reynolds Number divided by the local Mach Number as a function of the roughness height divided by the boundary layer thickness (Figure 5.3.2.15). To establish the correlation, transition data were obtained on a Shuttle model over a range of

parameters including free stream Reynolds Number, angle of attack and roughness heights. The Euler/approximate boundary layer technique was used to compute the flow conditions to form the correlation parameters. Note that in Figure 5.3.2.15 the line defined as incipient transition relates to a trip height that promotes transition downstream of the disturbance(as opposed to occurrence at the trip). Data below the incipient line denote laminar flow, and data above the effective line represent turbulent conditions. Also, the data for the wing attachment line shown in the figure were obtained in the current study. The correlation results were extended to the two fight conditions shown in Figure 5.2.5-15 by first computing the momentum thickness Reynolds Number to Mach Number ratio over the Shuttle and mapping at the same locations the corresponding effective roughness height to boundary layer thickness ratio. For the computed values of boundary layer thickness, the appropriate effective trip heights were then computed and shown in the figure.

5.6.5 STS-107 End of Mission (EOM) 3 Pre-Entry Trajectory

STS-107 EOM3 1/22/03 KSC15 FEBRUARY WT/234200 XCG/1079.1 INC/39.0 D/L 8 XR								
Time (Seconds)	Altitude (Feet)	Velocity (Feet/Sec)	Alpha (Degrees)	Beta (Degrees)	Δ Elevon (Degrees)	Δ Body Flap (Degrees)	FS Density (Slugs/Ft^3)	FS Temp (°R)
0	399984.1	24639.3	39.53	0.46	1.98	-4.40	3.84E-11	682.9
10	395245.6	24651.6	39.71	0.43	1.98	-4.40	4.57E-11	650.9
20	390509.6	24661.4	40.09	0.38	1.98	-4.40	5.48E-11	619.8
30	385776.5	24668.6	40.20	0.31	1.98	-4.40	6.60E-11	589.7
40	381047.2	24672.2	40.00	0.23	1.98	-4.40	7.98E-11	560.5
50	376322.3	24671.4	39.46	0.13	1.98	-4.40	9.71E-11	532.1
60	371602.0	24668.9	39.40	0.01	1.98	-4.40	1.19E-10	504.6
70	366887.2	24663.7	39.54	-0.13	1.98	-4.40	1.47E-10	477.7
80	362178.4	24656.2	39.91	-0.30	1.98	-4.40	1.84E-10	450.7
90	357476.6	24646.7	40.10	-0.31	1.98	-4.40	2.30E-10	427.2
100	352782.9	24635.5	39.64	-0.03	1.98	-4.40	2.91E-10	406.8
110	348097.6	24623.6	39.44	0.28	1.98	-4.40	3.71E-10	387.3
120	343421.9	24612.9	39.82	-0.05	1.98	-4.40	4.76E-10	370.8
130	338757.1	24603.3	39.52	0.45	1.98	-4.40	6.12E-10	358.3
140	334104.5	24595.3	39.56	-0.12	1.98	-4.40	7.89E-10	348.4
150	329465.6	24589.4	39.63	0.20	1.98	-4.40	1.02E-09	339.5
160	324842.9	24585.3	39.61	-0.29	1.98	-4.40	1.32E-09	334.1
170	320238.7	24583.5	39.59	-0.30	1.98	-4.40	1.70E-09	331.5
180	315656.4	24583.6	39.59	-0.42	1.98	-4.40	2.18E-09	329.1
190	311100.3	24584.5	39.57	-0.39	1.98	-4.40	2.80E-09	330.0
200	306575.6	24585.9	39.55	0.21	1.98	-4.40	3.56E-09	334.9
205	304327.1	24586.9	39.59	0.25	1.98	-4.40	4.01E-09	338.2
210	302089.3	24587.8	39.59	0.04	1.98	-4.40	4.50E-09	341.7
215	299863.2	24588.6	39.56	-0.31	1.98	-4.40	5.05E-09	345.4
220	297649.9	24589.0	39.55	-0.30	1.98	-4.40	5.65E-09	348.9
225	295450.7	24589.2	39.58	-0.36	1.98	-4.40	6.31E-09	352.1
230	293267.3	24587.7	39.57	-0.03	-0.10	-4.40	7.03E-09	354.9
235	291100.9	24584.5	39.56	0.01	-2.15	-3.15	7.81E-09	357.0
240	288953.2	24580.9	39.58	-0.31	-4.24	-1.82	8.66E-09	358.9
245	286825.9	24576.9	39.62	-0.53	-6.32	-1.82	9.58E-09	360.7
250	284720.9	24572.3	39.82	-0.45	-7.28	-3.59	1.06E-08	362.7
255	282640.6	24567.1	40.46	-0.62	-5.80	-4.69	1.17E-08	364.6
260	280587.2	24561.0	41.26	-0.36	-2.87	-6.35	1.29E-08	366.5
265	278564.2	24551.6	41.32	-0.07	-1.52	-6.35	1.42E-08	368.2
270	276574.4	24541.8	40.55	-0.05	-2.32	-6.35	1.57E-08	369.8
275	274620.0	24531.8	39.45	-0.37	-4.80	-6.35	1.72E-08	371.3
280	272703.3	24520.6	39.16	-0.21	-5.63	-6.35	1.89E-08	372.8
285	270827.1	24508.2	40.17	-0.21	-3.08	-7.73	2.07E-08	374.2
290	268996.3	24494.3	41.21	-0.36	-0.63	-8.16	2.27E-08	375.6
295	267216.2	24479.3	41.08	-0.27	-0.48	-8.16	2.47E-08	377.1
300	265491.1	24463.8	40.01	-0.30	-2.70	-6.44	2.69E-08	378.3
305	263823.5	24448.1	39.37	-0.17	-3.70	-6.44	2.91E-08	379.6

310	262216.6	24431.6	39.99	-0.29	-2.10	-6.44	3.14E-08	380.7
315	260676.1	24413.5	40.77	-0.07	-0.60	-5.58	3.38E-08	381.7
320	259207.7	24394.4	40.44	-0.24	-2.02	-3.87	3.61E-08	382.5
325	257815.7	24375.1	39.80	-0.14	-4.02	-3.02	3.85E-08	383.2
330	256503.1	24355.2	40.10	-0.09	-2.47	-3.02	4.09E-08	383.8
335	255274.6	24333.9	40.51	-0.05	-2.00	-3.02	4.32E-08	384.3
340	254135.1	24311.9	40.22	0.04	-2.68	-3.02	4.55E-08	385.0
345	253087.5	24289.6	40.19	-1.99	-2.41	-3.02	4.77E-08	385.4
350	252135.7	24266.0	40.72	-0.41	-0.41	-2.40	4.97E-08	385.9
355	251278.6	24241.6	40.27	-0.29	-1.81	-1.03	5.17E-08	386.3
360	250503.9	24217.5	39.83	0.67	-2.30	0.39	5.35E-08	386.8
365	249792.7	24193.1	39.67	0.32	-3.60	0.39	5.52E-08	387.1
370	249134.9	24168.1	39.98	0.27	-3.27	0.39	5.69E-08	387.5
375	248524.0	24142.2	40.14	0.18	-3.34	0.39	5.85E-08	387.8
380	247953.5	24115.8	40.05	0.21	-3.52	0.39	6.00E-08	388.1
385	247417.5	24089.3	40.01	0.21	-3.36	0.39	6.15E-08	388.5
390	246911.2	24062.9	39.98	0.16	-3.45	0.39	6.29E-08	388.8
395	246430.6	24036.0	40.06	0.12	-3.38	0.39	6.42E-08	389.0
400	245973.2	24008.5	40.08	0.05	-3.49	0.39	6.56E-08	389.3
405	245536.9	23980.5	40.02	-0.06	-3.22	0.39	6.69E-08	389.5
410	245119.6	23952.3	39.96	0.01	-3.35	0.39	6.81E-08	389.8
415	244718.0	23923.6	40.03	-0.05	-3.32	0.39	6.94E-08	390.1
420	244329.6	23894.3	40.09	-0.02	-3.04	0.39	7.06E-08	390.3
425	243951.4	23864.7	40.00	-0.09	-3.17	0.39	7.18E-08	390.5
430	243581.0	23834.7	39.94	0.01	-3.36	0.39	7.30E-08	390.7
435	243215.1	23804.4	40.02	-0.07	-3.26	0.39	7.42E-08	391.0
440	242851.1	23773.4	40.04	-0.01	-3.04	0.39	7.54E-08	391.2
445	242485.7	23742.3	39.94	0.08	-3.20	0.39	7.67E-08	391.4
450	242116.3	23710.7	39.96	0.05	-2.85	0.39	7.80E-08	391.7
455	241741.2	23678.6	40.04	0.07	-3.11	0.39	7.93E-08	391.9
460	241359.5	23645.9	40.00	0.05	-3.43	0.39	8.07E-08	392.1
465	240971.8	23613.0	39.92	0.02	-3.24	0.39	8.21E-08	392.4
470	240579.1	23579.7	40.00	-0.01	-3.25	0.39	8.36E-08	392.6
475	240183.4	23545.8	40.03	-0.02	-2.90	0.39	8.51E-08	392.8
480	239787.2	23511.4	39.94	-0.11	-3.24	0.39	8.66E-08	393.1
485	239393.0	23476.7	39.96	-0.10	-3.23	0.39	8.82E-08	393.4
490	239002.9	23441.3	40.05	-0.15	-2.91	0.39	8.98E-08	393.6
495	238618.7	23405.3	39.98	-0.15	-3.29	0.39	9.13E-08	393.8
500	238241.2	23369.0	39.92	-0.18	-3.07	0.39	9.29E-08	394.0
505	237870.2	23332.3	39.98	-0.14	-2.87	0.39	9.45E-08	394.3
510	237504.4	23294.8	40.01	-0.11	-2.77	0.39	9.61E-08	394.5
515	237141.4	23256.9	39.94	-0.01	-2.95	0.39	9.77E-08	394.7
520	236777.7	23218.7	39.91	-0.06	-3.14	0.39	9.94E-08	394.9
525	236411.6	23179.8	40.00	0.01	-2.89	0.39	1.01E-07	395.1
530	236040.2	23140.4	39.95	0.05	-3.12	0.39	1.03E-07	395.4
535	235662.3	23100.6	39.90	0.06	-3.04	0.39	1.05E-07	395.6
540	235277.9	23060.2	40.00	0.07	-2.91	0.39	1.06E-07	395.8
545	234888.7	23019.0	39.98	0.03	-2.94	0.39	1.08E-07	396.0
550	234498.6	22977.4	39.92	-0.09	-2.90	0.39	1.10E-07	396.3
555	234112.4	22935.3	39.95	-0.12	-2.67	0.39	1.12E-07	396.5

560	233734.7	22892.3	39.98	-0.17	-3.18	0.39	1.14E-07	396.7
565	233369.4	22849.0	39.93	-0.19	-2.78	0.39	1.16E-07	397.0
570	233018.4	22805.0	39.91	-0.22	-2.87	0.39	1.18E-07	397.2
575	232681.6	22760.6	39.94	-0.20	-2.79	0.39	1.20E-07	397.4
580	232356.9	22715.7	39.92	-0.14	-2.84	0.39	1.22E-07	397.6
585	232039.2	22670.3	39.94	-0.04	-2.81	0.39	1.24E-07	397.8
590	231722.1	22624.3	39.92	0.04	-2.81	0.39	1.26E-07	398.0
595	231399.7	22578.0	39.93	0.08	-2.84	0.39	1.27E-07	398.2
600	231067.7	22531.0	39.95	0.12	-2.93	0.39	1.29E-07	398.4
605	230723.7	22483.6	39.91	0.09	-2.43	0.39	1.32E-07	398.6
610	230368.9	22435.8	39.74	0.04	-2.91	0.39	1.34E-07	398.9
615	230007.4	22387.5	39.82	-0.07	-2.56	0.39	1.36E-07	399.1
620	229646.0	22338.7	39.65	-0.10	-2.71	0.39	1.38E-07	399.3
625	229290.8	22289.6	39.71	-0.18	-2.27	0.39	1.41E-07	399.6
630	228946.8	22239.9	39.51	-0.22	-2.89	0.39	1.43E-07	399.9
635	228616.4	22189.9	39.58	-0.22	-2.21	0.39	1.45E-07	400.1
640	228299.4	22139.4	39.54	-0.18	-2.40	0.39	1.47E-07	400.4
645	227992.3	22088.4	39.54	-0.07	-2.44	0.39	1.49E-07	400.6
650	227689.0	22036.9	39.54	-0.03	-2.39	0.39	1.51E-07	400.9
655	227383.4	21985.1	39.55	0.02	-2.47	0.39	1.54E-07	401.1
660	227070.9	21932.6	39.55	0.00	-2.38	0.39	1.56E-07	401.4
665	226748.5	21879.6	39.56	0.04	-2.39	0.39	1.58E-07	401.7
670	226414.7	21826.1	39.55	0.00	-2.41	0.39	1.61E-07	402.0
675	226070.6	21772.1	39.59	-0.05	-2.25	0.39	1.63E-07	402.3
680	225719.2	21717.4	39.56	-0.10	-2.43	0.39	1.66E-07	402.6
685	225363.4	21662.0	39.57	-0.06	-2.74	0.39	1.69E-07	403.0
690	225005.7	21606.1	39.58	-0.14	-2.37	0.39	1.71E-07	403.3
695	224649.0	21549.6	39.56	-0.15	-2.45	0.39	1.74E-07	403.6
700	224294.1	21492.3	39.59	-0.11	-2.30	0.39	1.77E-07	404.0
705	223939.5	21434.5	39.58	-0.10	-2.44	0.39	1.80E-07	404.4
710	223582.2	21376.0	39.59	-0.06	-2.66	0.39	1.83E-07	404.7
715	223218.1	21316.9	39.59	-0.02	-2.38	0.39	1.86E-07	405.1
720	222843.4	21257.2	39.56	-0.03	-2.45	0.39	1.89E-07	405.5
725	222455.1	21196.6	39.60	0.00	-2.22	0.39	1.93E-07	405.9
730	222052.1	21135.4	39.59	0.00	-2.43	0.39	1.96E-07	406.3
735	221634.7	21073.3	39.51	-0.09	-2.50	0.39	2.00E-07	406.7
740	221205.8	21010.7	39.55	-0.07	-2.22	0.39	2.04E-07	407.1
745	220767.2	20947.2	39.54	-0.07	-2.15	0.39	2.08E-07	407.6
750	220320.4	20882.8	39.49	-0.07	-2.39	0.39	2.12E-07	408.1
755	219866.1	20818.0	39.47	1.91	-1.69	0.39	2.17E-07	408.5
760	219416.1	20750.2	39.74	0.39	-1.39	1.22	2.21E-07	408.9
765	219064.8	20683.0	39.21	-0.22	-1.59	2.88	2.25E-07	409.2
770	218859.4	20616.0	39.23	-0.30	-1.80	2.88	2.27E-07	409.5
775	218768.1	20549.0	39.22	-0.16	-2.22	2.88	2.28E-07	409.6
780	218696.7	20482.4	39.41	-1.77	-3.45	2.88	2.29E-07	409.6
785	218569.9	20414.7	39.91	-0.13	-3.75	2.88	2.30E-07	409.7
790	218392.9	20345.5	40.30	-0.07	-3.76	1.95	2.32E-07	409.9
795	218166.4	20274.7	40.60	-0.03	-3.31	1.02	2.34E-07	410.2
800	217889.0	20203.2	40.65	-0.04	-3.48	1.02	2.37E-07	410.4
805	217555.9	20130.6	40.84	-0.12	-3.62	1.02	2.41E-07	410.7

810	217162.0	20057.2	40.83	-0.20	-3.58	0.30	2.45E-07	411.1
815	216705.4	19982.2	41.03	-0.09	-3.44	0.09	2.51E-07	411.6
820	216190.2	19906.1	41.04	-0.14	-3.35	0.09	2.56E-07	412.1
825	215621.9	19828.7	41.04	-0.09	-3.67	0.09	2.63E-07	412.7
830	215009.4	19749.8	41.01	-0.09	-3.61	0.09	2.70E-07	413.2
835	214362.1	19669.6	40.86	-0.05	-3.29	0.09	2.78E-07	413.9
840	213690.7	19588.8	40.72	0.01	-3.23	0.09	2.87E-07	414.6
845	213005.6	19506.7	40.57	0.02	-3.18	0.09	2.95E-07	415.3
850	212313.4	19423.8	40.40	-0.10	-2.86	0.09	3.04E-07	416.0
855	211617.7	19339.5	40.27	-0.02	-2.91	0.09	3.14E-07	416.7
860	210923.6	19254.1	40.11	-0.02	-2.81	0.09	3.23E-07	417.5
865	210234.9	19167.5	39.99	-0.08	-2.75	0.09	3.33E-07	418.3
870	209553.6	19079.7	39.87	-0.08	-2.69	0.09	3.43E-07	419.0
875	208882.0	18990.7	39.75	-0.04	-2.77	0.09	3.53E-07	419.7
880	208222.7	18900.2	39.72	-0.08	-2.42	0.09	3.63E-07	420.4
885	207576.7	18808.7	39.64	-0.04	-2.59	0.09	3.73E-07	421.1
890	206944.3	18715.7	39.54	-0.06	-2.41	0.09	3.83E-07	421.8
895	206326.2	18621.5	39.55	-0.04	-2.39	0.09	3.93E-07	422.5
900	205722.0	18525.8	39.55	-0.10	-2.46	0.09	4.04E-07	423.2
905	205129.3	18428.6	39.54	-0.03	-2.47	0.09	4.14E-07	423.8
910	204545.9	18330.0	39.55	-0.08	-2.45	0.09	4.24E-07	424.4
915	203967.2	18230.1	39.55	-0.05	-2.46	0.09	4.35E-07	425.1
920	203388.7	18128.8	39.56	-0.04	-2.48	0.09	4.45E-07	425.8
925	202806.1	18026.1	39.55	-0.04	-2.51	0.09	4.56E-07	426.4
930	202213.9	17922.2	39.55	-0.10	-2.54	0.09	4.68E-07	427.1
935	201606.7	17816.8	39.65	-0.06	-2.59	0.09	4.80E-07	427.7
940	200980.4	17709.5	39.68	-0.06	-2.37	0.09	4.92E-07	428.5
945	200330.4	17600.9	39.75	-0.14	-2.52	0.09	5.06E-07	429.3
950	199653.1	17489.9	39.85	-0.07	-2.72	0.09	5.20E-07	430.0
955	198950.2	17377.0	39.92	-0.05	-2.90	0.09	5.35E-07	430.9
960	198224.3	17261.9	39.90	-0.10	-2.71	0.09	5.52E-07	431.8
965	197476.9	17144.9	39.98	-0.04	-2.77	0.09	5.69E-07	432.7
970	196710.1	17025.8	39.93	-0.08	-3.00	0.09	5.87E-07	433.7
975	195925.2	16904.5	40.01	-0.09	-2.91	0.09	6.06E-07	434.6
980	195124.4	16781.0	39.95	-0.03	-2.84	0.09	6.25E-07	435.8
985	194310.2	16656.0	39.99	-0.06	-3.13	0.09	6.46E-07	436.8
990	193484.9	16529.1	39.96	-0.08	-3.08	0.09	6.68E-07	438.0
995	192649.8	16400.4	39.94	-0.03	-3.07	0.09	6.90E-07	439.2
1000	191807.3	16269.1	39.94	-0.07	-3.00	0.09	7.14E-07	440.4
1005	190957.4	16135.7	39.98	-0.06	-3.12	0.09	7.38E-07	441.7
1010	190100.0	16000.1	39.95	-0.05	-3.02	0.09	7.63E-07	443.0
1015	189235.4	15862.3	39.95	-0.09	-3.26	0.09	7.89E-07	444.3
1020	188362.9	15722.2	39.93	-0.07	-3.49	0.09	8.16E-07	445.6
1025	187481.4	15579.5	40.00	-0.06	-3.56	0.09	8.45E-07	447.0
1030	186589.8	15434.7	39.97	-0.05	-3.53	0.09	8.74E-07	448.4
1035	185686.8	15287.5	40.03	-0.06	-3.61	0.09	9.05E-07	449.8
1040	184770.8	15137.9	40.06	-0.05	-3.89	0.09	9.37E-07	451.2
1045	183839.6	14985.8	40.10	-0.08	-4.09	0.09	9.71E-07	452.5
1050	182888.3	14831.0	40.17	-0.06	-4.19	0.09	1.01E-06	454.0
1055	181913.1	14673.7	40.19	-0.07	-4.57	0.09	1.04E-06	455.3

1060	180910.5	14513.1	40.36	-0.36	-4.71	0.09	1.09E-06	456.6
1065	179889.1	14350.3	40.21	-0.08	-4.64	0.09	1.13E-06	457.9
1070	178918.9	14186.9	39.91	0.21	-4.86	0.09	1.17E-06	459.1
1075	178067.7	14023.6	39.67	0.19	-4.56	0.09	1.21E-06	460.1
1080	177347.1	13860.6	39.52	0.03	-4.68	0.09	1.24E-06	460.9
1085	176724.9	13697.9	39.43	-0.13	-4.90	0.09	1.27E-06	461.6
1090	176152.3	13536.1	39.39	-0.16	-4.82	0.09	1.30E-06	462.2
1095	175593.1	13374.4	39.46	-0.10	-5.16	0.09	1.33E-06	462.8
1100	175031.4	13213.0	39.50	-0.08	-5.51	0.09	1.36E-06	463.5
1105	174461.4	13051.5	39.58	-0.05	-5.86	0.09	1.39E-06	464.1
1110	173878.9	12890.1	39.66	-0.07	-6.34	0.09	1.42E-06	464.8
1115	173276.2	12728.6	39.73	-0.05	-6.69	0.09	1.45E-06	465.5
1120	172645.7	12567.1	39.79	-0.05	-6.89	0.09	1.48E-06	466.1
1125	171982.4	12405.4	39.90	-0.03	-6.49	-0.86	1.52E-06	466.9
1130	171283.6	12244.0	39.84	-0.04	-6.75	-0.86	1.56E-06	467.7
1135	170547.6	12082.6	39.84	-0.08	-6.61	-0.86	1.60E-06	468.5
1140	169773.5	11921.5	39.83	-0.06	-6.99	-0.86	1.65E-06	469.3
1145	168966.5	11760.6	39.75	-0.06	-7.13	-0.86	1.70E-06	470.2
1150	168134.2	11599.5	39.69	-0.04	-7.35	-0.86	1.75E-06	471.1
1155	167281.4	11438.7	39.65	-0.03	-7.33	-0.86	1.81E-06	471.9
1160	166408.7	11278.1	39.59	-0.04	-7.40	-0.86	1.87E-06	472.8
1165	165514.7	11117.6	39.47	-0.05	-7.45	-0.86	1.93E-06	473.5
1170	164596.2	10957.6	39.34	-0.08	-7.39	-0.86	2.00E-06	474.2
1175	163649.5	10798.0	39.21	-0.06	-7.59	-0.86	2.07E-06	474.8
1180	162672.1	10638.6	39.10	-0.34	-7.24	-0.86	2.15E-06	475.5
1185	161677.1	10477.8	39.06	-0.24	-7.18	-0.86	2.23E-06	475.9
1190	160830.2	10316.7	38.82	-0.20	-6.97	-0.86	2.30E-06	476.1
1195	160265.4	10156.2	38.73	-0.10	-6.93	-0.86	2.35E-06	476.2
1200	159937.2	9996.5	38.68	-0.05	-7.19	-0.86	2.38E-06	476.2
1205	159630.2	9840.8	38.65	0.21	-8.15	-0.86	2.41E-06	476.3
1210	159171.9	9686.7	38.84	0.22	-7.97	-2.72	2.46E-06	476.3
1215	158523.9	9534.9	38.76	0.19	-7.55	-2.76	2.52E-06	476.3
1220	157702.7	9385.1	38.64	0.10	-7.61	-2.76	2.60E-06	476.3
1225	156769.7	9237.0	38.31	-0.20	-7.54	-2.76	2.69E-06	476.3
1230	155801.8	9091.0	37.98	-0.30	-7.25	-2.76	2.80E-06	476.3
1235	154846.5	8947.1	37.61	-0.26	-7.07	-2.76	2.90E-06	476.4
1240	153910.6	8805.3	37.26	-0.12	-6.93	-2.76	3.01E-06	476.6
1245	152971.8	8665.4	36.89	0.03	-6.59	-2.76	3.12E-06	476.8
1250	151997.5	8527.8	36.58	0.09	-6.64	-2.76	3.23E-06	477.1
1255	150968.2	8391.9	36.26	0.09	-6.35	-2.76	3.36E-06	477.3
1260	149885.0	8257.8	35.92	0.02	-6.47	-2.76	3.51E-06	477.3
1265	148768.0	8125.5	35.51	-0.09	-6.15	-2.76	3.66E-06	477.2
1270	147644.2	7994.6	35.13	-0.15	-5.97	-2.76	3.83E-06	476.8
1275	146532.0	7865.3	34.77	-0.17	-5.66	-2.76	4.00E-06	476.1
1280	145434.1	7737.4	34.33	-0.08	-5.61	-2.76	4.19E-06	475.1
1285	144338.0	7611.0	33.93	-0.02	-5.39	-2.76	4.38E-06	474.0
1290	143225.8	7486.2	33.58	0.01	-5.26	-2.76	4.58E-06	472.7
1295	142085.4	7362.9	33.18	-0.02	-5.15	-2.76	4.81E-06	471.4
1300	140912.7	7241.0	32.78	-0.06	-5.00	-2.76	5.05E-06	470.2
1305	139708.6	7120.4	32.39	-0.06	-4.60	-3.61	5.31E-06	468.8

1310	138474.9	7001.0	31.91	0.00	-4.52	-3.69	5.59E-06	467.6
1315	137213.0	6883.0	31.49	-0.02	-4.32	-3.69	5.89E-06	466.3
1320	135927.7	6766.3	31.05	-0.07	-4.05	-4.61	6.21E-06	464.9
1325	134625.6	6650.7	30.60	-0.05	-4.23	-4.61	6.56E-06	463.5
1330	133313.5	6534.3	30.44	-0.06	-3.76	-5.53	6.94E-06	462.1
1335	131989.1	6418.4	29.99	0.03	-3.55	-5.83	7.34E-06	460.6
1340	130641.9	6303.3	29.54	-0.02	-3.06	-7.37	7.78E-06	458.9
1345	129273.4	6189.6	29.02	-0.04	-3.27	-7.37	8.25E-06	457.1
1350	127888.4	6077.3	28.53	-0.04	-2.97	-7.50	8.76E-06	455.3
1355	126494.6	5965.6	28.07	-0.04	-2.65	-9.19	9.32E-06	453.3
1360	125095.7	5855.4	27.57	-0.03	-2.59	-9.19	9.91E-06	451.3
1365	123694.3	5746.2	27.08	-0.03	-2.59	-9.19	1.06E-05	449.2
1370	122292.7	5637.8	26.66	-0.02	-2.38	-10.10	1.12E-05	447.2
1375	120891.7	5530.4	26.15	-0.02	-2.25	-11.01	1.20E-05	445.2
1380	119488.9	5424.5	25.68	0.00	-2.31	-11.01	1.27E-05	443.2
1385	118083.1	5319.7	25.24	-0.04	-2.44	-11.01	1.36E-05	441.1
1390	116676.7	5215.7	24.84	-0.01	-2.59	-11.01	1.45E-05	439.1
1395	115269.8	5112.6	24.36	-0.04	-2.76	-11.01	1.54E-05	437.0
1400	113861.7	5010.4	23.89	-0.03	-2.78	-11.01	1.64E-05	434.9
1405	112454.1	4909.3	23.38	-0.01	-2.57	-11.01	1.76E-05	432.8
1410	111049.2	4809.3	22.88	0.00	-2.48	-11.01	1.87E-05	430.6
1415	109649.6	4710.2	22.40	0.00	-2.53	-11.01	2.00E-05	428.4
1420	108257.4	4612.0	21.98	0.59	-2.03	-11.01	2.14E-05	426.2
1425	106943.1	4512.5	21.62	0.15	-1.82	-11.01	2.27E-05	424.1
1430	105846.0	4412.5	21.20	0.12	-1.91	-11.01	2.39E-05	422.4
1435	104929.4	4313.0	20.92	-0.18	-2.00	-11.01	2.50E-05	420.9
1440	104021.4	4215.3	20.63	-0.01	-2.55	-11.01	2.61E-05	419.5
1445	103047.8	4119.0	20.47	0.03	-2.24	-11.01	2.73E-05	418.1
1450	102006.9	4024.6	20.19	-0.02	-2.48	-11.01	2.87E-05	416.5
1455	100890.1	3930.9	20.03	0.01	-2.38	-11.01	3.03E-05	414.8
1460	99695.7	3838.1	19.74	-0.03	-2.14	-11.01	3.21E-05	413.1
1465	98427.7	3746.1	19.43	0.01	-1.80	-11.01	3.42E-05	411.3
1470	97103.3	3655.7	18.97	0.00	-1.69	-11.01	3.64E-05	409.5
1475	95739.6	3566.6	18.56	0.00	-1.36	-11.01	3.89E-05	407.7
1480	94355.4	3477.7	18.15	0.01	-1.01	-11.01	4.16E-05	406.0
1485	92967.9	3389.3	17.72	0.04	-0.55	-11.01	4.46E-05	404.4
1490	91587.4	3301.5	17.29	0.04	-0.48	-11.01	4.77E-05	402.7
1495	90220.6	3214.1	16.78	0.01	-0.21	-11.01	5.10E-05	401.1
1500	88871.4	3127.4	16.35	0.03	-0.15	-11.01	5.45E-05	399.6
1525	82491.2	2702.0	14.77	0.03	-1.47	-11.01	7.49E-05	392.1
1550	76943.2	2283.9	13.52	0.20	-3.26	-11.01	9.92E-05	386.9
1575	72271.4	1882.0	11.73	0.10	-4.83	-11.01	1.26E-04	381.3
1600	66475.0	1568.7	10.26	0.10	-6.25	-11.01	1.72E-04	373.1
1625	59398.3	1276.8	9.30	0.17	-2.91	-11.01	2.52E-04	365.6
1650	52749.6	1010.9	8.98	0.27	2.18	-11.01	3.50E-04	368.7
1675	46737.0	848.5	10.47	0.28	7.04	-7.42	4.61E-04	378.1
1700	40406.4	777.7	11.07	-0.35	6.16	0.35	6.04E-04	392.0
1725	31130.9	801.1	10.03	-0.03	0.08	8.62	8.64E-04	420.0
1750	25762.5	735.9	8.30	-0.01	0.74	4.90	1.04E-03	441.3
1775	22151.3	675.3	8.16	-0.02	1.19	4.90	1.17E-03	455.9

1800	18315.8	636.5	7.52	-0.12	2.44	9.85	1.32E-03	470.8
1825	13676.3	604.1	7.19	-0.23	3.71	12.31	1.53E-03	485.9
1850	8865.0	593.3	5.14	-0.05	6.47	1.16	1.78E-03	500.7
1875	4352.1	544.0	5.17	-0.10	6.62	0.35	2.05E-03	511.1
1900	474.5	526.8	7.25	-0.07	2.96	0.35	2.31E-03	521.9
1923.48	-168.8	365.5	9.00	-0.02	2.14	0.35	2.35E-03	524.1

6 THERMAL

6.1 Panel 8/9 Spar & Clevis Thermal Analysis

A thermal analysis was conducted to compare the flight data instrumentation of the spar (V09T9895) and clevis (V09T9910) to the predicted thermal response in a plume heating environment of each of these panel 9 locations. The wing leading edge (WLE) cavity is shown in Figure 6-1. Two independent thermal math models, one from JSC and the other from Boeing Huntington Beach (B-HB), were utilized to perform this analysis.

The B-HB RCC panel 9 finite element model includes the entire RCC panel/T-Seal, internal insulation and metallic hardware including the spar aluminum honeycomb. Radiation between the RCC IML and internal insulation was simulated using the Thermal Radiation Analyzer System (TRASYS) software. Radiation was also simulated from the aluminum spar to the wing cavity using an existing structural model of the upper and lower wing without damage. The RCC inner mold line (IML), internal insulation, and metallic hardware, at the thermocouple locations, were compared to flight data to assure accuracy of the model. The flight certified model is used to support RCC mission life evaluation. This TMM was modified to simulate RCC damage with 6 and 10 inch holes at the center of the RCC panel. STS-107 nominal End-Of-Mission2 (EOM2) was utilized for the outer mold line (OML) heating. Internal plume heating, to be discussed later in detail, was taken from reference heating mapped on the internal RCC and insulation components with stagnation heating of 1.9 times the entering plume and significantly reduced over the spanner beam and spar insulation. As the internal components' material temperature limit exceeded its melting point the analysis was stopped in order to re-configure the TMM. A new geometry was developed to account for missing components and additional heating. The internal component material melting points used in the analysis are listed; Inconel (2500°F), Nextel Fabric (3000°F), Cerachrome (2600°F), and Aluminum (1000°F).

A simplified finite element TMM of the spar, spar insulation, and RCC fitting was developed by the JSC for this investigation. The spar is made entirely of Aluminum 2024-T6 with 0.03-inch thick facesheets that are adhesively bonded to a 1.0-inch thick honeycomb core. The Generic Honeycomb Modeling Tool was used to generate the effective heat transfer properties for the honeycomb spar. The honeycomb attributes for the spar in the region of panel 8 and 9 were gathered from stress report STS89-0537. These effective properties were then used to model the spar in the simplified finite element thermal model of the spar. The embedded aluminum fitting support bars are also included in the model. The spar insulation was modeled and an emittance of 0.85 was used for the outer Inconel foil material. The aluminum/cerachrome interface was assumed to be in intimate contact with no temperature difference at the gap. The four RCC attach fittings are made of steel A-286 and attached to the clevis hardware on the RCC. The RCC attach fittings were modeled each as a single diffusion node. The fitting temperatures are representative of the clevis temperatures and are reported as the clevis temperatures. Nominally, the clevis temperatures do not change until after 550 sec; well after STS-107 V09T9910 went off scale low. During this time, conduction from the RCC is insignificant and the only paths for heat to flow to the clevis are from the RCC fittings and through additional convective heating. The radiative boundary conditions for entry were based on the entry RCC inner mold line (IML) temperatures predicted for STS-107 by the Boeing Houston aero-thermal group. These boundary conditions were applied to the outer spar insulation surface. On the backside of the spar, where the inner wing structure is located, a constant boundary temperature of 22°F is used.

For the ascent thermal analysis using the JSC model, the boundary conditions are changed to the predicted ascent RCC IML temperatures. On the backside, the radiative boundary temperatures decreased from 55°F to 30°F. The backside spar ascent boundary conditions were determined by correlating the data to STS-109, since they had identical initial temperatures prior to the temperature increases at 300 seconds from launch.

The plume heating estimates for stagnation are and distributions within the cavity are discussed in section 5.3.3 and results summarized here for varying breach hole sizes in panel 8. Using equation (6-1), the time varying heat rate on panel 9 was generated.

$$\dot{q}(x,y,z,t,d_{hole}) = \dot{q}/\dot{q}_{plate}(x,y,z,d_{hole}) \times \frac{\bar{q}_{\infty}(t)}{\bar{q}_{\infty}(488)} \times \frac{V_{\infty}^{2}(t)}{V^{2}{}_{\infty}(488)} \times \dot{q}_{plate}(d_{hole}) \quad (6\text{-}1)$$

where;

$\dot{q}_{plate}(d_{hole})$ is 27.1, 30.1, 55.9 BTU/ft^2-sec for a 4 inch, 6 inch, and 10 inch hole respectively.

Figure 6-2 shows how $\dot{q}/\dot{q}_{plate}(x,y,z,d_{hole})$ varies for a 10 inch hole. The average distribution factor of the stagnation heating value over panel 9 for a 4 inch, 6 inch, and 10 inch hole are .02, .08, and .12, respectively. Additional heating behind the spar insulation, directly on the aluminum near bottom clevis locations, is also considered as a fraction of the panel 9 heating.

The ascent heating for internal flow impingement on the spar insulation was determined by normalizing the panel 8 stagnation heating with body point 5505 entry heating. The normalization factors are then applied to the STS-107 predicted ascent heating for body point 5505. The normalization factors used for the 4 inch, 6 inch, and 10 inch holes are 0.89, 1.0, and 1.8, respectively. The same distribution factors are then applied to the panel 9 spar insulation for ascent heating.

The thermal math models were solved using the Systems Improved Numerical Differencing Analyzer (SINDA). The B-HB model results are shown in Figure 6-3, through Figure 6-5. Figure 6-3 suggests that the heating through a 10 inch hole will produce a temperature rise on the back of the panel 9 spar that matches flight data V09T9895. The assumption of sneak flow directly onto the clevis, on the order of 1%, is necessary to match the flight data of V09T9910 as shown in the comparison of Figure 6-4 and Figure 6-5.

The JSC model predictions in Figure 6-6 and Figure 6-7 are shown for a 6 inch, and 10 inch hole. Figure 6-6 shows the instrumentation location on Panel 9 thermal response to varying hole sizes. A hole size between 6 inch and 10 inch will match the flight data V09T9895. The JSC model also requires a sneak flow assumption of 10% to match the clevis flight data, V09T9910 as shown in Figure 6-8. In Figure 6-9, sensitivity analysis of the thermal response was considered for a 50% variation in the heating data due to uncertainties.

The results from the ascent analysis are shown in Figure 6-10. Here it is shown that the predicted spar temperature rise during ascent is slightly higher with a pre-existing hole in the wing leading edge. STS-109 (undamaged condition) and STS-107 (presumably damaged condition) flight data are compared to these analytical results. It can be surmised that the thermal response of the STS-107 flight data is consistent with the analytical predictions for a damaged wing leading edge during ascent.

6.1.1 Damaged Tee-seal

An auxiliary analysis was performed to assess the feasibility for a damaged tee-seal between panel 8 and panel 9 to cause the observed flight data in the Panel 8/9 region. This analysis assumed that the tee-seal was damaged to the extent that it was completely missing for a 20 inch length on the lower portion of the seal. The same methodology as described in section 6.1 was used to compute the spar breach time and temperature response of the flight measurements using the heating rates described in section 5.3.3.

Analysis results using the Boeing-HB thermal math model is shown in Figure 6-11. This figure shows the computed temperature transients for the spar insulation immediately behind the tee-seal. This insulation does not have the Nextel fabric under the inconel foil and therefore has a lower failure temperature of about 2,600°F. Here the insulation fails within 400-500 seconds. The temperature response for the aluminum spar behind the insulation is predicted to fail at 360 seconds. This is earlier than the estimated actual spar breach time of 487 seconds.

Figure 6-12 shows the spar temperature transient prediction compared to the measured flight data. Here it is seen that the predicted temperature rise is much quicker than the flight data. Note that this analysis

is invalid after about 500 seconds because hot gases know to be within the wheel well at this time were not simulated. Figure 6-13 shows the analytical clevis temperature compared to the flight data. Here it is seen that the analytical prediction rises slightly earlier than the flight data but is not totally out of proportion.

This analysis and the analysis presented in section 6.5.1 suggests that a damaged tee-seal is not a likely scenario for initial damage to the wing leading edge.

6.2 Spar Burn Through Analysis

Several scenario-based and flight data-based data suggest that the wing leading spar experienced a breach during the mission. The most significant of these is the failure of the wire cables which run along the backside of the wing leading edge. Figure 6-14 shows a picture of this region and summarizes the failure times for each of these cables. Thermal analysis and torch testing has shown that the time for failure of one of these cables is less than three seconds. Therefore it is believed that the cable failure time gives a good indication of the when the spar is breached immediately in front of the cable. Since the cables do not provide full coverage of the spar and the original location of the breach is unknown, the exact time of the breach is uncertain but occurred no later than 487 seconds.

A geometric analysis was used to determine if the hole size as a function of time could be determined from the cable failure times. The result of this assessment is shown in Figure 6-15. Here it is predicted that the spar hole could reach a size of 580 in^2 by 520 seconds. It can be rationalized that the hole growth is eventually stunted and arrested as shown by the analysis due to the following factors:

- High mass of the spar embedded aluminum fitting support bars effectively “frames out” a rectangular limit for the hole
- Plume effect on the spar from the wing leading edge hole is arrested by the limited growth of the hole in the RCC.

A parametric analysis was also performed with this model to determine the initial breach time. Here the initial location was parametrically varied and the initial breach time computed. From these analyses, the spar could have been breached from 478 to 487 seconds from entry interface. Although the strain measurements and associated structural analysis suggest that the breach occurred between 420 and 470 seconds from entry interface, supporting data for a spar breach in this time frame comes from:

- Bundle 3 wire harness failure (before 498 sec)
- Bit flip in wheel well (488 sec)
- PNL 8/9 thermal analysis (490 sec)

6.3 Wheel Well Thermal Analysis

A thermal analysis was used to compare predicted heating to the flight data instrumentation summarized in Table 6-1 for the wheel well. Here a hot gas plume originating from the wing leading edge spar is assumed to impact the outboard wheel well wall. The hot outboard wall then conducts heat into the adjoining walls and radiates into the main landing gear (MLG) wheel well and the associated sensors within.

Table 6-1 - Wheel Well Sensor Summary

MEAS. NO.	DESCRIPTION
V58T0125A	SYS 1 LMG UPLK ACT UNLK LN
V58T0405A	L H MLG STRUT ACTUATOR
V58T0841A	SYS 2 L AFT BK SW VLV RTN
V58T0842A	SYS 3 L FWD BK SW VLV RTN
V58T1700A	L MLG BRK HTR LN 1 SYS 1&3
V58T1701A	L MLG BRK HTR LN 3 SYS 2&3
V58T1702A	L MLG BRK HTR LN 2 SYS 1&3
V58T1703A	L MLG BRK HTR LN 4 SYS 2&3

A thermal math model shown in Figure 6-16 was developed directly from computer aided design (CAD) models and used to predict the sensor responses in this presumed scenario. Shell elements were used where possible for simplicity with the remaining geometry represented by solid tetrahedral elements. Main Landing Gear (MLG) components were then thermally connected by combining nodes at joint locations. This allowed for faster analysis since arbitrarily low conductors (which is a common method to join components) can significantly reduce the time step in order to maintain a required accuracy. Internal radiation was also modeled using the Monte Carlo technique with 16000 rays per node. All of the nodes representing sensor locations had an initial temperature corresponding to the flight data. The rest of the components and the wheel well walls had an assumed initial temperature of 80°F.

The predicted plume heating distribution model is described in section 5.3.3. The heating was calculated for a 5 inch diameter hole in the wing leading edge spar assumed to appear instantaneously at EI+488sec (13:52:17 GMT). The plume impinged upon the outboard wheel well wall at location xo=1105, zo=309 and at a distance of 56 inch from the spar. Correction factors were applied for the 31.5 degree off normal impact angle as well as the internal wing pressure. The center of the plume had a heating rate of 22.1 BTU/ft^2-sec with the heating dropping off radially from the centerline. Melting of the outboard wall was not modeled, therefore, once a node reached melting temperature (935°F) it was then held at this temperature.

The thermal math model was solved using the Systems Improved Numerical Differencing Analyzer (SINDA). Predicted temperatures for the hydraulic lines and the strut actuator were obtained and are shown in Figure 6-17 through Figure 6-24. Initially, all the sensors begin to trend towards 80°F from radiation exchange with the 80°F surrounding structure. At 488 sec (GMT 13:52:17) the plume heating is applied to the outboard wall and the temperatures begin to trend upward at a rate dependant on their view factor to the outboard wall.

Table 6-2 - Sensor location and view factor summary

Sensor	Location	View Factor
V58T1700A	Bottom of strut	Good
V58T1701A	Bottom of strut	Good
V58T1702A	On inboard wall	Partial
V58T1703A	On inboard wall under debris shield	Poor
V58T0841A	On inboard wall under debris shield	Poor
V58T0842A	On inboard wall	Poor
V58T0125A	On upper wall behind structure	Poor
V58T0405A	Aft inboard corner of wheel well	Partial

At first glance sensors V58T1700A and V58T1701 correlate very well with the flight data. However, past EI+510 sec (GMT 13:52:39) the low mass honeycomb access panel has reached its melting temperature in the analysis as shown in Figure 6-25. This would allow hot gases to enter the wheel well and deposit energy through convection directly on the MLG components. However, one could argue that this convective energy then replaces radiative energy but CFD would have to confirm this. After EI+586 sec (GMT 13:53:55) the wall at the center of the plume reached its melting temperature as shown in . At this point the area available for hot gases to enter the wheel well increases rapidly as more of the outboard wall melts. The assumption of holding the wheel well wall at its melting temperature (935°F) is no longer valid for this analysis and CFD is required to determine the hot gas flow inside the wheel well in order to account for the convective heating.

From this analysis, it is possible to conclude that a portion of the hydraulic line temperature increase seen in the flight data can be attributed to radiation from the outboard wheel well wall being heating by a plume due to a spar breach.

6.4 Wire Bundle Burn-Through Tests

An Arc jet test program designed to simulate the flow of superheated air through a breach in the Space Shuttle Orbiter's Wing Leading Edge was performed at the Johnson Space Center's (JSC) Atmospheric Re-entry Materials and Structures Evaluation Facility (ARMSEF). Several of the test objectives listed in the test plan were met in this program. These objectives were:

- obtain test data to correlate and validate the axisymmetric plume heating methodology;
- obtain the failure mechanism characteristics, failure initiation time, failure rate, and burn-through time of a cable bundle when subjected to hot gas impingement with representative reentry plume environment;
- evaluate aluminum hole growth rates for aluminum flat plates;
- and evaluate aluminum burning phenomena and the effect of potential exothermic reactions on plume heating.

The test was accomplished through the use of a specially designed water-cooled "plume box" which was inserted in the arc jet flow field. The box was designed with interchangeable front plates with different hole sizes cut into them to represent the breach. The tests performed with this box show that a high enthalpy flow passing thorough a breach in Columbia's wing structure is not only capable of causing failures in flight-type wire bundles similar to what was seen flight, it is also capable of exacerbating the problem by rapidly increasing the size of the breach.

A total of three cable bundle tests were performed in this program. Each test was accomplished with a different plume box configuration. These configurations were, one-inch diameter hole in a cooled copper plate (the cooled plate resulted in a constant hole diameter), a two-inch diameter hole in a cooled copper plate, and a one-inch diameter hole in an uncooled aluminum plate. The arc heater power level for each test configuration were as follows: 3.27 MW for the one-inch hole test and 3.63 MW for both two inch hole tests. The one inch hole test resulted in a total of 6 wire failures in 837 seconds. That failure rate, a much lower rate than seen in the flight, necessitated an increase in heater power for the subsequent test runs. The increased power with a two-inch diameter fixed hole resulted in 33 wire failures (the total number of wires monitored) in 538 seconds. That rate approached what was experienced in the flight. The uncooled aluminum plate resulted in all 33 wires failing in 68 seconds as well as a complete disintegration of the bundle. The hole in the plate also grew from 1 inch in diameter to over 4 inches in diameter in approximately 13 seconds. This agreed well with pre-test analytical predictions.

Several calibration test runs were made to support the development of the analytical math models used to characterize the plume generated within the box. These test runs consisted of taking pressure and heat flux measurements along the centerline of the plume at different distances from the front hole. The heat flux and pressure of the arc jet free stream, the pressure on the front of the box, the static pressure within the box, and the static pressure of the test chamber were also measured. To estimate the heat flux that the cable bundle experienced, a tube calorimeter was built. The calorimeter consisted of a stainless steel thin walled tube with the same diameter as a cable bundle. To the inside of this tube were attached fine-gage thermocouples in a grid-like pattern. This tube was mounted inside the box in the same orientation as the cable bundles then exposed to the same environment. The response of the thermocouples was used to back out the absorbed flux.

Each cable bundle test article was approximately 1.75 inches in diameter and constructed to simulate the cable bundles that are routed along the Orbiter wheel well in the left wing. Each test bundle consists of 290 cables, of these, 33 cables were monitored with an auxiliary data system. Conductor-to-conductor resistance within each of the 33 cables was recorded during test operations. Each cable in the bundle was a Kapton insulated, 24 AWG, twisted, shielded, pair. Aluminum clamps from the vehicle installation were used to hold the bundle of cables together and for attachment to the box. A picture of the cable bundle test article is shown in Figure 6-27.

Previous test programs demonstrated the failure mode for Kapton insulated cables when subjected to extreme heating – a short circuit develops between the two conductors within a twisted shield pair cable. This occurs because the Kapton insulation breaks down and changes from an insulator to a resistor over a finite period of time. This means the resistance between the two conductors within a twisted pair cable changes from a very high value to a low value. An example of this from a previous test program is shown

in Figure 6-28. The cables of interest are connected to various sensors (temperature, pressure, strain). Measurements of conductor to conductor resistance are normalized by converting them to what the Orbiter signal conditioner would output for a –75 to 250°F hydraulic temperature sensor channel assuming initial actual temperature of 100°F and a short of this magnitude occurring in the cable. An example of the results from this conversion are shown in Figure 6-29. Note that this plot is similar to the actual sensor data observed from STS-107.

This test program was performed in Test Position #2 (TP2) of the ARMSEF. A video camera mounted on the test chamber was used to visually monitor the flow field and interior of the test chamber. This video was used to help determine if and when a particular test run should be terminated. A camera was also available to monitor the front of the box when a destructive test of that front plate was performed. A smaller camera was mounted inside the plume box and used to monitor the test specimens and determine if and when a particular test run should be terminated.

This test program was intended to simulate an internal convective plume resulting from penetration damage to the Orbiter wing. To facilitate a re-creation of this environment, a water-cooled copper box was fabricated and mounted to a specially designed insertion arm. The box was made of a stainless steel frame with 0.25-inch thick copper plates making up the walls and 0.25 inch diameter copper tubes were brazed to these walls to provide cooling. These walls also protect the test articles from the heating associated with reflected shocks within the test chamber. The front of the box had a 10”x10” square opening over which interchangeable faces could be attached. This position was designated the forward position. Four types of plates were manufactured to occupy this position. They were:

- Water-cooled copper plate with a 1-inch diameter hole
- Water-cooled copper plate with a 2-inch diameter hole
- Aluminum plate with a 1-inch diameter hole
- Aluminum honeycomb with a 1 inch diameter hole

Stainless steel brackets were mounted inside the box at 15 inches and 20 inches from this forward plate. The various test articles, cable bundles, calorimeters, etc., were attached to these brackets. These locations were designated the aft positions. Figure 6-30 gives a sketch of this set-up and Figure 6-31 shows the configuration and design of the box. Also within the box was mounted a video camera to record the response of the test article.

The test program consisted of two distinct phases: the calibration phase and the engineering test phase. Two different sized holes in the forward position provide two different plume geometries and two different ζ positions for the test article provide an array of test locations for this test program.

The test conditions attempted to match the arc jet flow free stream stagnation pressure and centerline enthalpy to the flight stagnation pressure and total enthalpy. The targeted conditions and results of arc jet calibration runs are shown graphically in Figure 6-32. The resultant heat rate at these conditions was measured. The calibration data for the flowfield free stream is compiled in Table 6-3

Table 6-3 – Test Conditions

Date	Run Number	Z-distance (in)	Current (amps)	Mass Flow (lbm/s)	Bulk Enthalpy (BTU/lbm)	Power (MW)	CL Pressure (psf)	CL Heat Rate 1" D (BTU/ft2-s)	CL Enthalpy (BTU/lbm)
05/01/2003	2-2509-3	10	530	0.2	3600	1.25	not measured	not measured	not calculated
05/01/2003	2-2509-3	10	1200	0.4	5400	3.62	not measured	not measured	not calculated
05/05/2003	2-2510-3	21.25	530	0.2	4100	1.25	15	52	5517
05/05/2003	2-2510-3	21.25	1400	0.4	6200	4.27	36	198	13560
05/05/2003	2-2510-3	21.25	1200	0.6	4700	4.44	46	149	9027
05/05/2003	2-2510-3	21.25	1300	0.67	4800	5.1	52	162	9231
05/05/2003	2-2510-3	21.25	1300	0.8	4500	5.43	60	not measured	not calculated
05/06/2003	2-2511-3	21.25	1000	0.3	5500	2.8	25	120	9862
05/06/2003	2-2511-3	21.25	1200	0.3	6400	3.26	27	154	12178
05/06/2003	2-2511-3	21.25	530	0.2	4080	1.26	15	60	6366
05/28/2003	2-2516-3	20.05	1200	0.4	5450	3.63	32	139	10097

Calibration runs were also performed to collect data on the plume generated within the box. The centerline pressure and heating rate of this plume was measured at specific test points established in the flow field calibration phase. In addition, a specially designed calorimeter was used to measure the heating distribution on a cylinder the same diameter as a cable bundle. This consisted of a 1.75-inch diameter thin-walled stainless steel tube to which several small gauge thermocouples were attached in a grid like pattern. The response of these t/c's to the plume environments was recorded and from this data the heat flux was determined. All of this data will be used to refine the thermal models used to analyze the cable bundle response to the breach environment. The results of these calibration runs are presented in Table 6-4.

Table 6-4 – Test Condition Summary

Arc-jet Parameters		Arc-jet Flow Conditions					Box Measurements							
Current	Flow Rate	Bulk Enthalpy	Chamber Pressure	q-4" FF	q-1" FF	P-4" FF	Hole Dia.	P-front	P-internal	Ppitot-10"	Ppitot-15"	q-probe-10"	q-probe-15"	q-cyl stag-15"
(amps)	(lbm/sec)	(Btu/lbm)	(psf) /w box in flow	(Btu/ft2-s)	(Btu/ft2-s)	(psf)	(inches)	(psf)	(psf)	(psf)	(psf)	(Btu/ft2-s)	(Btu/ft2-s)	(Btu/ft2-s)
1000	0.3	5800	0.902	62	122	26	1	28	0.78	2.06	No Data	No Data	No Data	4.3
1200	0.3	6600	0.966	74	154	27	1	29	0.88	No Data	No Data	No Data	No Data	4.7
1000	0.3	5800	0.902	62	122	26	2	28	0.47	1.45	2.06	No Data	11	7.9
1200	0.3	6600	0.966	74	154	27	2	29	0.42	1.49	2.02	No Data	13	9.4
1200	0.4	5500	1.153	71	139	35	2	35	0.68	2.18	3.18	No Data	16	12.1

Three runs with a cable bundle were performed at the test conditions shown in Table 6-5. After arc jet activation, the insertion arm with box and cable bundle inside were inserted into the flow field while cable resistance was monitored. When sufficient cable failures were observed or other arc jet constraints were reached, the arc jet was deactivated and the arm was moved to remove the box from the flow field.

Table 6-5 – Test Configuration Summary

Item	Run 1	Run 2	Run 3
Box Forward Plate Type	Cooled	Cooled	Uncooled
Forward Plate Orifice Diameter (in)	1 in	2 in	1 in (starting)
Bundle Distance Aft of Orifice (in)	15 in	15 in	15 in
Arc Jet Current (amps)	1200	1200	1200
Arc Jet Mass Flow (lb/sec)	0.3	0.4	0.3

Run 1: The test set-up incorporated a 1-inch diameter orifice in the forward position of the box with the cable bundle 15 inches aft. The relatively low heating rate of run 1 produced only a few cable failures, but all were on the cable side facing the plume.

Run 2: The test set-up incorporated a 2-inch diameter orifice in the forward position of the box with the cable bundle 15 inches aft. Higher heating rates of run 2 produced failures faster and the entire cable bundle failed. Photographs in Figure 6-37 shows the appearance of the bundle before and after the test.

Run 3: The test set-up incorporated an uncooled aluminum, 0.1 inch thick flat plate in the forward position box. This plate had a 1 inch diameter orifice on the centerline with the cable bundle 15 inches aft. The test demonstrated a rapid erosion of the uncooled aluminum orifice. The orifice grew to an estimated 4 inch dia in approximately 13 seconds. Orifice growth was somewhat arrested after 4-5 inch due to a heat sink designed around the perimeter. The cable bundle showed a very rapid and increasing failure rate as orifice diameter increased.

Figure 6-34 and Figure 6-35 shows a comparison of cable failure rates for this test series and that observed on the vehicle. Based on the various observed cable failure rates, heating rate for the vehicle cable bundle must have been between those of Run 2 and Run 3.

Table 6-6 – Test Results Summary

Item	Run 1	Run 2	Run 3
Cable Run Time (sec)	837	538	68
Heating Rate from Calibration (BTU/ft^2-sec)	4.69	12.13	Greater and increasing during run, but could not be measured
Time When First Cable Begins Failure (sec)	107	14	13
Time When Last Cable Begins Failure (sec)	635	351	66
Total Cables Failed (33 monitored)	6	33	33

Cable bundles were tested at three different test conditions. Test results showed the arcjet-induced heating produces the same cable failure mechanism as occurred during previous cable overtemperature tests - a short circuit between the two conductors within a twisted shield pair cable. Data obtained for cable failure rate as a function of heating rate can be used to validate thermal models of the vehicle cable bundles for the STS-107 Columbia investigation. These models can be utilized to determine the heating rate which the STS-107 bundle experienced. This in turn can be used to gain a better understanding of the vehicle failure scenario.

6.5 Wire Bundle Burn-Through Thermal Analysis

A thermal analysis was performed on the wire bundles, MLG wheel well wall, and wing upper skin shown in Figure 6-39. Separate Thermal Desktop TMM's were created for each hardware region. These math models were used to calculate the required breach sizes and breach locations along the wing leading edge spar that would cause failure of each item. Their best estimated failure times were determined from the flight data. The results of each analysis were mapped against each other at defined zones along the wheel well to determine if a common breach size and location could explain their collective failure. The zones and panel locations are defined in Figure 6-40.

The spar breach hole size is assumed to be constant with no growth for the purposes of this comparative analysis. In addition, any oxidation and combustion effects were not modeled. The plume is assumed to be perpendicular to the respective spar. In each analysis it is assumed to impinge directly upon the object (wire bundle, wheel well, upper wing). This is significant in that the wheel well wall should always have a direct impingement while the bundle will not necessarily have a direct plume impingent. The spar breach is assumed to be at EI+487 seconds.

The flat plate plume heating induced from a wing leading edge breach at EI+491 seconds as a function of hole size and distance was used in this analysis and is discussed in section 5.3.3. Figure 6-41 and Figure 6-42 show the heating rates for impingement on a flat plate and a 1-inch diameter cylinder, respectively. A heating factor time array was included to adjust the heating to represent a breach earlier in the re-entry profile. Also, adjustments were made for increased hole sizes and distances. The plume heating adjustment for breach hole sizes greater than 2-inch diameter are shown in equation 6-2 while plume heating adjustments for breach distances greater than 60 inches are shown in equation 6-3.

$$qdot(d_{hole}) = qdot_{2.0"hole} \cdot \left(\frac{d_{hole}}{2"} \right)^{2.6} \quad \textbf{(6-2)}$$

$$qdot(x) = qdot_{dist} \cdot \left(\frac{dist}{x} \right)^{2} \quad \textbf{(6-3)}$$

Corrections for local pressure coefficients, off-normal angle impingements, and radial distribution from the stagnation point are shown in Figure 6-43 though Figure 6-45. Plume impingement on the bundle was also adjusted for radius and circumferential distribution as shown in Figure 6-46 and Figure 6-47.

The wire bundles are comprised of several harnesses each comprised of cables. Each cable consists of 2, 3, or 4 wires as shown in Figure 6-48. The lost in-flight measurements experienced were due to cable failure.

Testing as described in section 6.4 was performed to correlate and gain confidence in the wire bundle TMM. Here, 1¾ inch diameter bundles were subjected to 8.08 BTU/ft^2-sec (large propane torch test), 4.69 BTU/ft^2-sec (arc jet test #1), and 12.13 BTU/ft^2-sec (arc jet test #2) heating rates (determined through calorimeter test runs). The TMM bundle failure rate test predictions were mapped against their respective test results in Figure 6-49 and Figure 6-50.

The wire bundle TMM represented the bundle as a lumped mass rather than a group of individual cables. A specific heat of 0.225 BTU/lb$_m$-F and thermal conductivity (along the length of the bundle) of 166 BTU/hr-ft-F were used. The density was calculated by dividing the bundle mass per unit length (0.197 lb$_m$/inch) by its cross sectional area. A factor of 2.14 was applied to account for the additional surface area present in the bundles but not in the TMM. A radiative boundary condition of 70°F (emittance = 0.88) was used. Bundle radial heat transfer and cable failure temperatures (800°F) were determined through large propane torch testing. How the cable failure temperature is determined is shown in Figure 6-51.

Heating was applied via film coefficients and a 1700°F flame recovery temperature during the large propane test correlation but was adjusted to the plume configuration for the arc jet test TMM simulations.

The test correlated TMM was adjusted to flight conditions by applying the corrected plume heating. It was also modified to represent flight bundle 3 as shown in Figure 6-52 by adjusting the mass per unit length to 0.303 lb$_m$/inch. A flight radiative boundary condition of 20°F was used (emittance = 0.88). Flight bundle 3 is assumed to have failed completely due to the likelihood that the measured failed cables are distributed throughout the bundle. The heating required to match flight bundle 3 failure rate was determined to be 89 BTU/ft^2-sec. This was used to determine the required spar breach sizes and locations.

The wheel well wall is constructed of ribbed aluminum 2024-T6 surfaces of varying thicknesses. Effective thicknesses were used along the wall to capture the appropriate thermal mass response as shown in Figure 6-53. Radiative boundary conditions were assumed to be 70°F based on wing structural temperatures. Koropon primer (emittance = 0.86) was assumed to be present during the duration of the analysis. A failure temperature of 935°F was assumed. Wall burn through was assumed at EI+599 due to the first indicated temperature rises of the wheel well. A failure time of 112 seconds (EI+599 – EI+487) was used to determine spar breach sizes and locations.

The upper wing is made up of Aluminum 2024-T6 honeycomb structure (melting temperature of 935°F). The thicknesses of the honeycomb facesheets and core are 0.025 and 0.9684 inches respectively. The Generic Honeycomb Modeling Tool was used to generate the effective conductivity through the honeycomb core. An adiabatic upper surface boundary condition and a lower surface radiative boundary condition (70°F) were assumed. A Koropon coating (emittance = 0.86) was applied and assumed to be present throughout the analysis. Upon burn through of the lower facesheet, heating is applied to the upper facesheet. The FRSI layer attached to the upper surface of the wing is assumed to fail when or slightly before the wing structure fails. A burn through time of EI+536 seconds is assumed due to a plateau in the wire bundle failure rate. Spar breach hole sizes and locations were determined using a failure time of 49 seconds (EI+536 – EI+487).

The TMM spar breach results for flight wire bundle 3, the wheel well wall, and the upper wing (for the partitioned zones of the wheel well) are compared in Figure 6-54 through Figure 6-57. Since the assumed failure times of the wheel well and the upper wing are not exact, error bars are included for the wall in zone 2 to indicate the sensitivity of the comparison to the chosen failure times. The locations of highest probability for the plume impingement are zone 1 (panel spar 6 and 7 coverage) and zone 2 (panel spar 8 coverage).

In this analysis, the most probable spar breach diameters ranges from 2 to 6 inches. This estimated hole size in the spar is not entirely consistent with the analysis described in section 6.1. It should be realized that this analysis had to make gross assumptions for the plume characteristics which biased the heating rates on the high side. Application of these heating rates resulted in demise rates for the cable which were higher than actually observed in flight. Therefore, from the cable demise rates which were correlated to the observed flight data, the estimated spar hole size should be considered as a lower bound.

6.5.1 Tee-seal scenario

In addition to the damaged tee-seal analysis comparison to the flight data in the panel area described in section 6.1.1, the damaged tee-seal scenario was evaluated for wire cable bundle burn rates. In the case of a damaged tee-seal where the flow entrance area aspect ratio is high in comparison to a round-shape hole, the plume heating drops off much quicker along the flow axis (refer to section 5.3.3). To bound this analysis in terms of feasibility, assumptions were biased to predict the most rapid burn rate for the cable bundle. The bundle was assumed to be directly behind the spar although the closet bundle is actually at least 12 additional inches away from the spar. Using the heating rate profile shown in figure 5.3.2-27, the predicted wire burn rate is shown in Figure 6-58. In comparison to the burn rate observed in flight, this analytically predicted burn rate is lower due to rapid drop in heating rate. This analysis coupled with the panel 8/9 thermal analysis provides evidence that a damaged tee-seal scenario is not consistent with the flight data and observations.

6.6 Orbiter Sidewall Bondline Thermal Analysis

A thermal analysis was performed on the area surrounding OV102's V34T1106 sidewall bondline temperature sensor. The sensor is located on the inboard surface of the port sidewall at XO: 1215.5, ZO: 355.5 as shown in Figure 6-59. A Thermal Desktop TMM was created to determine whether its temperature rise during the re-entry was produced by increased external heating, by the addition of internal heating, or by the loss of the FRSI layer. The assumptions used in the analysis, the TMM correlation with flight data, the analysis and its results are discussed below.

The sidewall is an aluminum honeycomb structure with a layer of FRSI on the outboard surface as shown in Figure 6-60. Conduction was assumed to be 1-D through the sidewall. Internal and external convection were negligible. Radiation heat loss was assumed from the FRSI (emittance = 0.8) to the external air temperature and from the inboard facesheet (emittance = 0.86) to the Orbiter internal structure. The internal structure temperatures are shown in Figure 6-61 and Figure 6-62 for STS-109 and STS-107 respectively. Conduction through the honeycomb core (density = 3.8 lb/ft^3) was assumed to be 0.095 BTU/hr-in-F. The honeycomb facesheet densities were adjusted to account for the honeycomb adhesive. The RTV density surrounding the sensor was modified to account for the sensor mass (1.5 g).

The inner facesheet, outer facesheet, and RTV densities became 223, 201.7, and 278.4 lb/ft^3, respectively.

Confidence in the TMM was obtained through correlation with STS-109 flight data as shown in Figure 6-63. Nominal STS-109 external heating can be seen in Figure 6-64 and corresponding pressure profiles were used in the analysis. To achieve correlation a factor of 1.986 was applied to the inboard RTV density to account for missing thermal mass.

Upon correlation, the TMM was used to investigate the possible STS-107 heating cases shown in Figure 6-65. Nominal STS-107 external heating and pressure profiles were applied except as otherwise noted.

The study showed that the temperature rise can be explained by an external heating 13x nominal applied after EI+600 seconds or the application of internal fuselage heating (0.16 Btu/ft2-sec) after EI+648 seconds. These heating profiles are shown in Figure 6-66 and Figure 6-67 respectively. The temperature rise, however, cannot be explained by the loss of the FRSI layer under nominal external heating. The results of the three cases studied are mapped against STS-107 re-entry flight data in Figure 6-68 (external heating case), Figure 6-69 (internal heating case), and Figure 6-70 (loss of FRSI case).

6.7 Damaged Wing Leading Edge Coupled Aero-Thermal-Structural Analysis

A multidisciplinary process was developed to simulate the initiation and propagation of thermal/structural failure in the left wing during reentry. The objective of the analysis was to evaluate the plausibility of RCC damage in the form of 6 or 10 inch diameter holes near the apex of panel 7 in leading to the observed pattern of thermal/structural failure established for STS-107. Critical conditions assessed during the simulation included front wing spar burn-through time, panel 8 spar rear facesheet temperature response, and eventual failure of the RCC panels and attachments.

The process, depicted in Figure 6-71, consisted of defining external and internal aerodynamic heating and airloads environments throughout the entry, generating high fidelity thermal response of the internal insulation blankets, wing and spar structure, and RCC panels, and performing a detailed structural failure analysis of the thermally and mechanically loaded system. Multiple failure mechanisms were examined including failure of wing spar insulation, aluminum melting, honeycomb face sheet/core debond and loss of structural integrity, and loss of RCC wing leading edge attachments. This section of the report describes the analysis methodology and solution results for a damage scenario consisting of vehicle reentry with a 6 or 10 inch diameter hole in the left wing leading edge. Predicted temperature distributions and structural analysis results showing material failure and damage propagation during entry are presented and compared with available flight data.

To provide a common basis for the multidisciplinary analysis, a detailed finite element model of the wing leading edge covering RCC panels 6 through 8 was developed and is shown in Figure 6-72. In addition to the RCC panels, the model encompassed the associated honeycomb wing spar, internal insulation blankets and earmuff, representative attachment fittings and spanner beam, surrounding wing acreage TPS and underlying honeycomb wing structure.

Utilizing a CFD solution derived from the Orbiter common grid system described in Section 5.2.4.2 and trajectory flight condition at 491.4 seconds after entry interface, external aerodynamic heating and pressure distributions were mapped onto the finite element model as analysis boundary conditions. These values were scaled with STS-107 trajectory-based reference stagnation heating and freestream dynamic pressure levels, respectively, to provide time-dependent external environments for analysis. On surfaces inside the RCC cavity, an internal convective heating distribution described in Section 5.3.7.2 – scaled with reference stagnation heating - and internal pressure level predicted by the coupled flow CFD solution described in Section 5.3.6.1.2 - scaled with freestream dynamic pressure - were applied to the model to serve as time-dependent internal environments.

Using the SINDA thermal analyzer code (Ref 6-3), transient temperature distributions were computed throughout the model due to the internal and external aerodynamic heating. Although absent from the finite element model due to their complexity, surrogate surfaces were added in the thermal model to represent T-seals, completing the internal radiation enclosure within the leading edge. Other features of the analysis included:

- Radiation from external surfaces to space at 0°F
- Surface-to-surface radiation within the RCC cavity, earmuff/spanner beam cavity, wing bay cavity, and spar honeycomb structure
- Temperature-dependent material properties

To simulate the melting failure of affected surfaces within the limited schedule available for the analysis, internal convective heating was applied to interior portions of the model as outer surfaces reached their melting temperature limits. This avoided the time-consuming process of node removal and, coupled with the imposition of temperature limits for failed nodes to prevent nonphysical levels during the analysis, served as a reasonable approximation to the actual structural heating during failure. The heat of fusion for the materials was not accounted for in this study. Resulting temperature histories throughout the insulation and spar are shown in Figure 6-73 for both the 6-inch and 10-inch damage cases.

Next, time-dependent temperature distributions were coupled with pressure-based mechanical loads during structural analysis to determine the sequence and timing of structural failure within the model. NASTRAN structural solutions were coupled with a with a progressive failure analysis and life prediction software code, Generalized Optimizer and Analyzer (GENOA, Ref. 6-5) to provide detailed information on temperature and stress distributions within the structure and consequent levels of physical damage such as fracturing, melting and displacement within the structure. Solutions were generated at ten-second time intervals throughout the entry. Upon achieving measurable levels of structural damage, subsequent solutions were processed using equilibrium analysis at each succeeding time step, allowing removal of melted/failed material and redistribution of mechanical loads to surviving structure.

To accommodate the challenging schedule associated with this effort, the present analysis contains a number of limitations and uncertainties. The use of panel 7 as the site of the initial RCC breach was based on the most current working scenario at the time of the analysis. More recent thinking during the investigation has placed the likely hole location at panel 8 with the bulk of internal thermal damage occurring at the junction of panels 8 and 9. This analysis is thought to be relevant even for this scenario by considering the damaged panel in the model as representative of panel 8 and viewing the results occurring between panels 8 and 9. Consistent with such an approach, the OEX flight data for the panel 9 spar rear facesheet thermocouple, V09T9895, has been compared with the thermal response of a comparable panel 8 location in the model as discussed in the Results section below. Other analysis limitations are reflected in the uncertainties surrounding the internal convective heating environment, the approximate nature of the RCC attachment fittings, the absence of inertial loads, and the absence of T-seals in the structural model.

Several events observed during the course of the solutions were considered particularly significant with respect to the overall structural failure of the wing leading edge. In order of occurrence they are listed below:

- Melting of the Inconel 601 foil overwrap on the internal insulation blankets indicated the onset of thermal failure of the insulation, eventually allowing convective heating to approach the spar.
- Initiation of wing spar damage and fracture.
- Melting of the rear facesheet indicated breach of the spar has occurred.
- RCC panel failure.

Analysis results at these conditions are shown in Figure 6-74 through Figure 6-77 for the 10 inch case and Figure 6-78 through Figure 6-81 for the 6 inch case. Predictions for both damage cases show eventual failure of RCC panels through fracturing and breakup.

A comparison of the times at which these critical events occur during the entry is shown in Table 6-7. As expected, failure times are accelerated for the 10 inch case compared with the 6 inch due to the higher levels of internal heating. Thermal response of instrumentation within the left wing of STS-107 have suggested the initial breach through the spar occurred at 491 seconds after entry interface. With a predicted spar breach time of 470 seconds, the 6 inch provides a better comparison to flight data than the 10 inch case. As shown in Figure 6-82, better agreement for the 6 inch damage case can also be seen by comparing the temperature response of V09T9895 (panel 9 spar rear facesheet thermocouple) from the OEX flight data with the model predictions at an analogous location on panel 8 (in this case panel 8 in the model is used as a surrogate for panel 9 as noted previously). The average predicted temperature of two nodes on the rear facesheet are used in the comparison for each damage case. Up to

the flight estimated time of spar breach at approximately 490 seconds the predicted thermal response for the 6 inch case is in reasonable agreement. After this point, the predicted temperature rise rates are much slower than flight data, indicating the effect of convective heating experienced during flight in this area from the hot gas jet expanding into the wing interior. Modeling of such heating was not included in this analysis.

Table 6-7 - Critical Failure Times For 6 Inch and 10 Inch Damage Cases

Critical Event	*10 inch hole*	*6 inch hole*	*Time difference*
Failure of Inconel 601 foil overwrap on thermal insulation.	***210 seconds***	***230 seconds***	***20 seconds***
Heating is applied to the aluminum spar surface. Initial structural failure of spar.	***320 seconds***	***380 seconds***	***60 seconds***
Initial spar breach. Inside now exposed with small gaps, growing into a large spar breach (28 inches x 4 inches; 38 inches is spar height).	***380 – 410 seconds***	***470 – 510 seconds***	***90 – 100 seconds***
Fracturing of RCC Panels Evident	***450 seconds***	***500 seconds***	***50 seconds***

6.8 Chin Panel Temperature Anomaly

Starting at 490 seconds from entry interface, a temperature measurement on the RCC chin panel recorded a sharp rise in temperature followed by a drop. Eventually, the temperature measurement recorded a trend that followed the expected nominal transient. The transient is shown in Figure 6-83. It has been concluded that this transient had to have been caused by a data system anomaly rather than an anomaly with the chin panel hardware of thermal environment.

- The anomalous transient picks up the thermal profile where it left off is unlikely for a real transient. This is very coincidental for a thermal transient since there is no reason for the temperature to return to the previous slope and absolute value (extrapolated).
- The recorded temperature actually cools down repeatedly during the transient. It is very difficult to cool this structure during entry because:
  - The surrounding hardware contributing to the radiation environment is getting hotter and the convection environment during this time period is heating (not cooling)
  - Thermocouple is on a heavy piece of hardware interior to the chin panel
- Anomalous behavior occurs after wing breach at 487 seconds. Postulate that the hot gases and associated heating and/or free electrons cause a data system malfunction.

6.9 Truss Tube Thermal Analysis

A thermal sensitivity study was performed on OV-102's left wing truss tubes. A Thermal Desktop TMM was created to gain an understanding if and when the tubes would fail if exposed to plume heating caused by a breach in the wing leading edge spar. Tubes at various distances from the spar were chosen as shown in Figure 6-84. The size of the breach was varied.

The tubes are aluminum 2024-T6. For analysis sake they are designated tubes 1 through 4. Table 6-8 shows their differences in outer diameter, wall thickness, length, and distance from spar panel 8.

Table 6-8 – Tube Summary

Tube	Outer Diameter (in)	Wall Thickness (in)	Length (in)	Distance (in)
1	3.75	0.048	48.41	15.94
2	3.75	0.031	39.04	96.44
3	2.00	0.018	38.37	37.80
4	2.25	0.020	38.02	94.49

Their diameters and wall thicknesses were assumed to be constant throughout their respective lengths. Their distances were measured in plane from their midpoints to the spar.

A radiative boundary condition of 20°F was assumed. The tubes were coated with Koropon (emittance = 0.86) throughout the duration of the analysis.

A spar breach is assumed at EI+488 seconds. It was assumed to be in spar panel 8 and to be constant in size. Oxidation and combustion effects were ignored. The plume was assumed to impact the middle portion of the tubes directly. Plume heating methodologies similar to section 6.5 were incorporated in this analysis. Correction for panel 8's local pressure coefficient, off-normal angle impingement, and radial distribution from the stagnation point were applied. The plume heating used is shown in Figure 6-85 and the heating correction for angular impingement is shown in Figure 6-86. Plume impingement on the tubes was also adjusted for radius and circumferential effects.

Failure was determined when the entire cross section of the tube at the point of plume impingement reached a temperature of 935°F. The failure times of the 4 tubes are shown in Figure 6-87 for varying breach hole sizes.

6.10 RCC Knife Edge Tests

STS-107 recovered debris for reinforced carbon-carbon (RCC) panels 8 and 9 showed "knife-edge" erosion. A test program was initiated in order to confirm uncoated RCC sharpening and determine if coated RCC will sharpen as seen in Columbia debris of RCC Panels 8/9 rib sections.

Two test fixtures were designed and developed for this test and are shown in Figure 6-88. The single plate fixture was used to simulate flow impinging onto a breach edge with an angle of 20°. The dual plate fixture was used to simulate flow impinging onto a near-normal (70°) surface representative of the RCC panel ribs.

RCC test specimens were prepared from an existing RCC panel rib section and RCC plate. The RCC test plates for the single plate fixture were 2.5"x3" in dimension and .25-inch thick. Closeout RCC pieces were used to prevent flow from entering into the copper holder and were of the same thickness of the single plate test specimen. Two uncoated specimens and one coated specimen were tested.

The RCC test plates for the dual RCC plate test fixture were 3"x3" in dimension and .375-inch thick. Smaller plates were used to model an offset RCC rib and were 1.6"x3" with an equivalent thickness. A coated and uncoated offset RCC plate was tested.

This test program was performed in test position #2 of the JSC Atmospheric Reentry and Structures Evaluation Facility (ARMSEF). Inside this facility, test gases (77% nitrogen and 23% oxygen) are head by a segmented constricted arc heater and injected into a vacuum chamber through a water-cooled 5-inch diameter nozzle that has a 15-degree half angle. While tests are in progress the facility vacuum chamber is maintained below 200 microns of mercury. Test models are mounted on a two water-cooled, remotely actuated sting arms that allow them to be inserted after test conditions are stabilized. The stagnation pressures experienced by test specimens were determined with a 0.5-inch diameter water-cooled pitot probe prior to specimen insertion.

Laser pyrometers monitored the center of the test specimens away from the edge to evaluate the gross temperature response of the RCC using an emissivity of 0.9. In addition, a stroboscopic camera was used to monitor the RCC test specimen edge for knife-edging. This camera provided real-time video data, which eliminated the effects of temperature on the image.

The test conditions were defined by enthalpy and pressure. The test points were derived from the predicted STS-107 RCC hole edge impact pressure and total enthalpy provided by JSC/EG. Three test conditions were established based on the profile shown in Figure 6-89.

A dual calibration model with a 1" flat face heat rate sensor and a pitot probe measurement was used to determine the heat rate and pressure. The actual test points that were calibrated for in the arc jet simulation are shown in Table 6-9.

Table 6-9 – Target Test Conditions

	Test Conditions	
	Pressure (psf)	Bulk Enthalpy (BTU/lb)
Condition #1	75	11200
Condition #2	129	10800
Condition #3	147	7400

The three test conditions were used to simulate a flight profile. For the first two tests, only condition #1 was used. Based on the results from these tests, conditions #2 and #3 were added and the flight profile developed. Figure 6-90 illustrates the simulated flight profile used during testing. It should be noted that the enthalpy specified is the centerline enthalpy and should be multiplied by a factor of two to correspond to the targeted total enthalpy.

In evaluating the results of the testing, the boundary conditions should be taken into account. The RCC test specimens were mounted in water-cooled copper holders, thus, slightly affecting the three mounted edges of RCC through conduction. There was an effort to minimize radiative losses from the back of the specimens using insulation and graphfoil (used to prevent any chemical reactions). However, both test fixtures could not prevent the large view factors from the front of the main RCC pieces to the chamber walls. The test run configurations are shown in Table 6-10.

Table 6-10 – Test Run Configuration

Run #	Angle	# of Plates	Offset	Coating
1	70	2	no	coated/coated
2	70	2	yes	coated/uncoated
3	20	1	n/a	uncoated
4	70	2	yes	coated/uncoated
5	20	1	n/a	coated

Test #1 produced no knife-edging since the conditions could not generate temperatures on the RCC specimen greater than 3250°F. Pre- and post-test photos are shown in Figure 6-91.

Test #2 used the same test conditions as Test #1, but the front specimen was exchanged with an offset RCC plate representing an offset RCC rib. Condition #1 could not produce temperatures greater than 3250°F on the SiC coating, but did oxidize the exposed carbon, leaving a white residue from the impregnated TEOS, as seen in Figure 6-92.

Test #3a utilized the simulated flight profile with conditions #1 though #3. Condition #1 did not create knife-edging, only localized oxidation on the exposed carbon. Condition #2 began after 200 seconds in

the stream, and created temperatures on the edge above 3250°F and initiated knife-edge like erosion. After 69 seconds at Condition #2, the environment was changed to condition #3. Condition #3 was a significant reduction in heating compared to condition #2, and the knife-edge features began to blunt. The decision was made to preserve the knife-edge features created in Condition #2 by removing the sting arm out of the flow. The pre- and post-test photos are shown in Figure 6-93.

Test #3b used another uncoated piece of RCC with the same simulated flight profile. The test, although, not required to run, reproduced the results in Test #3a with the same knife-edging.

Test #4 involved the same specimens tested in Test Run#2 in the dual plate fixture since there was minimal oxidation on the exposed edge and a limited amount of test specimens. The simulated flight profile was used, but the copper test fixture could not withstand the high heating rates at condition #2. Prior to the sting arm being removed from the flow, the SiC coating began eroding at the center of the front offset RCC piece. This suggests that the hottest portion of the RCC at this condition was not at the edge and that erosion would have propagated from the center outward. It must be noted that the front of the copper holder could have influenced the flow field and altered the heating distribution along the plate. Pre- and post-test photos are shown in Figure 6-94.

Test #5 used the single plate fixture with a coated RCC specimen. Knife-edging was produced on the main RCC specimen as shown in Figure 8. Test conditions did produce temperatures above 3250°F. The test condition profile was stopped at condition #2 in order to preserve the knife-edging features for posttest evaluation. A diagram showing the approximate dimensions of the knife-edging is shown in Figure 6-95.

In addition to the main RCC knife-edging on Test #5, the closeout RCC pieces also produced knife-edging as seen in Figure 6-96. The closeout pieces prevent flow from entering the copper test fixture. The erosion occurred from a secondary shock impinging on the closeout pieces. The knife-edging was sharper than what occurred on the main RCC piece.

The test facility was able to simulate predicted environments on RCC ribs and breach edge on six RCC test specimens. Knife-edging was apparent on specimens where the temperature on the SiC coating was above 3250°F. Knife-edging was also apparent on the closeout piece in test #5. This data along with the results from previous RCC testing suggests that under stagnation flow with temperatures above 3250°F, the RCC will erode in a knife-edge manner. If hot gases flowed into the wing leading edge through a breach with sufficient enthalpy and impact pressure, the RCC would have eroded in a similar manner as seen in the debris.

6.11 Leading Edge Reinforced Carbon-Carbon (RCC) Hole Growth Thermal Analysis

A prediction of RCC hole growth was performed using JSC arc jet test data obtained from hypervelocity impacted RCC test specimens when subject to a high temperature entry environment. The objective of the arc jet testing was to establish the oxidation characteristics of RCC with thru holes obtained from hypervelocity impacts. The specimens were exposed to constant heating conditions at temperatures of 2500 and 2800F and pressures of 50 to 180 psf. Correlations were developed from the data for use in trajectory simulations to predict hole growth and hot gas flow through an enlarging hole into the wing leading edge cavity.

A 0.75 inch diameter hole in the RCC was assumed for analysis purposes. Figure 6-97 shows the heat flux and pressure environment at the hole while Figure 6-98 shows the resulting RCC surface temperature as a function of time. The predicted RCC temperature of approximately 4800°F is assumed to be consistent with a diffusion-limited erosion regime for bare or uncoated RCC. With this assumption, the erosion or hole growth rate measured for the 2800°F arc jet tests can be used for erosion rate estimates here. The erosion rate in this flight environment and regime is .0032 in/sec. Figure 6-99 reveals the results of the analysis and shows the predicted growth to a final OML diameter of 4.0 inches. The predicted IML (back-face) diameter is slightly smaller at 3.0 inches. Extrapolation of this analysis to higher RCC temperatures (sublimation regime) or larger initial hole diameter is not recommended since the data base is very limited.

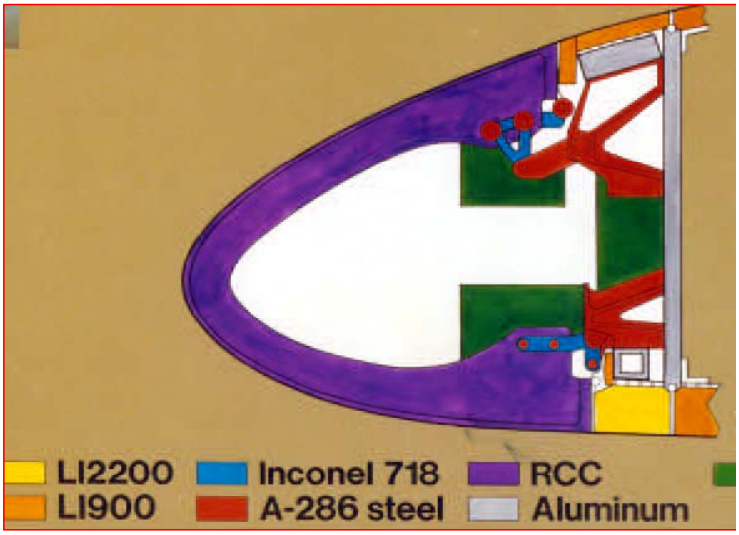

Figure 6-1 - Wing Leading Edge Cross-section

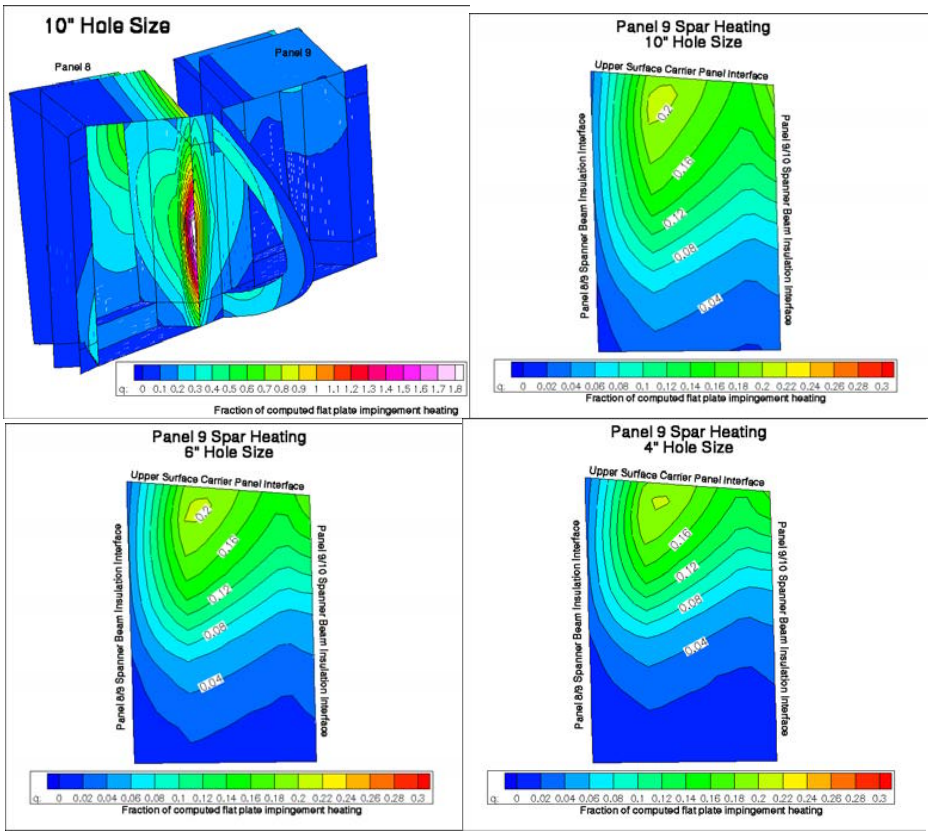

Figure 6-2 - Heating Distribution

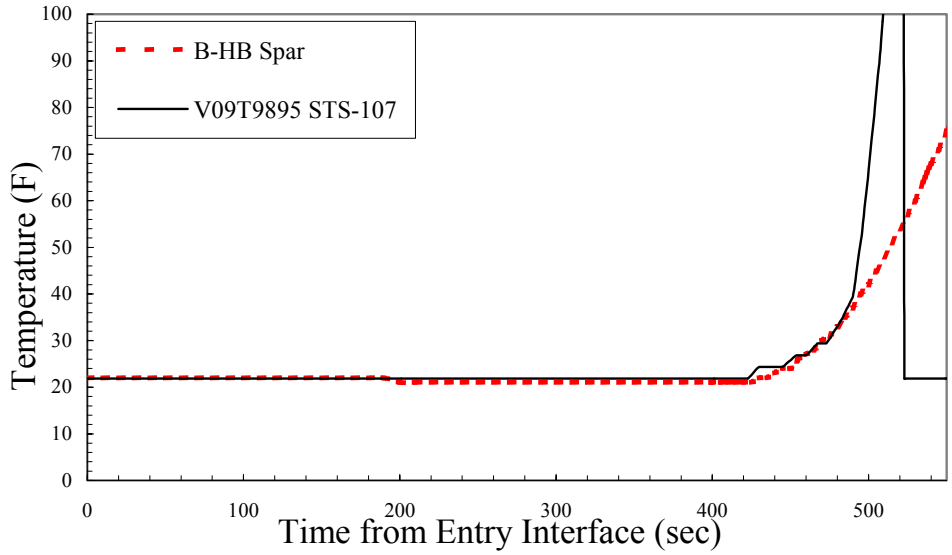

Figure 6-3 - Spar Temperature Prediction vs. Flight Data

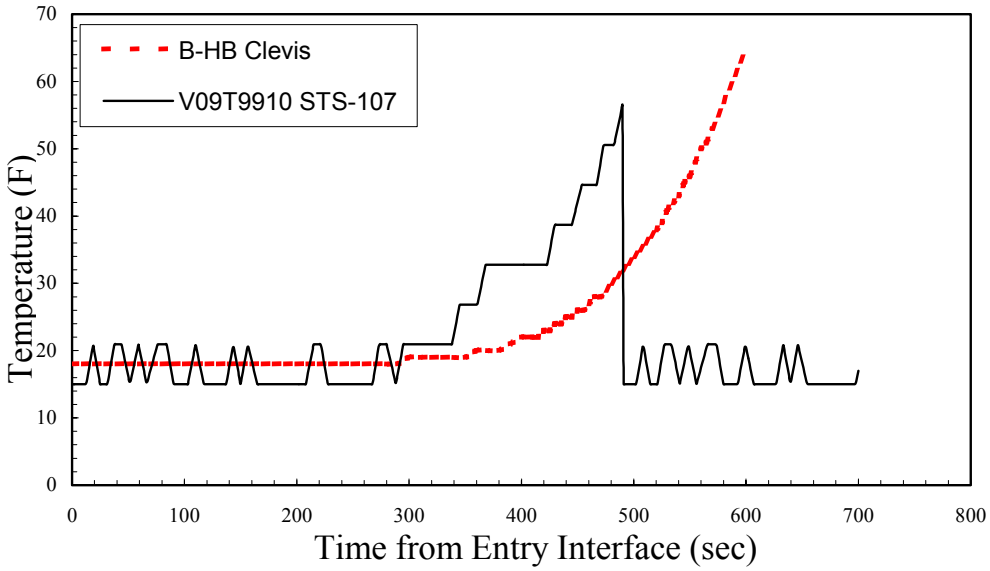

Figure 6-4 - Clevis Temperature Prediction vs. Flight Data

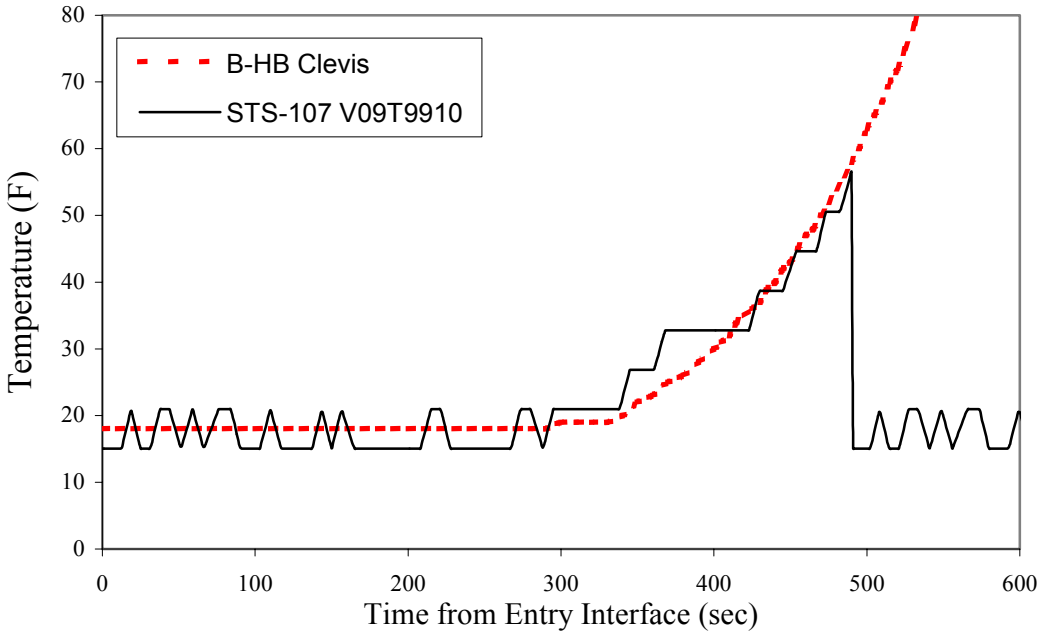

Figure 6-5 - Clevis Temperature Prediction vs. Flight Data

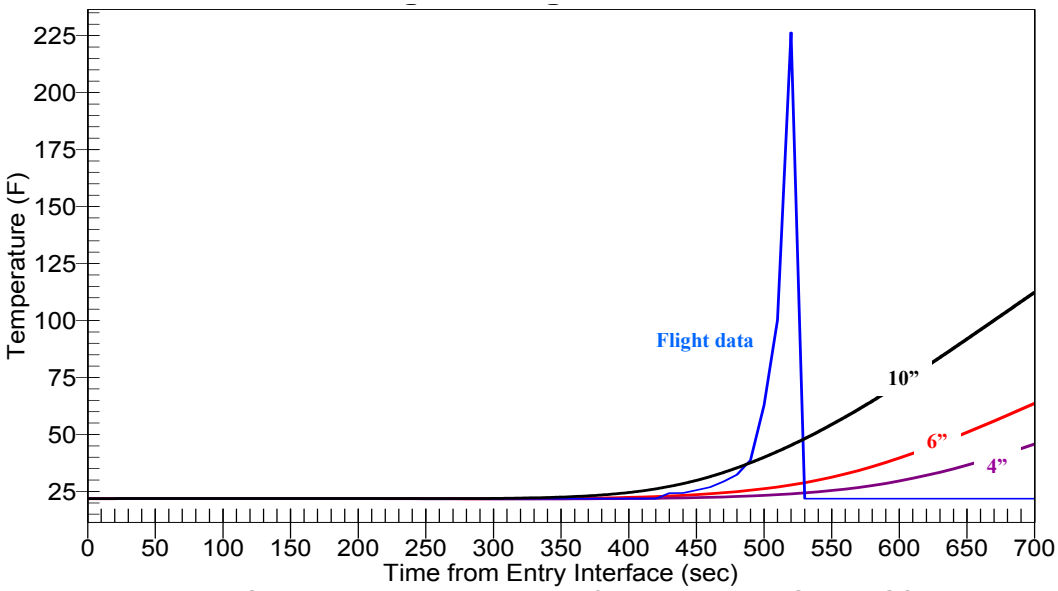

Figure 6-6 - Spar Temperature Prediction for Varying Hole Size – JSC TMM

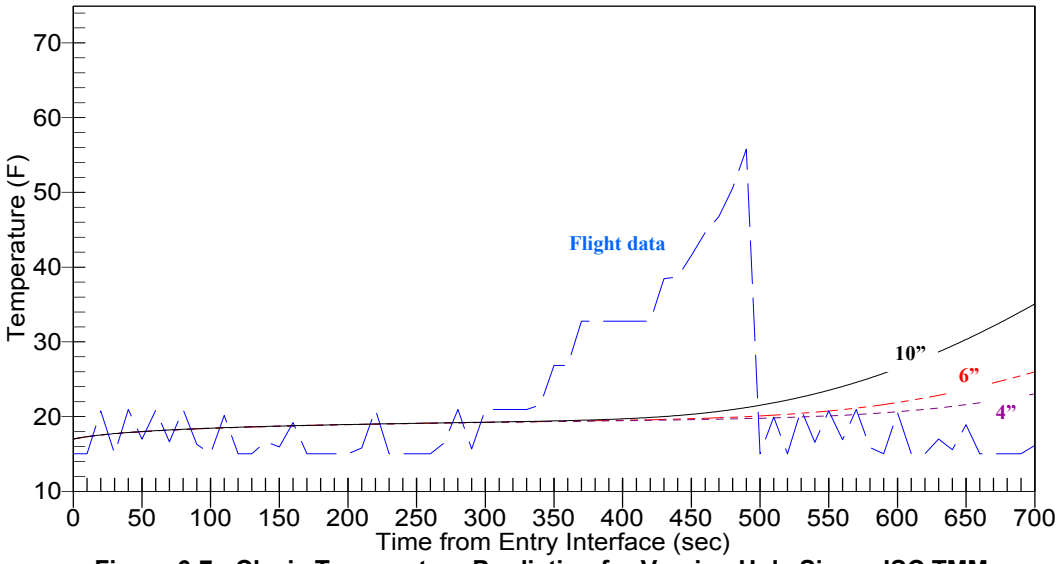

Figure 6-7 - Clevis Temperature Prediction for Varying Hole Size – JSC TMM

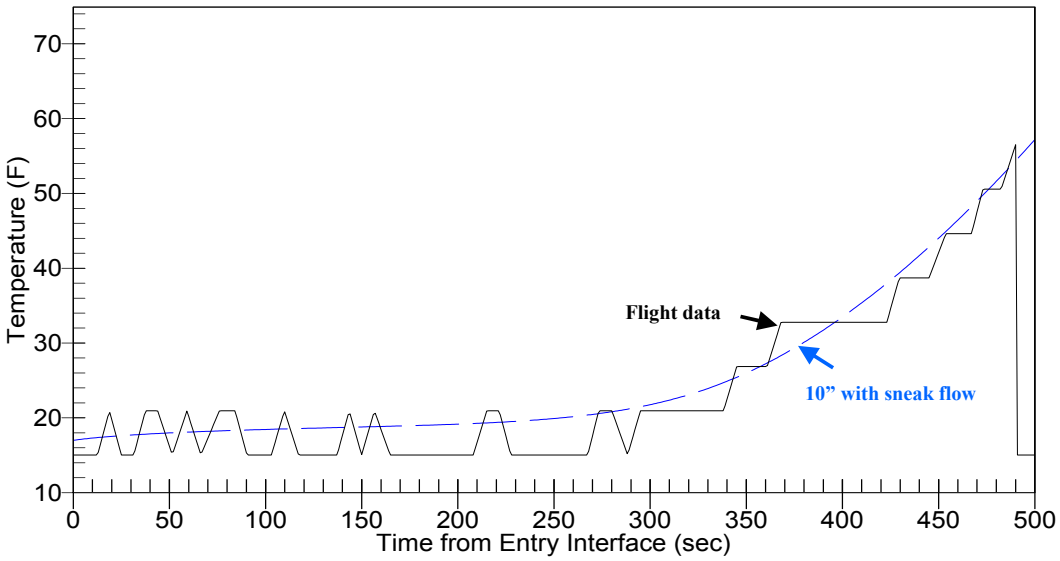

Figure 6-8 - Clevis Temperature Prediction (with 10% Sneak Flow) – JSC TMM

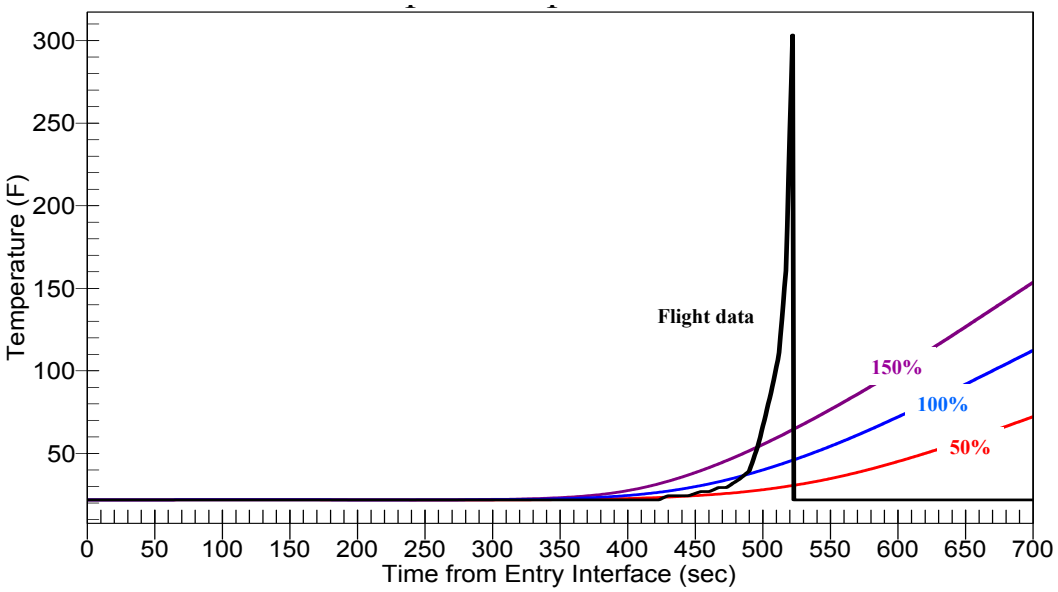

Figure 6-9 - Spar Temperature Predictions with Heating Uncertainties

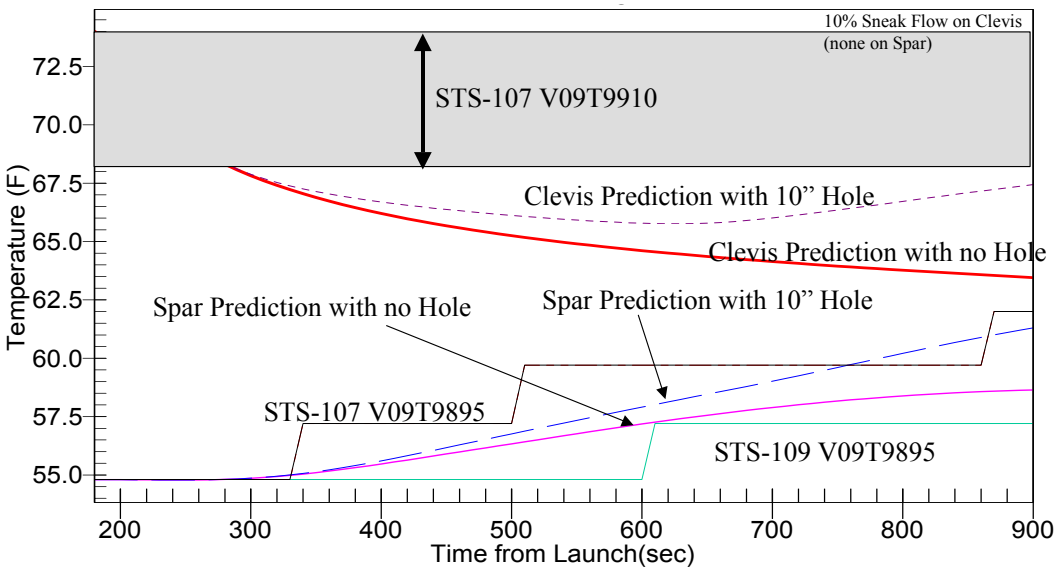

Figure 6-10 - Spar and Clevis Ascent Predictions Compared to Flight Data – JSC TMM

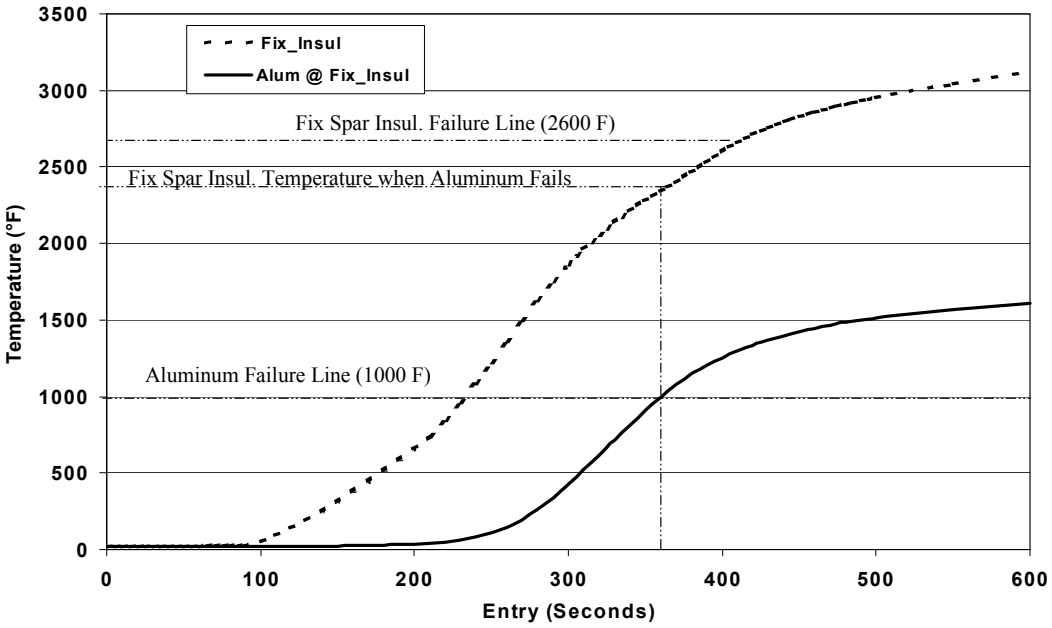

Figure 6-11 - Damaged Tee-Seal - Spar Insulation Transients

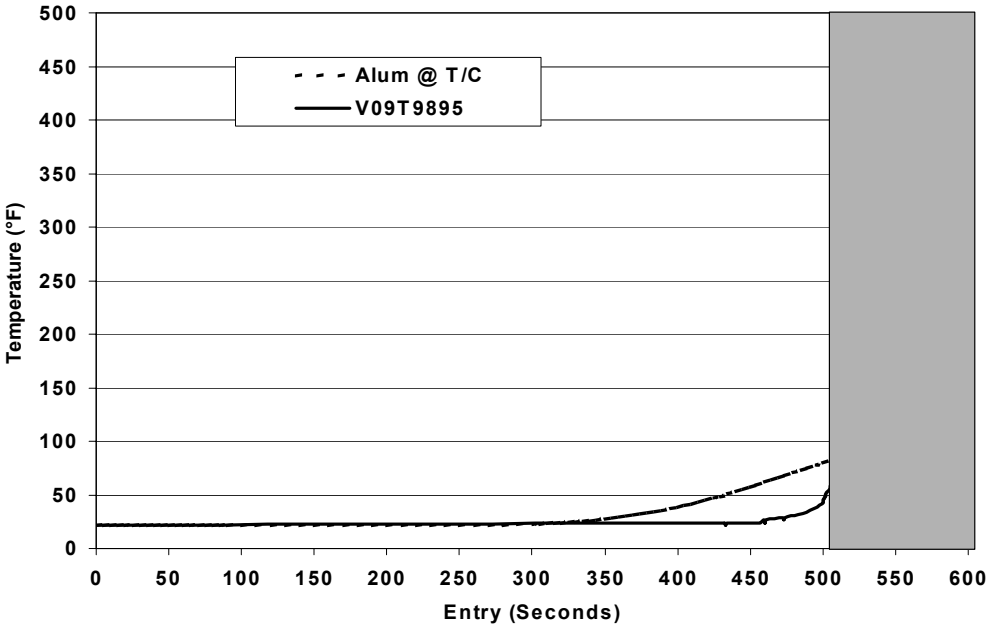

Figure 6-12 - Damaged Tee-seal - Spar Temperature Transients

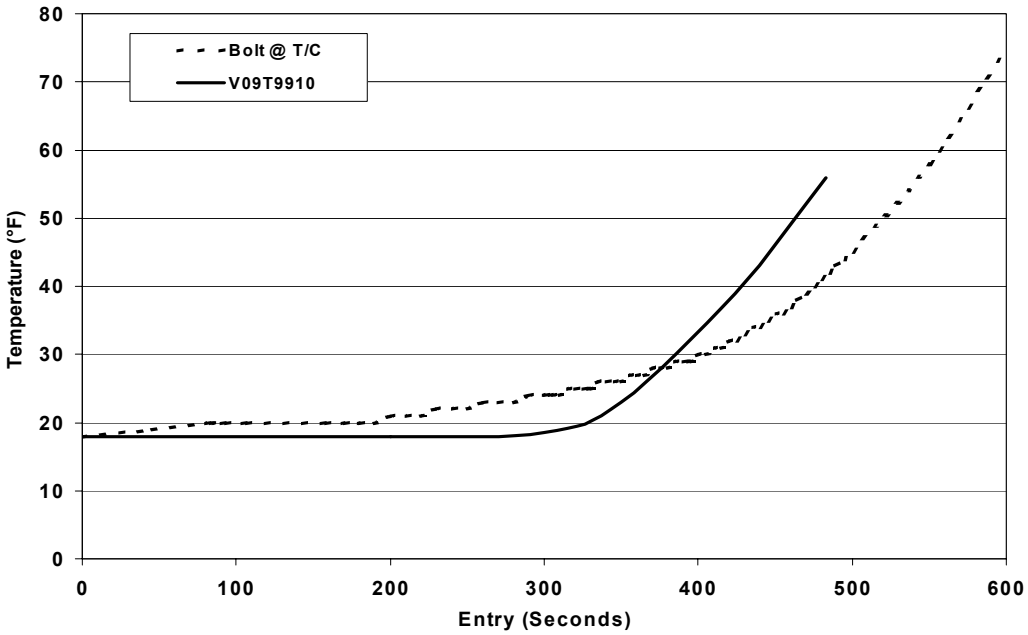

Figure 6-13 - Damaged Tee-seal - Clevis Transients

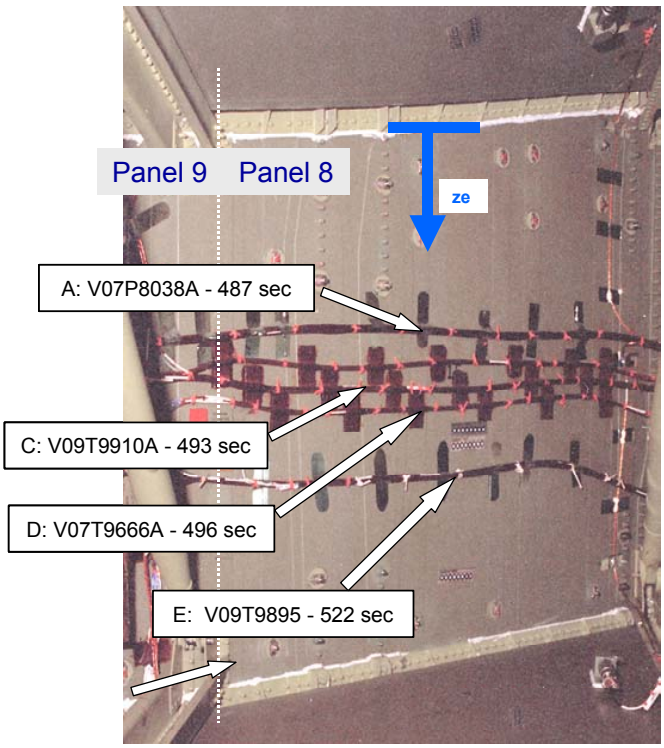

Flight data

	Time from e.i. (sec)	ze (in)
A	487.0	16.5
C	493.0	19.8
D	496.0	21.3
E	522.0	25.8
B		18.3

Figure 6-14 – Leading Edge Spar (view from within wing looking fwd)

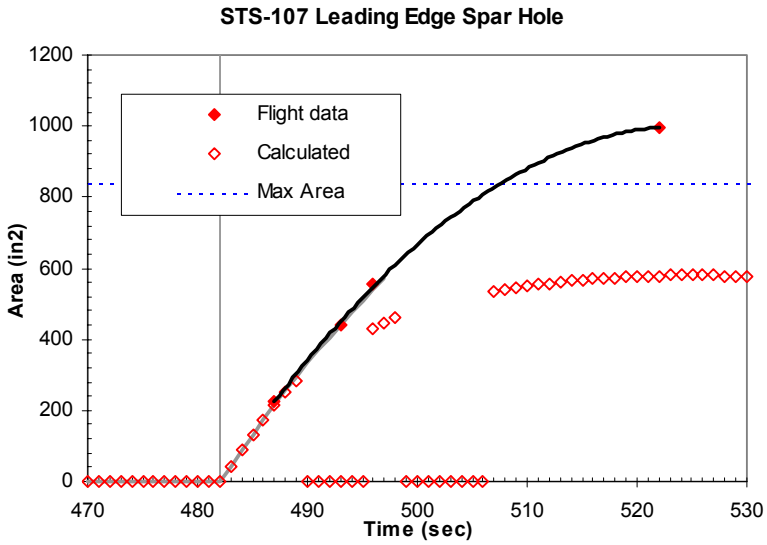

Figure 6-15 – Spar Hole Growth Analysis

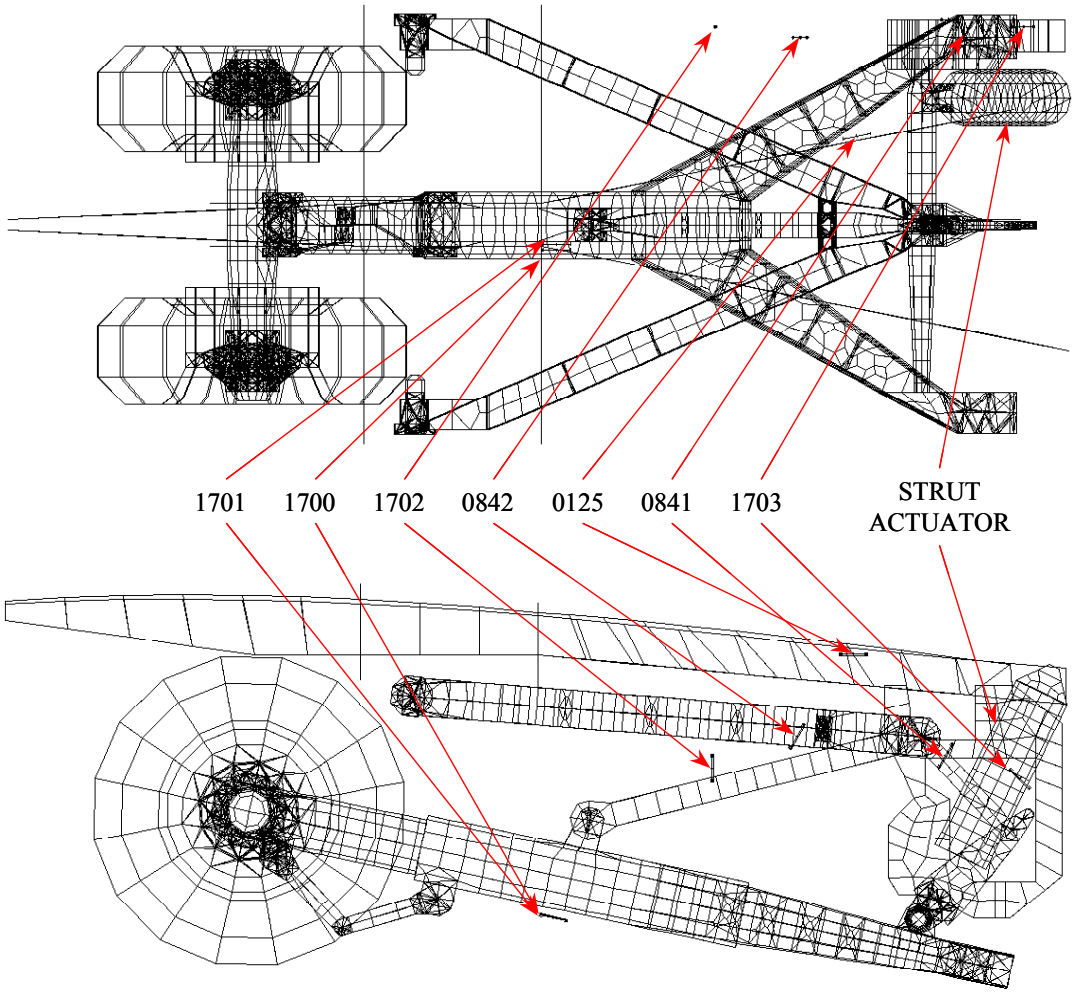

Figure 6-16 – Left Main Landing Gear Sensor Locations

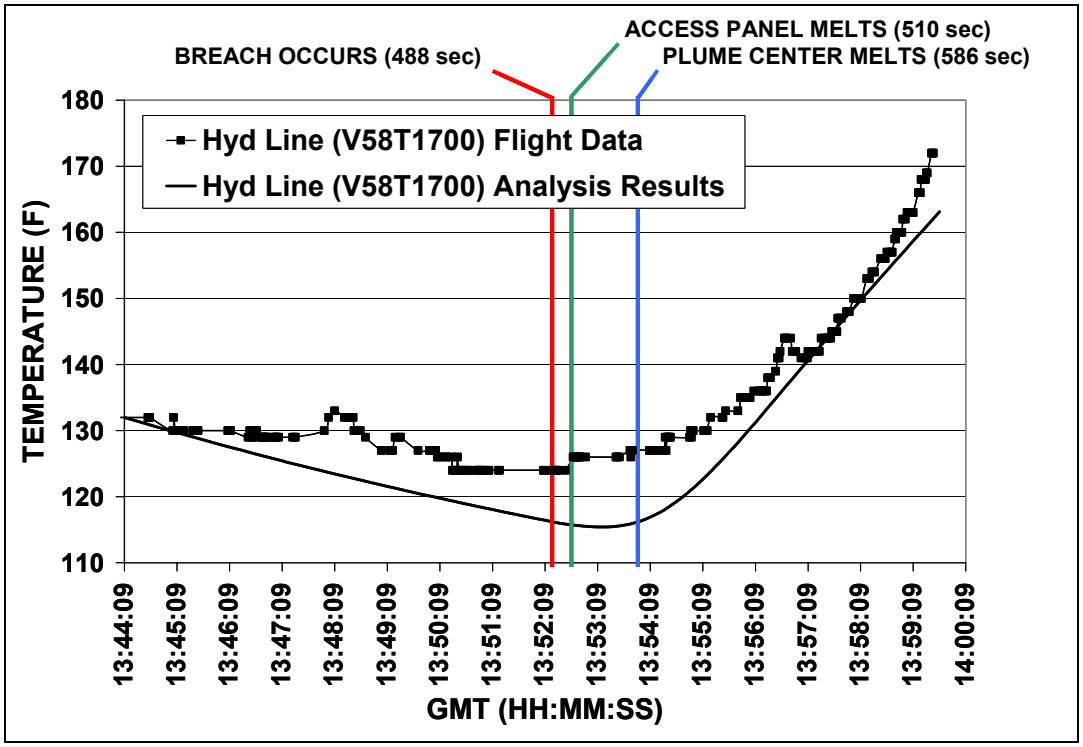

Figure 6-17 - V58T1700A analysis results

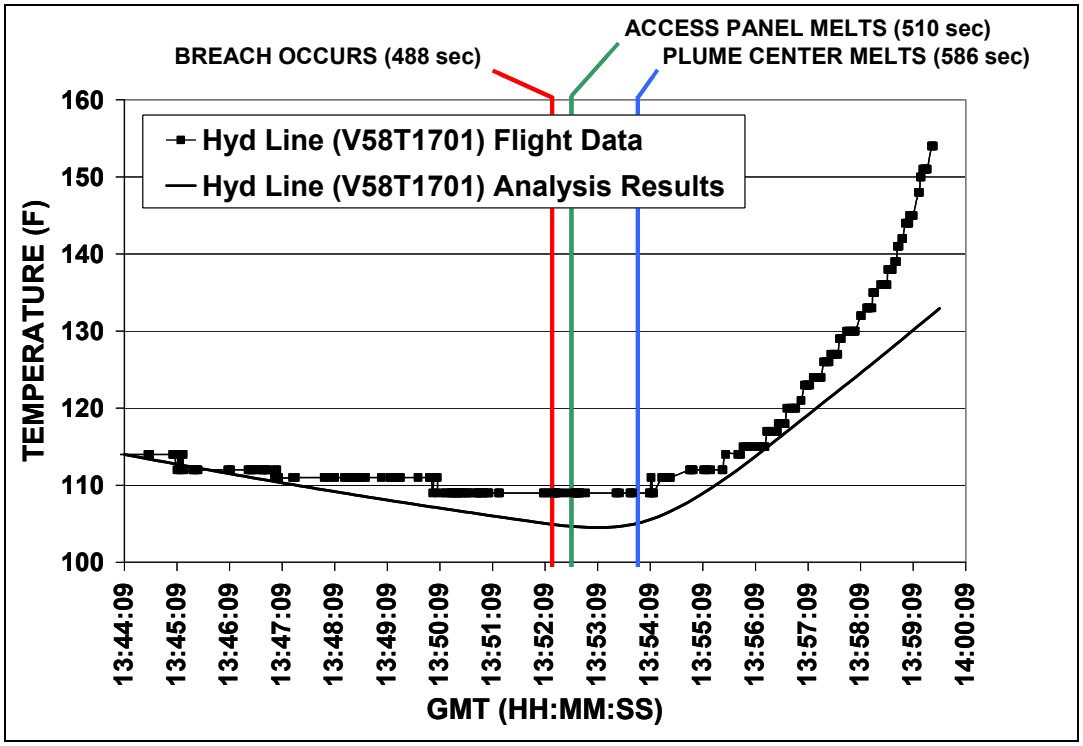

Figure 6-18 - V58T1701A analysis results

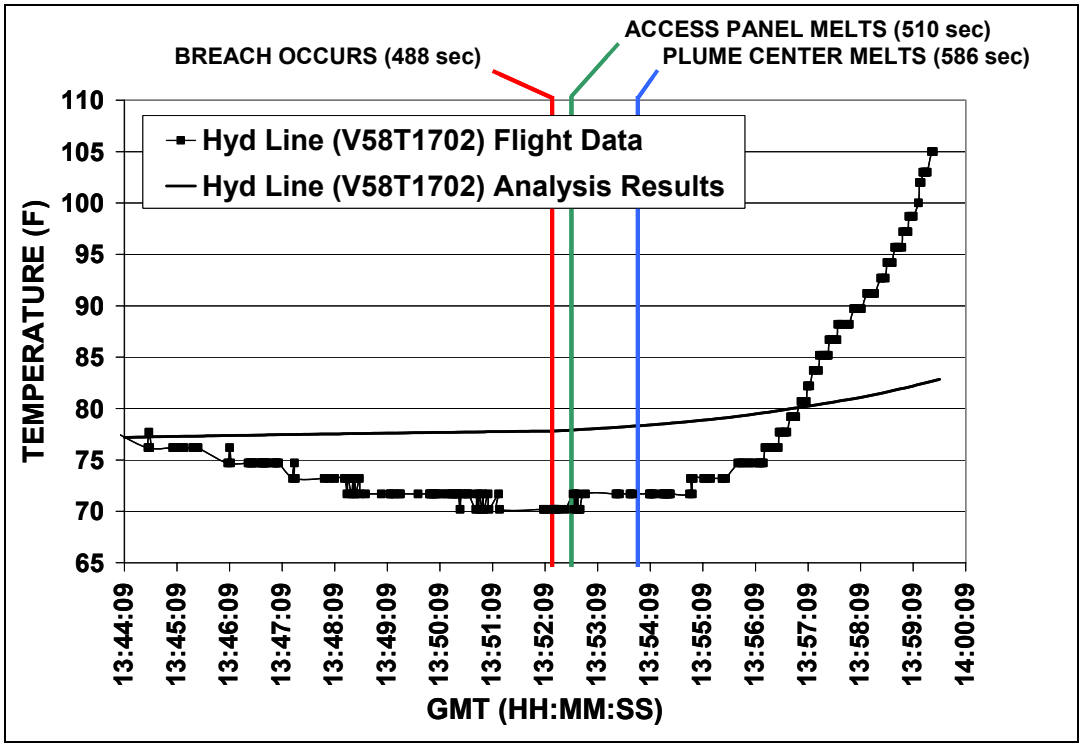

Figure 6-19 - V58T1702A analysis results

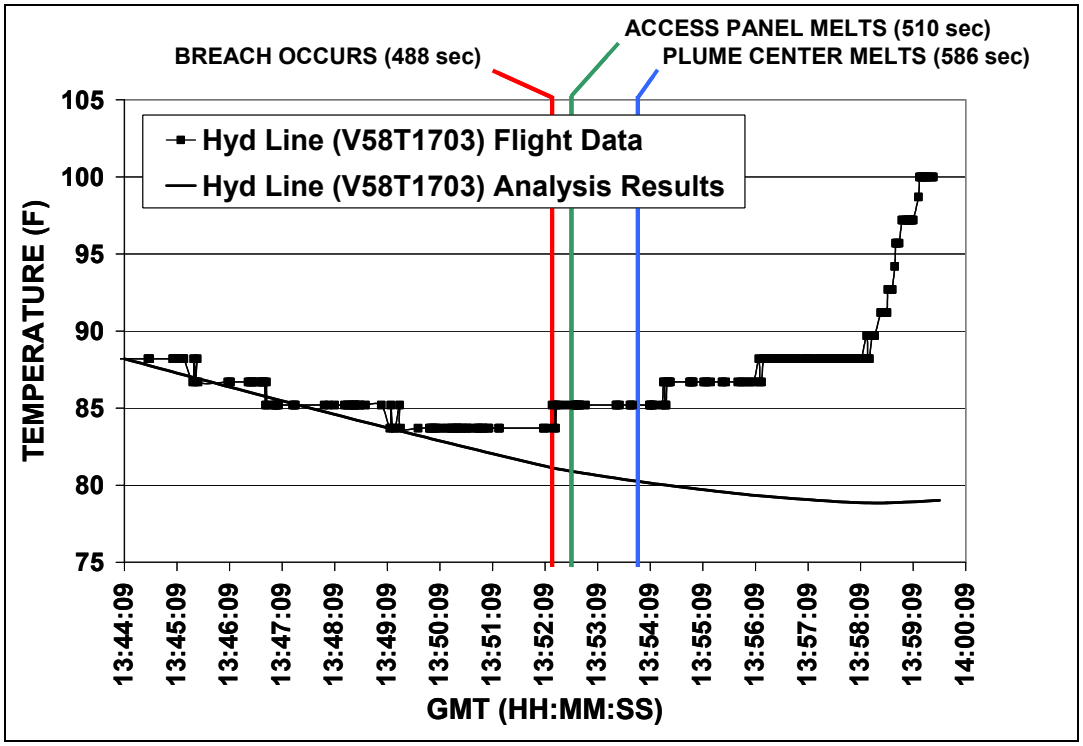

Figure 6-20 - V58T1703A analysis results

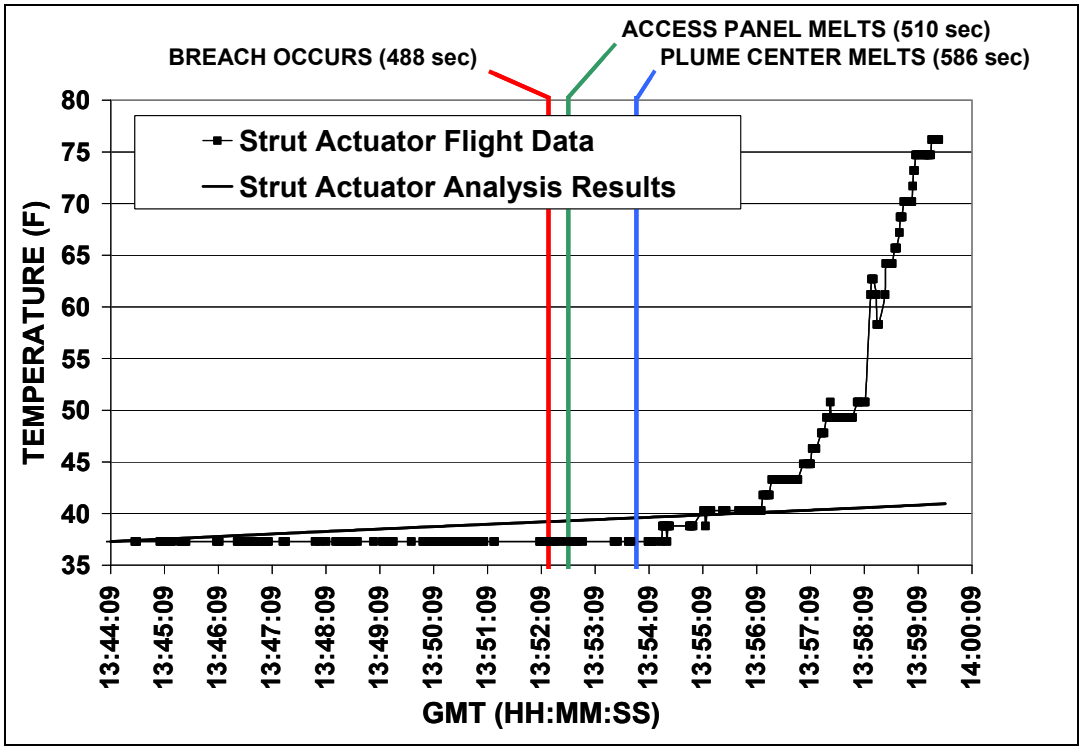

Figure 6-21 - V58T0405A (strut actuator) analysis results

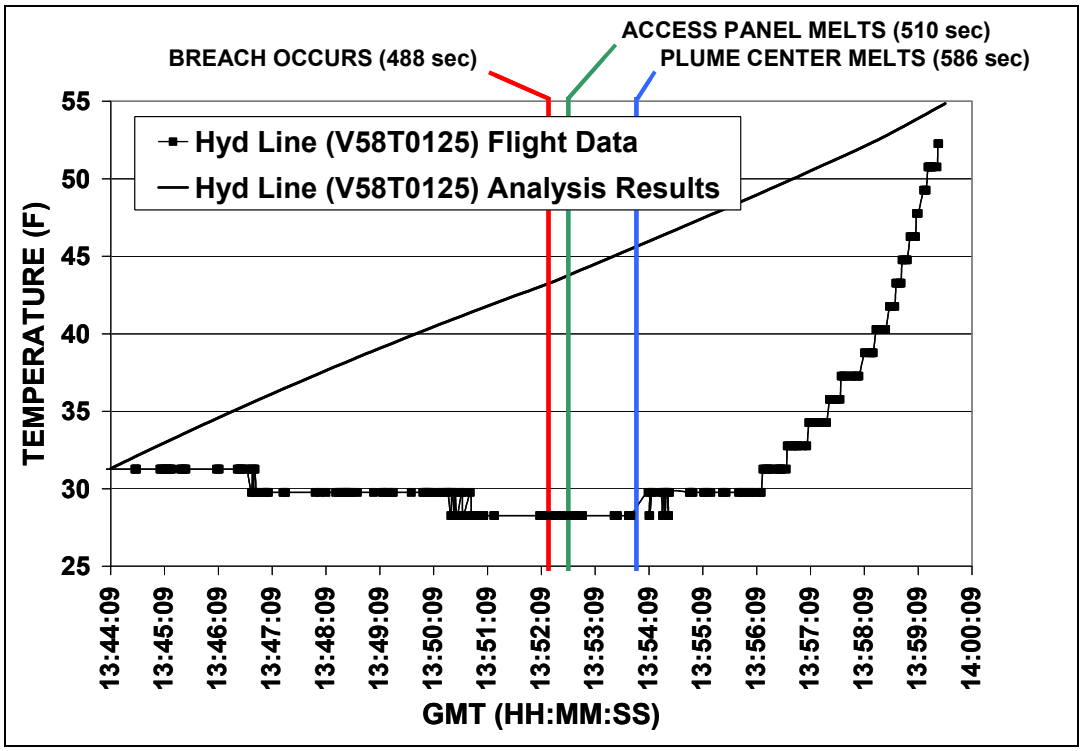

Figure 6-22 -V58T0125A analysis results

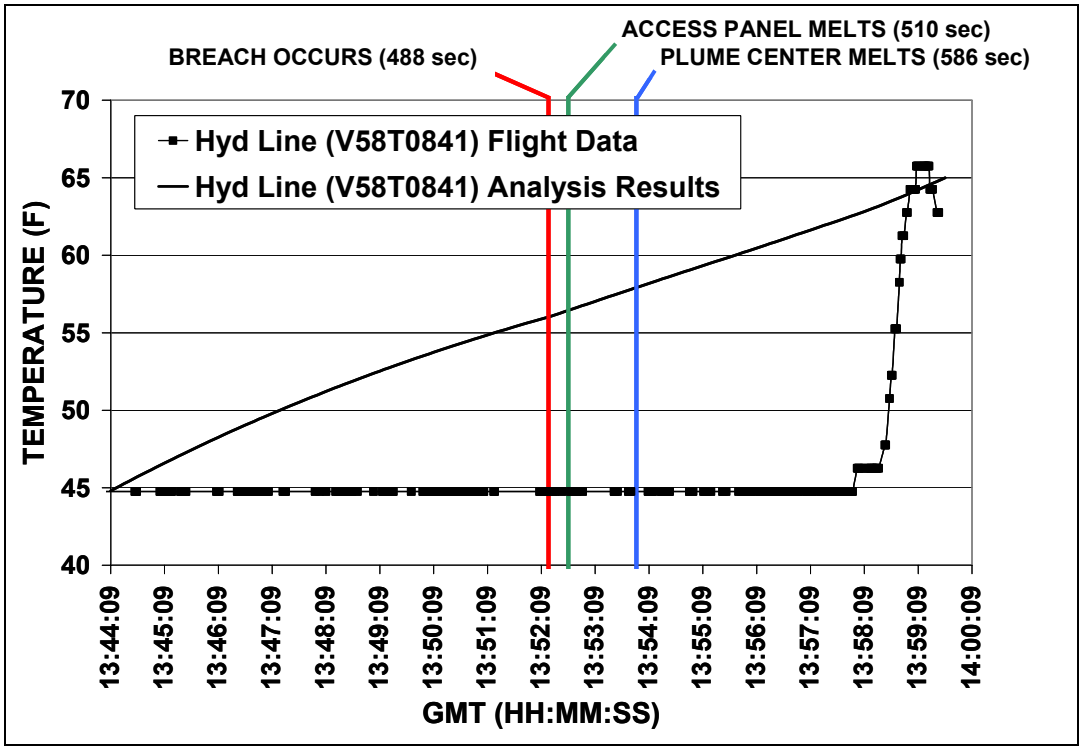

Figure 6-23 - V58T0841A analysis results

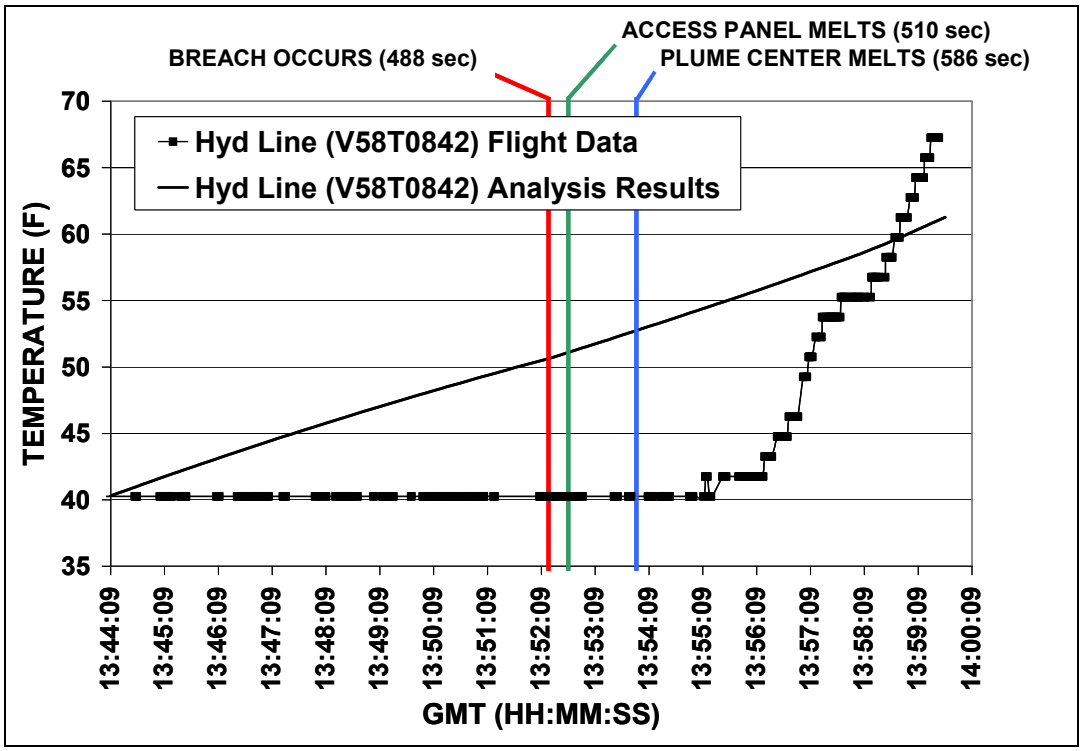

Figure 6-24 -V58T0842A analysis results

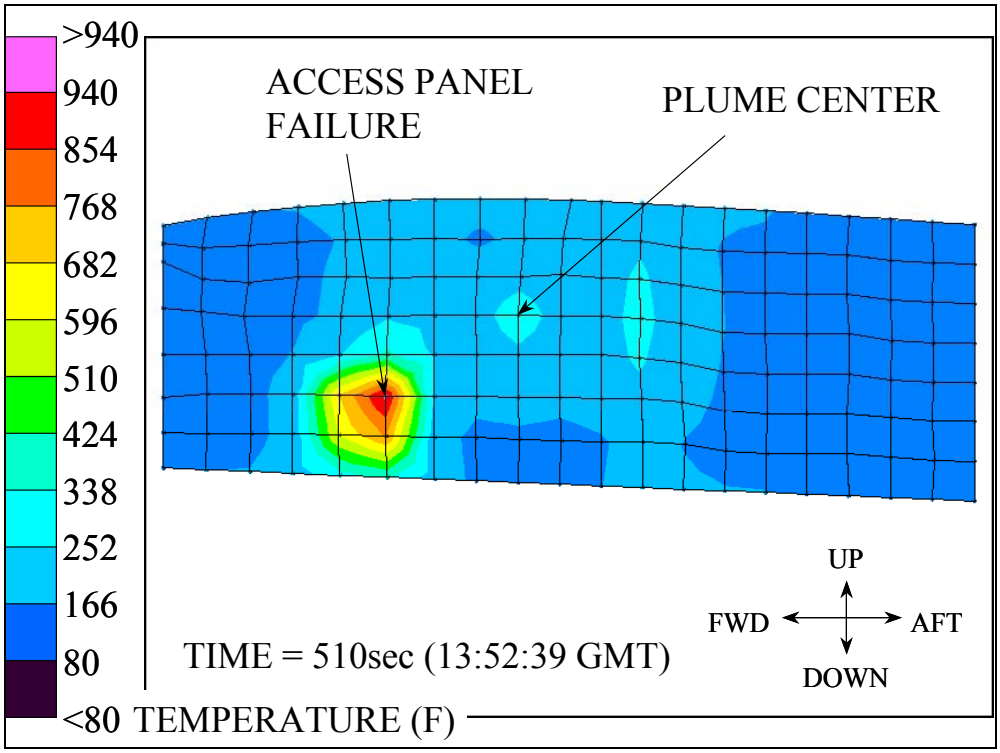

Figure 6-25 - Outboard wheel well wall temperature at 13:52:39 GMT

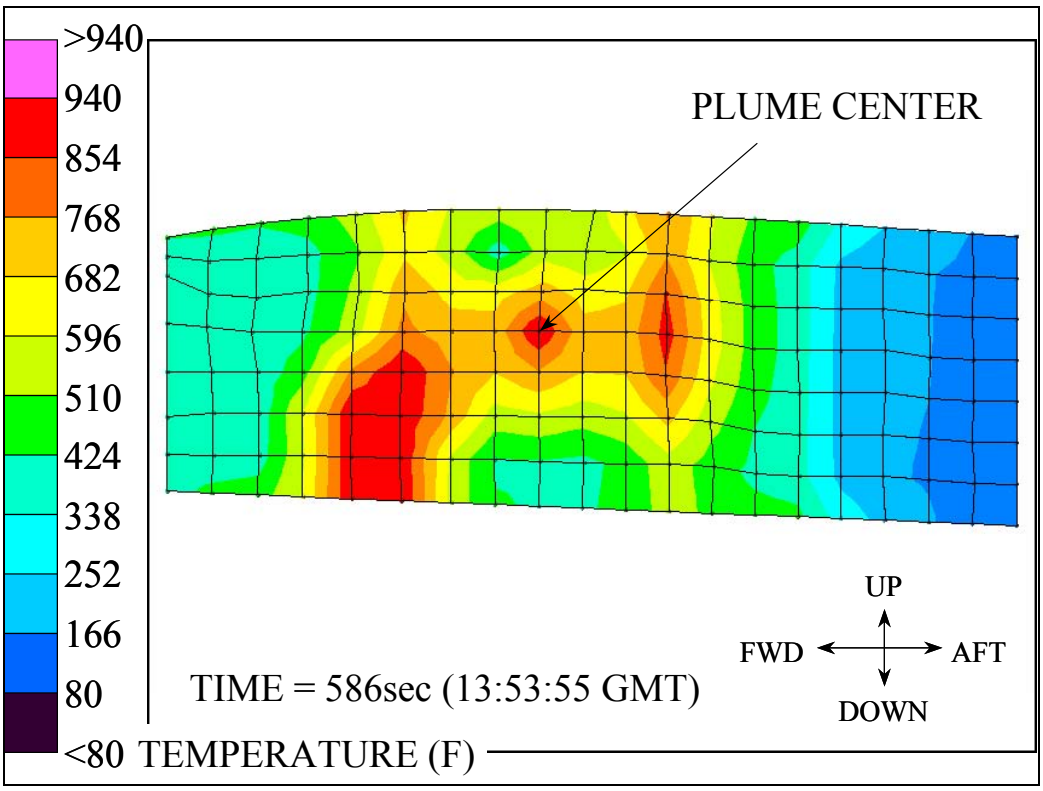

Figure 6-26 -Outboard wheel well wall temperature at 13:53:55 GMT

Figure 6-27 – Cable Bundle Test Article

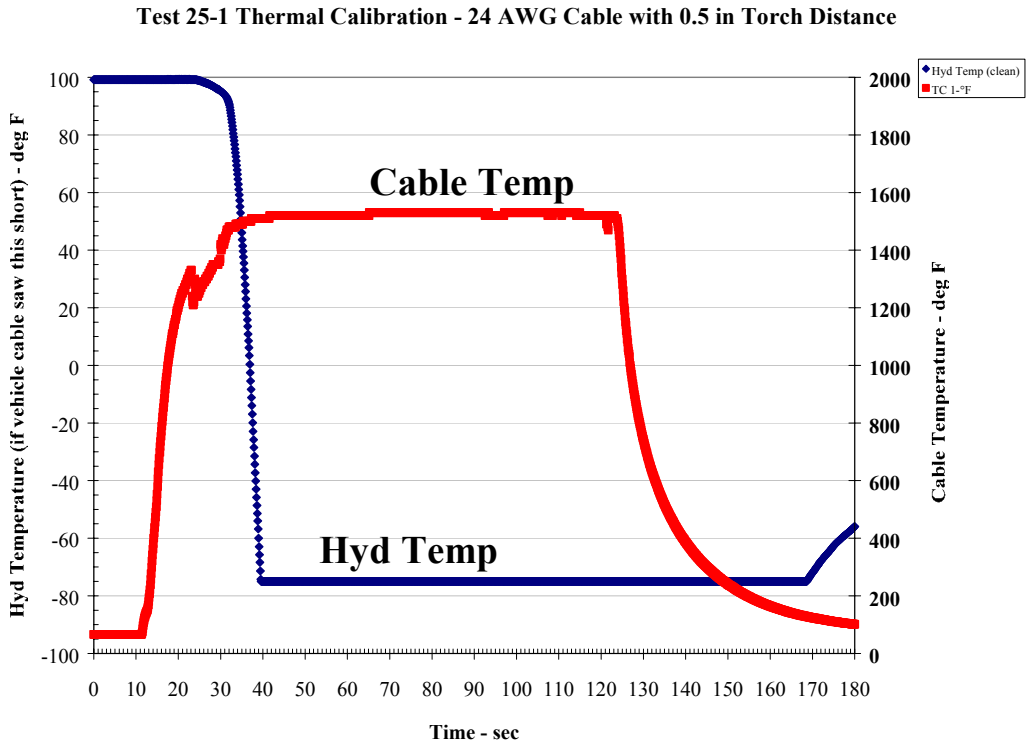

Figure 6-28 – Cable Failure Signature

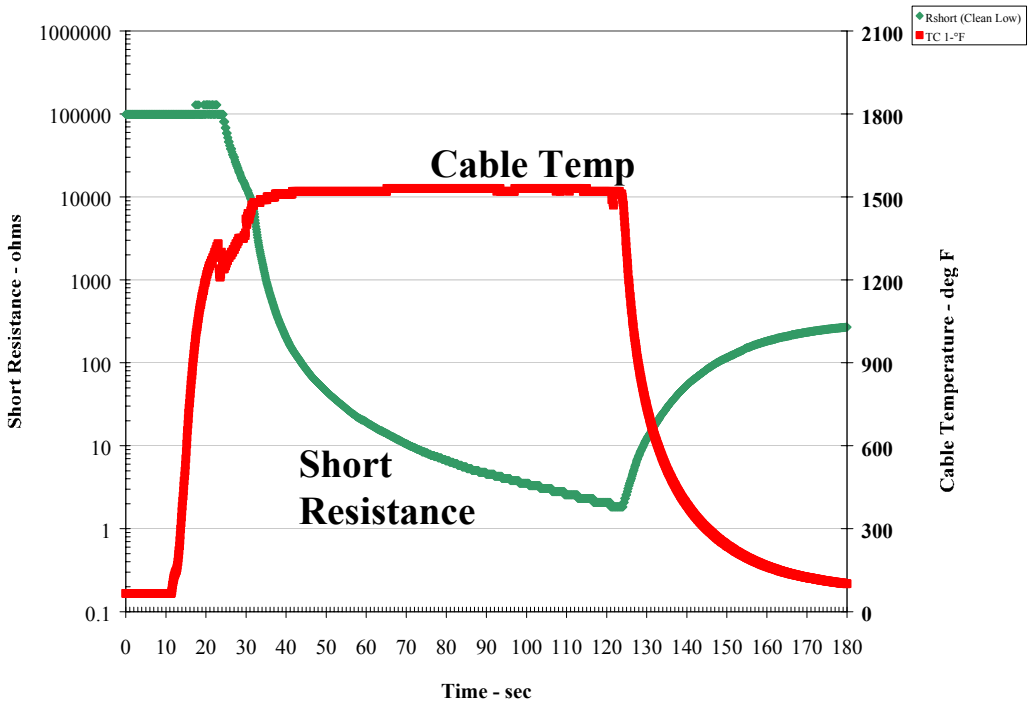

Figure 6-29 – Cable Failure Signature

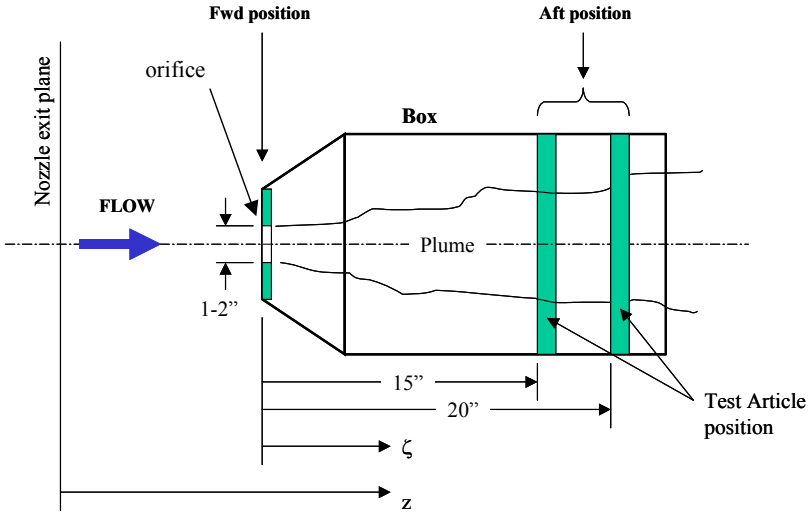

Figure 6-30 – Box Test Support Equipment

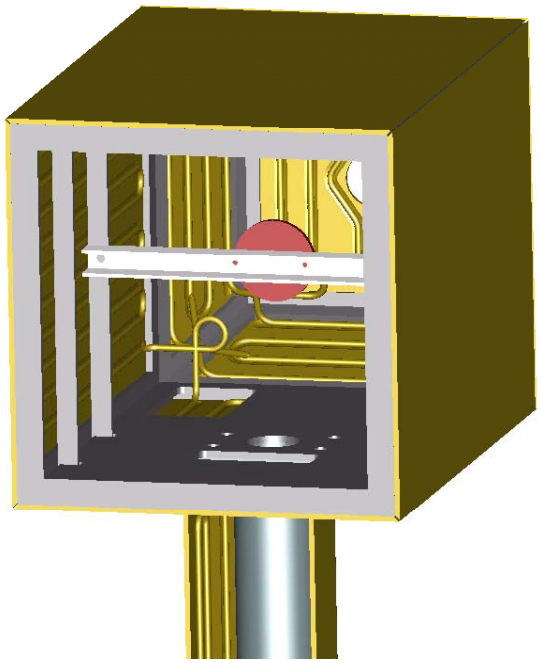

Figure 6-31 – Box Test Support Equipment

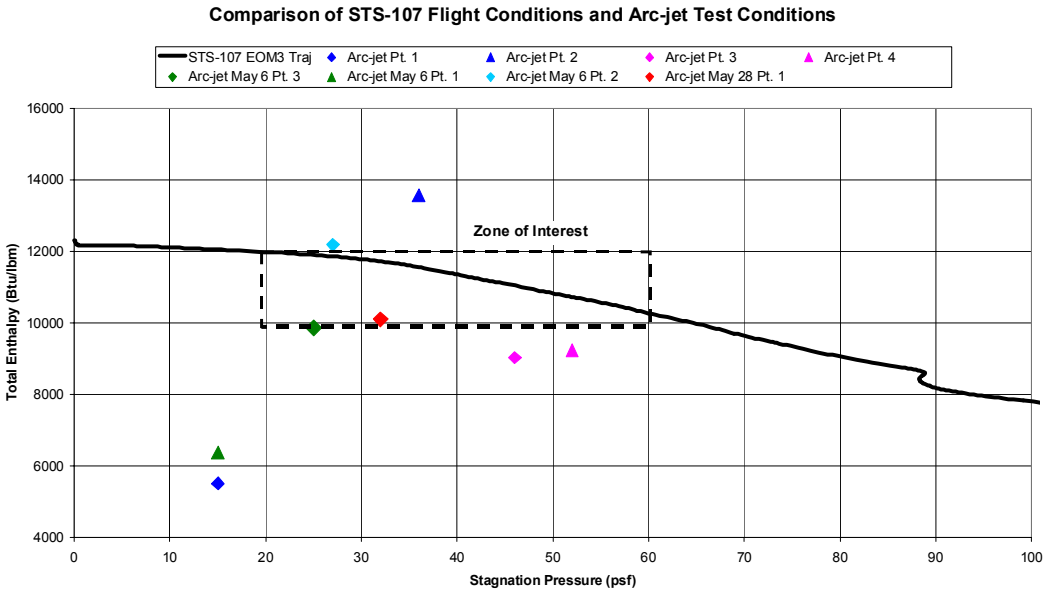

Figure 6-32 – Arc-Jet Test Conditions

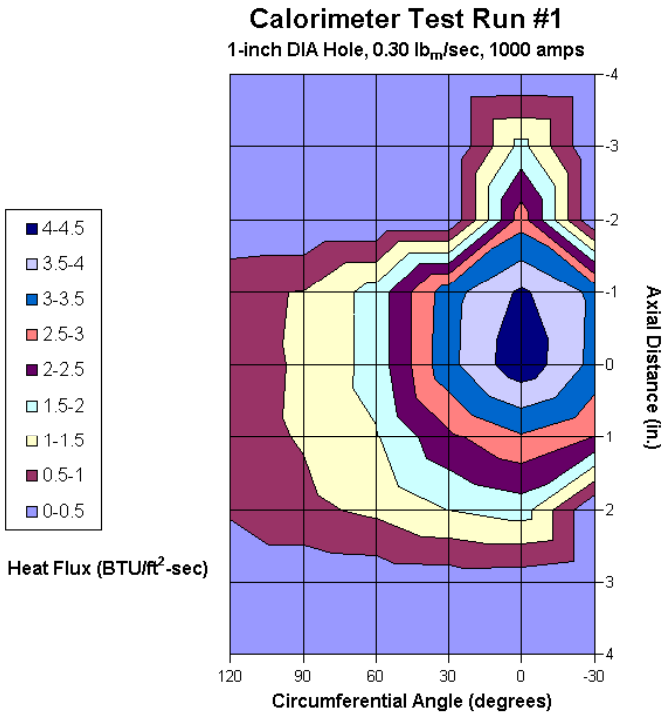

Figure 6-33 - Calorimeter

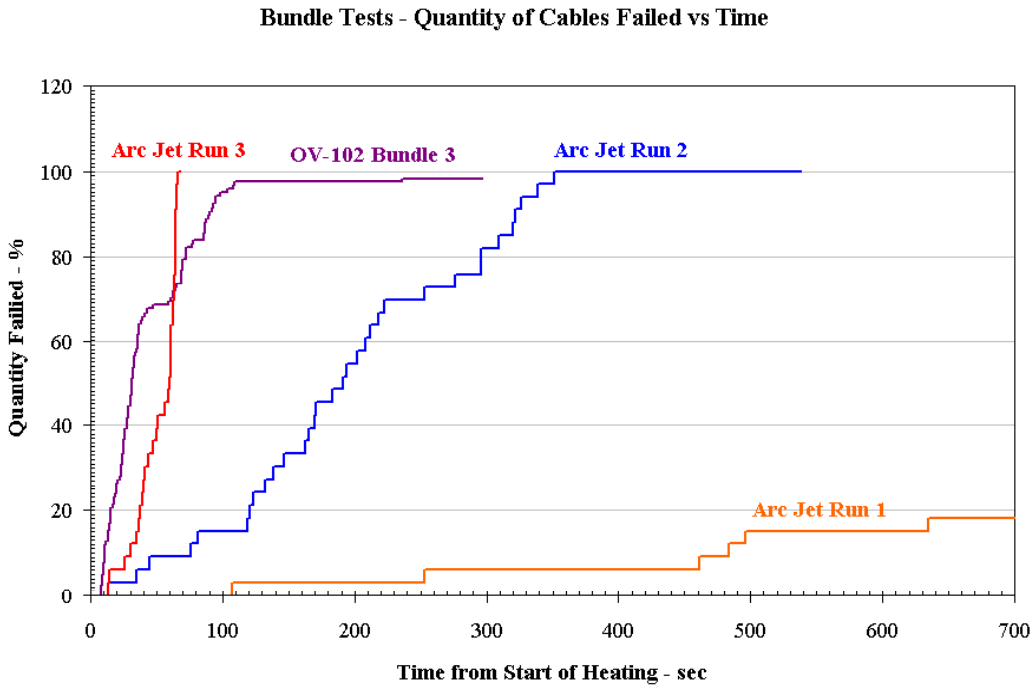

Figure 6-34 – Cable Failure Rates

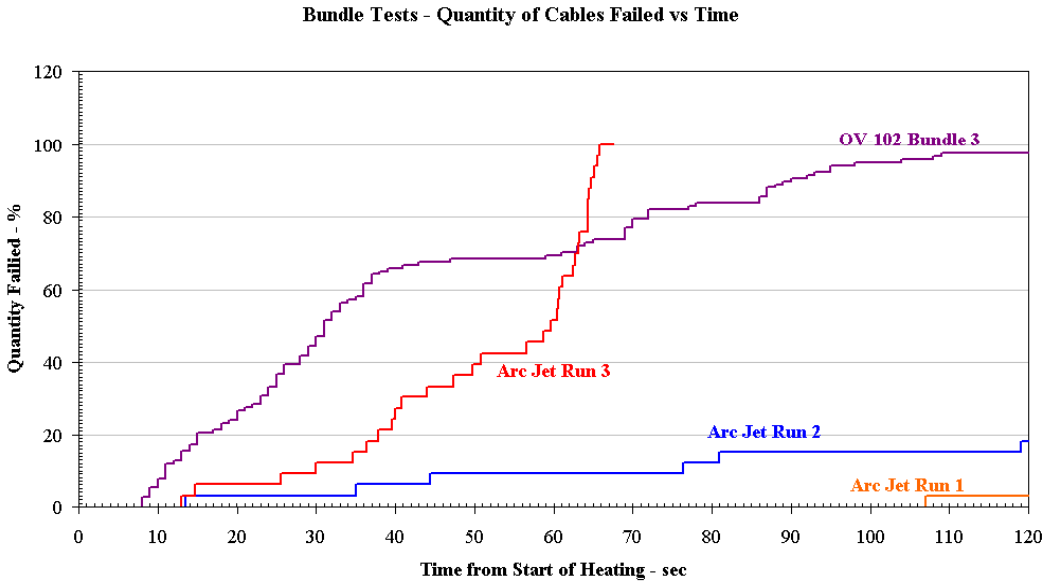

Figure 6-35 – Cable Failure Rates (expanded)

Figure 6-36: Wire bundle arc jet testing (before test)

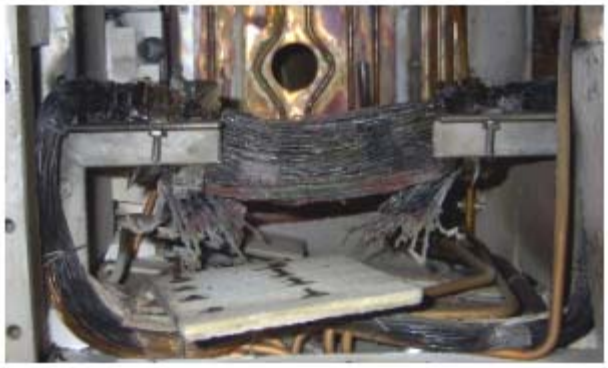

Figure 6-37 – Cable Bundle Post-Test Run #2

(1)
Test Article Inserted

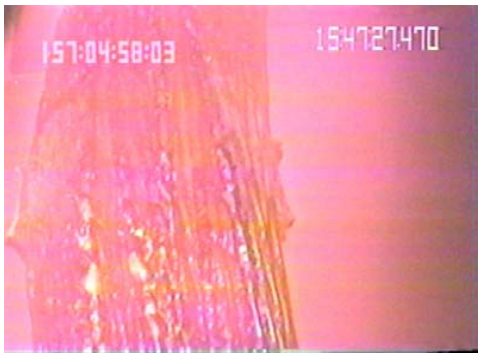

(2)

(3)

(4)

(5)

(6)

Figure 6-38 – Video Sequence of Cable Bundle Test (Run #3)

Figure 6-39 - MLG outboard sidewall (looking fwd)

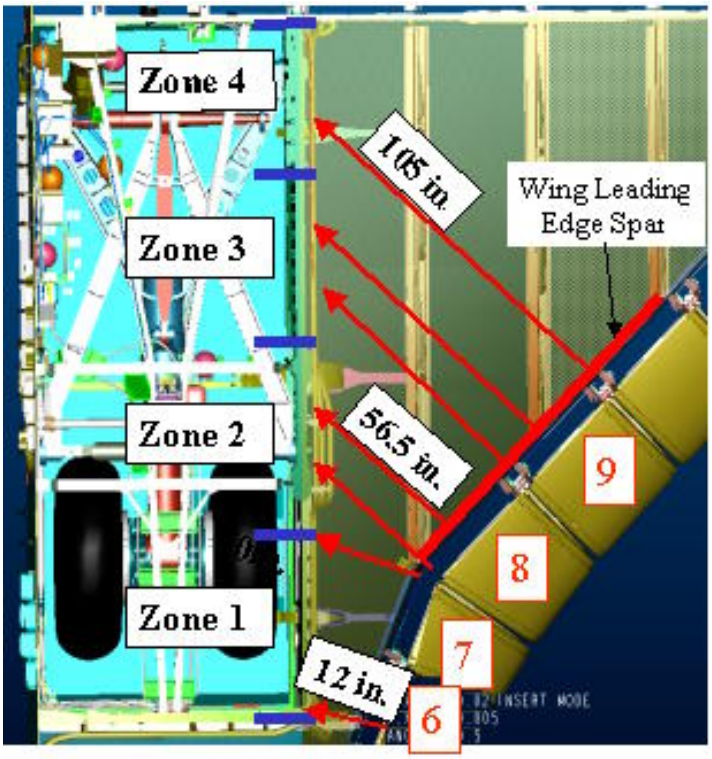

Figure 6-40 - MLG wheel well wall partitioning (view from top)

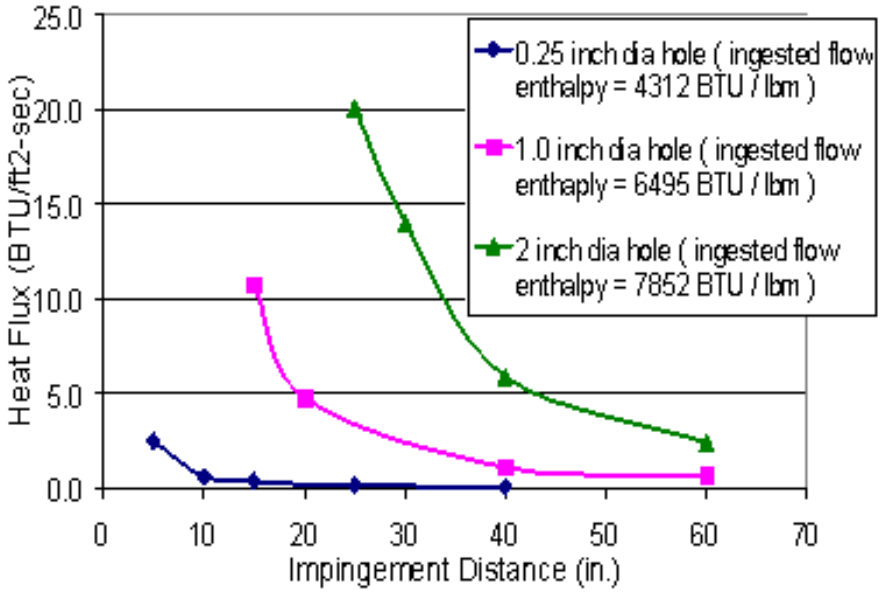

Figure 6-41 - Panel 9 internal plume flat plate impingement heating at EI+491 seconds

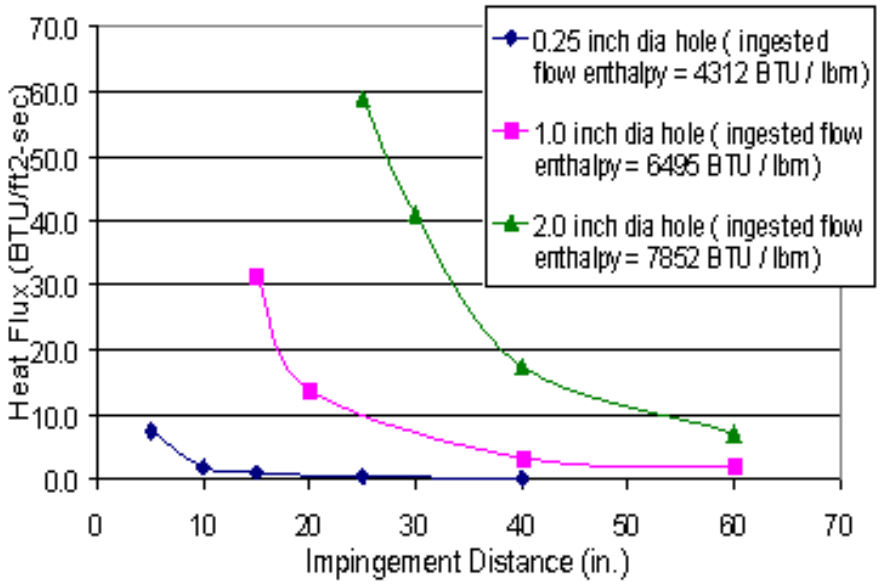

Figure 6-42 - Panel 9 internal plume impingement heating on 1" diameter cylinder at EI+491 seconds

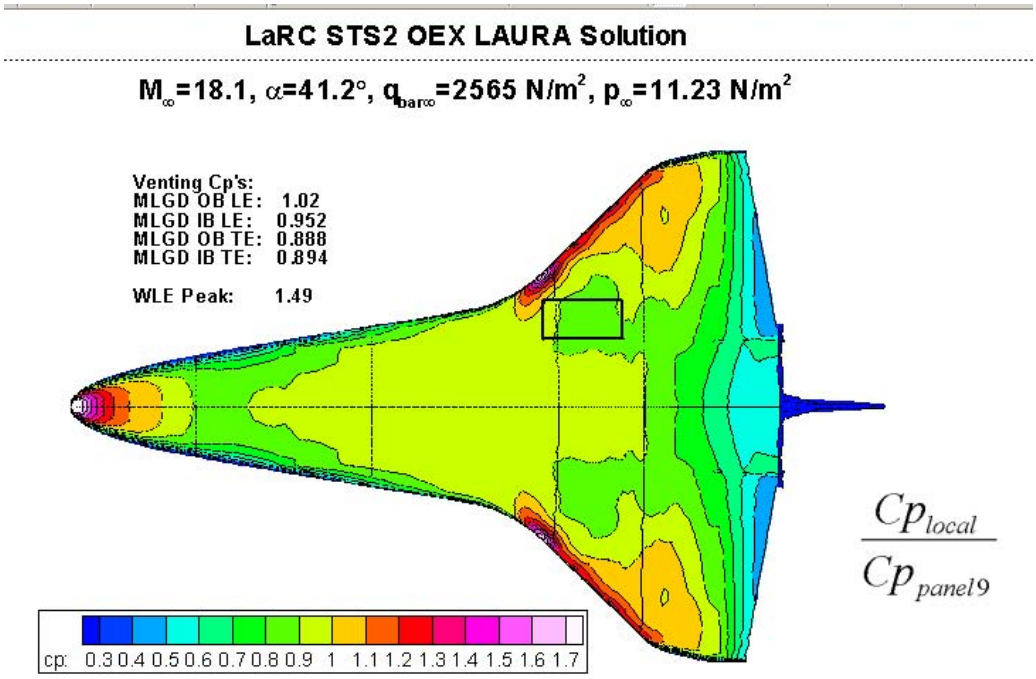

Figure 6-43 - Plume heating correction for local pressure coefficient

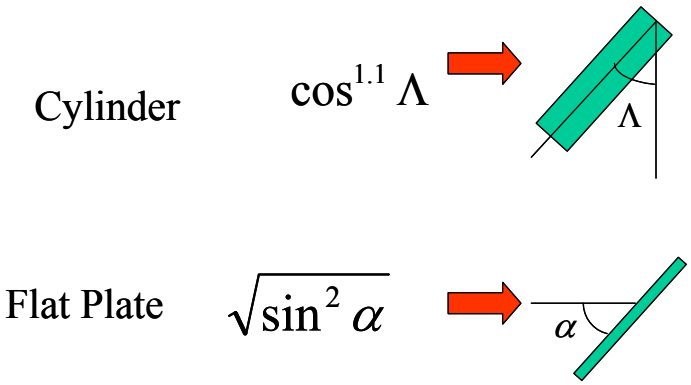

Zone	a	L
1	67.5	22.5
2	58.5	31.5
3	58.5	31.5
4	58.5	31.5

Figure 6-44 - Off-normal angle impingement plume heating correction for a cylinder and flat plate

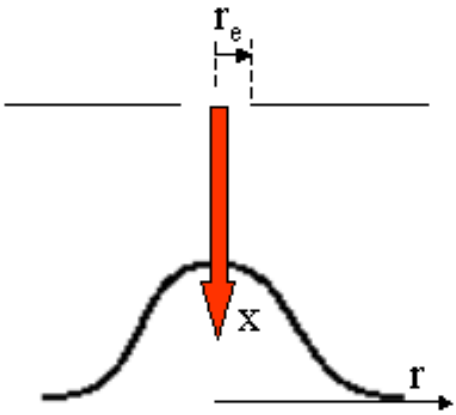

r/r_s	$qdot/(qdot)_0$
0	1.000
1	0.748
2	0.392
3	0.219
4	0.154
5	0.119
6	0.100
7	0.0808
8	0.0615
9	0.0423

$$r_S = r_e \quad \text{for } x \le 7.0 r_e$$

$$r_S = r_e + x \tan\left(\frac{\pi}{30}\right) \quad \text{for } x > 7.0 r_e$$

Figure 6-45 - Plume heating corrections for radial distribution from the stagnation point

$$\frac{\sqrt{r_{1"diametercylinder}}}{\sqrt{r_{bundle}}}$$

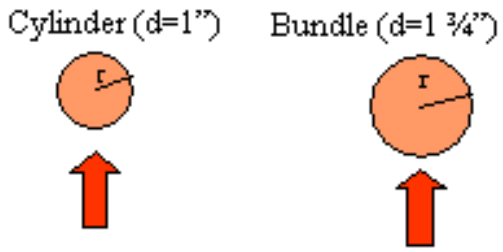

Figure 6-46 -Correction of plume heating due to radius effects

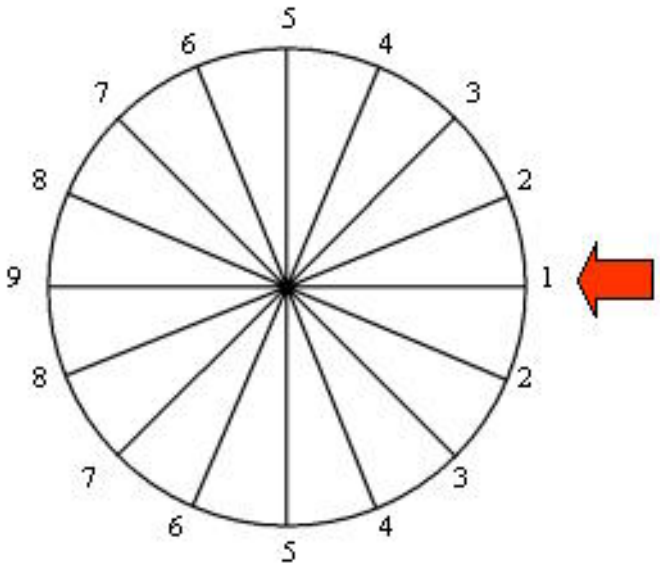

station	qdot/(qdot)$_0$
1	1.0000
2	0.9155
3	0.7080
4	0.4490
5	0.2230
6	0.0830
7	0.0320
8	0.0325
9	0.0370

Figure 6-47 - Circumferential plume heating corrections

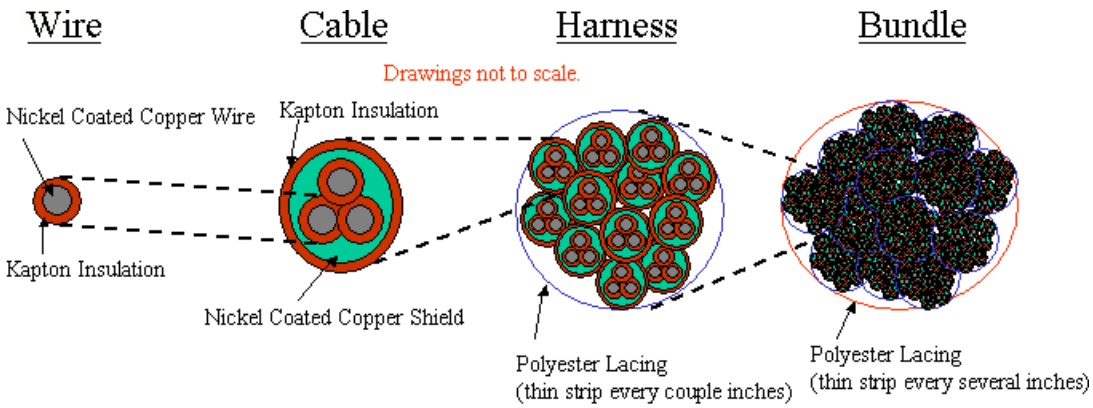

Figure 6-48 - Wire bundle configuration & terminology

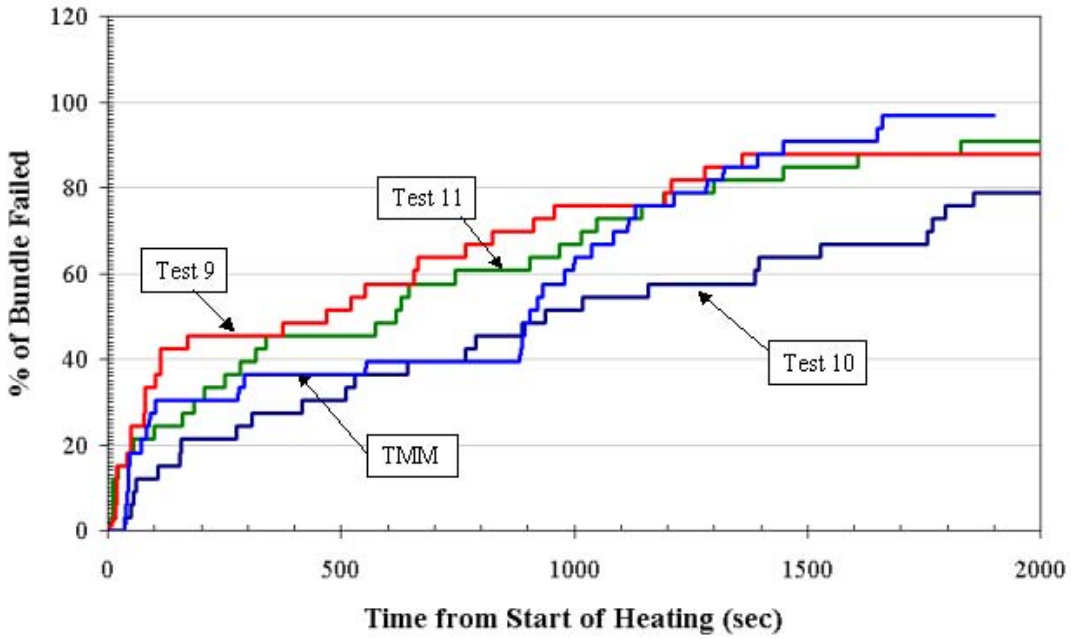

Figure 6-49 - Large propane torch test results vs. TMM test predictions

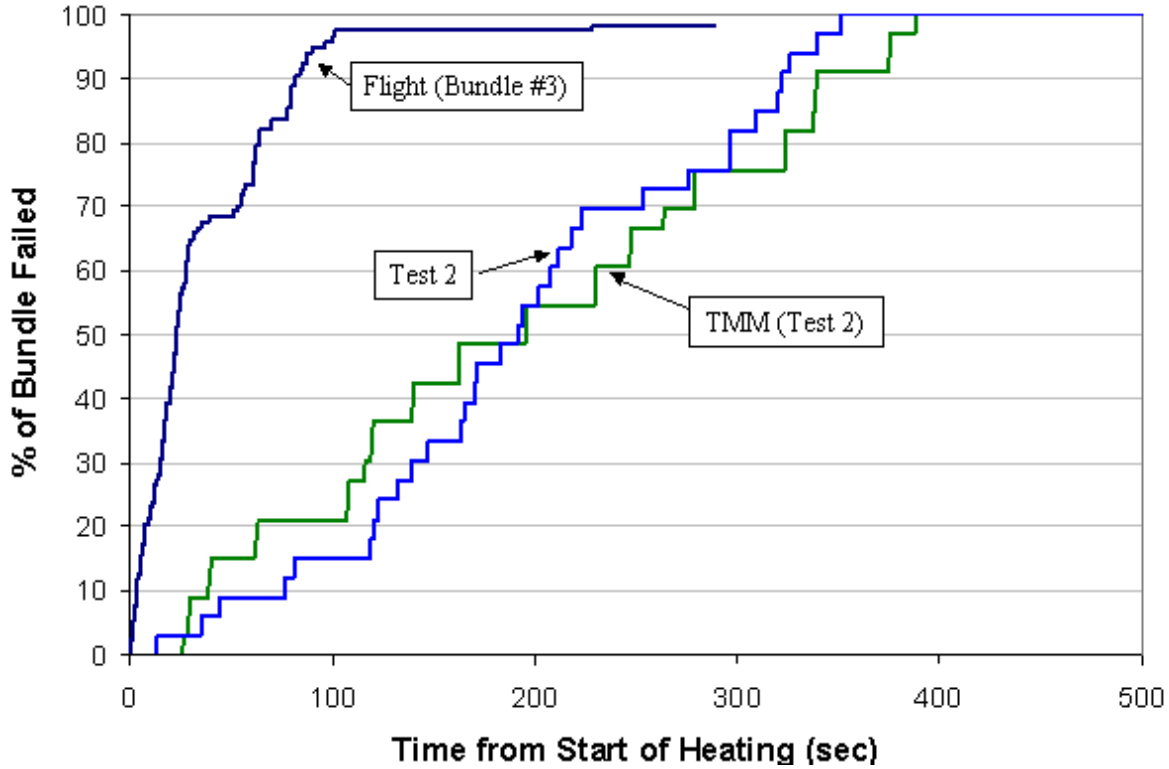

Figure 6-50 - Arc jet test 2 results vs. TMM test predictions

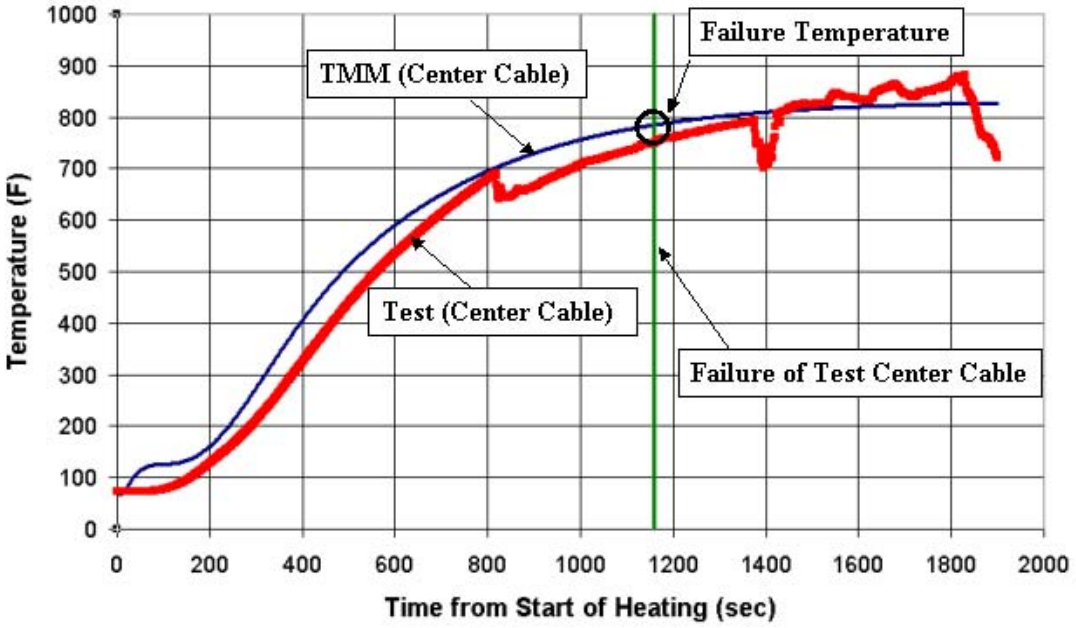

Figure 6-51 - TMM cable failure temperature determined through large propane torch testing

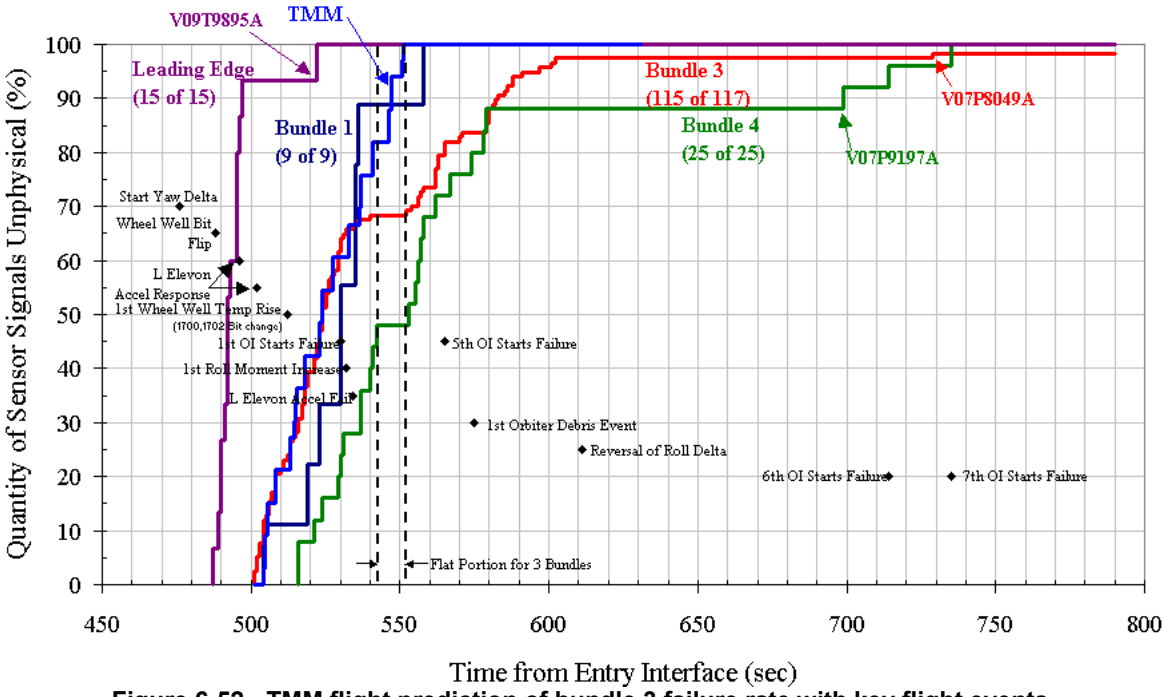

Figure 6-52 - TMM flight prediction of bundle 3 failure rate with key flight events

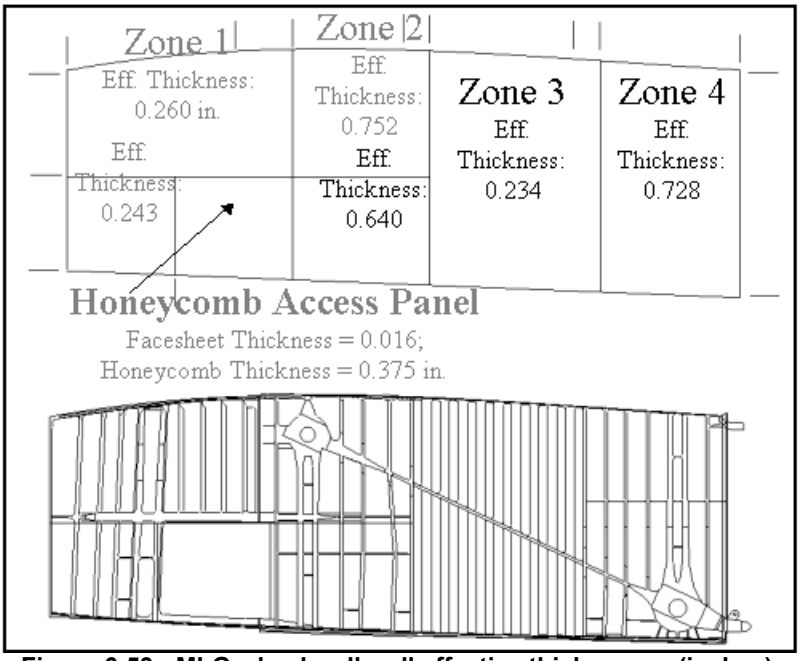

Figure 6-53 - MLG wheel well wall effective thicknesses (inches)

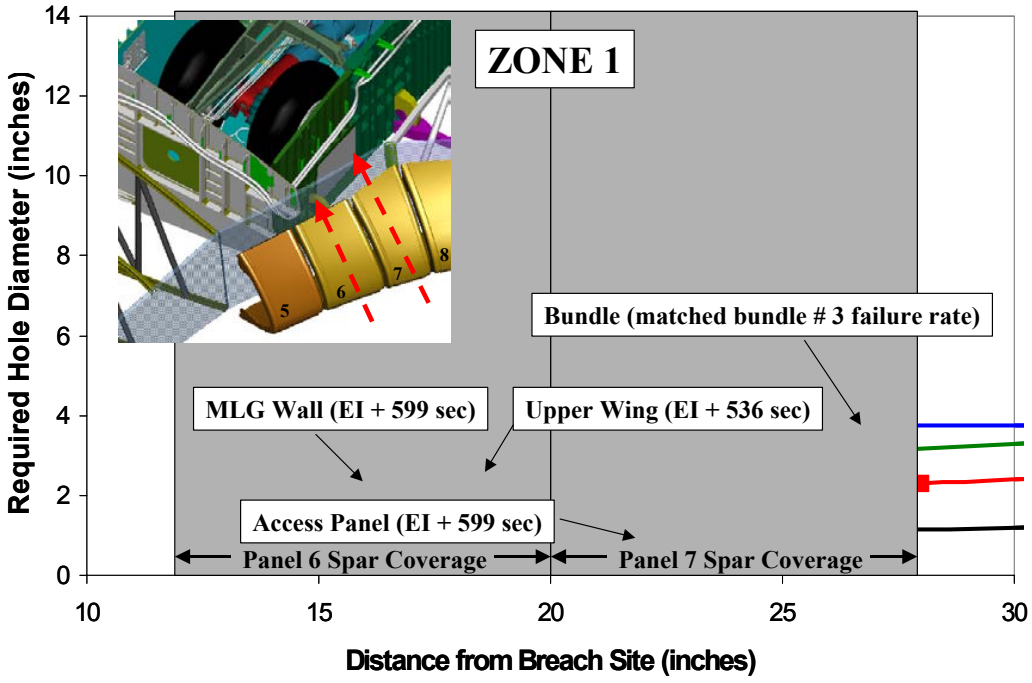

Figure 6-54 - Zone 1 plume heating result comparisons

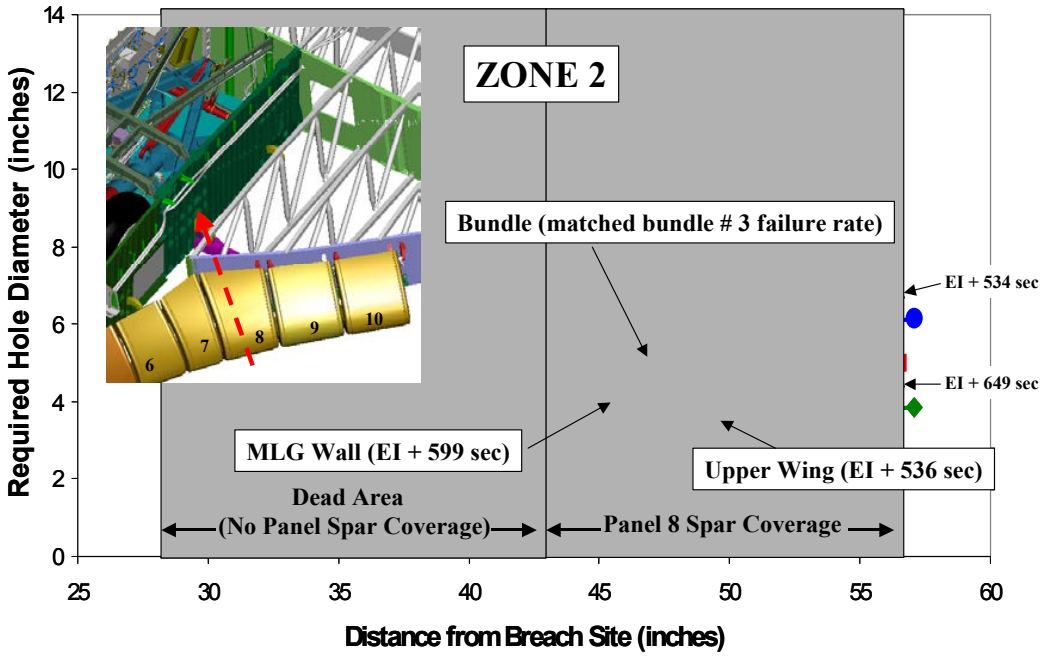

Figure 6-55 - Zone 2 plume heating result comparisons

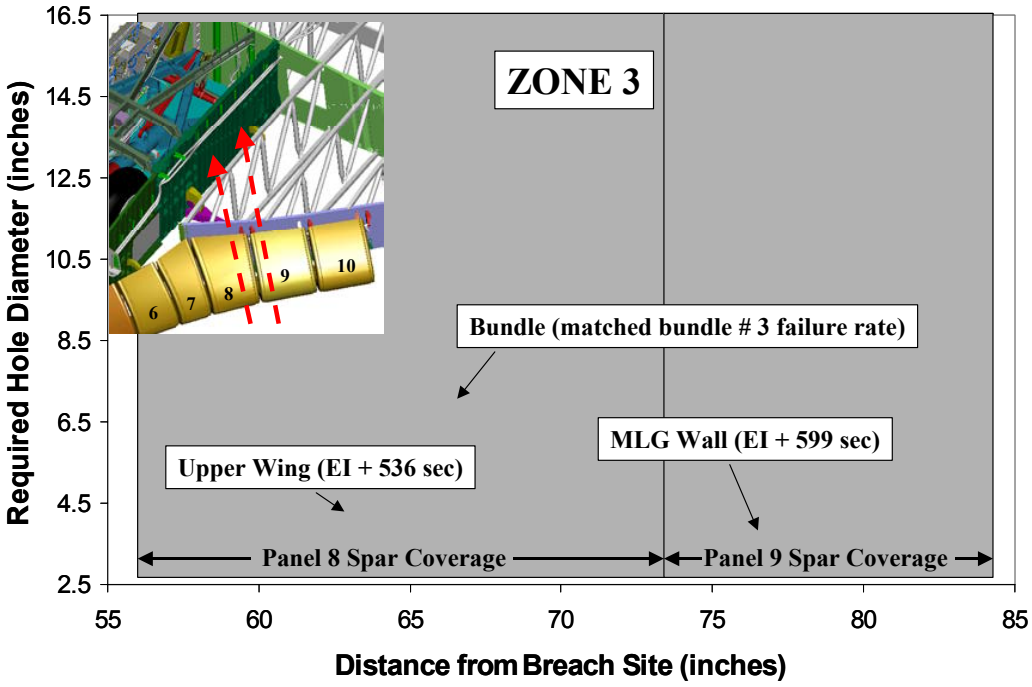

Figure 6-56 - Zone 3 plume heating result comparisons

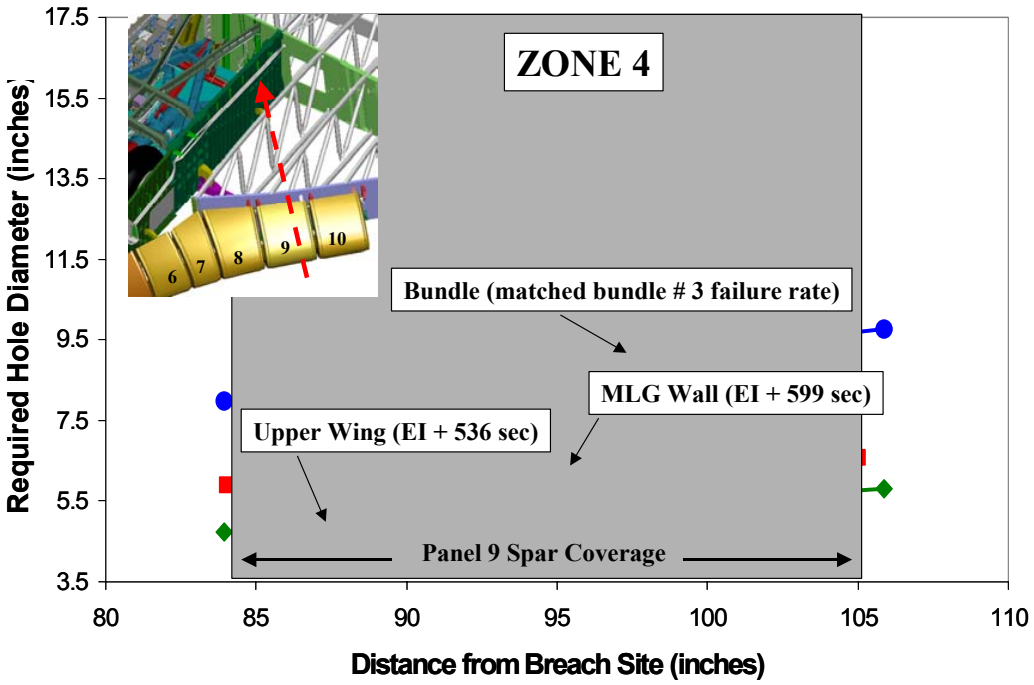

Figure 6-57 - Zone 4 plume heating result comparisons

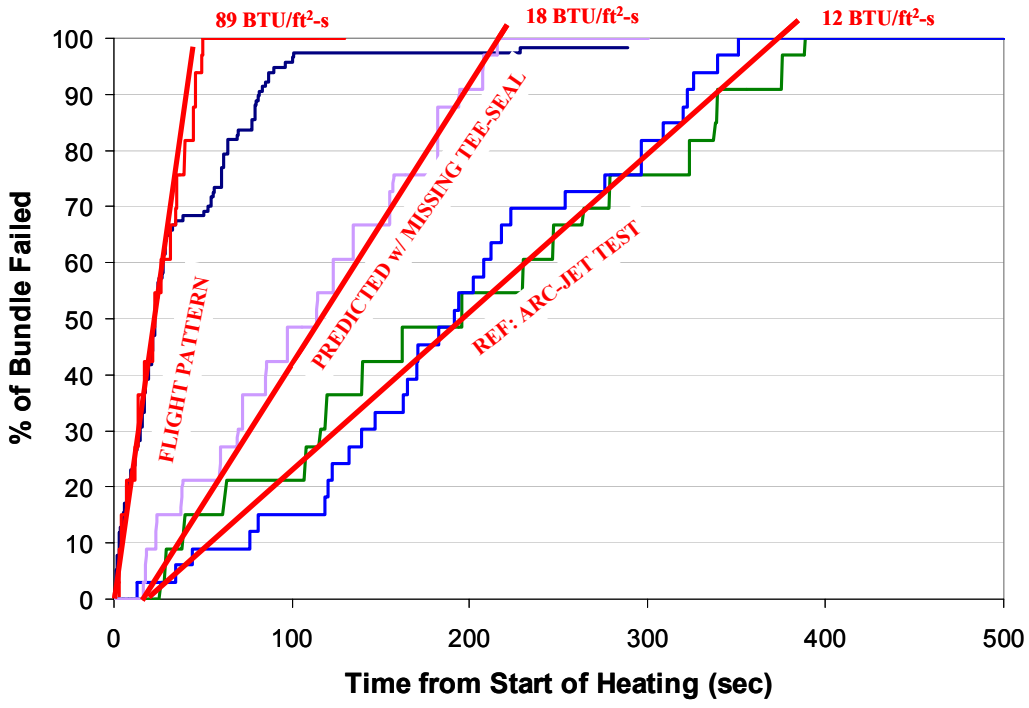

Figure 6-58 - Damaged Tee-Seal Bundle Failure

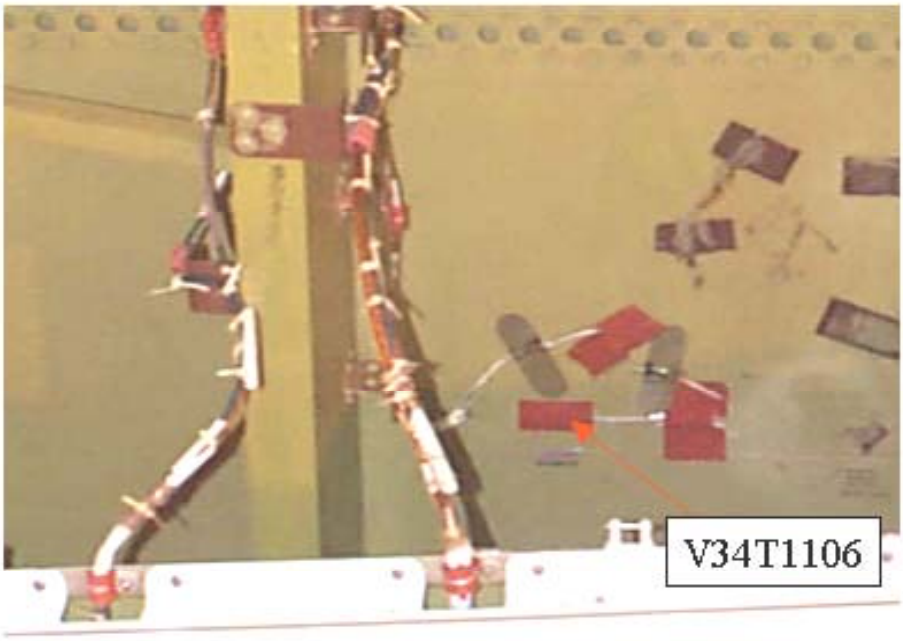

Figure 6-59 - OV-102 V34T1106 Temperature Sensor (looking outboard)

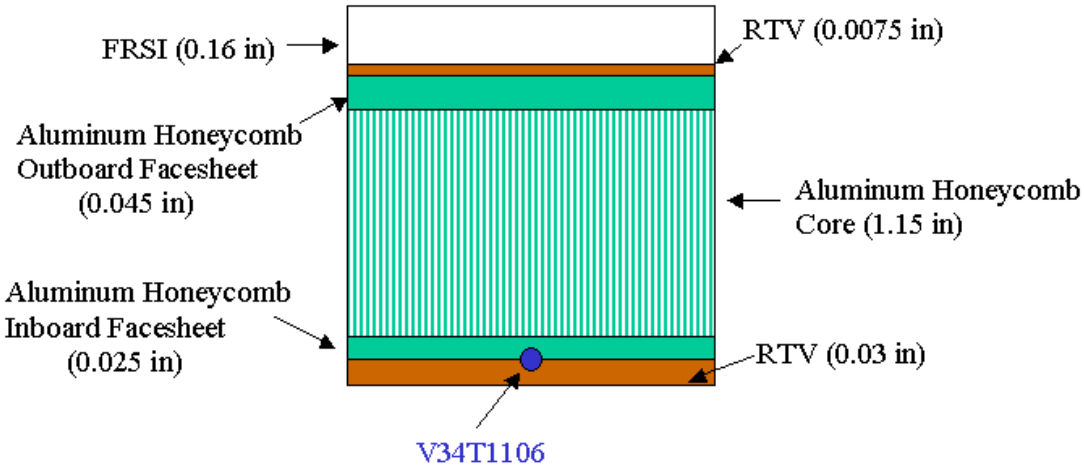

Figure 6-60 - OV-102 V34T1106 Port Sidewall Configuration for TMM

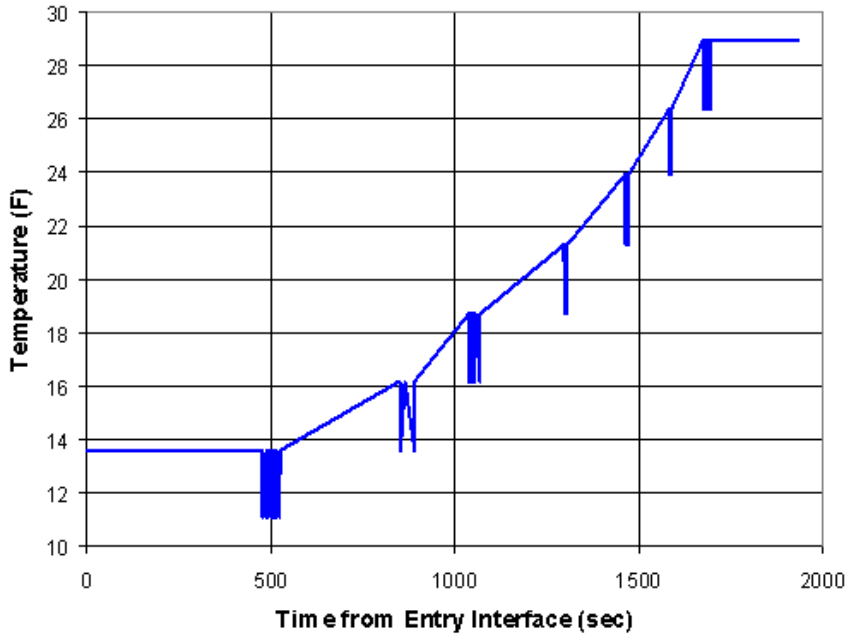

Figure 6-61 - STS-109 V34T1118 Structure Temperature Flight Data

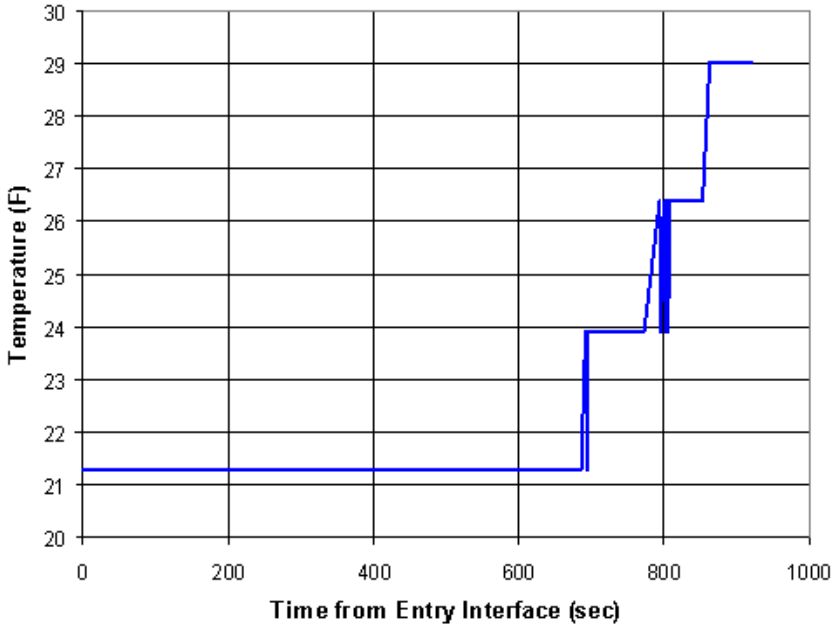

Figure 6-62 - STS-107 V34T1118 Structure Temperature

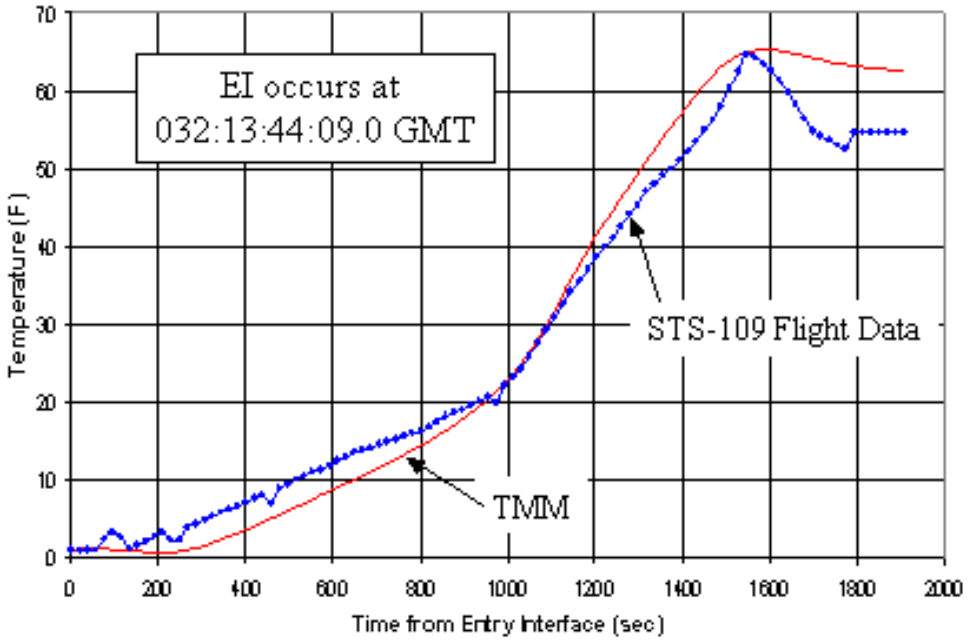

Figure 6-63 - STS-109 TMM Correlation to Flight Data

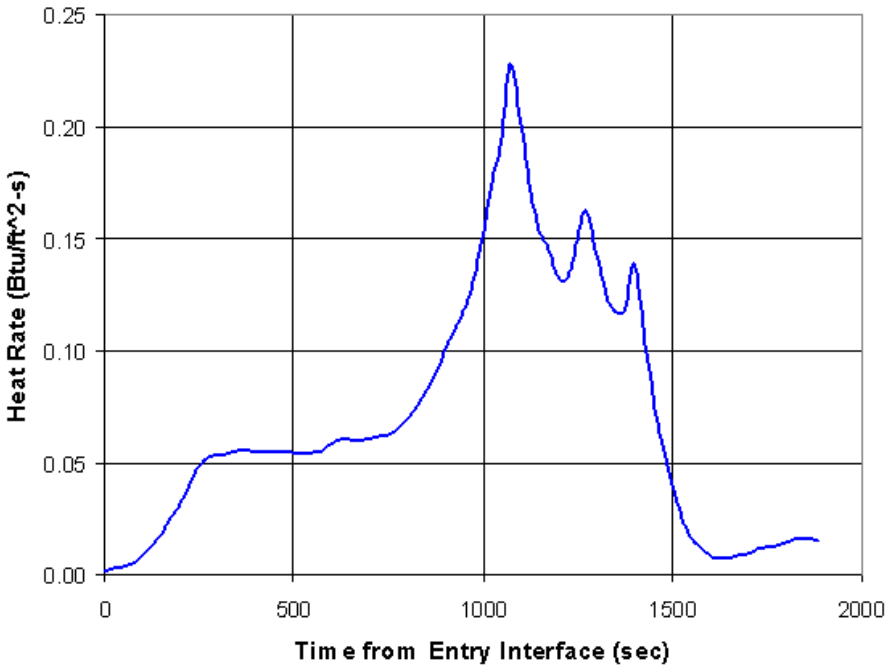

Figure 6-64 - STS-109 Nominal Aerothermodynamic Heating

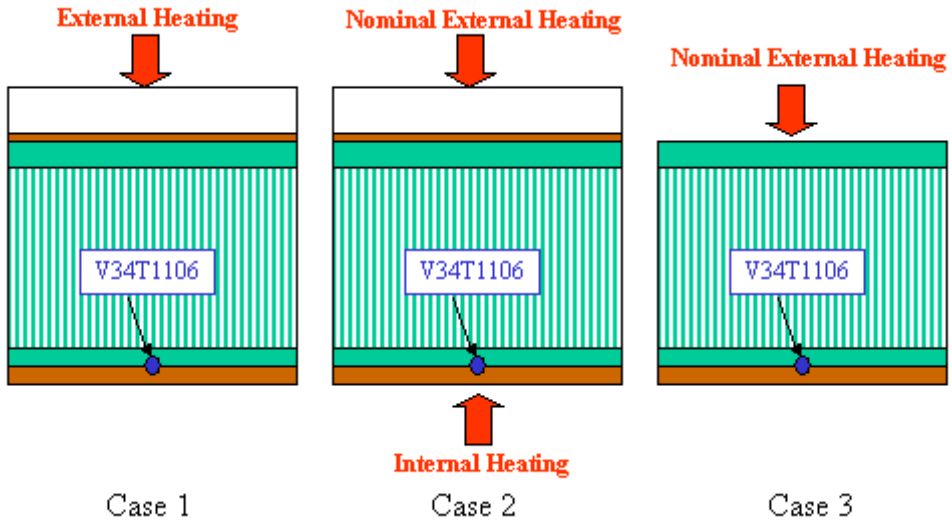

Figure 6-65 - Sidewall Heating Cases

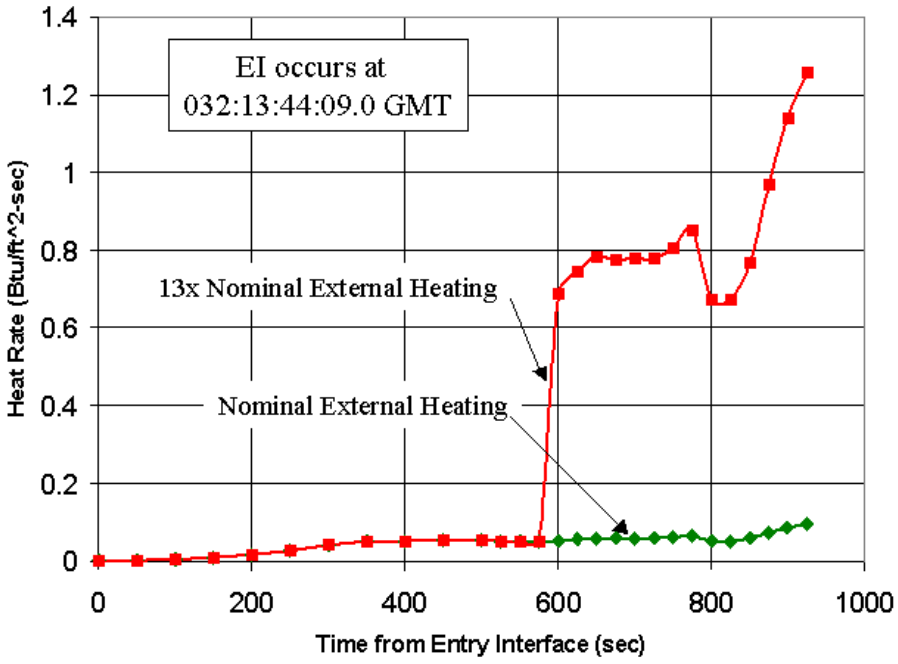

Figure 6-66 - STS-107 Aerothermodynamic Heating

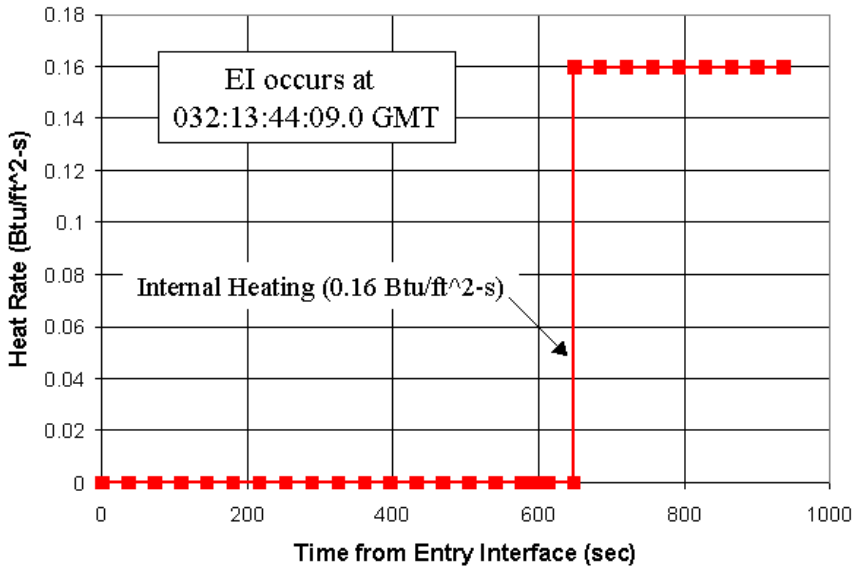

Figure 6-67 - STS-107 Internal Fuselage Heating

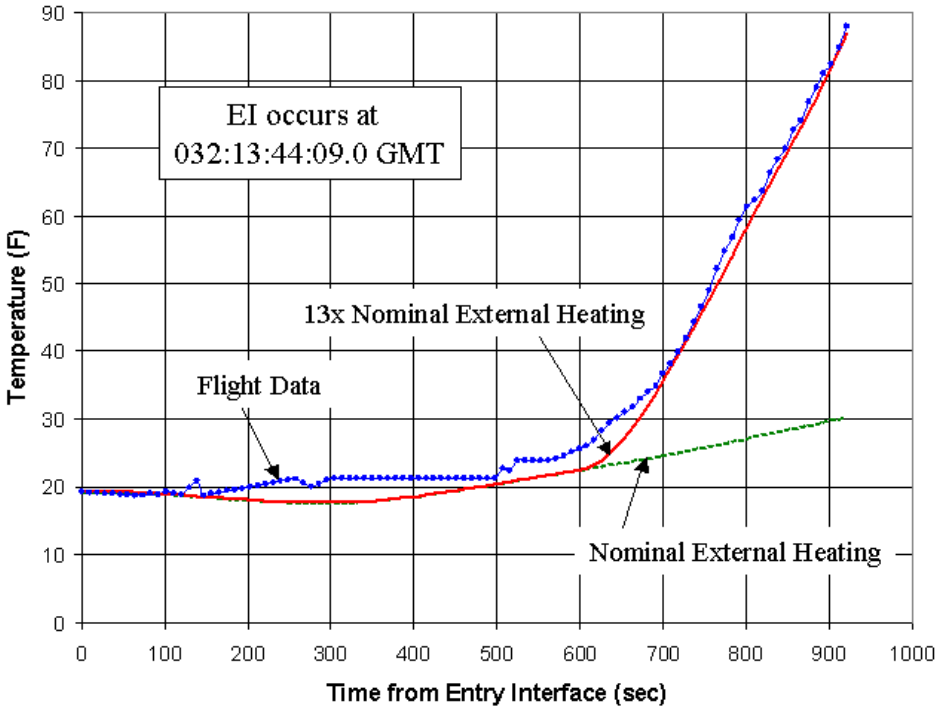

Figure 6-68 - Case 1: TMM Comparison to STS-107 Flight Data

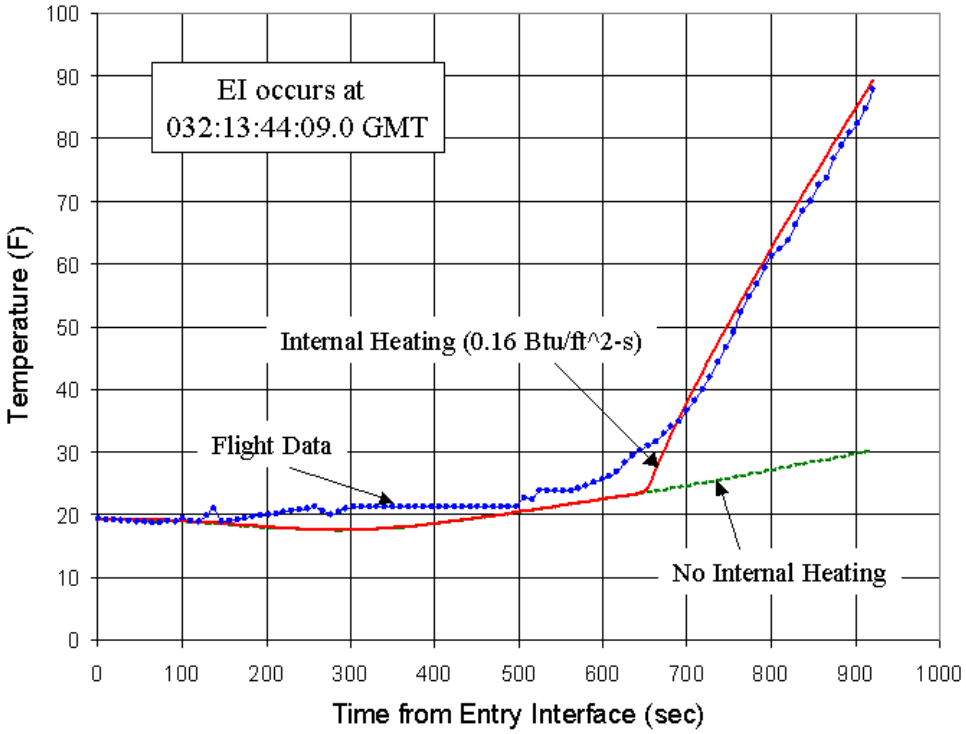

Figure 6-69 - Case 2: TMM Comparison to STS-107 Flight Data

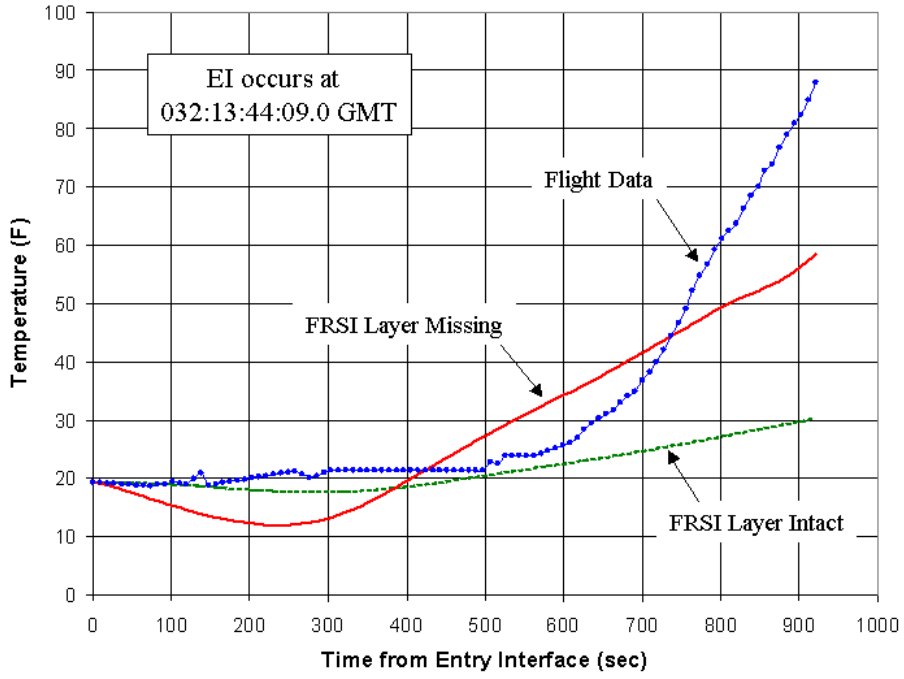

Figure 6-70 - Case 3: TMM Comparison to STS-107 Flight Data

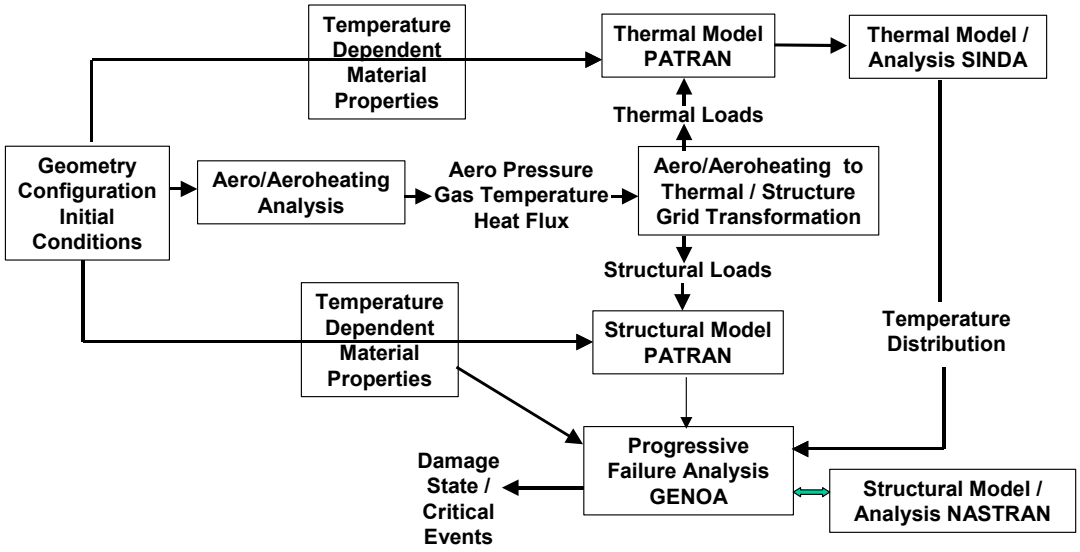

Figure 6-71 - Wing Leading Edge Failure Analysis Methodology

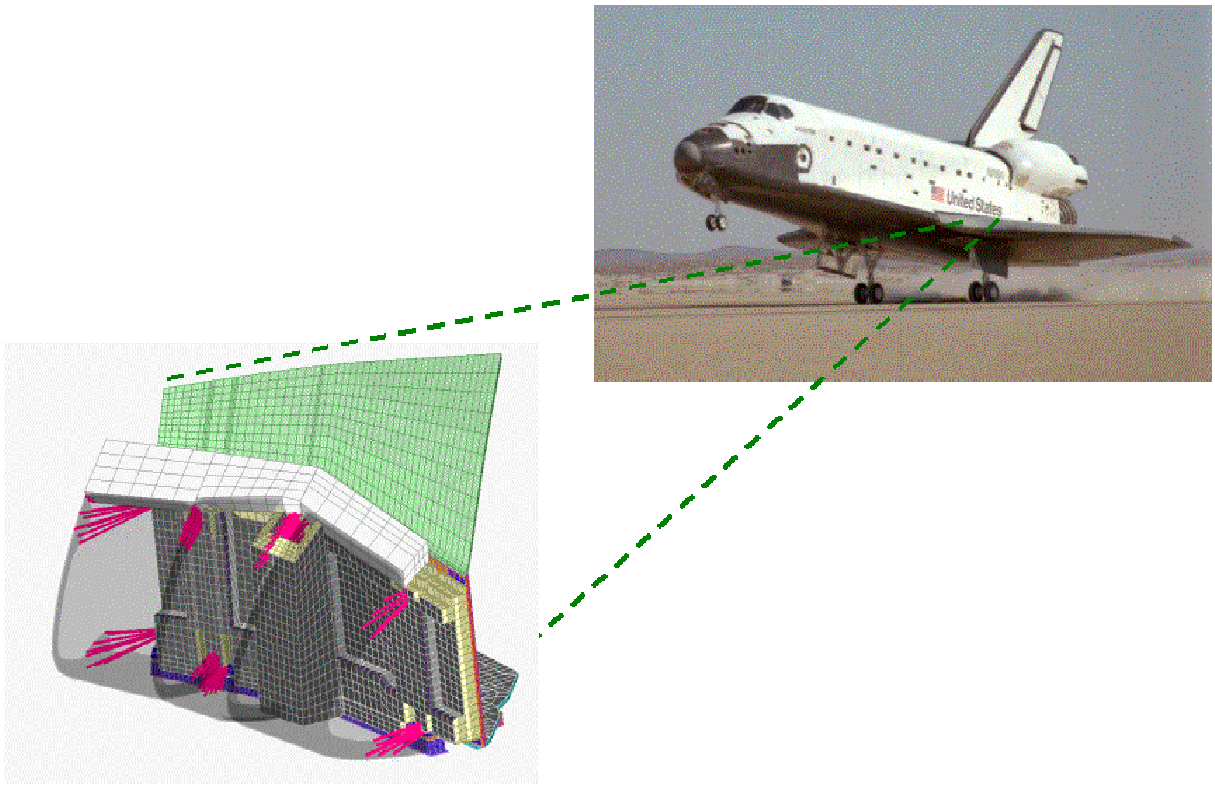

Figure 6-72 - Wing Leading Edge Finite Element Model

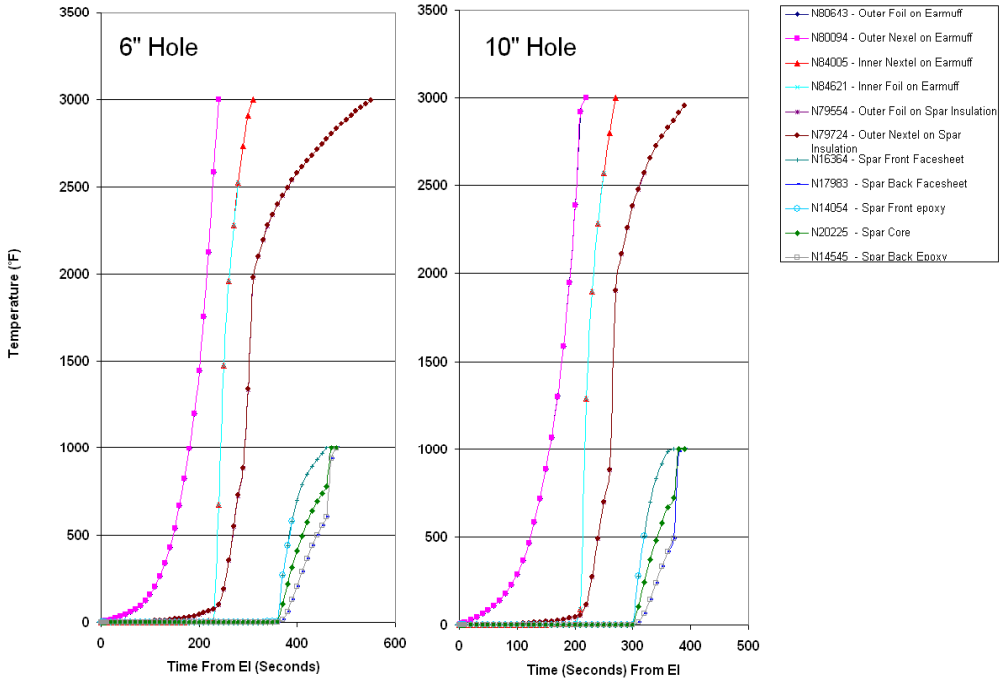

Figure 6-73 – Predicted Wing Spar Insulation and Structure Transients

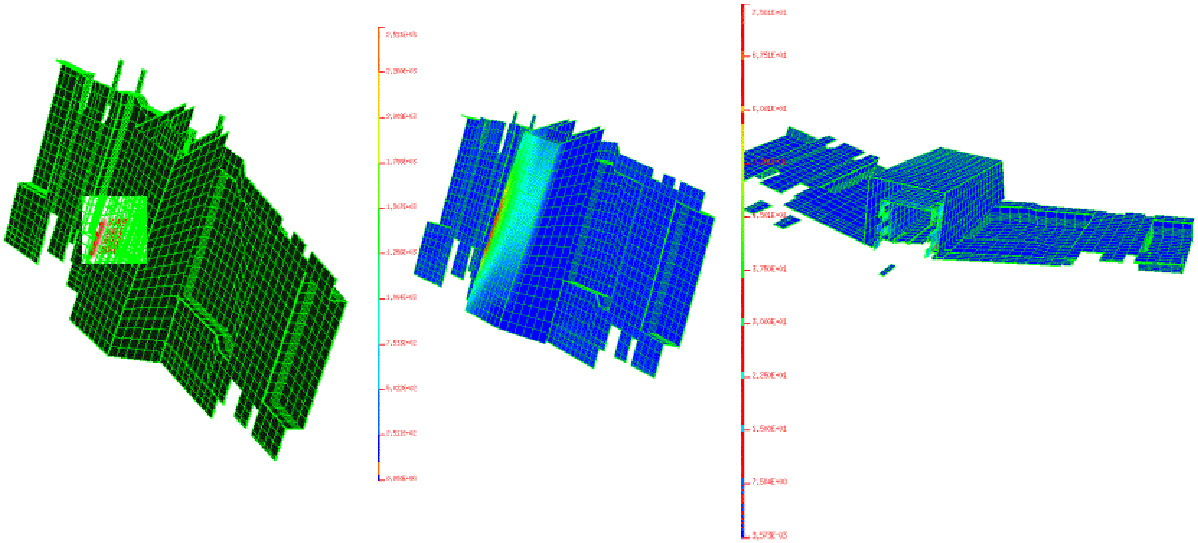

Figure 6-74 - Earmuff Insulation Analysis Results for 10 Inch Hole at t=210 Seconds

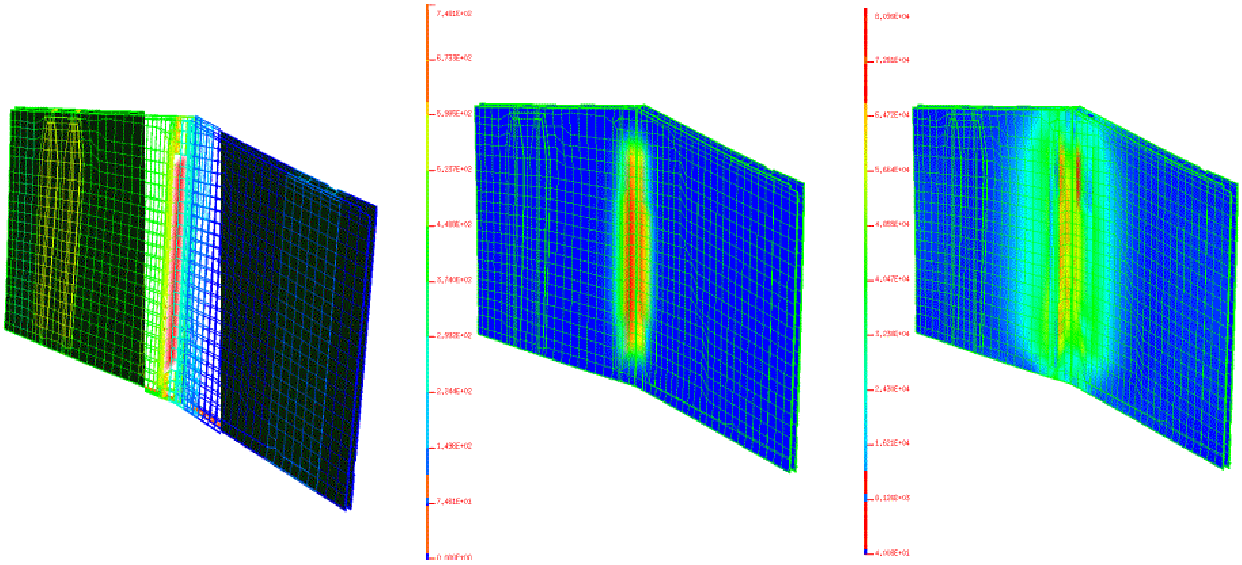

Figure 6-75 - Front Facesheet Analysis Results for 10 Inch Hole at t=320 Seconds

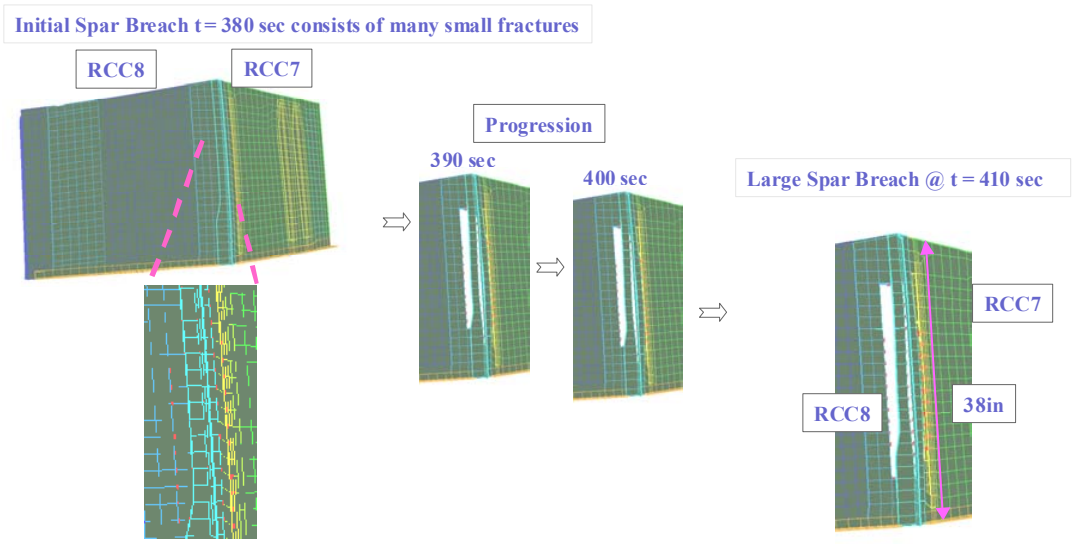

Figure 6-76 Rear Facesheet Analysis Results for 10 Inch Hole at t=380 Seconds (View of Spar From Inside Wing)

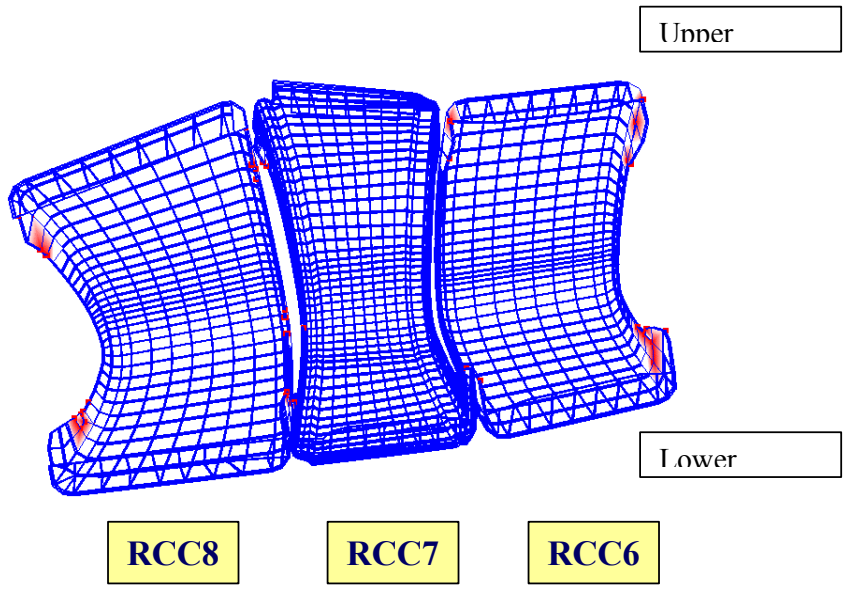

Figure 6-77 - RCC Panel Fracturing at 450 Seconds With 10 Inch Hole (View Looking From Inside RCC Cavity

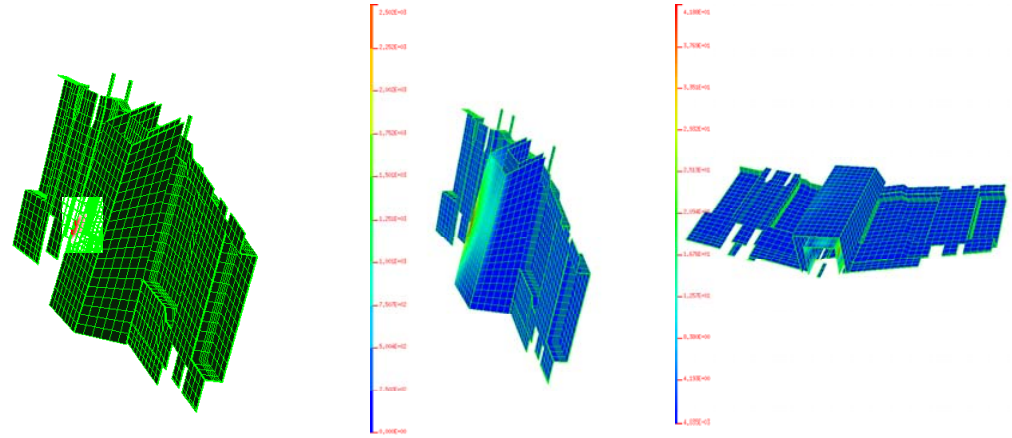

Figure 6-78 - Earmuff Insulation Analysis Results for 6 Inch Hole at t=230 Seconds

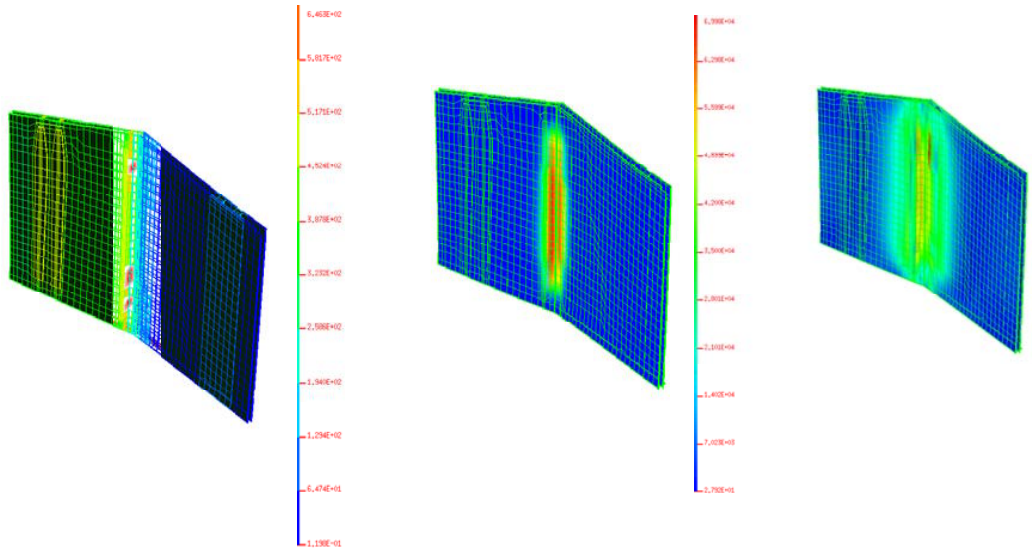

Figure 6-79 - Front Facesheet Analysis Results for 6 Inch Hole at t=380 Seconds

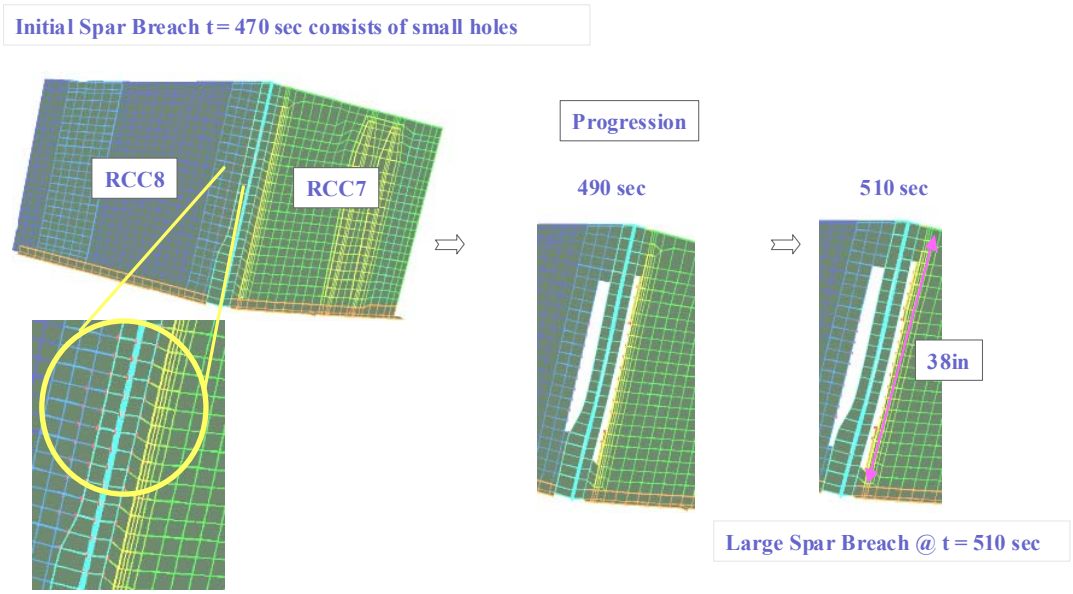

Figure 6-80 - Rear Facesheet Analysis Results for 6 Inch Hole at t=470 Seconds (View of Spar From Inside Wing)

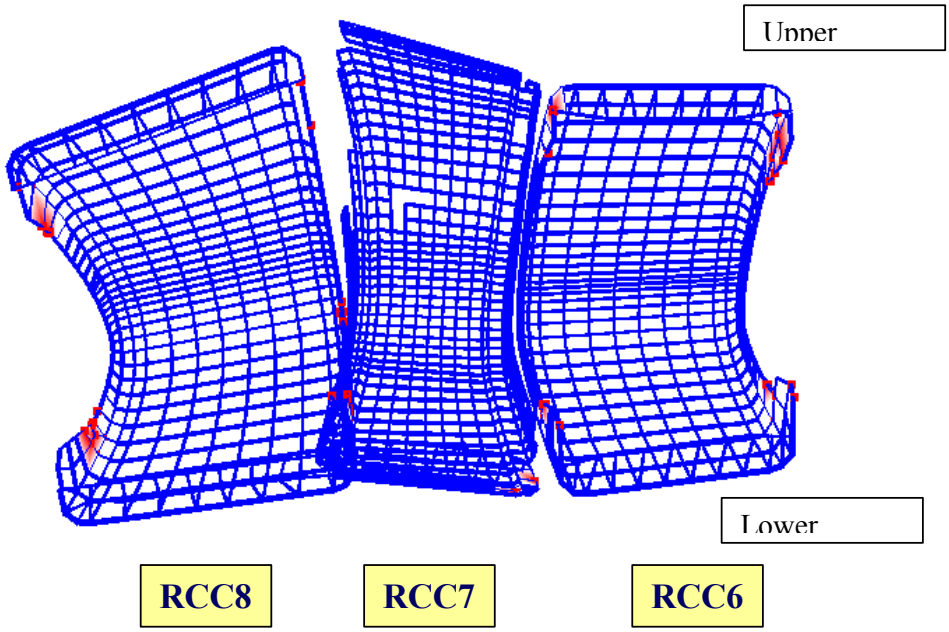

Figure 6-81 - RCC Panel Fracturing at 500 Seconds With 6 Inch Hole (View Looking From Inside RCC Cavity

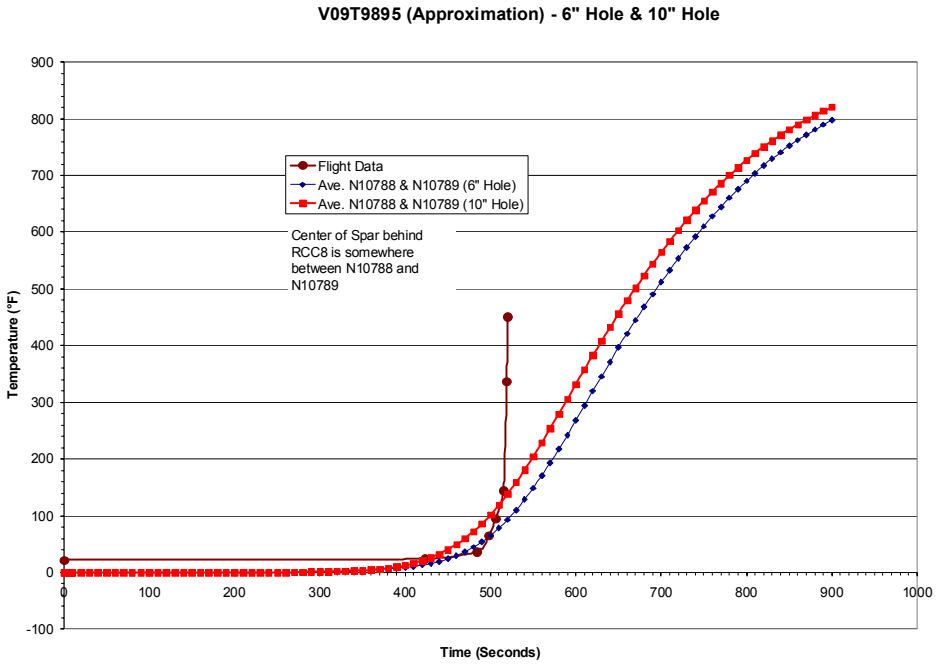

Figure 6-82 - Comparison of Panel 8 Rear Spar Temperature Prediction with Panel 9 Flight Data (V09T9895)

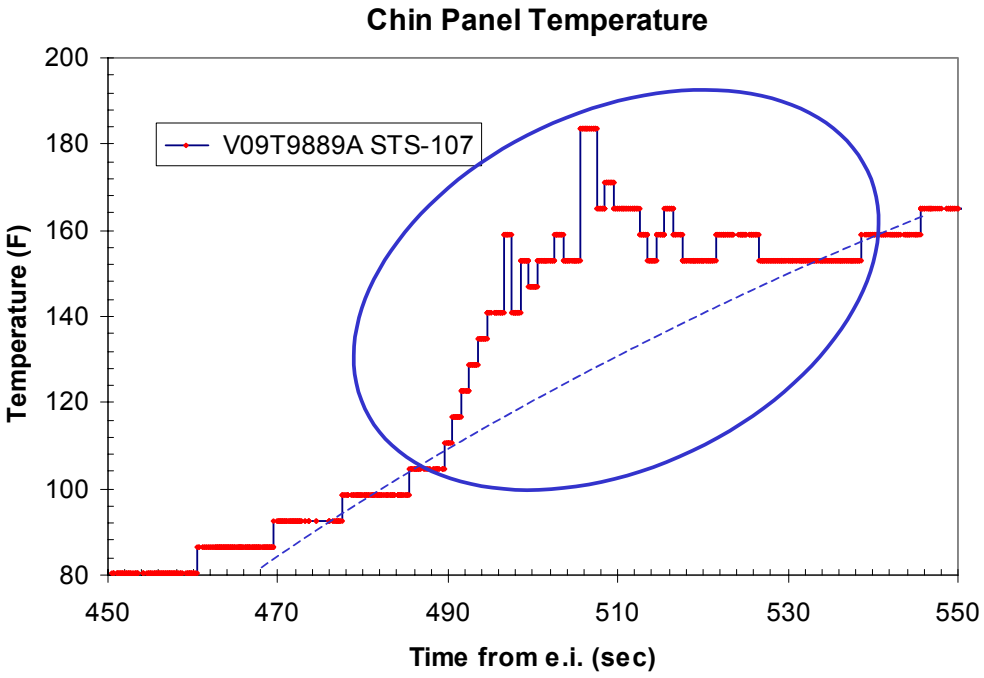

Figure 6-83 - Chin Panel Temperature Anomaly

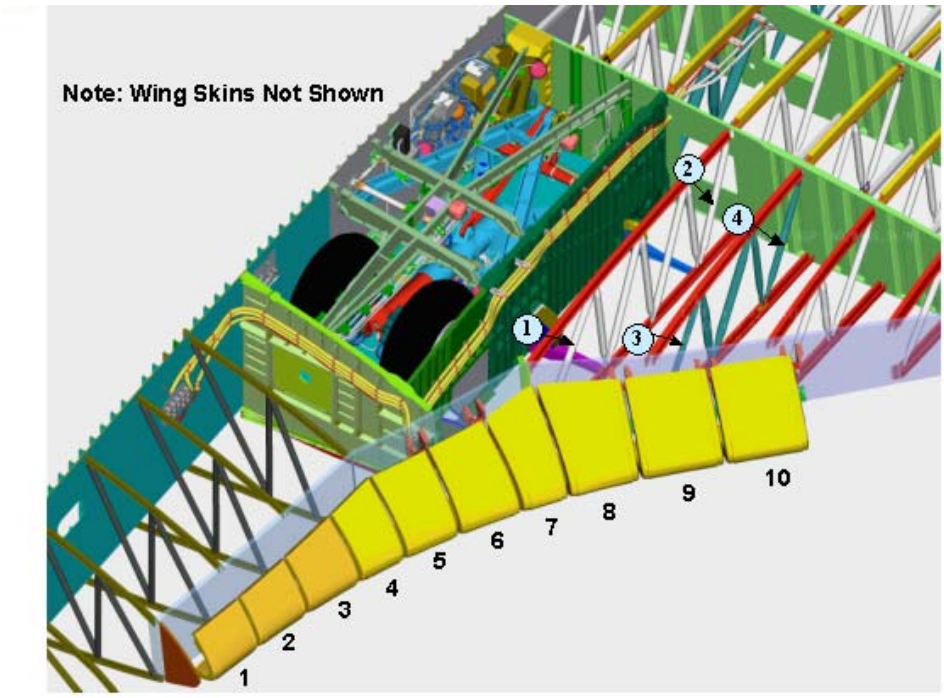

Figure 6-84 - Location of truss tubes (labeled 1-4) studied

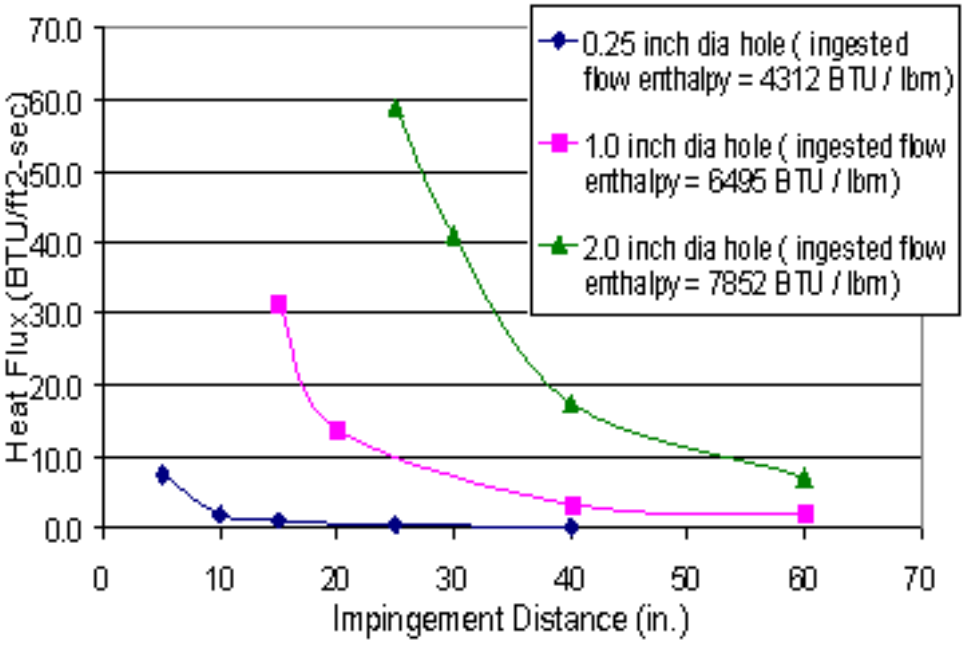

Figure 6-85 - Panel 9 internal plume impingement heating on 1" diameter cylinder at EI+491 seconds

$$\cos^{1.1}\Lambda_1 \cdot \cos^{1.1}\Lambda_2$$

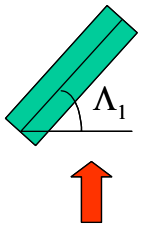

Tube	L_1	L_2
1	31.5	48
2	31.5	60
3	73.73	50
4	64.53	56

L_2 is out of the page

Figure 6-86 – Heating Correction for Angular Impingement

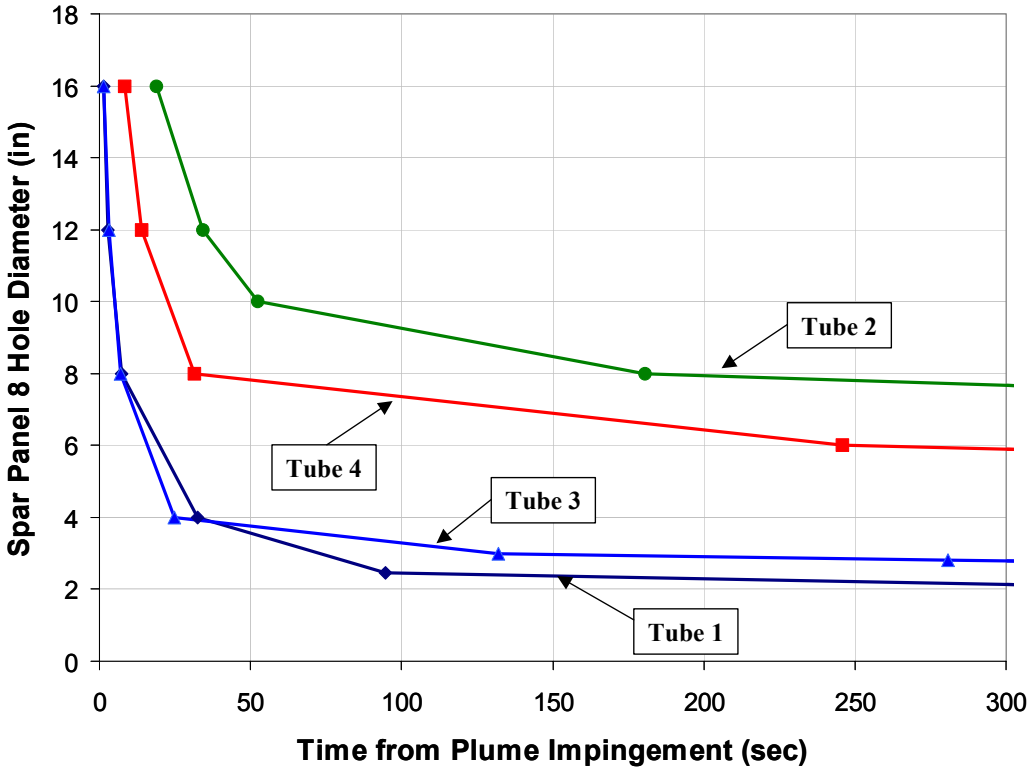

Figure 6-87 - Wing truss tube failure times with respect to breach sizes

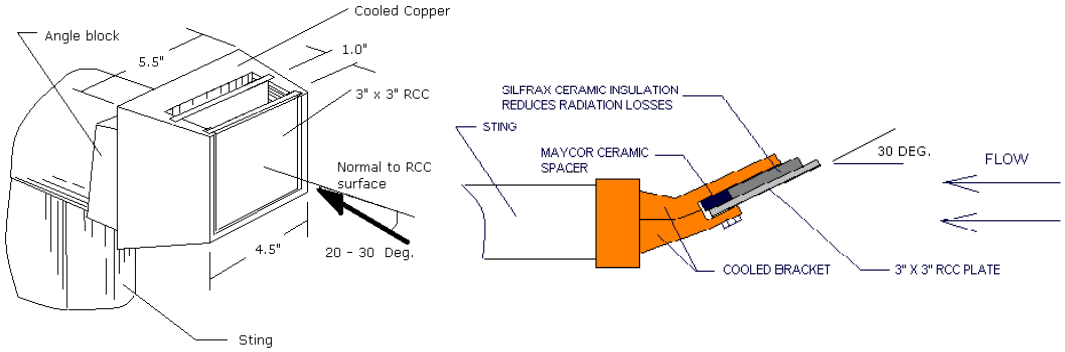

Figure 6-88 – Test Fixtures

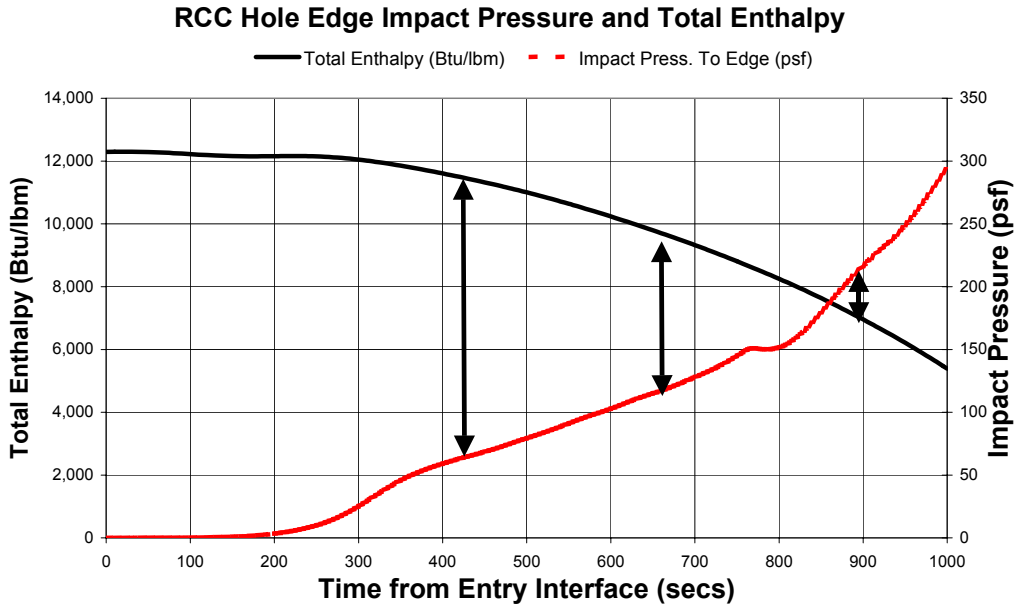

Figure 6-89 – Flight Environment

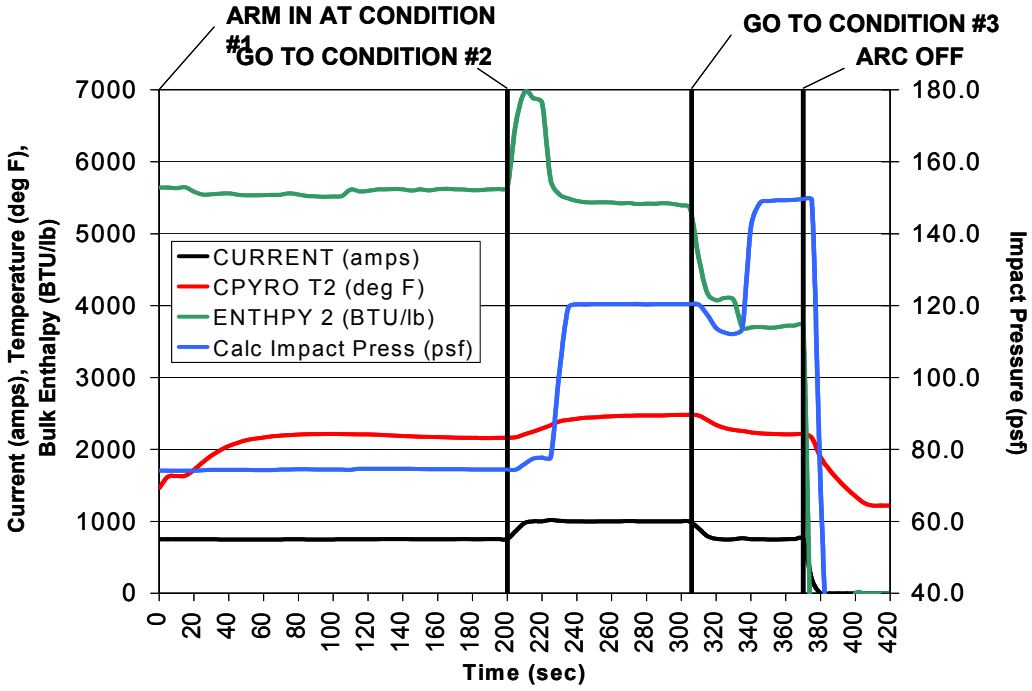

Figure 6-90 -Test Run #__ Actual Profile

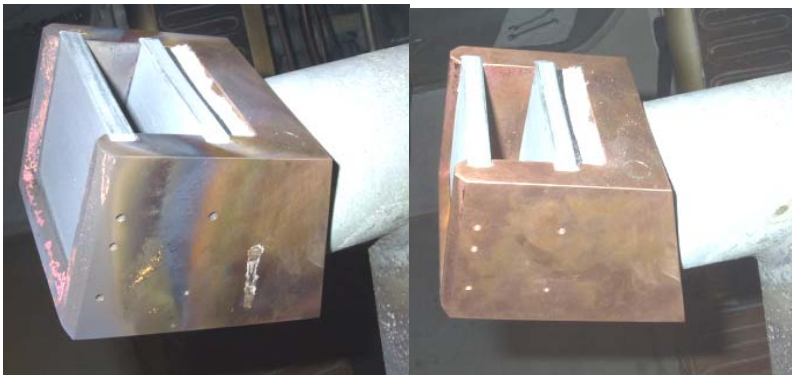

Figure 6-91 -Test #1 Pre and Post Test

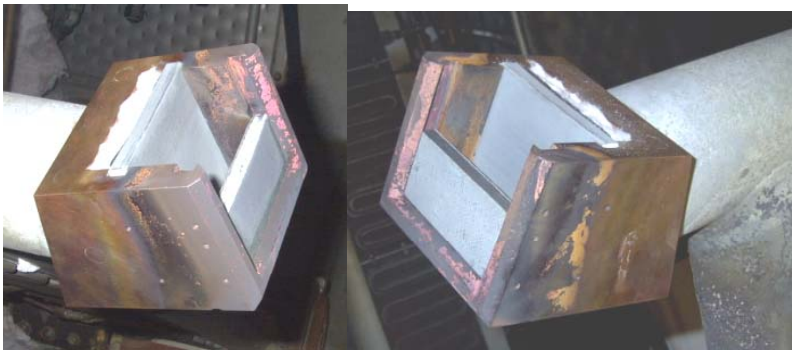

Figure 6-92 -Test #2 Pre and Post Test

Figure 6-93 -Test #3 Pre and Post Test - Knife-Edging Apparent

Figure 6-94 -Test #4 Pre and Post Test

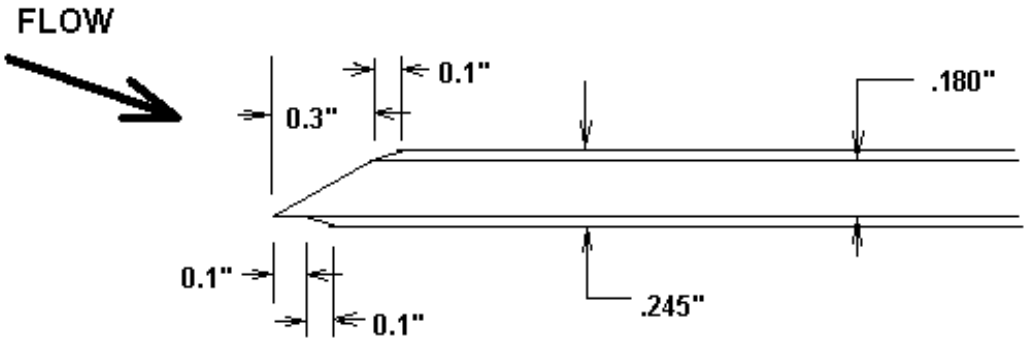

Figure 6-95 – Schematic of knife-edging dimensions

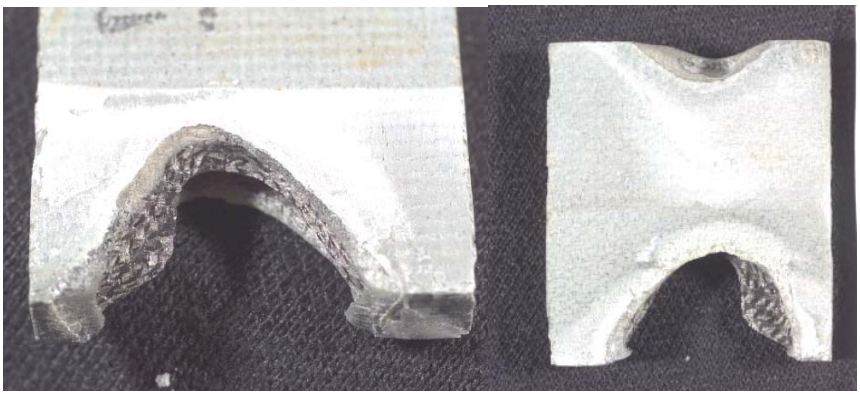

Figure 6-96 -Test #5 Closeout RCC Pieces with Knife-Edging

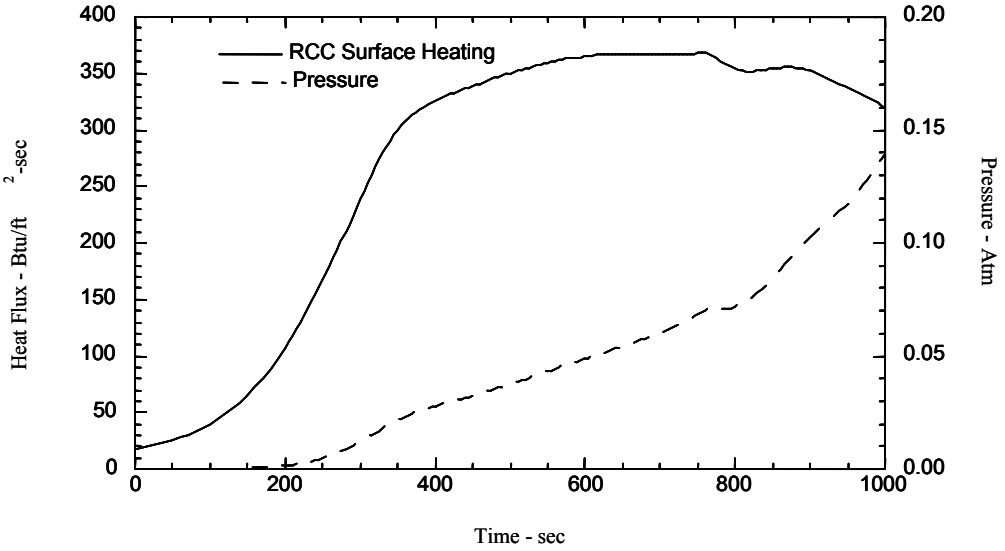

RCC Surface Heat Flux & Pressure History

Figure 6-97 – RCC Hole Environment

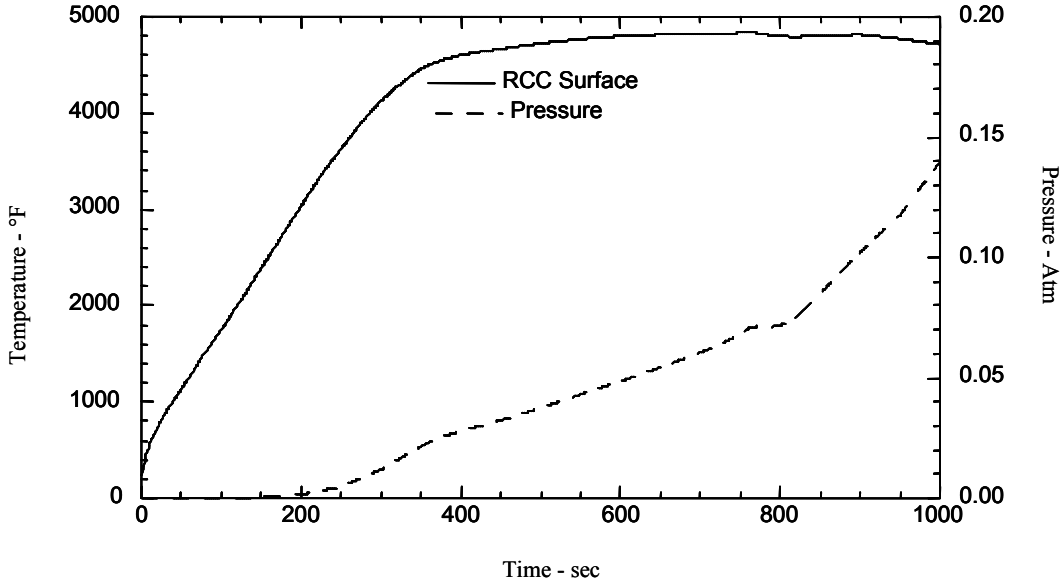

RCC Surface Temperature & Pressure

Figure 6-98 – RCC Temperature Response

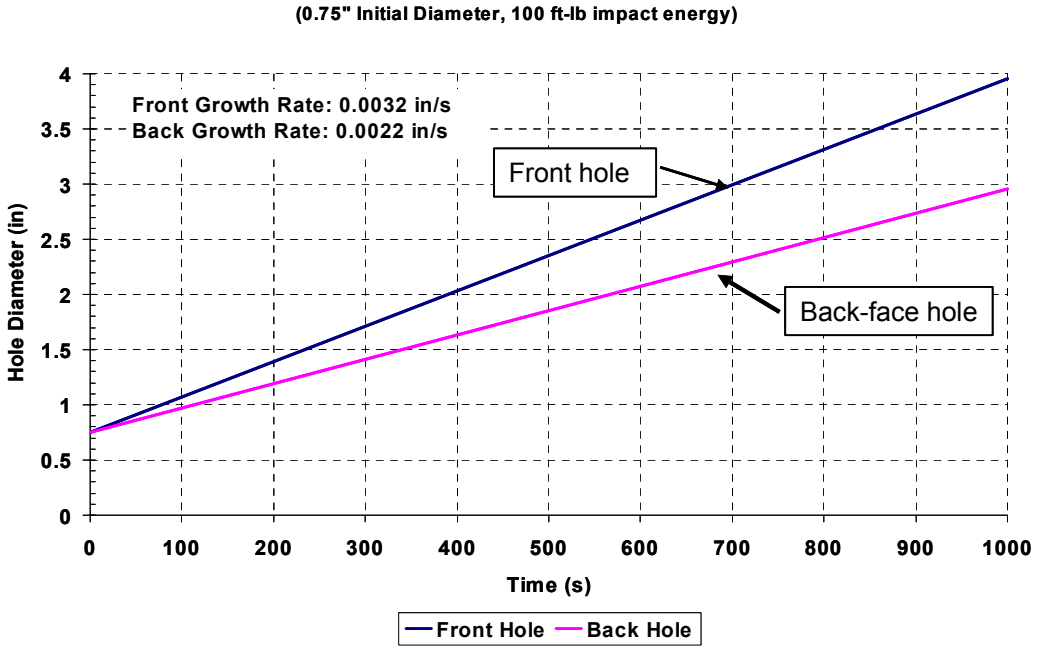

Figure 6-99 – RCC Hole Growth Calculation

References - Thermal

6-1. Generic Honeycomb Modeling Tool.
6-2. Stress report - STS89-0537
6-3. SINDA/FLUINT Version 4.4, C&R Technologies, Littleton CO.
6-4. Alpha Star Corporation, “Phase II Final Report, GENOA Progressive Failure Analysis of X-37 Reusable Launch Vehicle (RLV) Program”, June 24, 2000.
6-5. GENOA

7 STRESS

7.1 Panel 9 Spar Strain Gauge Evaluation

7.1.1 Analysis Objective

The objective of this analysis was to determine how a significant thermal event in the WLE spar would influence shear strain readings in the spar web shown in Figure 7.1-1. The location of the strain gage is shown in Figure 7.1-11. Primary focus was placed on thermal loading because mechanical loading would not produce the type of shear strain responses seen; maneuver type loads would have been seen on other strain gages and would have registered on the flight control systems. Mechanical load deviations would also be of relatively short duration. Pressure differentials across the WLE spar web would produce out of plane bending, but would not contribute to the shear strains in the web.

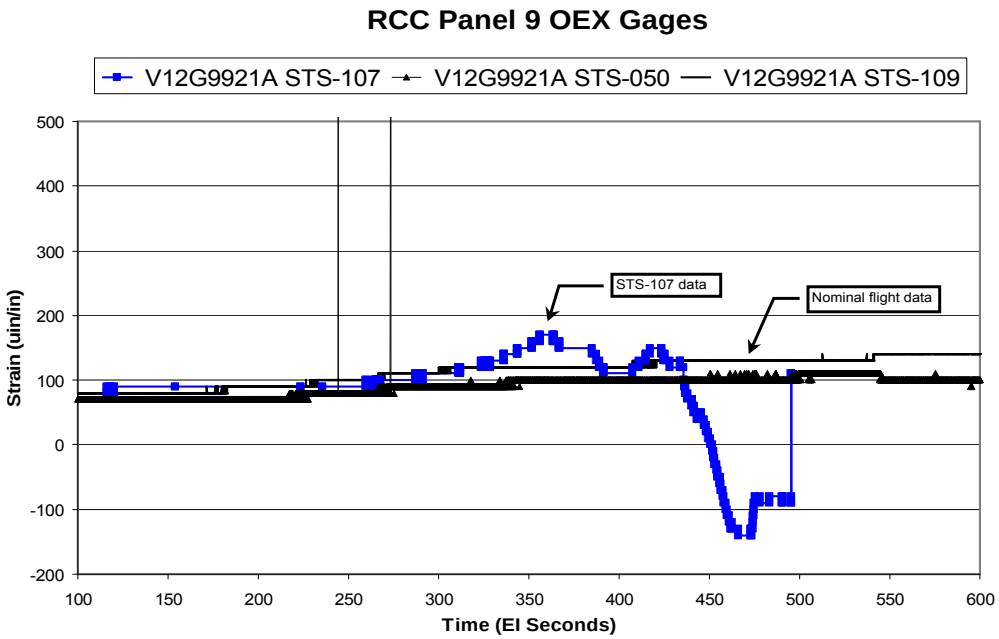

Figure 7.1-1 STS-107 V12G9921A strain gage data overlay with nominal strain gage flight data.

The two primary characteristics of the curve that need to be explained are the increase in shear strain with a sudden sign reversal. In addition to recreating the shear strain trends, interest was placed on how close to the thermal event would shear strain gage V12G9921A need to be to record the type of signal seen on STS-107. This gage is located roughly in the middle of the spar web near WLE panel 9. The thermal effects will register on the WLE spar strain gage even though it is some distance from the thermal event. Thermal sensors in the vicinity of panel 9 did not respond to a thermal event until much later. The quick response of the strain gage compared to the thermal sensors allows it to be used as a remote thermal sensor as shown in Figure 7.1-2. Near the boundary of a local thermal event, peak strains are expected because of the large thermal gradient. With increased distance from the thermal event the load will redistribute as illustrated and the influence of the thermally induced strain will eventually become negligible compared to the mechanical strain.

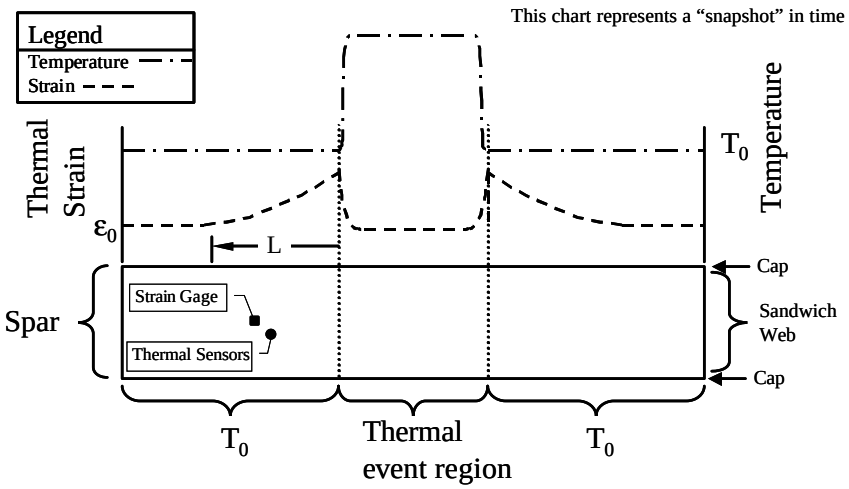

Figure 7.1-2 Temperature measurements lag strain measurements

7.1.2 Analytical Approach

A finite element model of the local wing area of interest was used because of the complex structural response to the thermal loading conditions. A total of 5 different assumed load cases were run. Initially a simple symmetric distribution was chosen. Because the strain gage is located near the middle of the WLE spar web, the shear strain response for a uniform thermal field is low. A number of unsymmetrical thermal fields were then analyzed, which created comparatively large shear strain responses similar to those seen during flight. The shear strain responses at the middle of the spar web were analyzed from the edge of the thermal event outward for each case. Based on the findings a possible scenario was then developed.

7.1.3 Model Description

The existing ASKA/NASTRAN loads finite element model of the wing was modified to perform a local analysis on the WLE spar. The coarse mesh on the original model in the WLE area near panel 9 was refined, as shown in Figure 7.1-3, to determine the local response of the structure to the thermal load cases being analyzed. In addition material properties were updated to include temperature dependent effects.

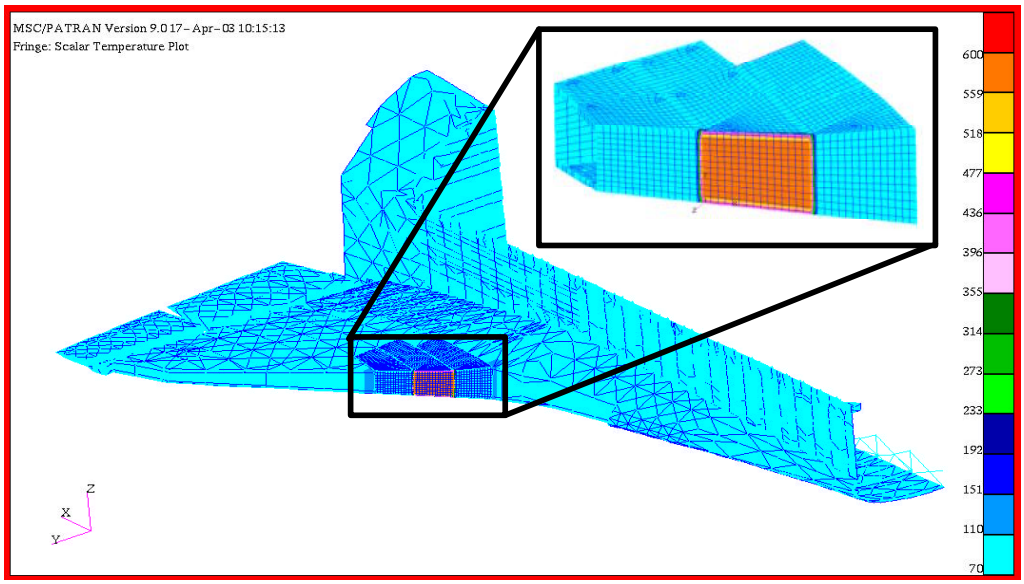

Figure 7.1-3 Refined region of wing used in thermally induced strain analysis

7.1.4 Thermal Profiles

Thermal profiles used in the analysis were assumed to be high heating events with large gradients between thermally protected and unprotected structure to induce large strain deviations from nominal flight data. A temperature of 600°F was chosen as the maximum temperature because reliable material properties were not available for higher temperatures. Also, since a uniform temperature region was used, this represented a reasonable average of temperatures ranging from melting of the aluminum (>900°F) to more moderate temperatures at the edge (400°F). Five different assumed thermal profiles were analyzed in developing the scenario.

Initially a temperature of 600°F was applied on WLE web while the spar caps were at 400°F. The rest of the structure was taken to be 70°F.

The second case assumed that the upper half WLE sees primary heating and it is initially heated to 300°F on upper half of WLE spar web and cap. Temperature from the middle of the WLE to the bottom of the WLE cap is linearly distributed from 300°F to 70°F and the rest of the structure is at 70°F. This case is an intermediate case between nominal heating and load case three.

For case three the upper half of the WLE sees continued primary heating up to 600°F on upper half of WLE spar web and cap with the temperature being linearly distributed from 600°F to 70°F at middle of WLE web to the bottom WLE cap. The rest of the structure is at 70°F.

For the fourth case a burn through is assumed on upper half WLE spar web. A temperature of 600°F is applied on upper WLE cap, wing skin, and wing ribs up to 16 inches from WLE. A linearly distributed temperature of 600°F to 70°F was applied from the edge of burn through (middle of WLE web) to bottom WLE cap. A temperature of 70°F was applied to the rest of structure.

The final case is a continuation of the fourth case. A burn through is now assumed on upper half WLE spar web and spar cap. A temperature of 600°F is applied on upper wing skin and wing ribs up to 16 inches from WLE. A linear temperature distribution of 600°F to 70°F from the edge of burn through (middle of WLE web) to bottom WLE cap is applied and the rest of the structure is sees 70°F. Contour plots of all five temperature profiles are shown in Figure 7.1-4 through Figure 7.1-7 below.

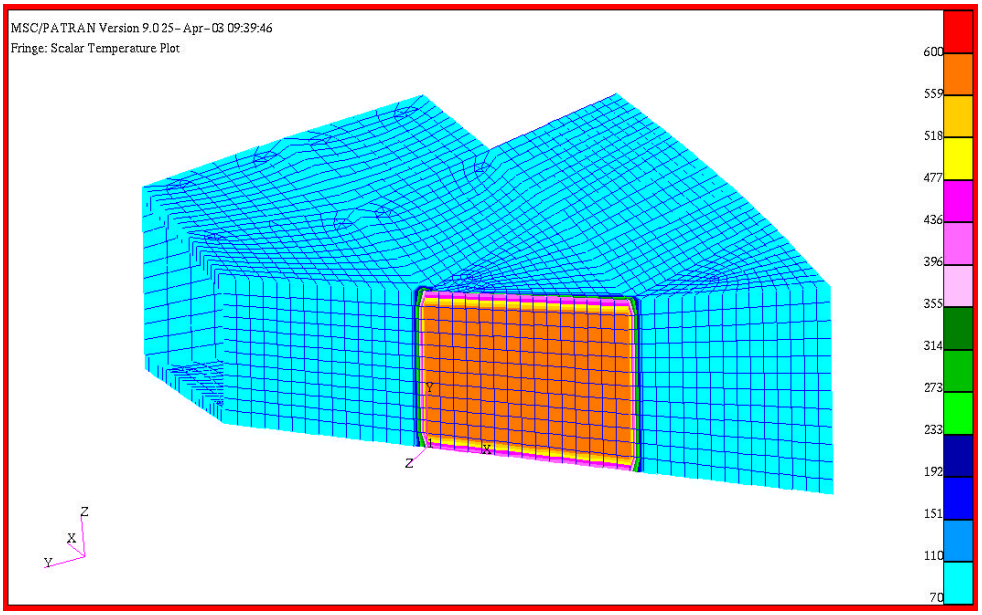

Figure 7.1-4 Contour plot of the initial symmetric temperature profile.

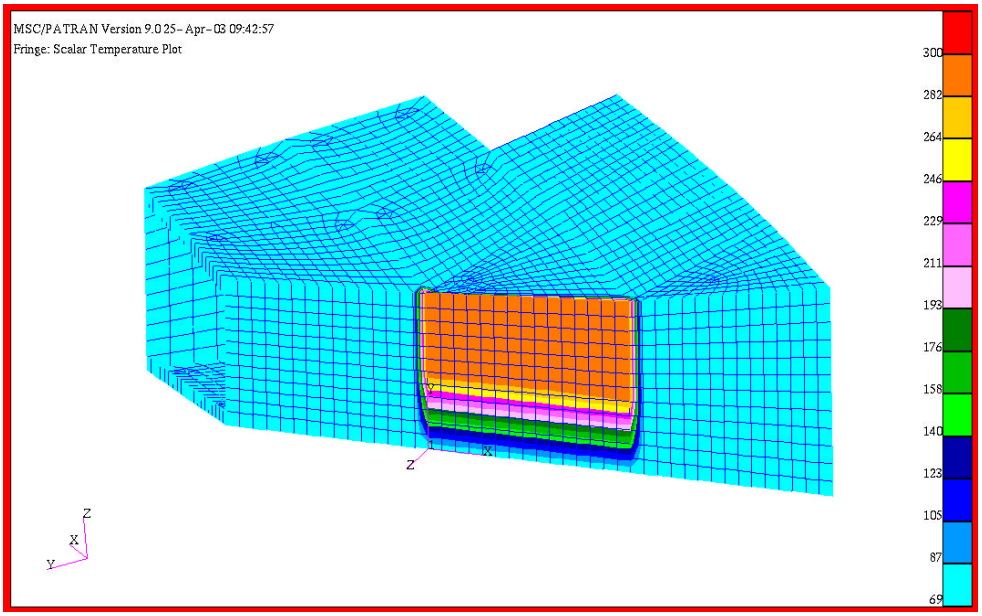

Figure 7.1-5 Temperature plot for the initial heating of WLE upper spar, second thermal profile.

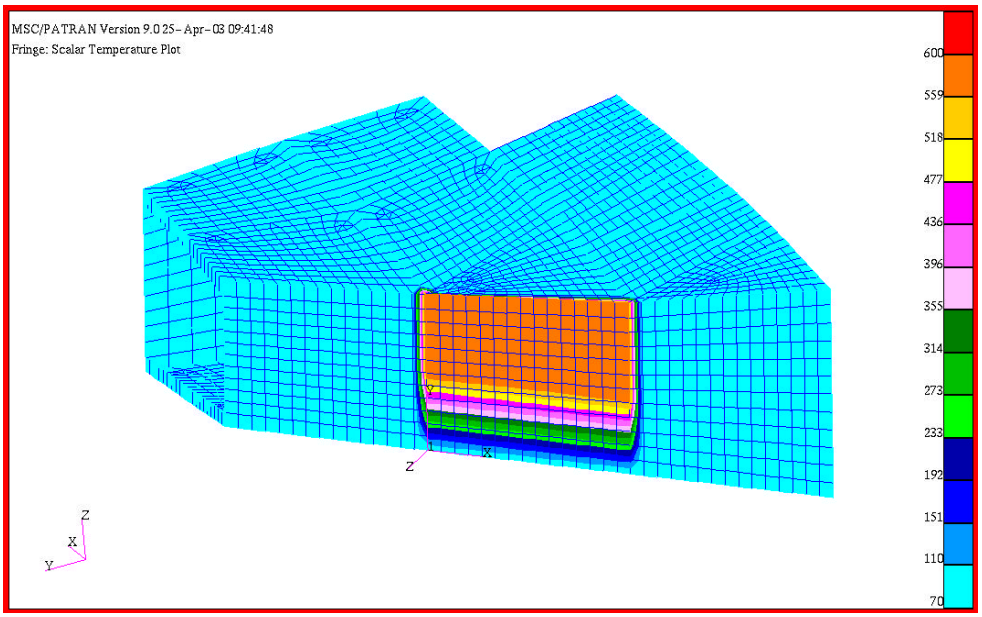

Figure 7.1-6 Contour plot for continued WLE upper spar heating, temperature profile three

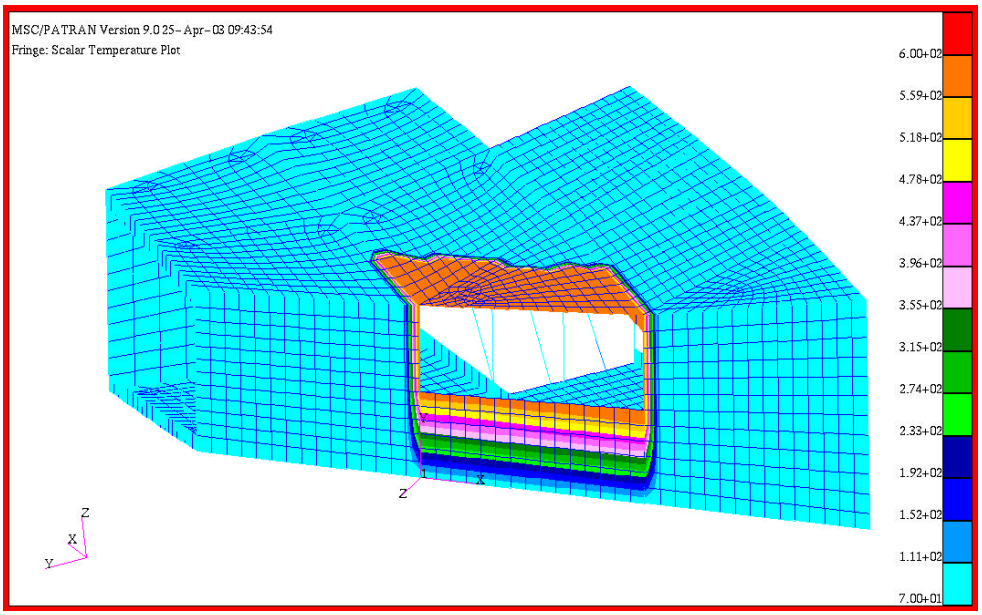

Figure 7.1-7 Temperature contour for WLE spar burn through, profiles four and five

7.1.5 Results

The shear strain results along the mid-span of the WLE spar outside of the thermal event for the five cases are shown in Figure 7.1-8 . The dashed lines on the chart show the amount of increase in shear strain that was seen during STS-107.

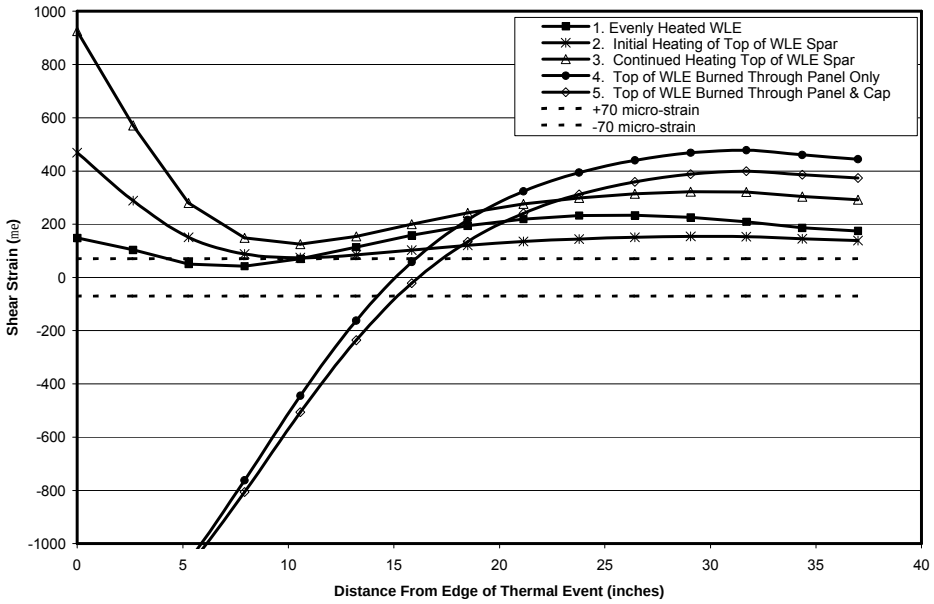

Figure 7.1-8 Shear strain results along midspan of WLE spar outside of the thermal event.

Thermal case one shows an increase in shear strain magnitude along the middle of WLE from the edge of thermal event outward but no significant magnitude. It is also noted that the sign remains the same for all locations plotted.

Thermal event two does show a significant rise in shear strain magnitude near the thermal event boundary that reduces with increased distance from the thermal event boundary. At distances greater than 18 inches from the thermal event boundary shear strain magnitude changes little. As with case one there is no change in sign of the shear strain at any distance from the thermal event.

Case three trends are very similar to case two trends but the magnitude of the shear strains has increased.

Case four produces the first reversal in shear strain sign. Even more than cases two and three there is a significant rise in shear strain magnitude near thermal event boundary. For distances less than 15 inches from thermal event boundary strain sign is negative. More importantly the shear strain from 15 to 19 inches reverses sign with magnitudes similar to the third case. There is a decrease in shear strain magnitude with increased distance from thermal event boundary as seen before. Shear strain magnitude changes little at distances greater than 26 inches from thermal event boundary.

Thermal event five is very similar to case four with increased magnitude. At distances less than 16 inches from the thermal event boundary the shear strain sign is negative and for the range of 16 to 23 inches from the boundary the shear strain is less than noted in the undamaged structure. With increased distance from the thermal event boundary the shear strain magnitude decreases and is relatively unchanging at distances greater than 26 inches from the thermal event boundary.

The results of cases four and five are significant findings. First it shows that a loss of the WLE spar structural capability is needed for a reversal of the shear strain sign seen on the gage. Additionally the results help bound the location of where the strain gage may be located. For both cases four and five sign reversals are see up to 15 or 16 inches away from the thermal event boundary, which establishes an outer limit location for this scenario.

7.1.6 Conclusions

Scenario Description

Based on the results of the five thermal cases coupled with previous OEX strain gage flight data, STS-107 strain gage and STS-107 thermal data, a possible scenario has been developed. It is hypothesized that a partial breech in a WLE RCC panel allowed hot gas impingement on WLE spar causing an unsymmetric temperature increase on WLE spar web and cap. The onset of this thermal event was slow to occur, probably due to the presence of WLE insulation, but caused shear strains to begin to deviate around 270 seconds as shown in a comparison to of STS-107 data with prior nominal flight data, Figure 7.1-9. The upper WLE spar web and cap were then subjected to heating and a temperature gradient occured on WLE spar from top to bottom. This increased shear strain gage readings until about 360 seconds from EI; during this time the structure remained intact. Shear strain data between approximately 360 to 400 seconds indicated the increasing temperatures were beginning to soften the structure but it was still carrying load in the heat affected region. Between 400 and 425 seconds there was a rise in shear strain that could be caused by heating at a second location closer to the strain gage; possibilities include a sudden loss of a large piece of insulation on the WLE spar or rapid temperature increase in the aft facesheet of the WLE sandwich panel. At 425 seconds, loss of structural capability was initiated causing the shear strain sign reversal. The loss could initially be attributed to debond on the facesheet of the WLE sandwich or significant loss of modulus (T>800°F) and, later, melting of the aluminum. Thermal stresses were relieved and the damage size continued to grow from this point on. The strain data is not considered reliable after about 470 seconds.

In summary, the main conclusion of this hypothetical scenario is that a loss of WLE spar structure is needed to reverse strain. Although this probably started as a facesheet debond or loss of modulus, it eventually proceeded to loss of the aluminum through melting. Secondly, the strain gage would need to be located in close proximity to the thermal event to record the type of signal seen for STS-107. For this scenario the strain gage would be located within 15” of edge of thermal as shown in Figure 7.1-8.

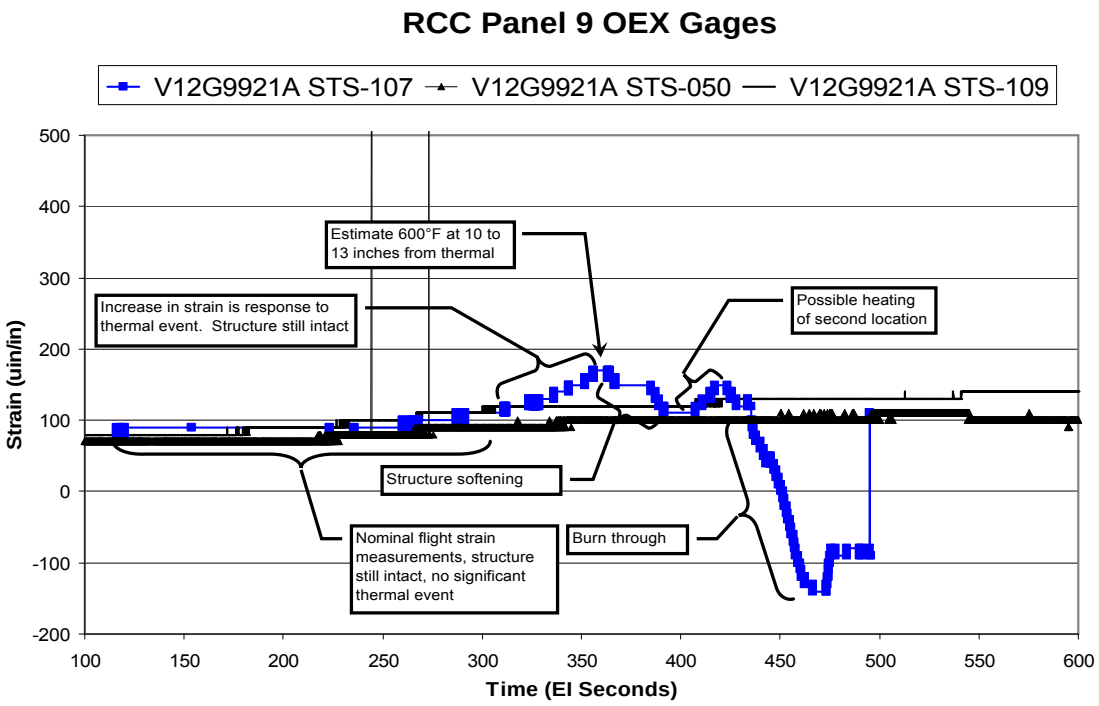

Figure 7.1-9 Scenario description overlay with nominal strain OEX strain gage data

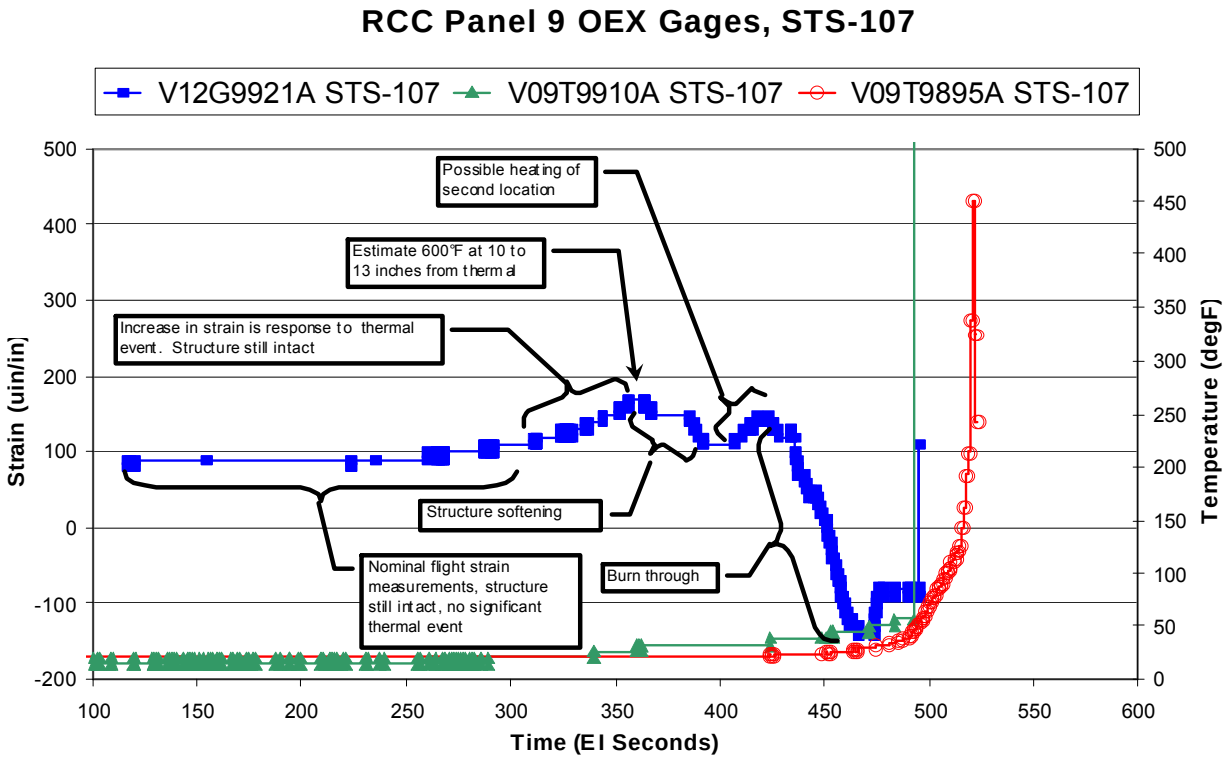

Figure 7.1-10 Scenario description overlay with STS-107 thermal flight data.

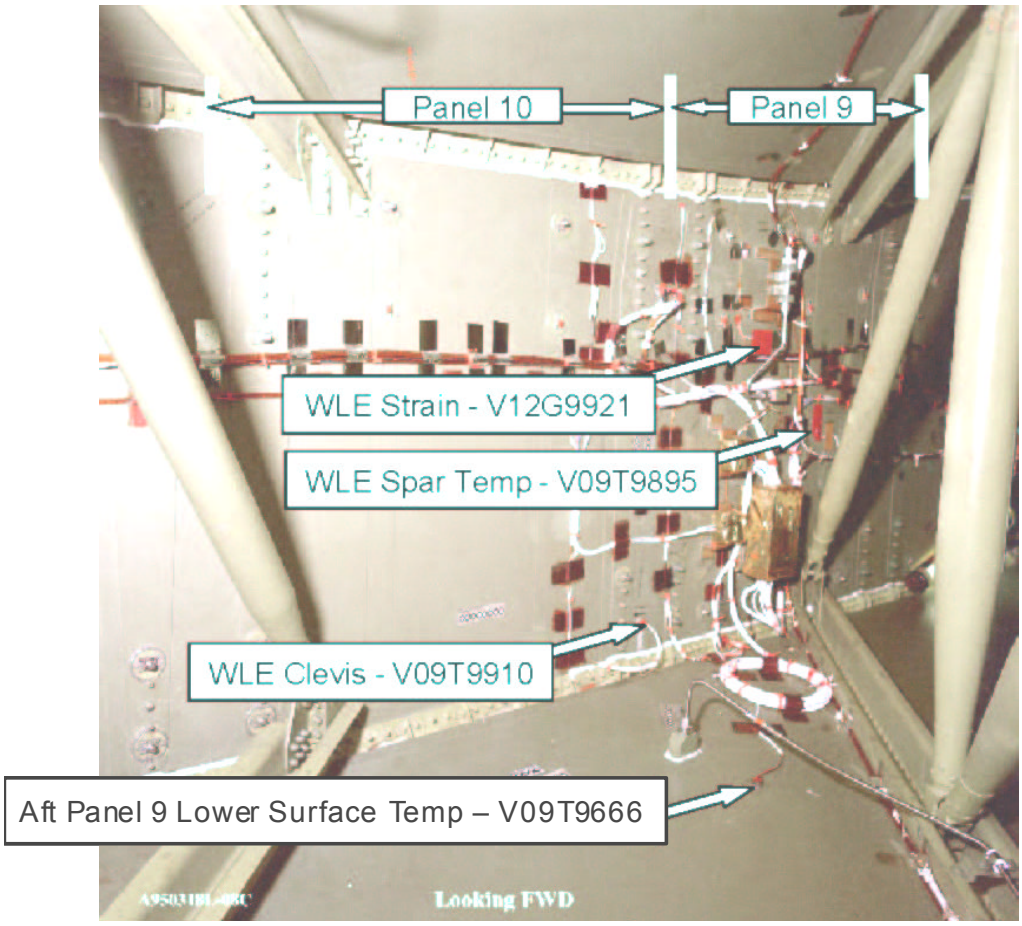

Figure 7.1-11 Location of WLE Strain Gage

7.2 1040 Spar Strain Gauge Evaluation

7.2.1 Analysis Objective

This analysis seeks to provide explanation for observed off-nominal strain signatures in gages V12G9048A and V12G9049A during STS-107 entry. Mechanical loading, pressure loading, load redistribution, thermally induced strain, and instrumentation malfunction were all considered as potential contributors. Strain due to local thermal effects in the region of the two gages is considered the most rational explanation, and is the primary focus of the analysis effort.

7.2.2 Analysis Inputs, Models, Assumptions, and Approach

7.2.2.1 Background

Axial strain gages V12G9048A and V12G9049A are located on the lower and upper caps of the left wing Xo1040 spar, respectively. The Xo1040 spar is the forwardmost of five major wing spars. Forward lies the wing glove area. Aft lie the main landing gear wheel well (behind the section of the spar inboard of the Yo167 rib), and the main wing cavity (behind the section of the spar outboard of the Yo167 rib). The outboard section of the spar includes a cutout that provides a path through to the main cavity of the left wing. There is also a cutout in the inboard section of the spar providing access to the MLG wheel well. Just forward of the Xo1040 spar on the Yo105 sidewall is a vent into the main fuselage. Figure 7.2-1 provides an illustration of the area.

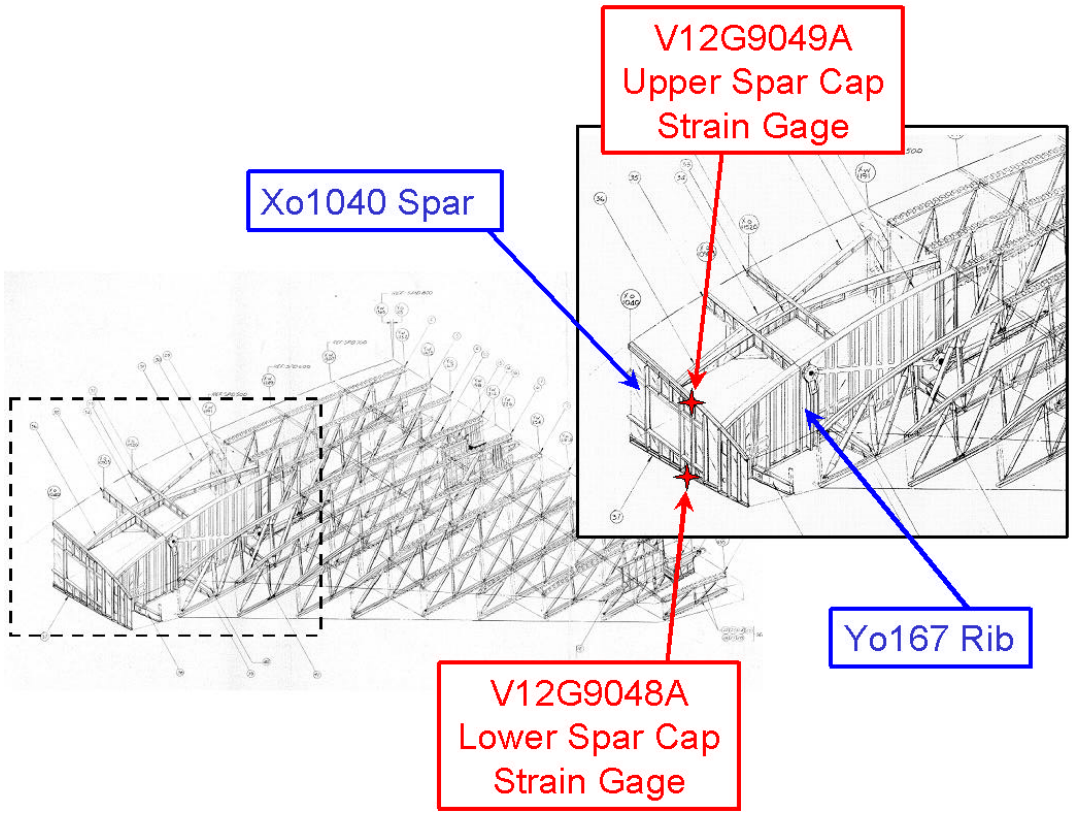

Figure 7.2-1 Xo1040 Spar Cap Strain Gage Locations

7.2.2.2 STS-107 Data Analysis & Reconstruction

As-recorded STS-107 data was refined in order to isolate suspected off-nominal behavior from nominal loading effects. To do so, a nominal profile, based on STS-109 (previous OV-102 flight) was compared with the recorded data. EI+488 seconds was chosen as an initial data point, up to which STS-107 data is considered nominal. The offset between STS-109 data and STS-107 data at this time was removed to generate a reconstructed nominal profile. Figure 7.2-2 illustrates the as-recorded STS-107 data versus the reconstructed nominal profile, based on STS-109.

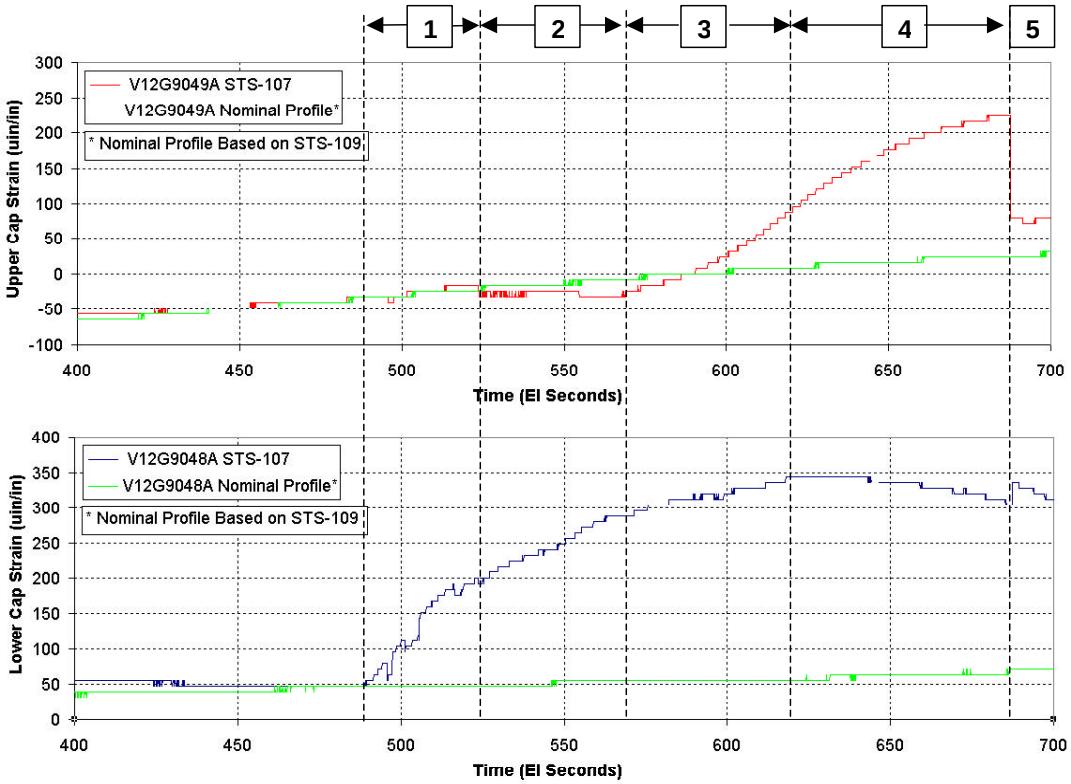

Figure 7.2-2 Observed STS-107 Strain Data versus Reconstructed Nominal Profile

Differentials between the nominal profile and the as-recorded profile represent strain values due to off-nominal loading during STS-107.

An illustration of the complete STS-107 Xo1040 spar cap strain data reconstruction is included for reference as Figure 7.6-2 of the Stress Appendix, Section 7.6.

The anomalous data profile has the following approximate timeline:

1. (EI+488 to EI+523 seconds)
   Minimal tension (8 µin/in) builds in the upper spar cap.
   Significant tension (152 µin/in) builds in lower spar cap.

2. (EI+523 to EI+569 seconds)
   Reversal causes minimal compression (-16 µin/in) in the upper spar cap.
   Tension continues to build to 232 µin/in in the lower spar cap.

3. (EI+569 to EI+618 seconds)
   Another reversal causes significant tension (72 µin/in) in the upper spar cap.
   Tension builds to a maximum (288 µin/in) in the lower spar cap.

4. (EI+618 to EI+687 seconds)
   Tension builds to a maximum (200 µin/in) in the upper spar cap.
   Tension reduces to 232 µin/in in the lower spar cap.

5. (EI+687 seconds)
   Instantaneous, high magnitude strain decrease (-144 µin/in) in the upper spar cap.
   Instantaneous, low magnitude strain increase (32 µin/in) in the lower spar cap.

Data following the instantaneous change at EI+687 seconds has not been conclusively verified as reliable strain data. There has been no instrumentation malfunction identified in these measurements at this time, or any time prior to EI+930 seconds. However, the instantaneous changes at EI+687 seconds are not considered rational from a real strain perspective. As such, there is no conclusive explanation for the instantaneous changes in strain values at that time. Without such an explanation, data beyond this point must be considered suspect, and therefore was not considered in the analysis that follows.

The observed off-nominal strain signatures during STS-107 are believed to be the result of instrumentation malfunction, thermally induced strain, or a combination of these two factors. Mechanical loading, pressure loading, and load redistribution were also evaluated as potential causes, but are believed to be unlikely explanations.

The primary evidence refuting mechanical loading, or more specifically, wing bending, is the agreement in sign between the off-nominal strains. That is, both the upper and lower caps show tensile loading. A nominal entry plot for these two gages from STS-109, included for reference as Figure 7.6-1 of the Stress Appendix, Section 7.6, illustrates that under significant wing bending loads in the TAEM portion of entry, the spar cap strains are of opposite sign; tension on the lower cap, compression on the upper cap. It should also be noted, however, that in the nominal profile, tensile loads exist in both spar caps during the period of entry in which off-nominal trends were recorded on STS-107. This phenomenon is attributed to the influence of upper skin heating, which generates a tensile effect in the upper cap that counteracts the mechanical compression load. The thermal effect on the lower cap is nominally much less pronounced.

An internal pressure load would not be consistent with the observed strain data, as the initiation times of off-nominal trends in the upper and lower spar caps, respectively, are not consistent with one another. Load redistribution also is largely unsupported by the data. The lower spar cap, for example, shows a reduction of tensile loading after EI+618 seconds, following the initial off-nominal rise. This would not be the expected behavior of a structure that had compensated for failure elsewhere by taking on additional load, namely as it would imply some sort of regaining of previously lost capability.

This evidence leaves localized thermal effects as the most reasonable explanation for the observed off-nominal strains. The analysis that follows considers thermal effects arising from intrusion of hot gas into the main wing cavity, which subsequently vents into the area in front of the Xo1040 spar. In combination with heating of the upper wing skin, due to breach into the main wing cavity and/or the MLG wheel well, localized heating in these regions could potentially give rise to temperature differentials that drive the observed spar cap strains.

7.2.2.3 Finite Element Model

The OV-102 Orbiter NASTRAN finite element model, based on the ASKA certification model, was used for assessment of localized heating. Selected FEM nodes were held at higher temperatures than others in order to produce thermally induced strain. FEM elements corresponding to the locations of the strain gages were then checked for strain response to the applied loads.

All elements in the model were assigned a default thermal expansion coefficient of a=0.000013/°F, and a default reference temperature of 70°F. Node temperatures by default were set to 70°F, with selected nodes raised to higher temperatures. It is important to note that the analysis does not attempt to model actual structural temperatures, but rather to gage structural response to local temperature differentials. The following structural areas were selected for application of local elevated temperature fields:

- Xo1040 Spar Web
- Xo1040 Upper Spar Cap
- Xo1040 Lower Spar Cap
- Wing Upper Skin, immediately forward of Xo1040
- Wing Lower Skin, immediately forward of Xo1040
- Wing Upper Skin between Xo1040 and Xo1090, Yo167 and Yo193
- Wing Lower Skin between Xo1040 and Xo1090, Yo167 and Yo193
- Wing Upper Skin between Xo1040 and Xo1090, Yo105 and Yo167
- Wing Leading Edge between Yw198 and Yw226 ribs
- Yo167 Rib Web between Xo1040 and Xo1098

Numerous combinations were run in order to assess the effects of different heating inputs on spar cap strains. These results were then compared to the observed strains to develop potential scenarios to explain the observed behavior.

Illustrations of the complete FEM, as well as specific areas of emphasis, are included for reference as Figure 7.6-3 to Figure 7.6-5 of the Stress Appendix, Section 7.6.

7.2.3 Results

The following table provides a qualitative summary of analyzed FEM cases and results:

Table 7.2-1 Qualitative FEM Results Summary

Case	Description	Upper Cap Reaction	Lower Cap Reaction
4A	Calibration (all nodes @ 70°F)	None	None
4B	Equal heating of spar web, forward upper and lower skins	Significant tension (20% higher than lower cap)	Significant tension
4C	Heating of outboard, aft, upper skin only	Significant tension	Very low tension
4D	Combined 4B and 4C	Significant tension (effects additive)	Significant tension (effects additive)
4F	Heating forward lower skin only	Very low compression	Significant tension
4G	Heating of WLE nodes	Very low compression	Low compression (2x upper cap)
4H	Heating of outboard, aft, lower skin only	Very low compression	Very low tension
4I	Heating of spar web nodes only	Very low tension	Low tension (2x upper cap)
4J	Heating of Yo167 rib sections	Very low tension	Very low tension
4L	Heating of upper spar cap only	Significant compression	Very low compression
4M	Heating of aft upper skin only	Significant tension	Very low compression

Numerical results from each of the load cases may be found in the Table 7.6-1 summary table of the Stress Appendix, Section 7.6.

The qualitative trends above were utilized to guide development of several temperature profiles that produce strains as observed in the STS-107 flight data. These profiles were screened versus scenario

evidence from the accident investigation team in order to define the most reasonable profile that could have produced the observed strains. The preferred profile, included in the scenario timeline that follows, corresponds to sequences 1-4 from the observed data timeline.

These results indicate that local temperature gradients on the order of 100-200°F could potentially explain the observed strains. These gradients may be consistent with scenarios involving hot gas intrusion from the wing cavity, passing in front of the Xo1040 spar enroute to the mid-fuselage, combined with heating of the wing upper skin just aft of the Xo1040 spar.

The major assumption of the selected temperature profile is that the lower spar cap has less heating than the structure around it; namely the upper spar cap, spar web, and wing skins immediately forward of Xo1040. The temperature rise in the lower spar cap thereby lags behind that of the adjacent structure and the upper spar cap. Note that sections A2 and A3 of the temperature profile indicate a transition from heating of the upper skin outboard of Yo167 to the upper skin atop the MLG wheel well, inboard of Yo167. This is one of a number of ways that a significant change in upper skin heating characteristics may be represented. The same effect could also be achieved, for example, by continued higher heating on the outboard section. It should be noted that the initiation of significant upper spar cap tension at this time is attributed to some substantial change in upper skin heating, but not necessarily by this particular means.

Scenario Timeline

1. (EI+488 to EI+523 seconds)
   Following WLE spar breach, hot gas vents into the region forward of the Xo1040 spar, providing heating to the spar web, nearby forward wing skins, and the upper spar cap. The lower spar cap temperatures lag behind the upper spar cap. Heating is also present in the upper wing skin just aft of the Xo1040 spar and outboard of the Yo167 rib.

2. (EI+523 to EI+569 seconds)
   Hot gas flow continues to drive temperature differentials in front of the Xo1040 spar, as the lower spar cap slowly begins to react. Heating to the upper wing skin outboard of Yo167 is effectively lost. Heating is now present only along skin at the top edge of the Yo167 rib.

3. (EI+569 to EI+618 seconds)
   Hot gas flow continues to drive temperature differentials in front of the Xo1040 spar. The lower cap is still slowly catching up. Breach into the MLG wheel well allows heating along the upper wing skin of the MLG well.

4. (EI+618 to EI+687 seconds)
   Xo1040 spar web, forward wing skins, and upper spar cap reach temperature equilibrium. Lower spar cap is slowly catching up, with continued heating of the upper wing skin above the MLG wheel well.

Table 7.2-2 Scenario Timeline FEM Results

Case	Description	Upper Cap Reaction	Lower Cap Reaction	Scenario
A1	+40°F applied to spar web, forward upper & lower skins, and upper spar cap +75°F applied to outboard, aft, upper skin	13 µin/in **(8 µin/in) (Recorded strain)**	146 µin/in **(152)**	Heating in front of spar and aft upper skin.
A2	+75°F applied to spar web, forward upper & lower skins, and upper spar cap +120°F applied to aft, upper skin along y167 rib +5°F applied to lower spar cap	-11 µin/in **(-16)**	225 µin/in **(232)**	Continued heating in front of spar and aft upper skin. Some heating in lower spar cap.
A3	+105°F applied to spar web, forward upper & lower skins, and upper spar cap +145°F applied to aft, upper skin above MLG wheel well +10°F applied to lower spar cap	73 µin/in **(72)**	291 µin/in **(288)**	Continued heating in front of spar and aft upper skin. Continued heating in lower spar cap.
A4	+105°F applied to spar web, forward upper & lower skins, and upper spar cap +190°F applied to aft, upper skin above MLG wheel well +20°F applied to lower spar cap	200 µin/in **(200)**	237 µin/in **(232)**	Thermal EQ in spar web, forward skins, and upper cap. Continued heating in lower cap. Continued heating of aft upper skin.

7.2.4 Conclusions

It is possible that the observed strains on V12G9048A and V12G9049A were a result of local thermal effects in the region of the Xo1040 spar. Given appropriate temperature gradients, the upper and lower spar caps are subjected to significant thermally induced strain, and could produce the observed strain gage signatures.

The STS-107 strain gage data offers some support for failure scenarios that involve intrusion of hot gas from the wing cavity into the glove area and/or the MLG wheel well. The timing of strain gage events shows some alignment with suspected breach times of the WLE and MLG well in these scenarios. Magnitudes of the observed strains, arising from local temperature gradients, could reasonably be generated by the suspected heat sources.

The strain gage data does not, however, conclusively indicate these scenarios. Numerous potential temperature profiles exist that would produce the observed strains. While a reasonable temperature profile has been suggested based upon corroborating evidence, this profile requires significant assumptions about the heat transfer properties of the local structure, the heat sources, and their combined ability to generate thermal gradients. A conclusive assessment would require conclusive identification of local structural temperatures, and significantly developed corroborating thermal analysis.

7.3 Overall Wing MADS Evaluation

7.3.1 Analysis Objective

This analysis compared recorded Modular Auxiliary Data System (MADS, a.k.a. OEX) wing strain gage measurements for STS-107 versus the same data for selected previous flights of the OV-102 vehicle. Both ascent and entry regimes were reviewed. Where appropriate, anomalous strain gage responses were identified, categorized, and in several cases, selected for additional in-depth analysis efforts.

7.3.2 Analysis Inputs, Models, Assumptions, and Approach

The OV-102 vehicle contained significantly greater MADS wing strain gage instrumentation than other vehicles in the STS fleet. There were 247 total strain gages available on the wings (Gage MSIDs begin with V12G); 121 of these gages were on the left wing, with the remaining 126 on the right. Additionally, 52 gages were located on the elevon structure, divided equally with 26 on each side of the vehicle (Gage MSIDs begin with V13G). In general, strain gage locations were symmetric between the two sides of the vehicle. Figure 7.6-23 and Figure 7.6-24 of the Stress Appendix, Section 7.6 illustrate strain gage locations on the vehicle. References in section 7.7 list relevant installation drawings.

OV-102 MADS strain gage data was recorded on three Pulse Code Modulation (PCM) data channels. Wing gages associated with channels PCM1 and PCM2 had continuous data recording at 10 samples per second for both ascent and entry flight regimes. There were 131 wing strain gages (45 left wing, 86 right wing) on channels PCM1 or PCM2. Gages associated with channel PCM3 had continuous 10 samples per second data recording during the ascent flight regime. During entry, PCM3 gage data was recorded in “snapshot mode” at periodic 1-minute-on, 4-minutes-off intervals (data rate during on-time was 10 samples per second). Elevon gages (PCM1 for right wing, PCM2 for left wing) had continuous data recording at 10 samples per second for the ascent regime. For entry, 20 of 52 gages (10 on each side) had continuous recording. The remaining 32 gages (16 on each side) were recorded in snapshot mode.

Seven previous OV-102 flights were selected for comparison with STS-107. These selections were made based upon similar mass properties and similar inclinations, starting with the most recent flights. Comparison flights were as follows:

STS-109, STS-093, STS-090, STS-087, STS-094, STS-073, and STS-050.

Comparison plots showing STS-107 data versus each of these previous flights were generated using in-house tools developed specifically for the STS-107 accident investigation. Comparison plots showed the entire duration of the ascent regime, and the first seventeen minutes of the entry regime, beginning at entry interface. This time frame includes all available data for STS-107, prior to loss of the vehicle and the end of data recording.

Comparison plots for each of the MADS strain gages were individually reviewed and assessed. Where appropriate, tabular point-by-point data was extracted, and additional analysis performed. Trends amongst gages were assessed, and gage response categories were defined.

7.3.3 Results

7.3.3.1 Ascent

All STS-107 MADS PCM strain data, without exception, was nominal during the ascent flight regime. No significant anomalies were noted. Comparison of ascent strain gage load indicators showed STS-107 ascent loads to be within the family of previous OV-102 flight experience. There was no discernable evidence of an impact load to the vehicle near MET +81.7 seconds. At the PCM sample rate of 10 samples per second, no such evidence is expected to be present. Both the extremely short duration of the impact load (0.003 to 0.005 seconds), and the range of wing modes (6 Hz and above) preclude such evidence. An interesting signature near this time was evident in some strain gages. The response was noted on left wing, right wing, and vertical tail gages. Further study and scrutiny showed that the signature was inconsistent with impact loading, and attributable to a nominal ascent load response. A review of accelerometer data did show signatures consistent with impact loading. This assessment is discussed in Section 7.4.

For reference, a typical PCM ascent strain gage comparison plot is shown in the Stress Appendix, Section 7.6, as Figure 7.6-6. Figure 7.6-7 illustrates the interesting signature noted near the suspect debris impact event, in comparison to data from STS-109, the previous flight of OV-102.

7.3.3.2 Entry - General

Comparison plots for the entry flight regime showed STS-107 data to be appreciably off-nominal versus previous flight experience after EI+490 seconds. Numerous anomalies were noted, most significantly on the left wing and elevon gages.

Due to the snapshot mode data recording on channel PCM3, data for these strain gages was largely not helpful in providing significant inputs to the analysis effort. Without continuous data, reliable conclusions regarding structural responses were not possible. Where possible, implications of off-nominal trends were identified, and data provided to the timeline team. This was the extent of the analysis effort for PCM3 strain gages.

Two sample PCM3 plots are included in the Stress Appendix, Section 7.6. Figure 7.6-8 shows a typical PCM3 comparison plot. Figure 7.6-9 illustrates a PCM3 gage with an apparent off-nominal trend.

The analysis effort focused on PCM1 and PCM2 gages that provided continuous data during the entry flight regime. This includes all PCM1 and PCM2 gages on the left and right wings, and 20 gages (10 on each side) on the elevon structure.

Loading levels during the initial stages of entry, prior to observation of significant off-nominal trends, were nominal as compared to previous flight experience. Maximum entry loading levels are nominally recorded during the TAEM region of flight, as shown by example in Figure 7.6-21.

7.3.3.3 Entry - Right Wing

In general, right wing strain gages showed nominal responses on STS-107 versus previous flights until immediately prior to loss of data (approximately 930 seconds after entry interface). Most, 49 of 85, right wing gages show this typical, nominal response, along with 8 of 10 right wing elevon gages. A sample plot is included for reference as Figure 7.6-10.

There were 19 right wing gages that show evidence of a brief, low magnitude off-nominal response initiating at EI+500 seconds. This signature is characterized by a 1 or 2 bit discrepancy versus previous flight experience, lasting as long as approximately 30 seconds. Following this time, strain values return to nominal tracking. This response was also noted on two right wing elevon gages. No instrumentation

malfunction has been identified in these gages at this time. The only reasonable hypothesis from a real strain perspective is internal pressurization following initial breach of the wing leading edge spar (both wings and the mid-fuselage share common venting). However, this hypothesis would not be consistent with the almost immediate return to nominal readings. The source of this phenomenon therefore is not conclusively understood at this time. A sample plot is included for reference as Figure 7.6-11.

There were 17 right wing gages that show an off-nominal response, initiating near EI+500 seconds, which creates a subsequent data offset versus previous flight experience. This signature is characterized by an off-nominal slope change of approximately 120 seconds duration, followed by a return to nominal tracking with a built-in offset, up to the loss of data. Again, this phenomenon may be explained by a transient internal pressurization effect, instigated by initial WLE spar breach, and relieved by a secondary external breach that subsequently reduces internal pressure. No instrumentation malfunction has been identified in these gages at this time. A sample plot is included for reference as Figure 7.6-12.

One right wing gage, V12G9653A (right wing upper skin at Xo1218, Yo245) showed a nominal response during ascent, but had no data recorded for entry. This gage is presumed to have failed at some point during the on-orbit period of STS-107. This type of on-orbit gage failure is not unusual in previous flight experience.

7.3.3.4 Entry - Left Wing

In contrast, the majority of left wing gages show indications of failure initiating between EI+486 seconds and EI+590 seconds. The vast majority, 42 of 45, of left wing gages, and all 10 left elevon gages show this typical response. The gage failure signature is characterized by sudden, rapid slope change driving strain to off-scale band edge values. In many instances, the gage signature oscillates between off-scale high and off-scale low values before settling at a “flatline”, steady-state response. This steady-state value is dictated by the instrumentation bias of a particular gage, and may or may not equal zero. Numerous gages show an off-nominal slope change that significantly precedes the dramatic off-scale event. The off-scale event, as well as the preceding off-nominal slope change, is attributed to burning of the strain gage wiring. These events are not consistent with literal strain responses to mechanical, thermal, or pressure loading. No significant correlation was found between strain gage location on the vehicle and initiation time of strain gage failure, as illustrated in Figure 7.6-22.

Significant unpredictability in the burning phenomenon dictates that individual gages show unique manifestations of the failure event. For example, not all gages “flatline” following the off-scale excursions. The period or number of oscillations between upper and lower band edge values also is variable from gage to gage.

Following the initial off-scale excursion, or off-nominal inflection toward such an excursion, strain gage data is considered invalid, due to the wire burning condition. Subsequent data therefore is an indication only of the wire-burning phenomenon, and not of structural strain gage responses.

Several representative samples of left wing and left wing elevon strain gage failure comparison plots are included for reference in the Stress Appendix, Section 7.6. Please refer to Figure 7.6-13 through Figure 7.6-17.

The remaining three left wing strain gages were the subjects of significant additional analysis effort. V12G9921A, located on the wing leading edge spar near RCC panel #9, showed the earliest off-nominal response of any strain gage, initiating near EI+270 seconds. Numerous slope changes and a change in sign of the strain value followed, prior to initiation of a gage failure signature after EI+470 seconds. Off-nominal strain values for this measurement are attributed to localized, thermally-induced strain and structural failure. This analysis is discussed separately in Section 7.1. The comparison plot for V12G9921A is included for reference as Figure 7.6-18.

Gages V12G9048A and V12G9049A, located on the lower and upper Xo1040 spar caps, respectively, in the center of the wheel well forward wall (Yo135) were the only two left wing gages that did not clearly indicate failure prior to EI+930 seconds. As these gages did not join wire bundles until just prior to

penetration of the mid-fuselage sidewall, this data would suggest an absence of direct plume impingement in the glove area forward of the wheel well. Both of these gages showed significant off-nominal trends, however, at earlier times. V12G9048A showed initiation of an off nominal trend at EI+489 seconds, which continued to the loss of data. Likewise, V12G9049A first showed initiation of an off-nominal trend at EI+568 seconds, again continuing until loss of data. These off-nominal trends are likely attributable to local thermal effects, possibly combined with instrumentation malfunction, as discussed separately in Section 7.2. Comparison plots for V12G9048A and V12G9049A are included for reference as Figure 7.6-19 and Figure 7.6-20, respectively.

7.3.4 Conclusions

Comparison of STS-107 MADS PCM strain gage data to previous flight data offers strong evidence and support for the STS-107 accident investigation. Specifically, the strain data offers support for failure scenarios with breach of the wing leading edge spar outboard of the Yo167 rib.

PCM strain gage data from the ascent regime shows no indications of off-nominal structural loads. Load levels for ascent are within the family of previous OV-102 flight experience.

During the entry regime, significant off-nominal behavior was identified. This off-nominal behavior is attributed primarily to combined influences of instrumentation failure and localized off-nominal thermal effects.

The typical left wing entry signature is indicative of instrumentation failure due to burning of wires inside the left wing. This failure pattern corroborates wire bundle burn-through scenarios developed in the previous analysis of telemetered OI data.

Significant early off-nominal strains in V12G9921A provide evidence of localized thermal effects in the area of RCC Panel #9.

Gages V12G9048A and V12G9049A, unlike all other left wing strain gages, do not show clear indications of instrumentation failure prior to loss of data. These two gages' wiring join bundles further forward than all other strain gages. Again, this data supports evidence of wire burning in the main left wing cavity. Off-nominal strains due to local thermal effects in these gages provide further clues regarding hot gas venting following initial intrusion into the left wing cavity.

7.4 Accelerometer Evaluation

Accelerometer and higher sample rate strain gage responses during STS-107 are studied during ascent and entry phases of the flight to identify any anomalous response. They were also compared to STS-109 and other OV-102 flight data to determine if the responses are within the family experience.

7.4.1 Ascent

The locations of the accelerometers are shown In Figure 7.4-1. They include 15 accelerometers on the wing/elevons, body flap and vertical tail/rudders, and 11 measurements on the longeron. In addition, there are 36 strain gages in the vertical tail and OMS deck area.

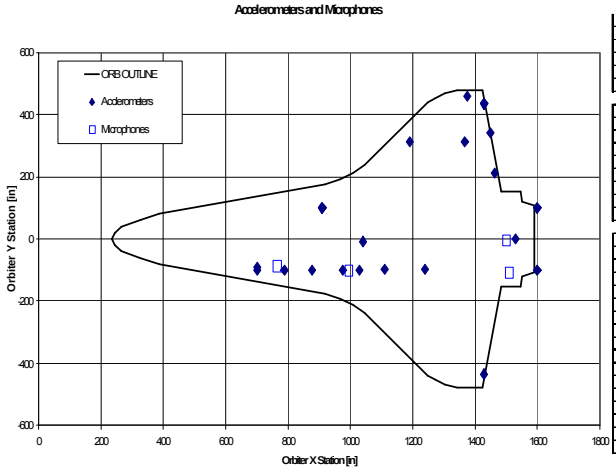

MISD	DFI	NOMENCLATURE	X	-Y	Z
		Microphones			
V08Y8006A	MADS	LH PAYLOAD BAY VENT #3 X765	765.3	-86.5	382.6
V08Y8039A	MADS	PAYLOAD BAY LH VENT NO 5 X994	994.0	-100.0	
V08Y9684A	MADS	AM ON HT SHLD Y-100 Z320 MAF004	1510.1	-107.3	316.4
V08Y9686A	MADS	AM AFT FUS HS CTR YO Z400 MAF006	1499.6	-2.4	384.9
		Accelerometers			
V34A9432A	MADS	LH LNGN ACCEL Z-AXIS X976	976.5	-101.5	407.5
V34A9460A	MADS	LH LNGN ACCEL Y-AXIS X701	701.2	-100.8	407.0
V34A9461A	MADS	LH LNGN ACCEL Z-AXIS X701	701.2	-91.3	407.5
V34A9464A	MADS	LH LNGN ACCEL Z-AXIS X877	877.2	-101.3	407.5
V34A9481A	MADS	KEEL ACCEL V-AXIS X1040,Y=0	1040.0	-8.5	LWR
V34A9482A	MADS	LH LNGN ACCEL Z-AXIS X790	788.3	-101.3	407.5
V34A9483A	MADS	LH LNGN ACCEL X-AXIS X1029	1029.0	-101.3	407.7
V34A9484A	MADS	LH LNGN ACCEL Z-AXIS X1110	1110.0	-96.8	407.3
V34A9485A	MADS	LH LNGN ACCEL Z-AXIS X1229	1238.7	-97.0	407.5
		Accelerometers			
V08D8037A	MADS	RH LONGERON Y-AXIS VIB	910.0	99.4	409.0
V08D8038A	MADS	RH LONGERON Z-AXIS VIB	910.0	99.4	409.0
V08D9062A	MADS	LFAF BF AFT-R Z-VIB AOB-16	1600.0	100.0	
V08D9063A	MADS	LFAF BF AFT-L Z-VIB AOB-17	1600.0	-100.0	
V08D9064A	MADS	LFAF BF HL CTR Z-VIB AOB-18	1530.0	0.0	
V08D9699A	MADS	LFAF L OTBD ELEV OTBD Y-VIB	1429.4	435.0	
V08D9729A	MADS	LFAF R OTBD ELEV OTBD Z-VIB	1428.6	-435.0	
V08D9737A	MADS	LFAF R OTBD ELEV OTBD Z-VIB	1428.6	435.0	
V08D9738A	MADS	LFAF R OTBD ELEV INBD Z-VIB	1449.1	342.5	
V08D9764A	MADS	LFAF R WING TIP AFT Z-VIB	1376.0	460.0	
V08D9765A	MADS	LFAF R WING OTBD-MID Z-VIB	1191.0	312.5	
V08D9766A	MADS	LFAF R WING X1365,Y312 Z-VIB	1367.0	312.0	
V08D9784A	MADS	LFAF R INBD ELEV-CTR Z-VIB	1462.6	212.0	
V08D9694A	MADS	LFAF V/S RSS262 A SPAR Y-VIB	1569.9	LH	710.0
V08D9789A	MADS	LFAF V/S RSS158 F SPAR Z-VIB	1459.9		671.5
V08D9795A	MADS	LFAF R SP BK UPR BOT Y-VIB	1620.9	RH	633.0
V08D9797A	MADS	LFAF R SP BK LWR TOP Y-VIB	1600.4	RH	593.2

Figure 7.4-1 Measurement Locations

In general, the responses from STS-107 and STS-109 are very similar for the most part. Shown in Figure 7.4-2 is a comparison of typical accelerometer responses. The magnitude is very comparable throughout the flight. The large amplitude responses at near M=1 are also very similar. (The peak response noted at ~82 seconds will be discussed later in detail) The RMS (Root Mean Square) values of all accelerometers for wing and tail accelerometers are shown in Table 7.4-1 and illustrate the overall amplitude is very similar. The PSD's of three measurements (Left outboard elevon, Right wing tip, Body flap) are shown in Figure 7.4-3. The results computed using 20-80 second data block demonstrate no significant change in the magnitude and frequency contents between the two flights.

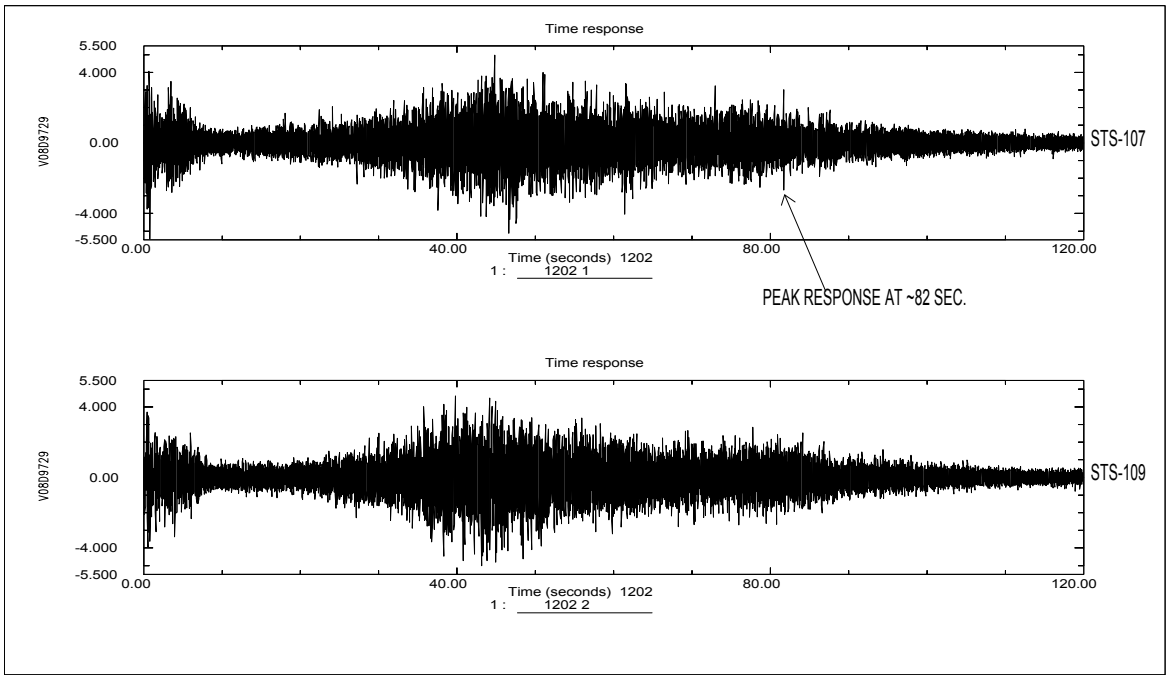

Figure 7.4-2 Comparison of Left Outboard Elevon Response (STS-107 VS. STS-109)

Table 7.4-1 Summary of RMS Acceleration

	T= 0-120 sec		T= 20-80sec.	
	STS107	STS109	STS107	STS109
VO8D9729A (L. OB Elevon)	.74	.78	.92	.98
VO8D9737A (R. OB Elevon)	.75	.75	.95	.95
VO8D9738A (R. OB Elevon)	.78	.75	.99	.95
VO8D9784A (R. IB Elevon)	.91	.90	1.23	1.22
VO8D9764A (R. Wing)	.73	.74	.92	.92
VO8D9766A (R. Wing)	.42	.41	.52	.51
VO8D9765A (R. Wing)	.35	.35	.40	.39
VO8D9064A (Body Flap)	.74	.85	.96	1.09
VO8D9062A (Body Flap)	3.51	3.79	4.85	5.09
VO8D9063A (Body Flap)	1.74	1.78	2.03	1.90
VO8D9699A (Vertical Tail)	.40	.36	.44	.37
VO8D9795A (Upper R. Rudder)	.52	.52	.68	.67
VO8D9694A (Vertical Tail)	.30	.28	.38	.33
VO8D9789A (Vertical Tail)	.43	.39	.52	.44
VO8D9797A (Lower R. Rudder)	---	---	---	---

Left Outboard Elevon Accelerometer

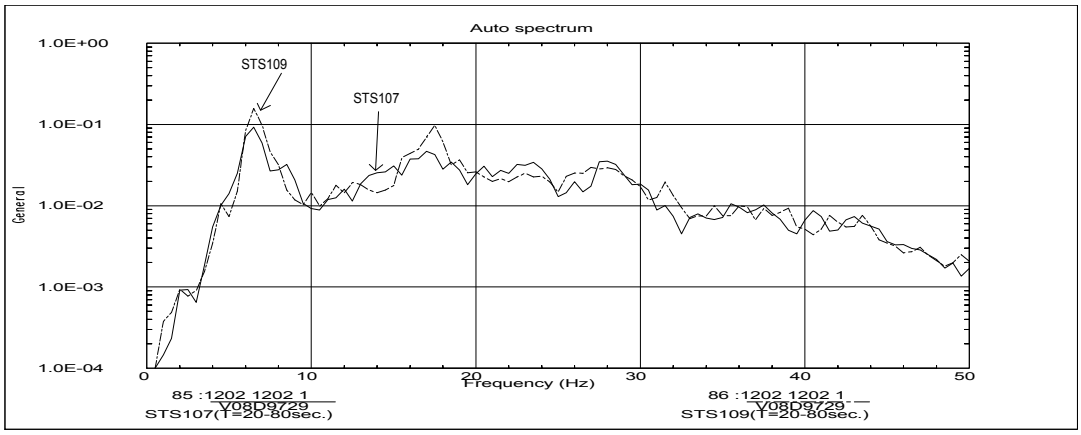

Right Wing Tip Accelerometer

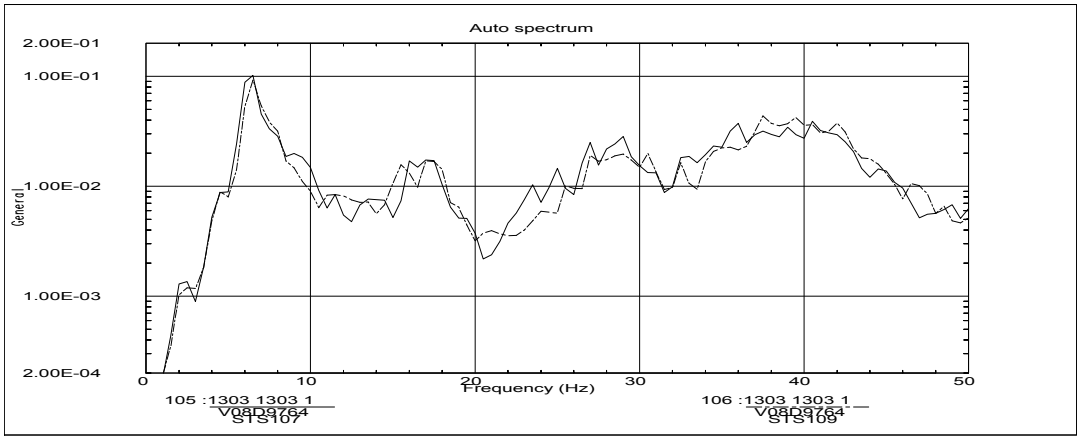

Body Flap Accelerometer

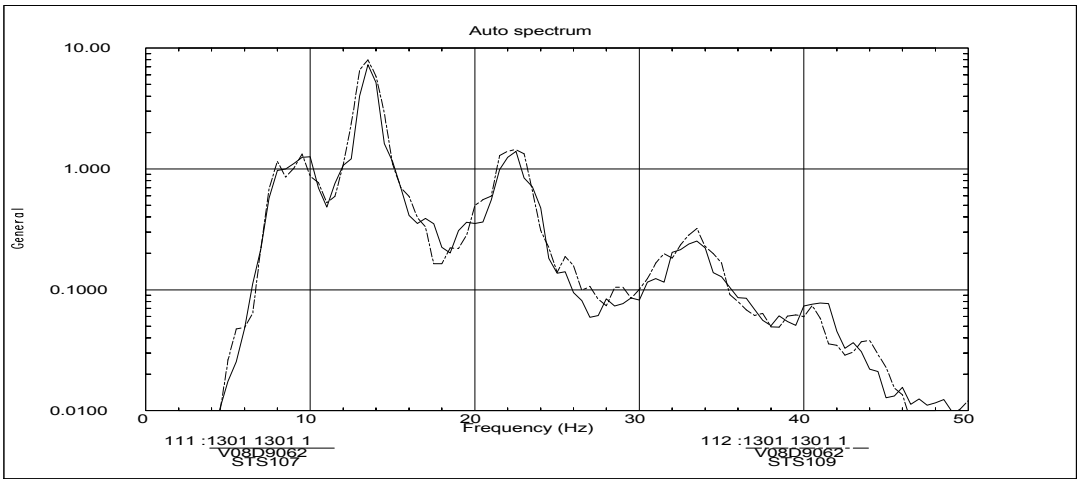

Figure 7.4-3 PSD's Comparison (STS-107 VS. STS109)

The only notable differences in the RMS acceleration are the three tail accelerometers, which are highlighted in the table. They show approximately 15-20% higher response during STS-107 compared to STS-109 results. The reason for the increase is the difference in the tail response near 40-42 second range, as noted in Figure 7.4-4. The PSD's during this time period shown in Figure 7.4-5 verify significantly higher response of the tail's 2nd and 3rd bending modes at the 20 to 40 Hz range.

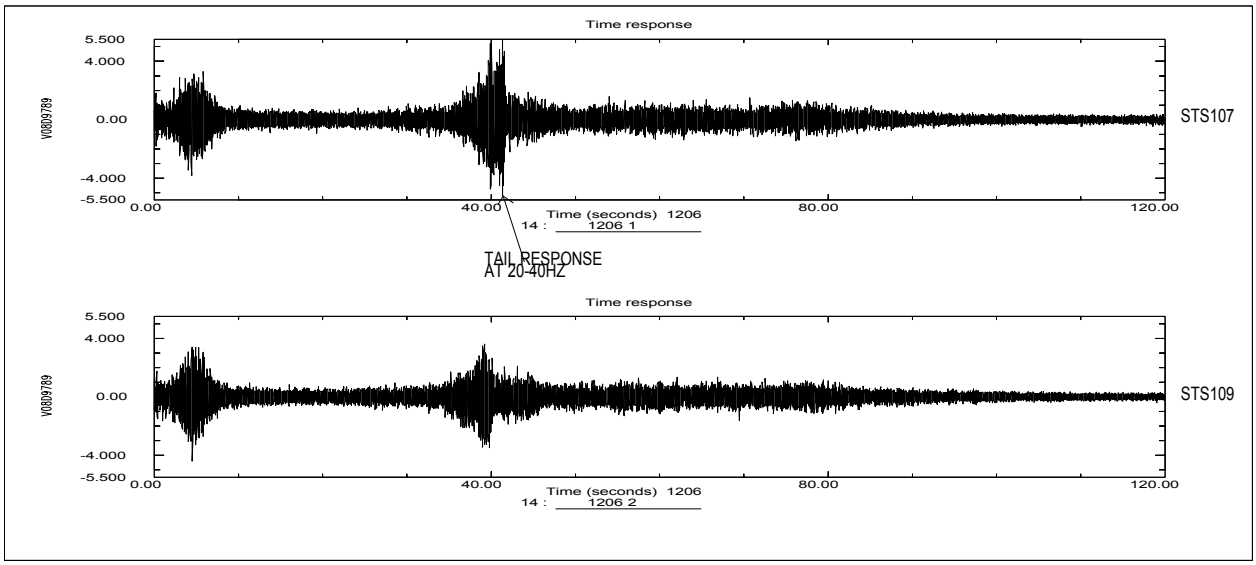

Figure 7.4-4 Vertical Tail Response during Ascent (STS-107 VS. STS-109)

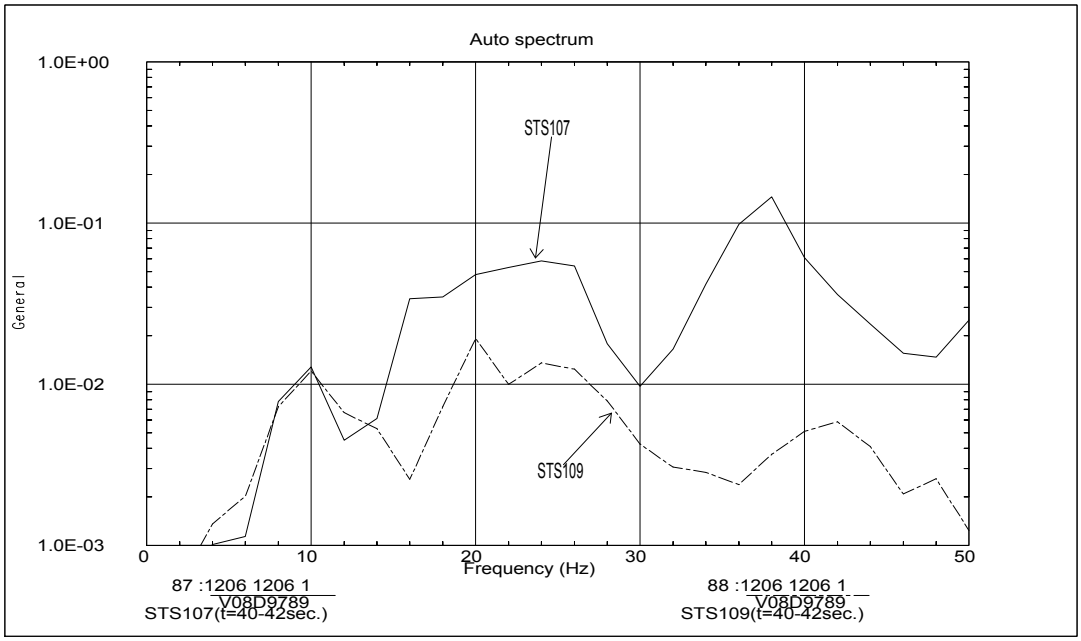

Figure 7.4-5 PSD Comparison of Vertical Tail Response at T=40-42 sec. (STS-107 VS. STS-109)

This type of variation in response is considered a normal behavior of tail reacting to buffeting environment near M=1, where the turbulent effect of the air is the greatest. The degree of turbulence level and the frequency content in air flow can vary flight to flight, which can result in different types of modes being excited. A similar characteristic was observed during STS-87 as presented in Figure 7.4-6. The PSD's from two flights are remarkably similar in magnitude and frequency contents. The results indicate the excitation of higher order tail mode during STS-107 is not unique and is considered within the family experience.

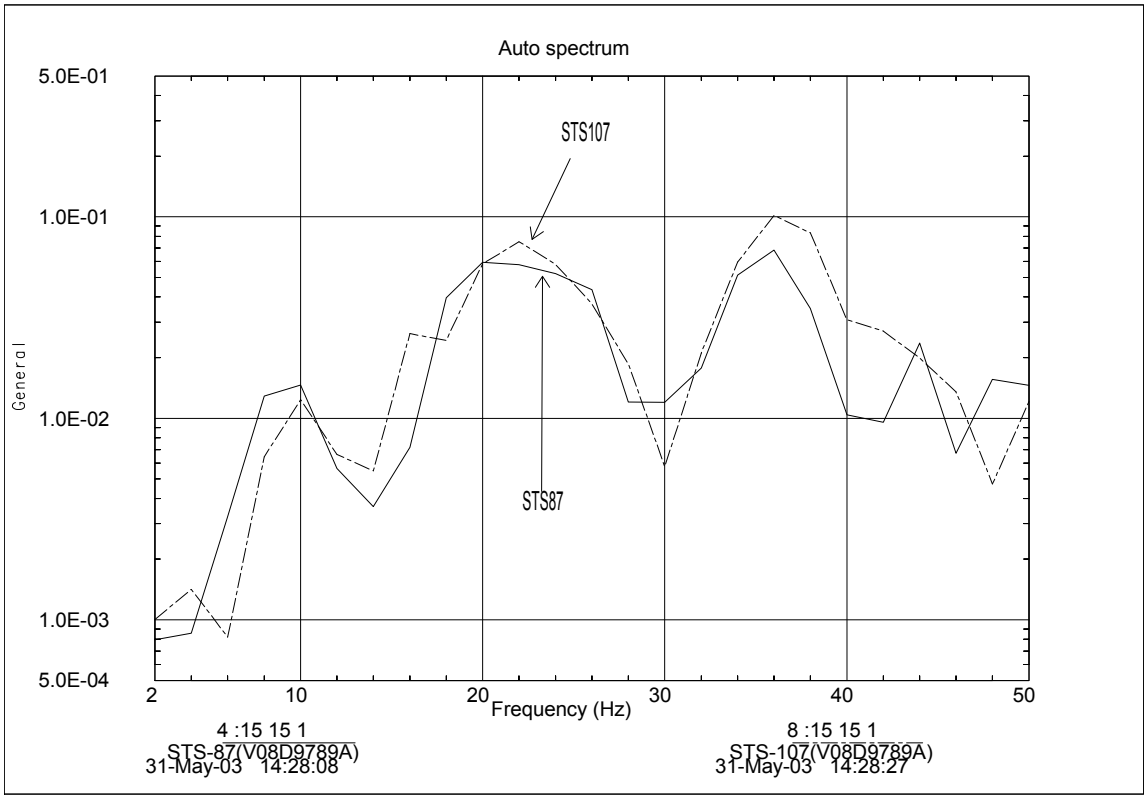

Figure 7.4-6 PSD Comparison of Tail Responses (STS-107 VS. STS-87) (T=40-42 sec.)

7.4.1.1 Evaluation of Peak Response at ~82 Seconds

An in-depth study was made to investigate if the peak responses observed at the left outboard elevon accelerometer at ~82 seconds is due to the debris impact. Normally, sharp spikes in acceleration are observed at times during the ascent phase of the flight due to buffeting event(s). The buffeting load is most significant during the transonic region. However, it still exists at higher Mach numbers, which results in structural excitation. Shown in Figure 7.4-7 is the left and right outboard elevon comparison for the 10 second period near 82 seconds. The peak response is noticeable only for the left outboard location. Filtered responses presented in Figure 7.4-8 verify several wing/elevons were excited at 82 seconds. The 2nd wing bending response constitutes the largest component of the peak amplitude. In addition, the responses of 3rd wing bending and elevon torsion modes contributed to the peak response.

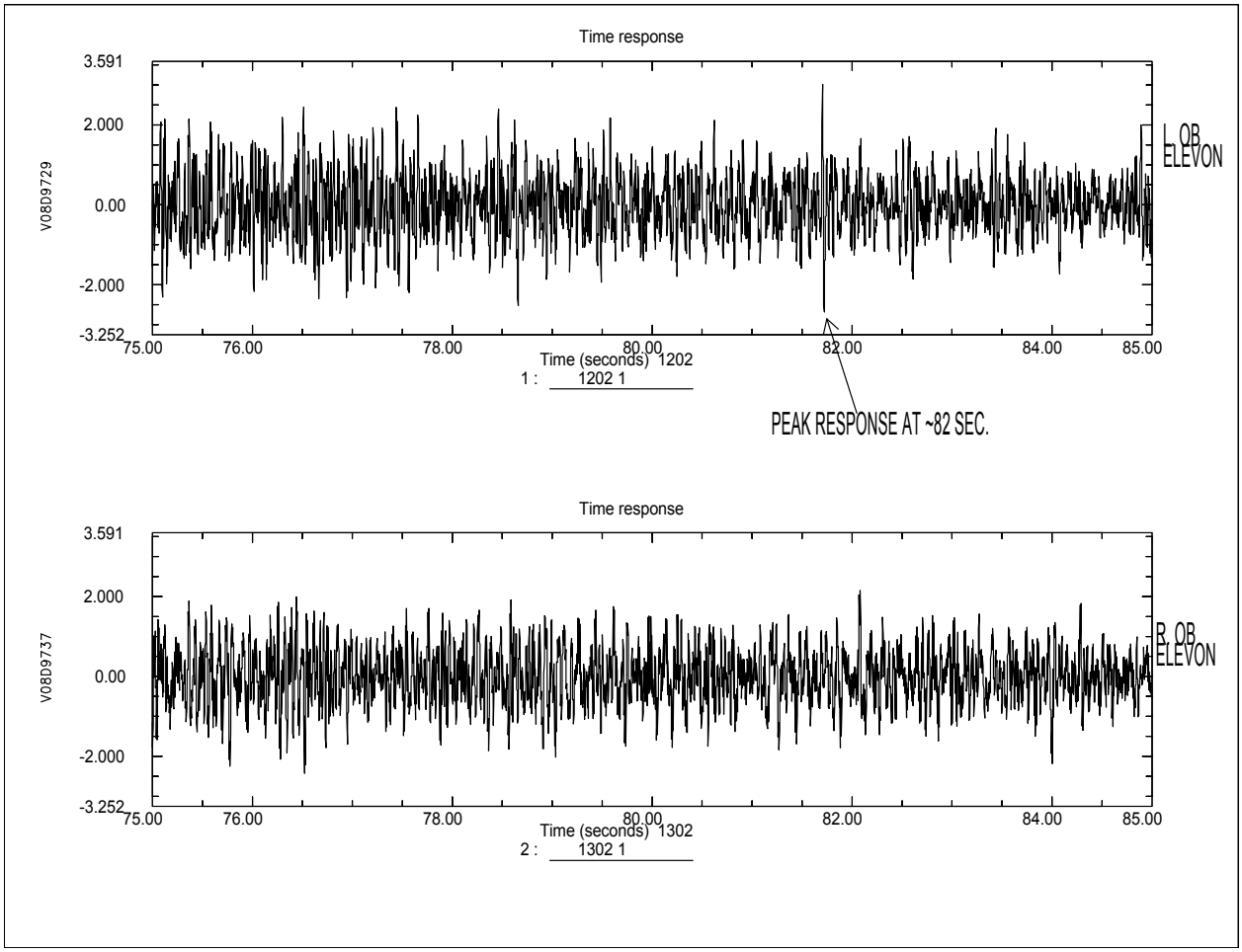

Figure 7.4-7 Right and Left Outboard Elevon Response at ~82 seconds

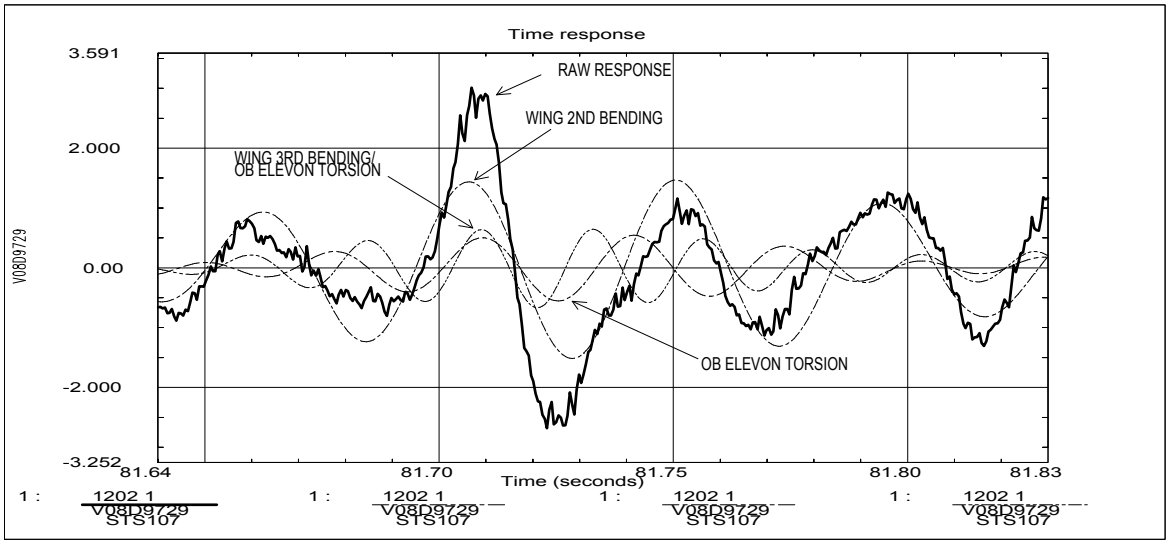

Figure 7.4-8 Excitation of Various Wing/Elevon Modes at ~82 sec. (Left Outboard Elevon)

To determine if the debris impact can cause the type of responses observed in the flight data, analyses were performed using the FEM model of the wing combined with the reduced model of the Orbiter, which provides the back-up structure's stiffness and mass (Figure 7.4-9). An impulse of 3,000 lbs force (with 0.005 second duration) in Z-direction was applied to the node closest to the RCC panel #8. The impulse of this magnitude is reasonable for a 1.5 lb object with a velocity of 530 MPH impacting the surface at 15 degrees inclination.

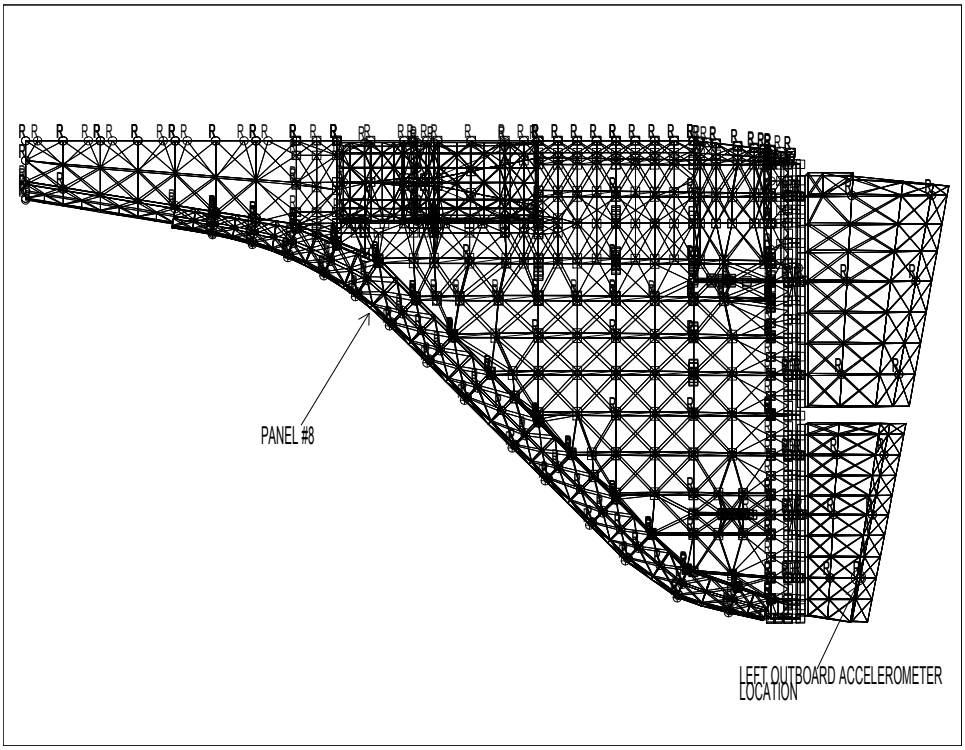

Figure 7.4-9 FEM Model of Wing Structure

Shown in Figure 7.4-10 is the recovered acceleration at the left outboard elevon location from the transient analysis. The FFT (Figure 7.4-11) of the response indicates excitation of several wing modes, including wing's 2nd and 3rd bending modes. The filtered responses shown in Figure 7.4-12 illustrate the 3rd wing bending mode constitutes the majority of the peak amplitude, while the 2nd wing bending and elevon torsion modes also contribute to the peak response. The acceleration computed using the FEM model is shown along with the flight measured data in Figure 7.4-13. The shapes of acceleration signatures are comparable at the onset of debris impact. The frequency from the analysis is higher, since the 3rd wing bending mode is excited the most compared with the 2nd wing bending mode experienced during STS-107. More pronounced 3rd wing bending response from analysis could be attributed to possible deviations from the assumed location and duration of impact event, and some uncertainty in the FEM models for higher order wing modes. Nevertheless, similar acceleration signature and the excitation of higher order wing modes from the analysis indicate that the debris impact quite possibly could have caused the peak acceleration on the left outboard elevon at ~82 seconds in addition to other aerodynamic disturbances, such as buffeting and shocks. An absence of additional sensors on the left wing make it difficult to make conclusive remarks.

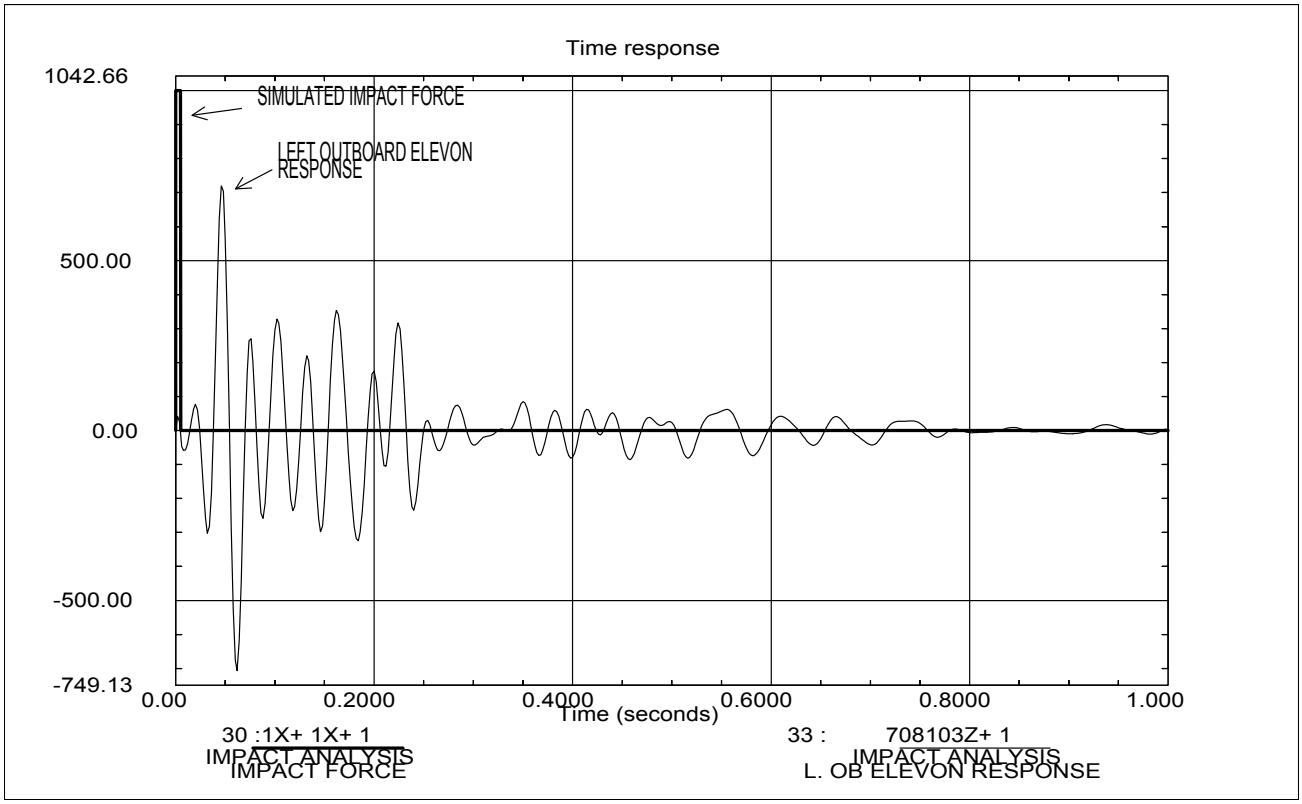

Figure 7.4-10 Outboard Elevon Response from Impact Analysis

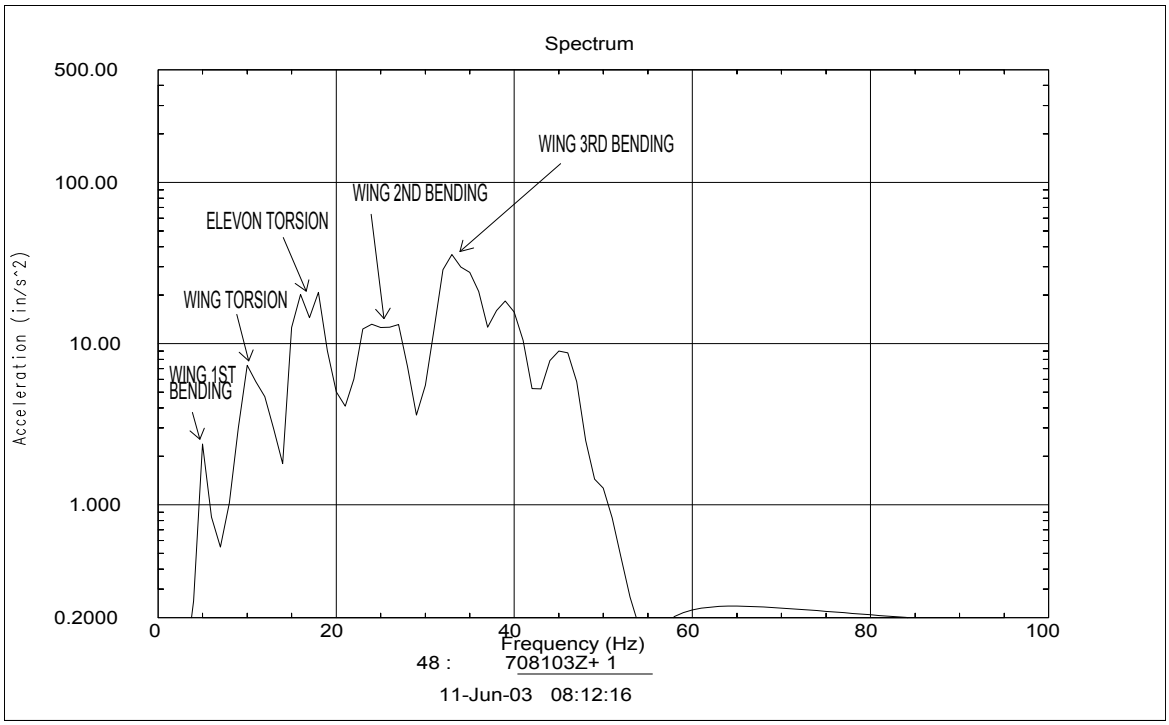

Figure 7.4-11 FFT at Outboard Elevon Location (Impact Analysis)

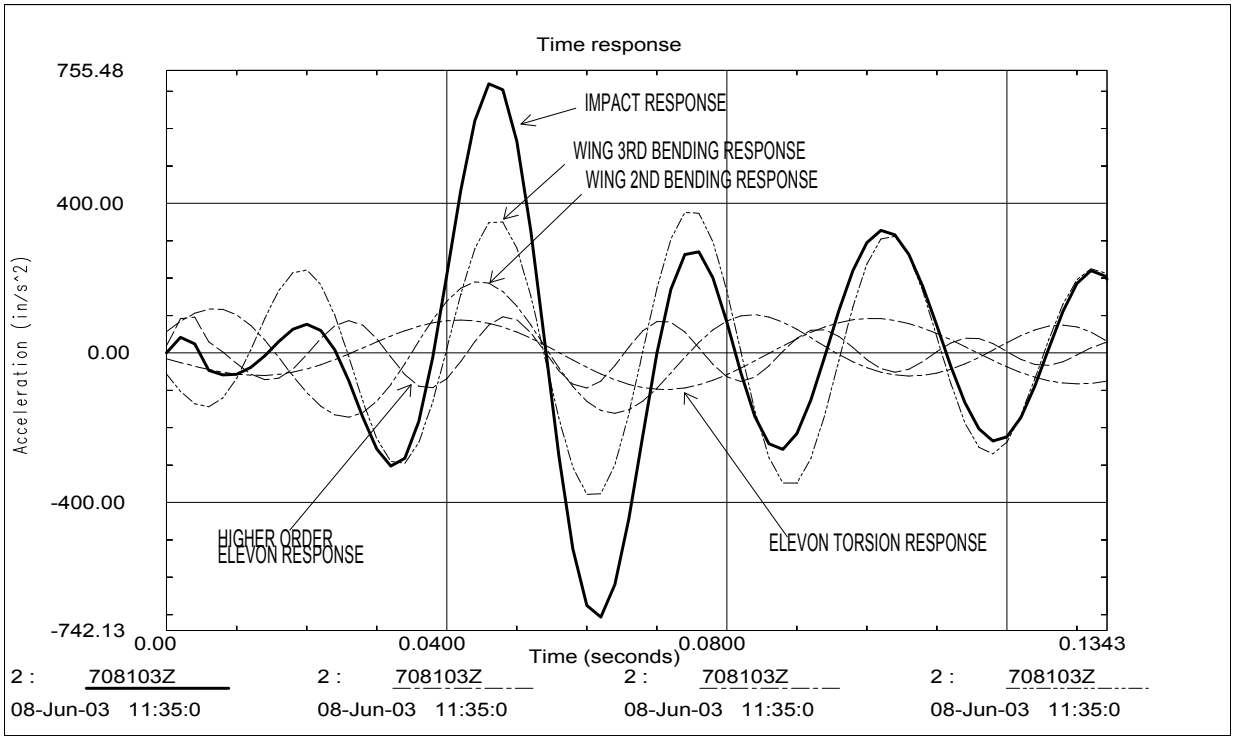

Figure 7.4-12 Excitation of Various Wing/Elevon Modes (Impact Analysis)

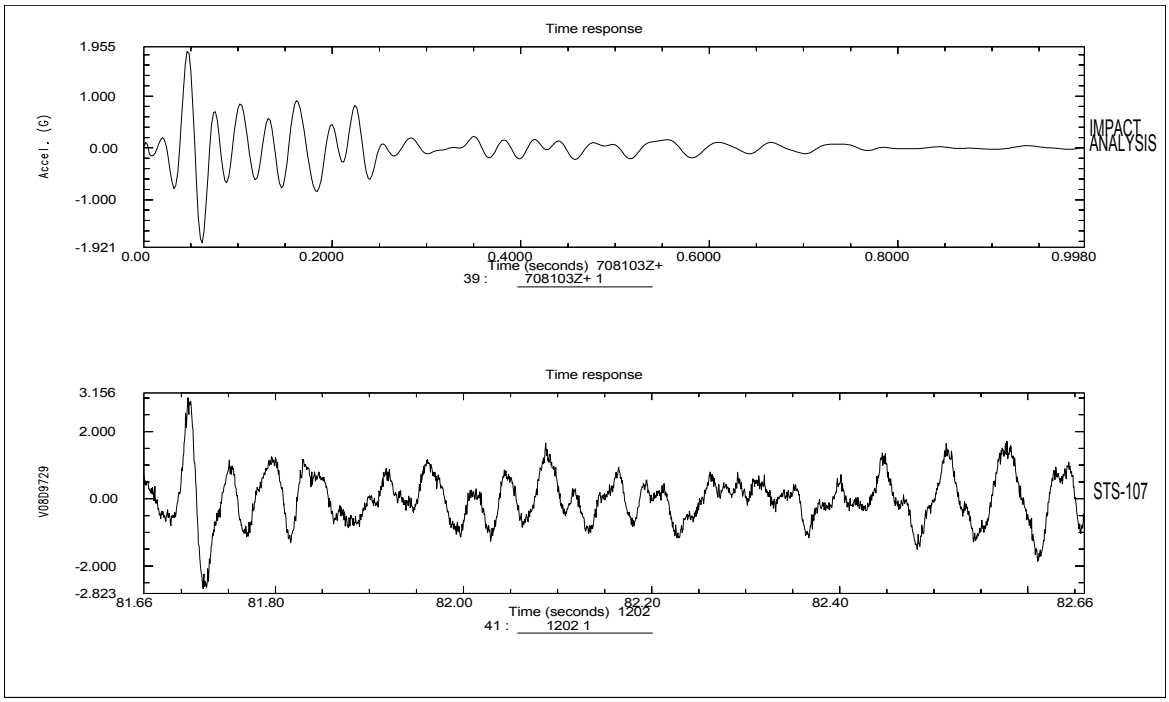

Figure 7.4-13 Comparison of Analysis and Flight Measurement

7.4.1.2 Flutter Assessment

A flutter assessment was made using wing and tail accelerometers. Previous flutter analysis had indicated the tail is the most critical component of the Orbiter for flutter instability. Flutter typically involves a coalescence of bending and torsion modes and is considered most critical near M=1. To determine if flutter had occurred during STS-107, PSD's from tail accelerometers were computed at various times during ascent. The results displayed in Figure 7.4-14 show distinct peaks for the 1st bending mode of tail at 3-4 Hz and the torsion mode at 10-11 Hz throughout the flight. This demonstrates that the mode coalescence did not occur and the tail was stable. Shown in Figure 7.4-15 are the filtered responses of the lower rudder. The raw accelerometer responses are filtered so that predominantly the bending and torsion responses are displayed. The figure illustrates that the response for critical modes always decayed after external disturbances. Also, the responses of the tail's bending and torsion mode are clearly visible, which verify that two modes did not coalesce and, consequently, the flutter instability did not occur.

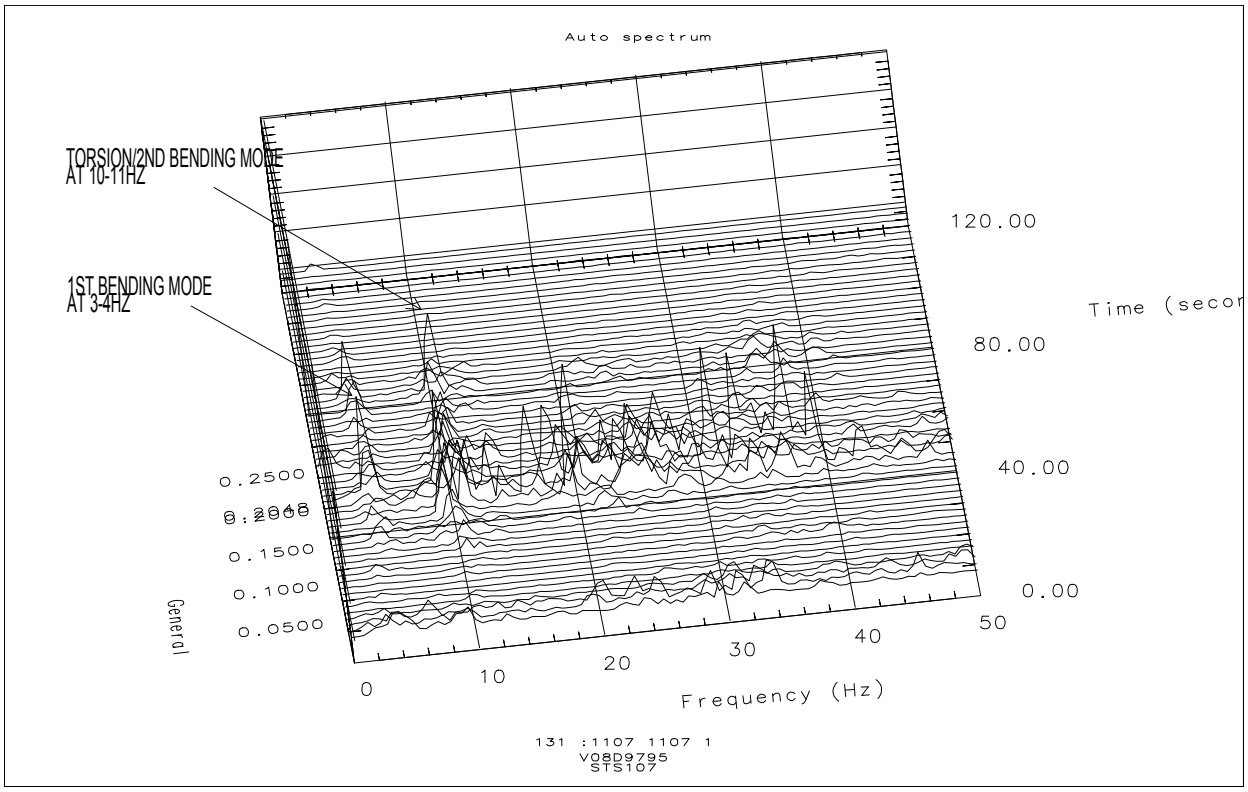

Figure 7.4-14 Vertical Tail Modes during STS-107

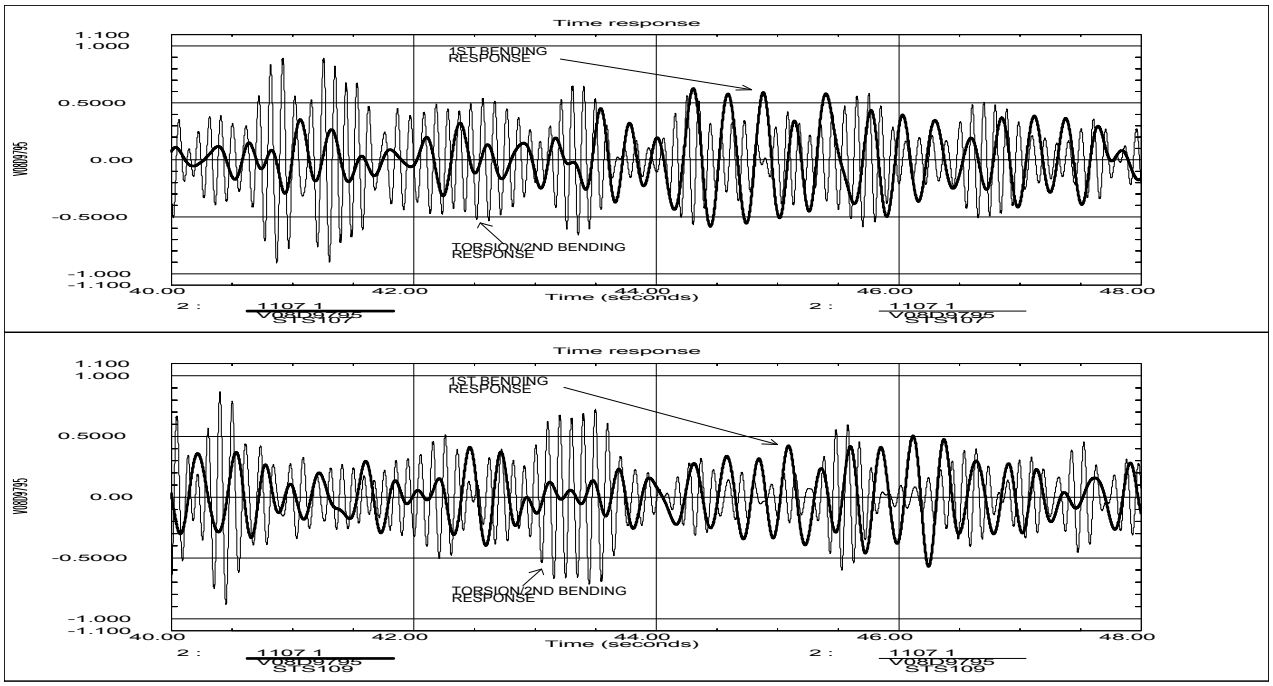

Figure 7.4-15 Filtered Response of Lower Rudder (STS-107 and STS-109)

For assessment of wing flutter instability, a similar process was employed. Presented in Figure 7.4-16 are the PSD's of the left outboard elevon accelerometer for STS-107 and STS-109. The distinct peaks for the 1st bending mode at ~6 Hz and torsion mode at ~8 Hz near M=1 are clearly visible. Thus, the mode coalescence did not occur for the wing during STS-107. The filtered responses shown in Figure 7.4-17 demonstrate the response of wing's bending and torsion modes did decay after aerodynamic disturbance, which confirms that the wing was far from flutter instability.

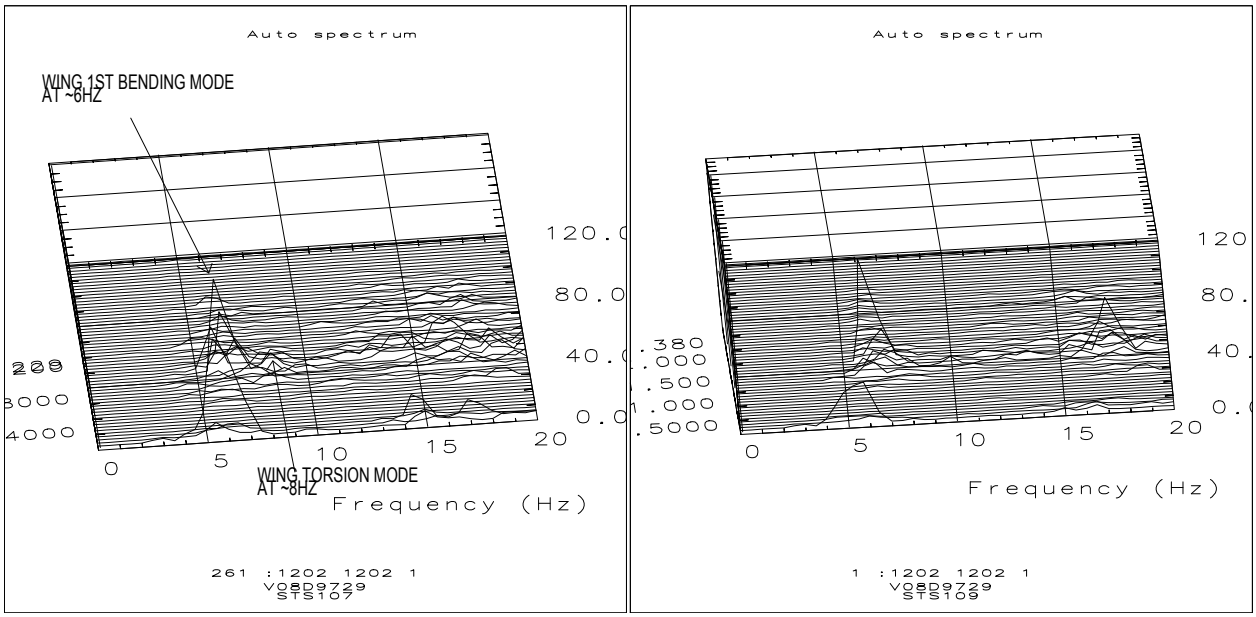

Figure 7.4-16 Wing Modes during STS-107 and STS-109

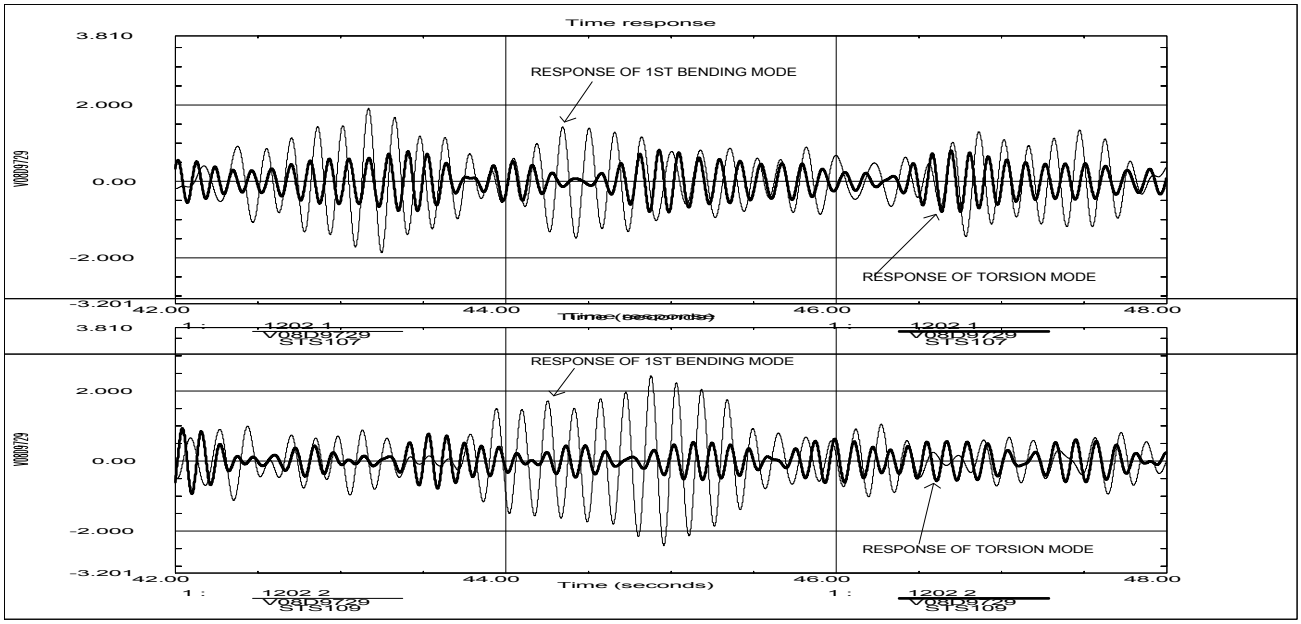

Figure 7.4-17 Filtered Response of Left Outboard Elevon (STS-107 and STS-109)

7.4.1.3 Strain Gage Response

The ascent strain gage data revealed the responses were very similar to STS-109. A comparison of typical gage response is shown in Figure 7.4-18. To compare the dynamic contents of the measurement, a 2-50 Hz band pass filter was applied to isolate the dynamic components. Plots shown in Figure 7.4-19 illustrate the response from two flights are very similar. The RMS values of strain shown in Table 7.4-2 also confirm that the overall level of dynamic strain is very comparable.

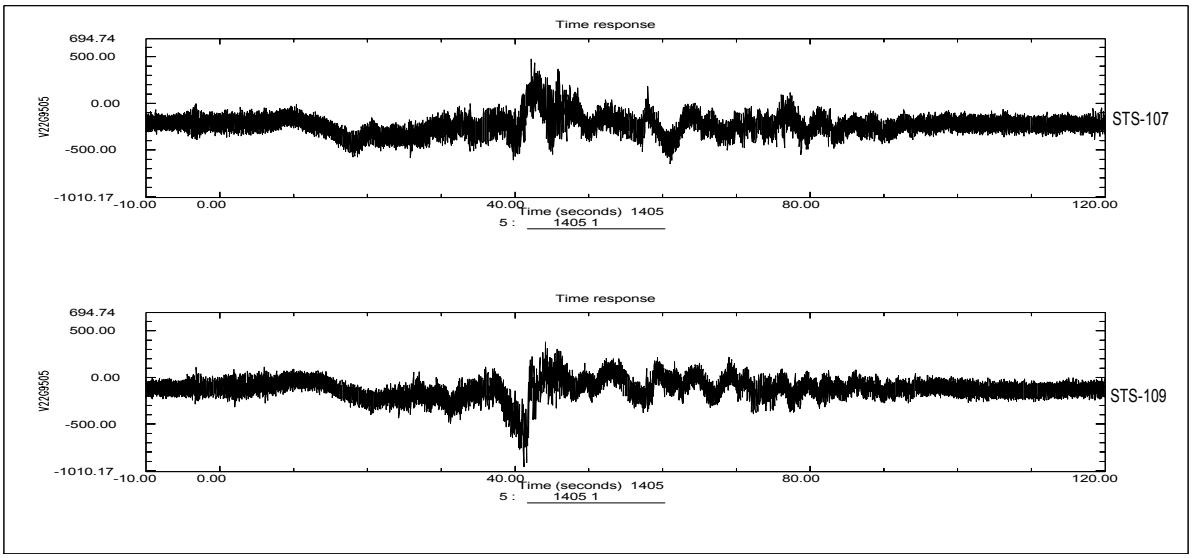

Figure 7.4-18 A Comparison of Strain Gage Response (Tail, Aft Spar Web)

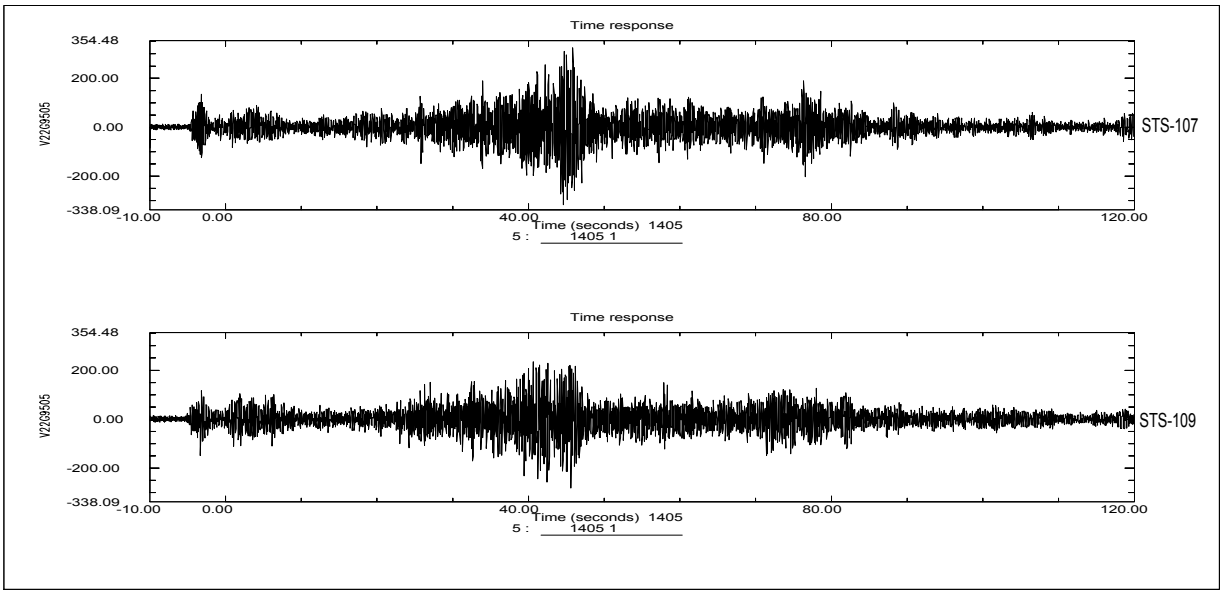

Figure 7.4-19 Dynamic Components of Strain Gage Response (Tail, Aft Spar Web)

Table 7.4-2 A Summary of RMS Values for Strain during Ascent

	T= 0-120 sec		T= 20-80sec.	
	STS107	STS109	STS107	STS109
V22G9501 A(V Fin, Aft Spar Web)	12.8	12.7	16.7	16.3
V22G9502 A(V Fin, Fwd Spar Web)	6.9	6.5	9.0	8.3
V22G9503A(V Fin, Aft Spar Web)	29.0	28.5	36.9	35.5
V22G9504A(V Fin, Fwd Spar Web)	8.9	8.3	11.7	10.9
V22G9505A(V Fin, Aft Spar Web)	45.1	41.5	59.6	53.6
V22G9506A(V Fin, Fwd Spar Web)	12.9	12.5	16.2	15.5
V35G9610A(Aft Fus, OMS Deck)	3.9	4.0	3.8	4.0
V35G9611A(Aft Fus, OMS Deck)	3.2	3.3	3.8	4.0
V35G9612A(Aft Fus, OMS Deck)	1.4	1.5	1.4	1.5
V35G9613A(Aft Fus, OMS Deck)	4.6	4.7	4.6	4.7
V35G9614A(Aft Fus, OMS Deck)	5.1	5.7	5.2	5.9
V35G9615A(Aft Fus, OMS Deck)	4.4	4.6	4.9	5.2
V35G9616A(Aft Fus, OMS Deck)	4.0	4.0	4.7	4.7
V35G9617A(Aft Fus, OMS Deck)	1.8	2.0	2.0	2.2
V35G9618A(Aft Fus, OMS Deck)	3.8	4.1	4.1	4.2
V35G9619A(Aft Fus, OMS Deck)	8.3	8.9	9.7	10.4
V35G9620A(Aft Fus, OMS Deck)	4.1	--	4.1	--
V35G9621A(Aft Fus, OMS Deck)	3.5	--	4.2	--
V35G9622A(Aft Fus, OMS Deck)	1.6	--	1.6	--
V35G9623A(Aft Fus, OMS Deck)	3.9	4.5	4.0	4.6
V35G9624A(Aft Fus, OMS Deck)	6.2	7.0	6.6	7.7
V35G9627A(Aft Fus, OMS Deck)	--	--	--	--
V23G9203A(L. Rud Hinge)	14.3	13.6	19.0	17.5
V23G9204A(L. Rud Hinge)	6.1	6.2	7.1	7.1
V23G9211A(L. Rud Hinge)	4.5	4.5	5.8	5.6
V23G9212A(L. Rud Hinge)	8.9	8.5	11.9	11.1
V23G9215A(L. Rud Hinge)	16.3	16.3	21.7	21.2
V23G9216A(L. Rud Hinge)	18.2	18.9	22.8	23.2
V23G9223A(R. Rud Hinge)	18.7	17.7	24.9	23.3
V23G9224A(R. Rud Hinge)	6.4	6.3	8.3	8.1
V23G9227A(R. Rud Hinge)	13.9	13.1	18.9	17.6
V23G9228A(R. Rud Hinge)	5.2	7.7	6.5	8.8
V23G9235A(R. Rud Hinge)	4.9	4.7	6.1	5.9
V23G9236A(R. Rud Hinge)	9.6	8.7	13.0	11.4
VO8G8041A(Heat Shield)	10.5	10.6	11.8	12.0
VO8G9091A(STN BHS Strut)	37.9	39.5	41.3	43.5

7.4.2 Descent

Although the overall level of acceleration during entry was small compared to ascent, accelerometer data were examined in detail to identify anomalous responses, which might correlate with events during entry. In particular, the left outboard elevon accelerometer (VO8D9729A) was thoroughly studied, since this was the only accelerometer on the left side of the wing. The responses of the accelerometer along with one on the right outboard elevon are shown in Figure 7.4-20. In the figure, responses following three particular events are of interest, thus, are studied in depth: Elevon activation at EI+223 sec., Transient responses at EI+496 and EI+502 sec., and Onset of signal saturation at EI+534 sec. (Note that frequent one-sided spikes are data anomalies and are not valid responses)

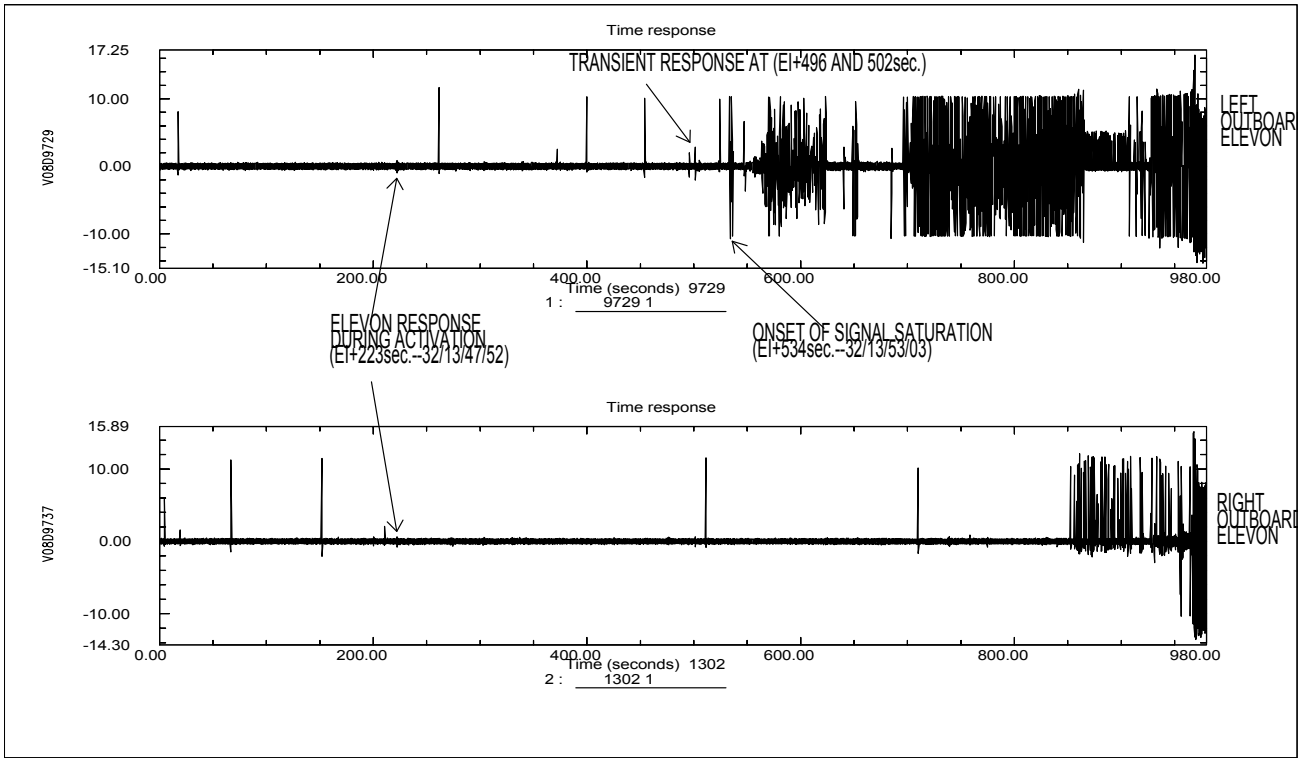

Figure 7.4-20 Left and Right Elevon Response During Entry (STS-107)

The detail plot of elevon response during activation is displayed in Figure 7.4-21. The 6 Hz response of the wing's 1st bending mode is clearly visible on both left and right outboard elevon channels. The presence of this mode verifies a proper operation of both accelerometers.

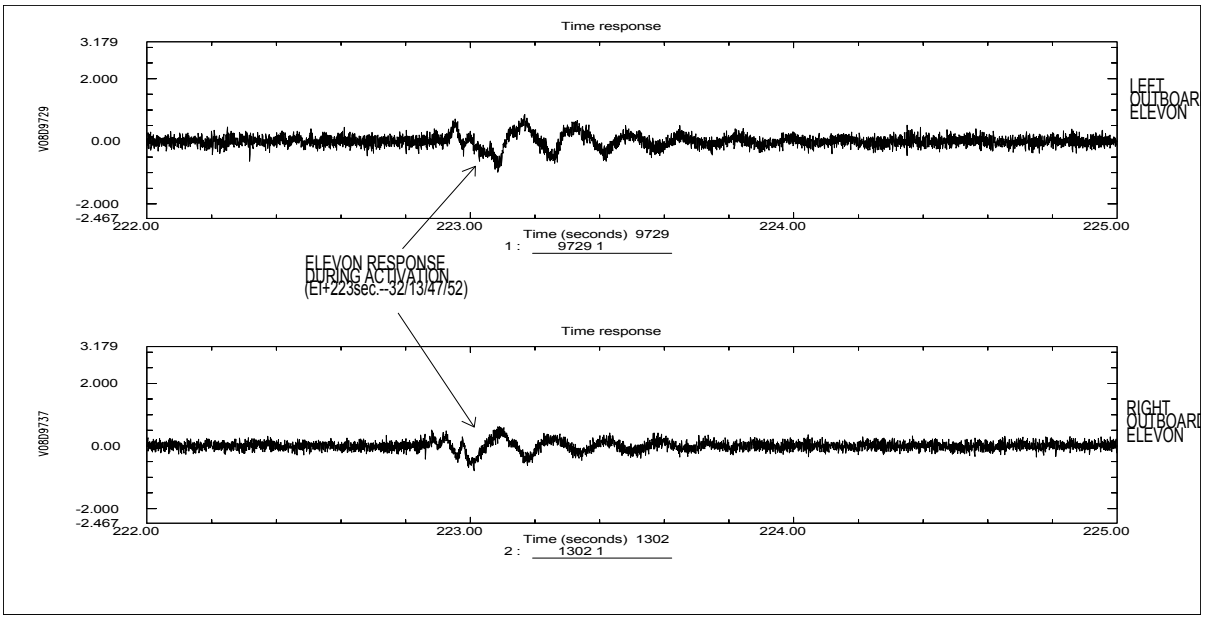

Figure 7.4-21 Elevon Responses during Elevon Activation at EI+223 sec

The second set of events occurred at EI + 496 and 502 seconds, which followed some type of external excitation. The transient response in Figure 7.4-22 was mainly noticeable for the left outboard channel. The PSD's (Figure 7.4-23) of the left outboard elevon channel following these disturbances confirm the existence of wing's 6 Hz bending and other wing/elevon modes. These times coincide with the RCS jet firings, however, similar type of transient response was not observed during other RCS jet firings.

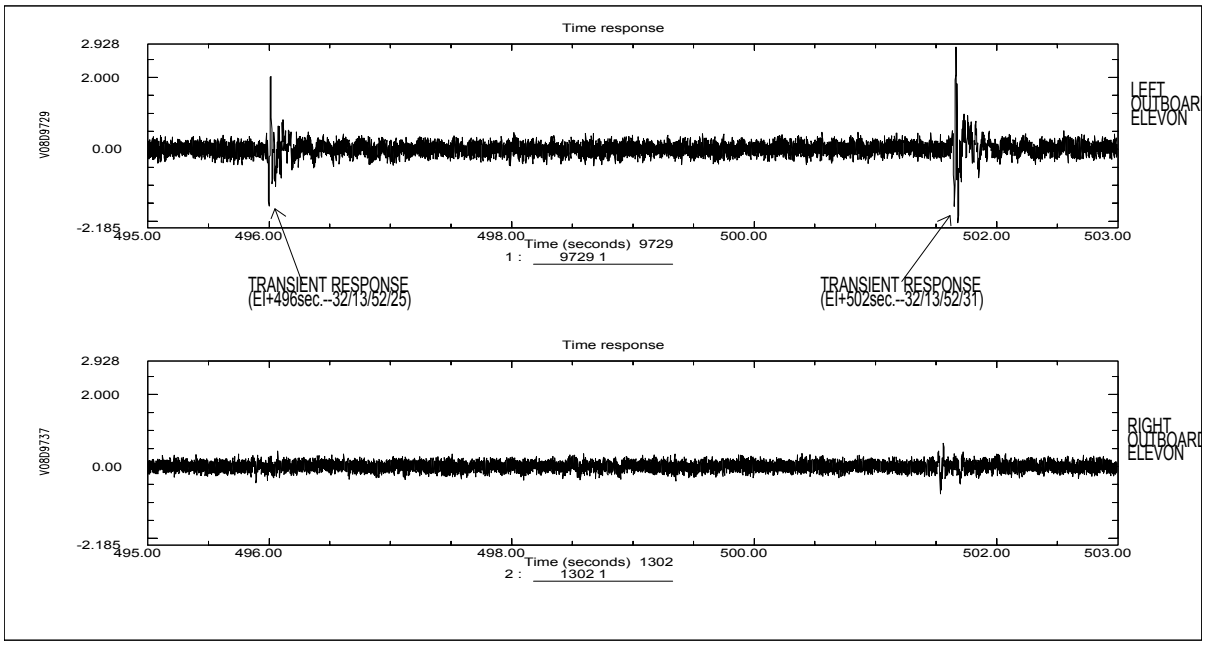

Figure 7.4-22 Transient Responses of Elevons at EI+496 and 502 sec.

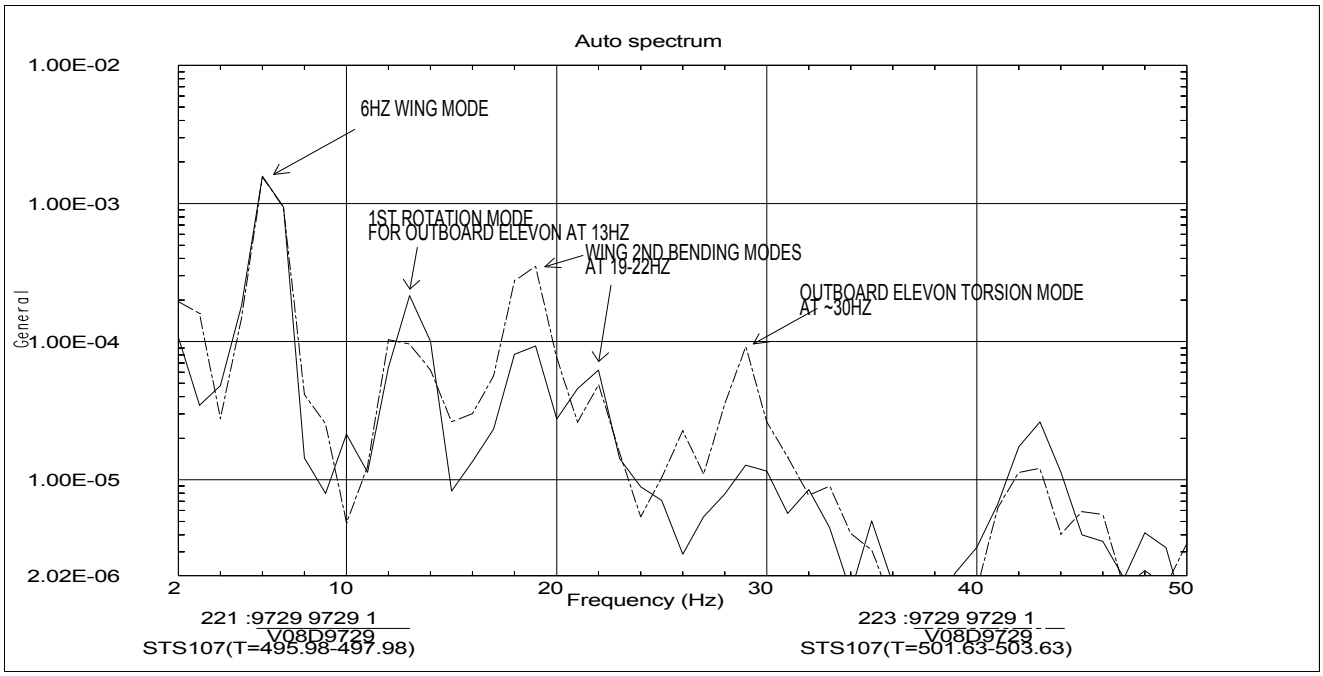

Figure 7.4-23 PSD's of Transient Response at EI+496 and EI+502 sec.

The third event observed at EI+534 indicates an onset of signal saturation for the left outboard channel. The accelerometer reading reached the maximum instrumentation range of 10G (Figure 7.4-24). The displacement computed (Figure 7.4-25) using the acceleration data results in an unrealistic number, which indicates a bad signal. The FFT's computed at various time segments during entry is shown in Figure 7.4-26. The figure illustrates a notable absence of 6 Hz response for the left outboard elevon channel after the onset of signal saturation, while the right outboard data exhibited 6 Hz response beyond EI+534 sec. This finding indicates malfunction of the left outboard channel past this time period.

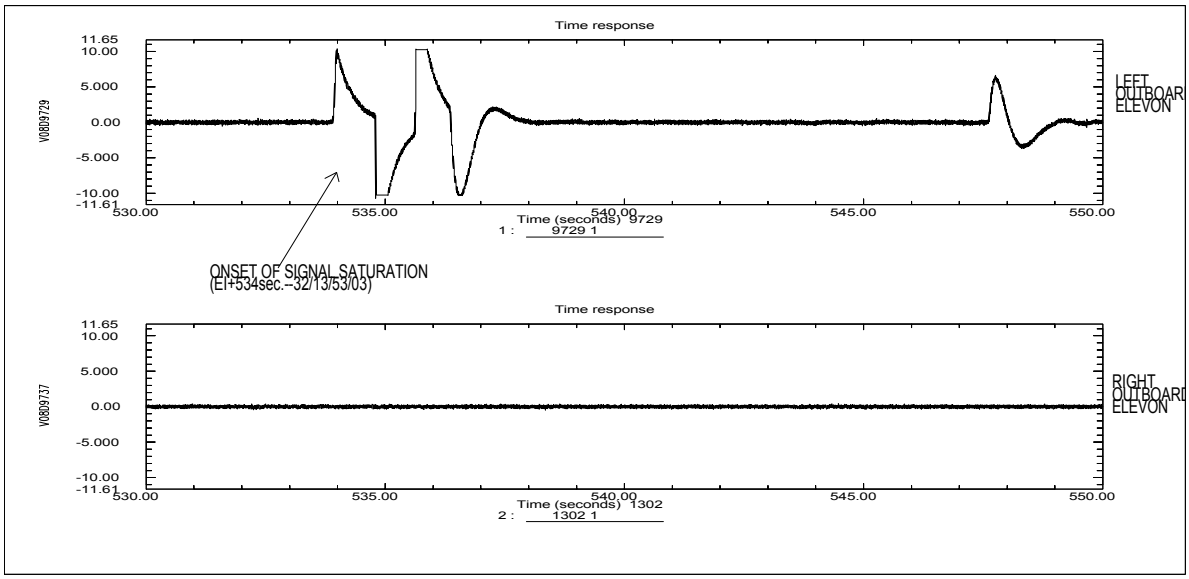

Figure 7.4-24 Onset of Signal Saturation for Left Outboard Elevon at EI+534 sec.

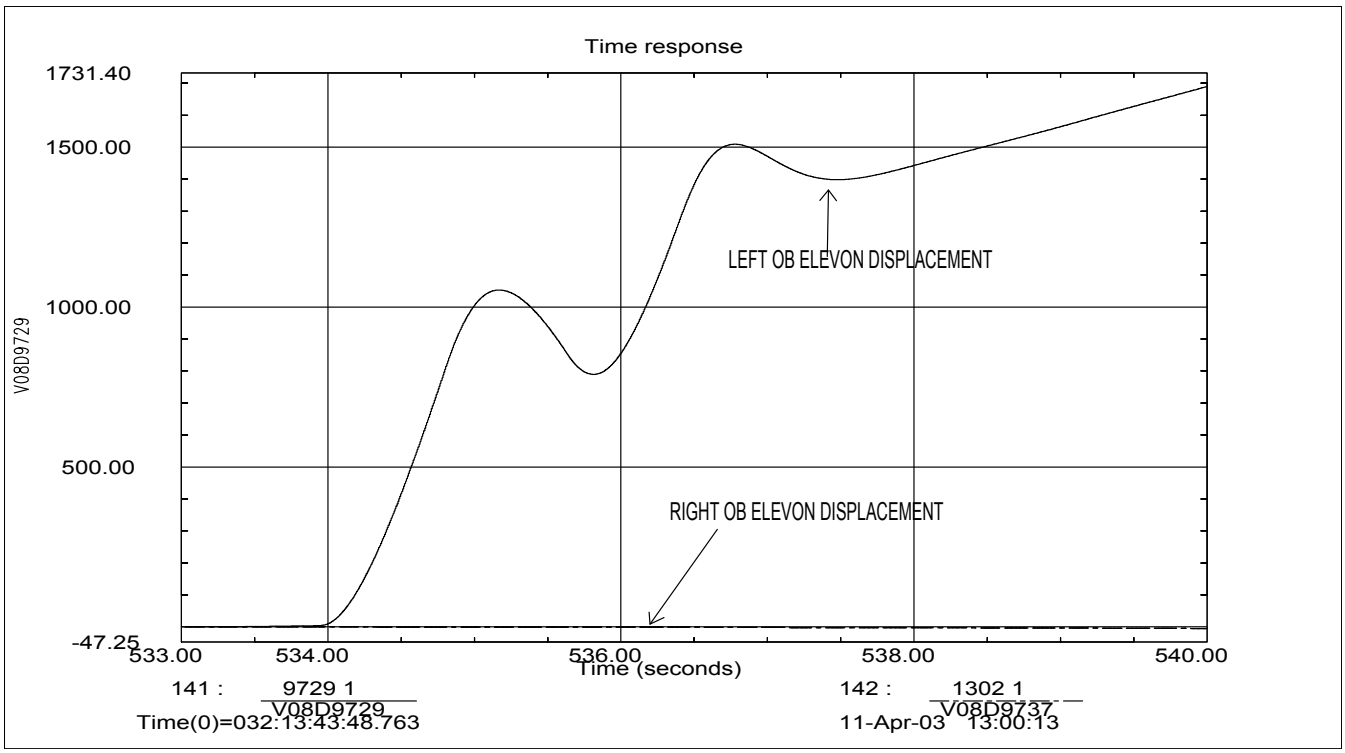

Figure 7.4-25 Displacement of Outboard Elevon Locations

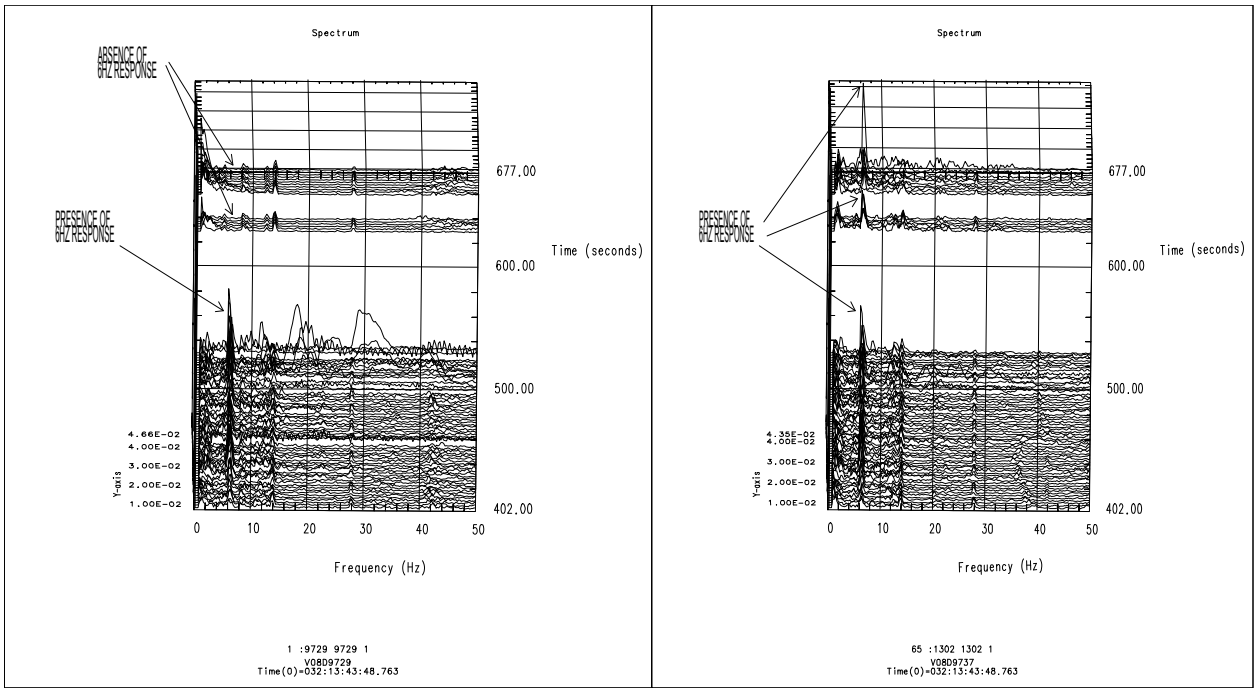

Left Outboard Elevon Right Outboard Elevon

Figure 7.4-26 FFT of Left and Right Outboard Elevon Responses

7.4.2.1 Strain Gage Data Evaluation

Typical strain gage responses are shown in Figure 7.4-27. For the most of entry phase, the strain gage channels are in "snap-shot" mode, where the readings are recorded for one minute and turned off for 4 minutes. Therefore, the only reading during the one minute period (where the strain level is near zero) is valid. In general, frequent one-sided spikes (which are not valid response and should be ignored) were observed during STS-107, which indicate the data quality was not quite as good. Also, extremely low strain level during "on" period makes the accurate assessment of the gage response very difficult. Only qualitative assessments are made. A PSD comparison for typical STS-107 and STS-109 strain data recorded at similar time period is shown in Figure 7.4-28. The figure illustrates the spectral contents are pretty similar. The large amplitude near 20 Hz and 40 Hz for STS-107 is due to the one-sided spikes, thus should be ignored.

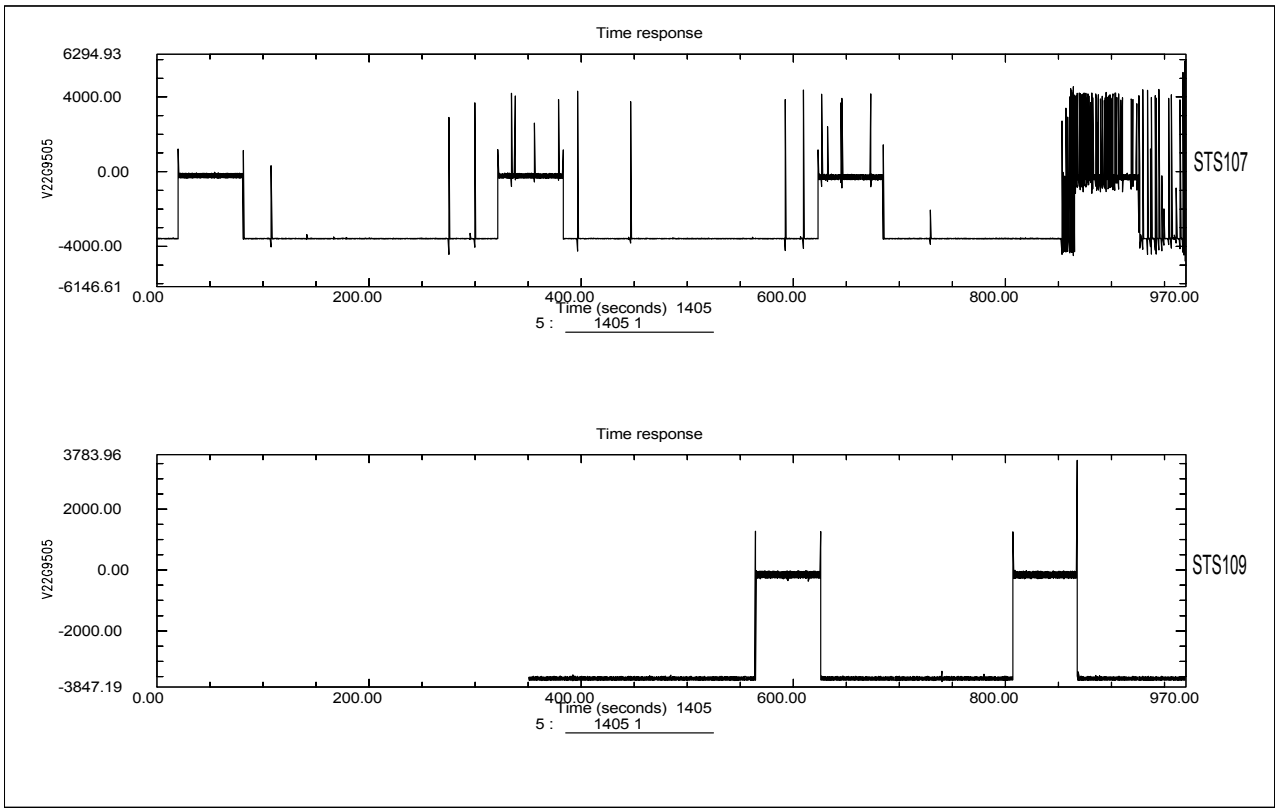

Figure 7.4-27 Strain Gage Response during Entry (Tail Aft Spar Web) STS-107 VS. STS-109

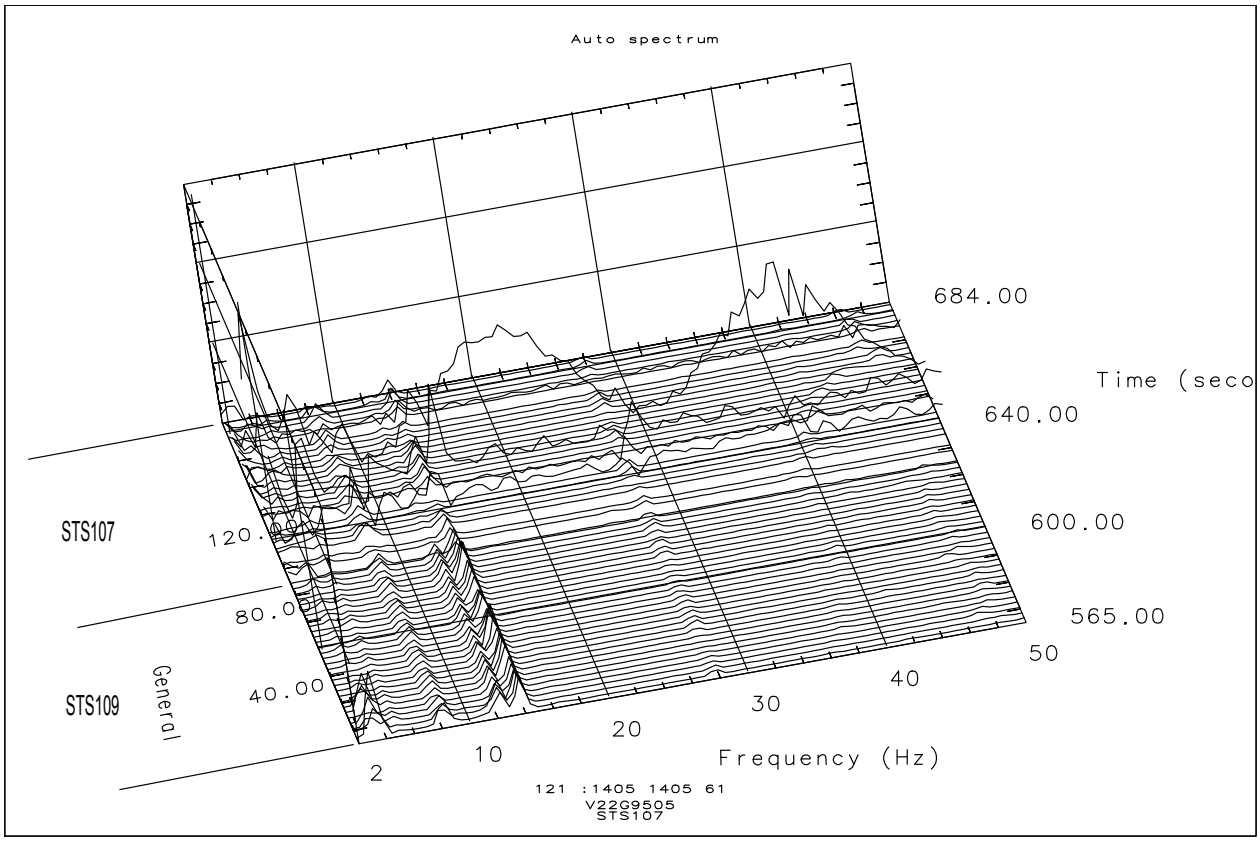

Figure 7.4-28 PSD Comparison of Strain Gage Response During Entry (STS-107 VS. STS-109)

7.4.3 Summary

Accelerometer and high sample rate strain gage responses were evaluated during ascent and entry phases of the STS-107 flight. The magnitude and the frequency contents of the measured acceleration and strain are considered within the family experience based on PSD's and computed RMS values. The excitation of the higher tail modes at 40-42 second period during ascent is similar to what's been experienced during STS-87, thus is considered normal. The distinct peaks observed for the bending and torsion modes of the wing and the tail demonstrate the flutter instability did not occur during ascent. The in-depth study of the left outboard elevon acceleration from flight and analysis using FEM models indicate the peak response observed at ~82 seconds could have come from the debris impact in addition to other aerodynamic disturbances. An absence of additional accelerometers on the left wing make it difficult to determine with certainty. During descent, the accelerometer data revealed the malfunction of the left outboard elevon accelerometer channel starting at EI+534 seconds

7.5 Feasible Wing Deformation Prior to Loss of Signature

7.5.1 Analysis Objective

The objective of the wing deflection analysis can be categorized into three distinct phases:

- Initial - the first analytical purpose was to assess OV-102 for gross left wing failure due to localized weakening of structural members. This analysis was performed during the early stages of the STS-107 accident investigation. Weakened structural members were assumed to occur from localized thermal heating due to damaged tile and RCC panels. This was considered the first approximation in determining the wing response due to various structural failure scenarios.
- Extended - the second analytical purpose was to expand the damage scenarios to include larger areas of the forward and intermediate wing sections. The analysis attempted to quantify the effects of losing major portions of the wing structure, instead of localized failure of structural elements. For this analysis, complete bottom to top cuts were made at critical structural locations around the main landing gear door wheel well, the wing leading edge spar and the honeycomb skin panels on the top and bottom wing surfaces. Structural member loss was assumed to occur from hot gas ingestion into the wing cavity; however, thermal degradation on the non-failed structures was assumed to be negligible.
- Refined - as the investigation continued, the analysis shifted from investigating various damage scenarios to cases that reflected the most probable events occurring during STS-107. The primary purpose of this analytical phase was to support an integrated analysis of the wing deformation with the aerodynamics group. The damage model was refined to represent a thermal breach at RCC panels 8 & 9, with subsequent hot gas flow into the intermediate wing cavity. Hot gas ingestion was assumed to lead to a loss of the intermediate wing tube struts and the upper wing skin panels. Also considered in this case was thermal weakening of the cavity walls, skins and rib caps.

7.5.2 OV-102 Wing Finite Element Model

A NASTRAN, OV-102 finite element model (FEM) was used to perform the analyses. An illustration of this model is shown in Figure 7.5-1. MSC-PATRAN was utilized for pre-processing of the model and post-processing of the results. The NASTRAN FEM was created from the original ASKA FEM and was previously used as part of the Performance Enhancement (PE) certification analyses, circa 1996. Due to the size and complexity of the FEM, only the wing and portions of the aft and mid fuselage were used. The mid-fuselage and the aft fuselage structure are present to allow for redistributing wing root reactions and deflections.

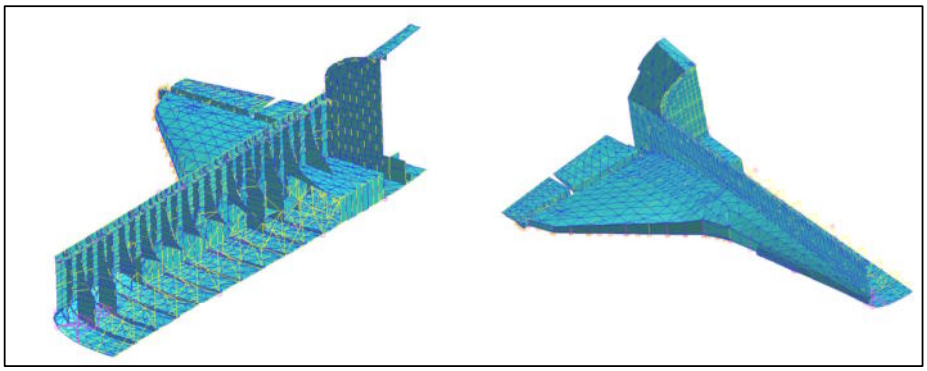

Figure 7.5-1 OV-102 Wing FEM

7.5.3 Load Cases

During the recent contingency abort project, a computational fluid dynamics (CFD) program was used to create a distributed aero pressure database for loads evaluation. This data provided Orbiter aerodynamic loads up to Mach 15. Subsequent to STS-107, and in support of the investigation, the database was expanded beyond Mach 18 in order to determine wing loads similar to those that occurred prior to the breakup. A portion of the Mach 18 expanded database is shown in Table 7.5-1. The dynamic pressure (Qbar) in the table is 70 psf and that angle of attack (Alpha) is 40 °. The load set that most closely resembles STS-107 is for an elevon angle of –2.98 degrees (De). This load set is highlighted in the table.

Table 7.5-1 Wing Loads, M=18

Wt	Xcg	Mach	Qbar	Altitude	Alpha	De	Dbf	Nx	Nz	Indicator		Wing Mx			Wing My			Wing Sz		
										Wing Mx	Wing Sz	Total	Aero	Inertial	Total	Aero	Inertial	Total	Aero	Inertial
234215	1078.3	18	70	207175	40	-11.37	11.30	0.05	0.92	0.267	0.181	4691114	6447031	-1755917	5296937	6648960	-1352023	39307	54275	-14968
234215	1078.3	18	70	207175	40	-10.40	10.60	0.05	0.92	0.253	0.181	4790338	6547683	-1757345	5229462	6582854	-1353391	39870	54851	-14980
234215	1078.3	18	70	207175	40	-9.64	9.90	0.05	0.92	0.243	0.181	4871794	6629995	-1758201	5174314	6528539	-1354225	40336	55324	-14988
234215	1078.3	18	70	207175	40	-9.02	9.20	0.05	0.92	0.233	0.181	4945690	6704639	-1758949	5124006	6478890	-1354883	40761	55755	-14994
234215	1078.3	18	70	207175	40	-8.40	8.50	0.05	0.92	0.223	0.182	5017525	6777221	-1759696	5075182	6430722	-1355540	41173	56174	-15001
234215	1078.3	18	70	207175	40	-7.78	7.80	0.04	0.92	0.214	0.182	5087389	6847831	-1760442	5027778	6383975	-1356196	41574	56581	-15007
234215	1078.3	18	70	207175	40	-7.16	7.10	0.04	0.92	0.205	0.182	5155312	6916500	-1761188	4981776	6338628	-1356853	41962	56976	-15013
234215	1078.3	18	70	207175	40	-6.54	6.40	0.04	0.92	0.196	0.182	5221298	6983232	-1761934	4937171	6294680	-1357509	42339	57359	-15020
234215	1078.3	18	70	207175	40	-5.92	5.70	0.04	0.92	0.187	0.182	5285425	7048106	-1762682	4893914	6252080	-1358166	42705	57731	-15026
234215	1078.3	18	70	207175	40	-5.48	5.00	0.04	0.92	0.181	0.182	5331767	7094767	-1763000	4862904	6221390	-1358486	42970	57999	-15029
234215	1078.3	18	70	207175	40	-5.10	4.30	0.04	0.92	0.176	0.183	5372428	7135619	-1763190	4835843	6194549	-1358706	43203	58233	-15030
234215	1078.3	18	70	207175	40	-4.74	3.60	0.04	0.92	0.171	0.183	5410271	7173639	-1763369	4810722	6169622	-1358900	43419	58451	-15032
234215	1078.3	18	70	207175	40	-4.44	2.90	0.04	0.92	0.166	0.183	5441861	7205389	-1763528	4789779	6148810	-1359031	43600	58633	-15033
234215	1078.3	18	70	207175	40	-4.14	2.20	0.04	0.92	0.162	0.183	5472515	7236202	-1763687	4769510	6128672	-1359163	43775	58810	-15035
234215	1078.3	18	70	207175	40	-3.84	1.50	0.04	0.92	0.158	0.183	5502245	7266091	-1763846	4749910	6109204	-1359294	43945	58981	-15036
234215	1078.3	18	70	207175	40	-3.54	0.80	0.04	0.92	0.157	0.183	5531060	7295065	-1764005	4730971	6090396	-1359426	44109	59146	-15037
234215	1078.3	18	70	207175	40	-3.25	0.10	0.04	0.92	0.157	0.183	5557818	7322008	-1764190	4713405	6072962	-1359557	44261	59300	-15039
234215	**1078.3**	**18**	**70**	**207175**	**40**	**-2.98**	**-0.60**	**0.04**	**0.92**	**0.157**	**0.183**	**5598759**	**7363171**	**-1764412**	**4685453**	**6045141**	**-1359688**	**44500**	**59540**	**-15041**
234215	1078.3	18	70	207175	40	-2.71	-1.30	0.04	0.92	0.157	0.183	5643147	7407781	-1764634	4655014	6014834	-1359820	44760	59802	-15043

A certification load case at Mach 18 does not exist for the Orbiter since structural significant loading does not occur during this portion of the descent phase. At the time of PE, descent load cases used for analyzing the Orbiter only extended to Mach 1.5. After STS-107, it was decided that creating a Mach 18 load case was not feasible due to the time constraint; therefore, it was decided that a currently existing load case would be used. Determining the applicable case was based upon two criteria: that the environment needed to be supersonic and that the wing shears and moments between the two load cases were of similar magnitude. A steady pitch terminal area energy management (TAEM) load case was selected. The aerodynamic loads for the selected case, TA2130, are shown in Table 7.5-2. Note that the wing moment values are approximately three times the aerodynamic values seen during STS-107. Root shear values are roughly 2 times the STS-107 conditions. Results, such as deflections and stresses, from this case need to be divided by 2 to approximate the STS-107 conditions just prior to vehicle break-up. It should be noted that the wing is designed to withstand root moments (Mx) up to a limit value of 32 million in-lbs, with a factor of safety of 1.4 above this load; the maximum loads for STS-107 entry were below 20% of the ultimate capability of an intact wing.

Table 7.5-2 Analytical Load Case

Report Condition	Mach	Description	Q (psf)	S/B (deg)	B/F (deg)	Elv (deg)	a (deg)	NZ (g's)	Mx	My	Sz
TA2130	**1.50**	**STEADY PITCH**	**375**	**55**	**16.57**	**-14.32**	**8.28**	**1.21**	**14,732,017**	**12,493,593**	**94,399**

7.5.4 Analytical Procedure

7.5.4.1 Damage Simulation

In order to simulate damage to the Orbiter wing, the modulus of elasticity for each damaged FEM element was reduced. This removed the stiffness of the elements, thus degrading the load carrying capability of the structural members. During the initial analysis phase, the modulus was reduced to 10% of nominal value for failed members. Reducing the stiffness by an order of magnitude was appropriate since the purpose was to gain an understanding of load distribution through the wing due to localized damage. The extended analytical phase; however, used a modulus of elasticity reduced to 1% of nominal value. This was done in order to help ensure that the damaged FEM elements were having no effect on the results. During the refined analytical phase, wing structures that were being heated, but not failed, were also reduced in stiffness. Wing honeycomb skin panels were reduced to 50% of nominal modulus value. This simulated de-bonded inner face-sheets. Other primary structural members, such as ribs, spars and skin panels away from the damage, but still exposed to thermal extremes were reduced to 30 % of modulus.

7.5.4.2 Screening Criteria

After running and obtaining results for the damage cases, a generalized screening process was used to find structures where load redistribution showed a significant increase. The screening was necessary to post-process large amounts of data in a reasonable amount of time and to provide a consistent methodology for the different analysts working on the project to employ.

The screening process consisted of comparing the stresses, loads and displacement for an undamaged element to a damaged element. A ratio of damaged to undamaged results was developed for each element and node within the wing. The definition of the load ratio is shown below:

$$R_{load} = \frac{\text{Damaged}}{\text{Undamaged}}$$

A large ratio does not necessarily equate to a significant change. A relatively small change could easily result in a large load ratio if the magnitudes of the data were small. As an example, a deflection changing from 0.001 inch to 0.002 inch would represent a 100% increase; however, due to the low magnitude, the increase would not represent a significant shift. Similarly, certain stress and load levels, depending on the magnitude, could be rationalized to be inconsequential. Table 7.5-3 shows the screening criteria that were established to reduce the amount of post-processed data.

Table 7.5-3 FEM Result Screening Criteria

FEM Entity	Data Type	Screening Criteria		Comment
		Load	Ratio	
Nodal	Displacement	--	> |15%|	--
Element	Stress	> 5000 psi	> |1.4|	Element types: CROD, CTRIA, CTRIA, CQUAD, CSHEAR
Element	Force	> 500 lbf	> |1.4|	Element types: CROD

7.5.4.3 Sub-Structuring

Wing elements and nodes were “sub-structured” into groups for comparative purposes. By organizing the structure into manageable groups, quicker conclusions could be drawn as to load re-distribution and deflections of the wing. Table 7.5-4 shows the sub-structure identification names associated with the associated portions of the model.

Table 7.5-4 Sub-Structured Identification

Location	Data Type	Sub-Structure ID
Leading Edge	Displacement	global_disp_LE
Leading Edge	Stress, Force	global_elem_LE
Fuselage to Wing Interface	Force	global_elem_IF
Global Wing Beams	Stress, Force	global_elem_Beams
Web Elements Inboard of Y_O198	Stress	global_webs_quad4 global_webs_tria3
Global Wing Nodes	Displacement	global_disp_WG

The first two sub-structured groups in Table 7.5-4 are for the wing leading edge (WLE) spar. Refer to Figure 7.5-2 and Figure 7.5-3 for the locations of these elements and nodes. The groups expand from panel 6, just forward of the Xo1040 spar, to the Xo1307 spar. The WLE was sub-structured separately from the rest of the wing due to the significance of the WLE in this investigation.

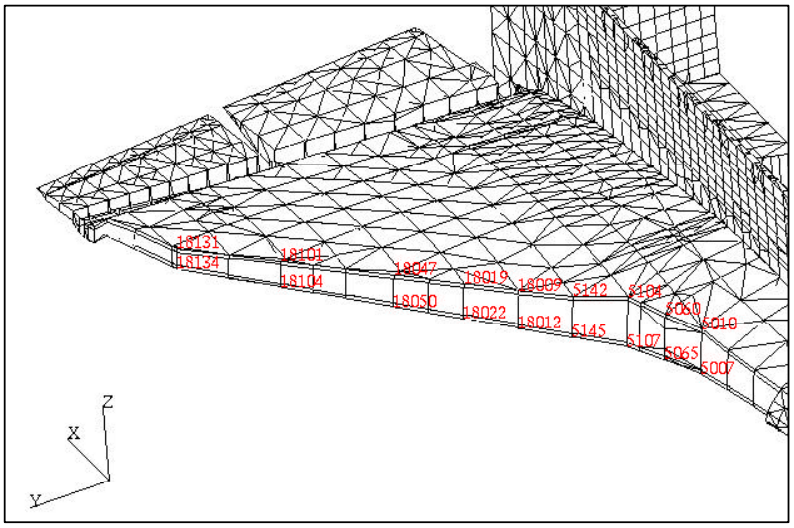

Figure 7.5-2 WLE Nodes

Only selected nodes along and the top and bottom of the WLE were sub-structured. Nodes were selected in order to provide an overall view of deflections along the WLE; therefore, a smaller sampling was appropriate. Similarly, only the WLE webs were selected for this sub-structured group. This was done in order to obtain an overall idea of the WLE load distribution as opposed to the rest of the wing.

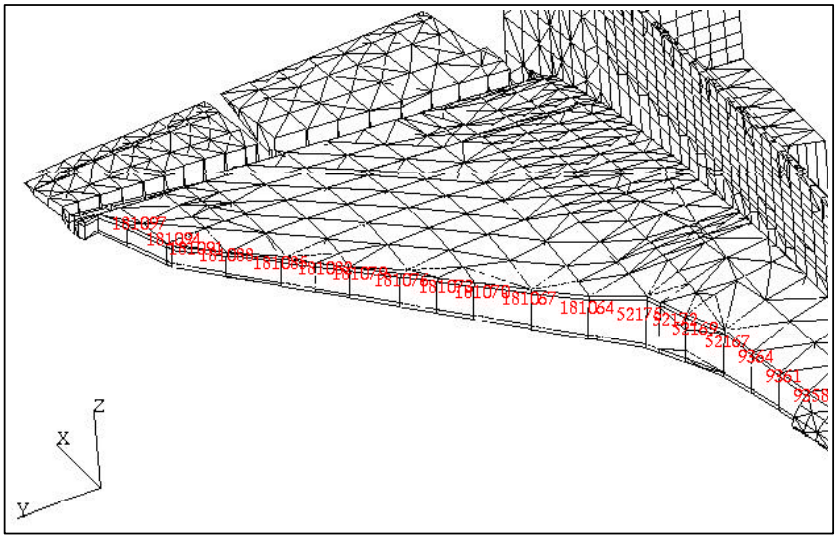

Figure 7.5-3 WLE Panel Elements

The wing torque box attaches to the wing carry thru (WCT) structure at locations Xo1191, Xo1249, Xo1307 and Xo1365. Additional bolts are located along the upper skin contour between the major spar attachments. The upper wing-to-WCT are loaded in tension and the lower wing-to-WCT is made through shear splices. Beam elements representing the wing interface bolt locations were sub-structured into a separate group. Figure 7.5-4 shows these elements and the location relative to the vehicle.

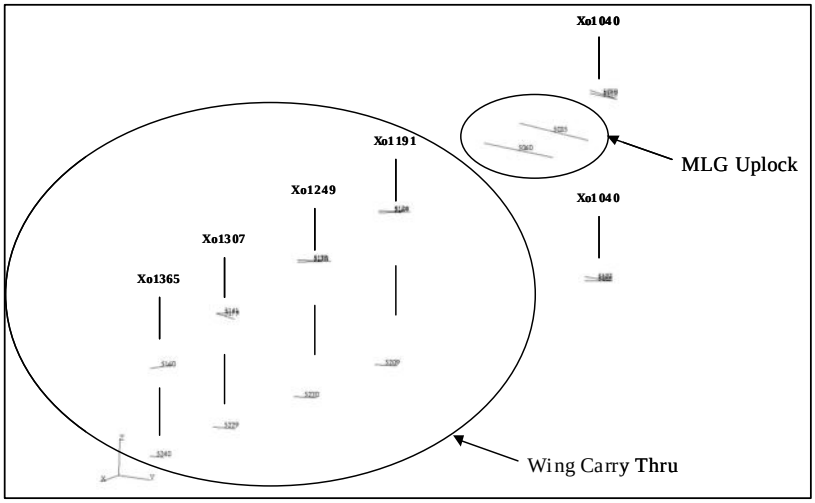

Figure 7.5-4 Wing-to-Fuselage Interface Elements

Due to criticality of the wing beam elements, most all were sub-structured for post-processing. These elements, shown if Figure 7.5-5, spanned the entire wing and included the glove area. Some areas, such as the main landing gear door hinges, were not included since damage would not produce a large effect to the wing.

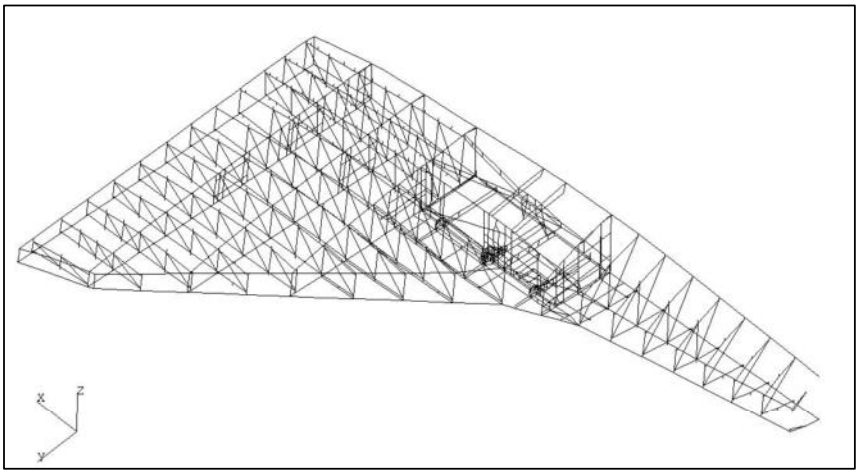

Figure 7.5-5 Wing Beam Elements

The wing model consists of a large amount of web elements. Early on in the analysis, it was decided that the beam elements provided good coverage for load distribution for the overall wing. This included load distribution through skin panels and spar webs. Therefore, to help limit the amount of elements data for post-processing, only the webs inboard of Yo198 would be sub-structured as being of particular interest relative to outboard rib webs. This group is shown in Figure 7.5-6. The X-station locations of the web elements spanned from Xo1010 to Xo1307.

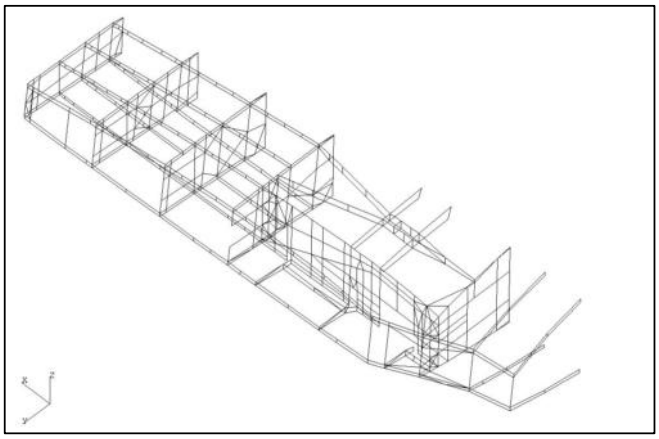

Figure 7.5-6 Inboard Wing Web Elements

As with the wing beam elements, all wing nodes were sub-structured. An illustration is provided in Figure 7.5-7. These groups of nodes were used to obtain an understanding of wing deflections based upon the various damage cases.

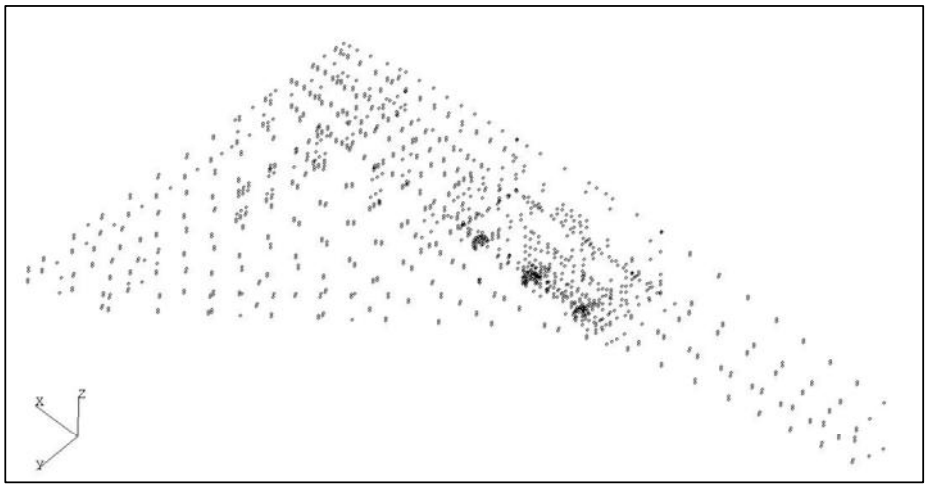

Figure 7.5-7 Wing Nodes

7.5.4.4 Post-Processing Tools

Two separate in-house Excel utilities were used for post-processing the analysis data. One utility reads the NASTRAN data output files for each damage case and creates separate files that categorizes results based upon the sub-structured elements. The second utility compares the results from each sub-structured data file to the undamaged results. Each utility was written in Visual Basic and provide a consistent and quick method for screening the sub-structured element by the criteria shown in Table 7.5-3.

7.5.5 Analysis Results

7.5.5.1 Initial (Small) Damage Analysis

The initial phase of the wing analysis attempted to assess the impact of localized skin, spar and rib damage to an overall effect on the wing. The analysis was performed for thermally weakened structure in locations deemed to be structurally significant. The screening criteria provided in Table 7.5-3 were used to determine wing areas where stresses, forces and displacements showed a significant increase in deflection and load.

The locations studied, along with the corresponding case files, are shown in Table 7.5-5. Most of the damaged areas are located in the intermediate wing with some WLE locations forward of the Xo1040 spar.

Table 7.5-5 Damage Locations, Initial Damage Failure Analysis

Case File	Location Studied
dam1191_1	Xo1191 lower spar cap and bottom skin aft of MLG well, aft, outboard corner
damle_1	MLG fwd hinge fitting, adjacent bottom skin and leading edge lower cap
damle_2	MLG fwd hinge fitting, adjacent bottom skin and leading edge lower cap and web to upper cap
damtube_1	Removed fwd diagonal truss tube from Yw198 rib (Elem 5812)
damtube_2	Removed fwd vertical truss tube from Yw198 rib (Elem 5561)
dis1191L	Disconnected Xo1191 spar cap and attached elements from mid-fuselage
dis1249L	Disconnected Xo1249 spar cap and attached elements from mid-fuselage
dis1307L	Disconnected Xo1307 spar cap and attached elements from mid-fuselage
dis1365L	Disconnected Xo1365 spar cap and attached elements from mid-fuselage
yo167_01	Yo167 rib lower spar cap at Xo1040 bulkhead
yo167_02	Yo167 rib lower spar cap at near door hinge point 1
yo167_03	Yo167 rib lower spar cap at near door hinge point 3
yo167_04	Yo167 rib lower spar cap at Xo1191bulkhead
yo167_05	Yo167 rib lower spar cap at near door hinge point 2
x1040y167-Damage1	Intersection Xo1040 spar and Yo167 rib at the lower wing surface

Table 7.5-6 lists the results for the initial damage failure analysis. As can be seen, the relative stress/load ratios show reasonable increases in element forces, stresses and displacements. The maximum load increases occurred for case damle_2. Wing beam elements showed a maximum increase 3.06 for case damle_2; however, the magnitude of the beam force was lower than the certified design load. The maximum wing-to-fuselage interface forces show a maximum increase of 8%. Based upon the capability of the interface bolts, an 8% increase is not considered significant. Maximum displacement was on the order of 39%. This was from a damaged element and was not considered realistic.

Table 7.5-6 Damage Locations, Initial Damage Failure Analysis

Case File	Maximum Load Ratio Results			
	Beam Force	Displ	LE Stress	IF Force
dam1191_1	1.54	1.03	1.02	1.08
damle_1	1.68	1.20	1.03	1.04
damle_2	3.06	1.39	1.16	1.08
damtube_1	2.29	1.08	1.07	1.02
damtube_2	1.72	1.03	1.02	1.02
dis1191L	2.00	1.17	1.05	1.06
dis1249L	2.00	1.17	1.01	1.02
dis1307L	2.90	1.23	1.00	1.03
dis1365L	1.06	1.06	1.00	1.01
yo167_01	1.58	1.01	1.00	1.00
yo167_02	2.18	1.01	1.00	1.01
yo167_03	1.41	1.01	1.00	1.01
yo167_04	--	1.01	1.00	1.01
yo167_05	1.92	1.01	1.00	1.00
x1040y167-Damage1	1.76	1.05	1.00	1.01

For the six separate locations along the Yo167 bottom rib cap, surrounding skins and web were checked for the effects of thermal degradation. Five of the damage locations were assessed along the Yo167 rib, lower cap and skins. For these cases, only the rib caps and skins were damaged. A sixth case with damaged Yo167 rib web elements was then considered. This case assumes impingement of hot gases onto the web and is indicative of burn through at Yo167 lower rib skins. Based upon the results, it was determined that localized failures of these locations are not sufficient to induced an overall wing structural failure. One element for all six damage locations violated screening criteria. As shown in Table 7.5-6, this element had a 2.18 load ratio. Element still maintains positive margin of safety based upon comparison to the certification database.

The conclusion from the analysis of small damage regions was that only the local areas were significantly affected. These would not produce a general wing failure, nor would they cause the local failure to propagate to a wider area.

7.5.5.2 Expanded Damage Analysis

The expanded damage analysis was performed to create more severe damage scenarios and to assess the wing response to a complete loss of load path due to damage in major structural areas. Seven damaged locations, shown in Figure 7.5-8, were examined during this phase of the analysis. The first two cases were centered about the WLE spar panels, just forward and aft of the Xo1040 spar. Cases 3 through 5 concentrated on the wheel well. In these areas, structure was assumed to be completely lost from the bottom wing surface to the top wing surface. Case 6 was created to see the effects of losing bottom surface honeycomb skin panels. Case 7 was the first attempt at specifically recreating the probable damage scenario experienced during STS-107. Case 7 was eventually modified to create the refined damage FEM.

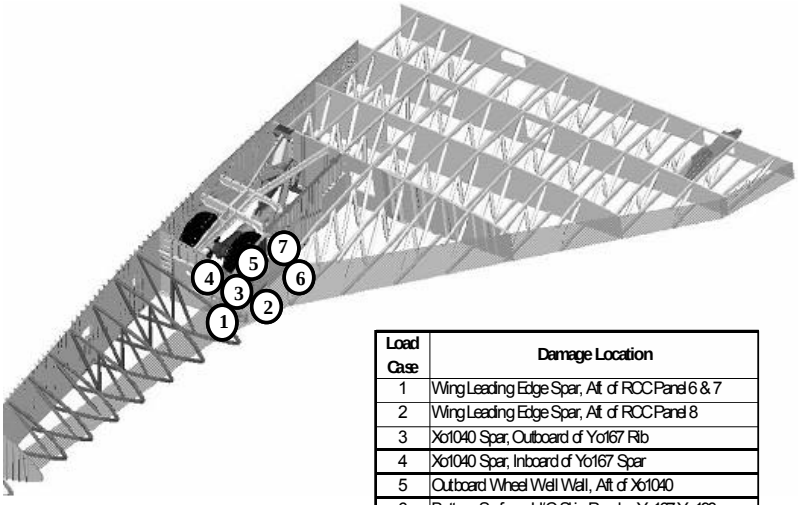

Load Case	Damage Location
1	Wing Leading Edge Spar, Aft of RCC Panel 6 & 7
2	Wing Leading Edge Spar, Aft of RCC Panel 8
3	Xo1040 Spar, Outboard of Yo167 Rib
4	Xo1040 Spar, Inboard of Yo167 Spar
5	Outboard Wheel Well Wall, Aft of Xo1040
6	Bottom Surface, H/C Skin Panels, Yo167-Yo198
7	- Upper Surface, H/C Skin Panel, Yo167-Yo198 - First Diagonal and Vertical Struts on Yo198 Frame

Figure 7.5-8 Damage Locations, Expanded Analysis

The total number of criteria violations for various data types, as described in Section 7.5.4.2, is shown in Table 7.5-7. From this table it can be noted that no significant fuselage interface violations occurred. This suggests that the amount of applied damage was not significant enough to cause the wing to detach from the main body. The total number of displacement criteria violations increases from the initial damage case, suggesting larger overall wing deflections. The stress violations also increase from the initial case. Some of these stress violations are significant, but a review of the certification analysis suggests that the parts still maintain a positive margin of safety. Overall, these results suggest a large amount of load redistribution does occur; however, wing failure from re-distribution is unlikely.

Table 7.5-7 Expanded Damage Analysis, Criteria Violations per Case

Damage Case	Stress	Displacement	Fuselage I/F Forces
1	135	26	0
2	94	11	0
3	94	0	0
4	61	0	0
5	20	0	0
6	131	21	0
7	142	0	0

7.5.5.2.1 Wing Displacements

Table 7.5-8 lists the total wing deflection criteria violations. Of the seven cases, cases 1, 2 and 6 showed displacement ratios greater than ±15%. The other cases displayed no criteria violations for deflections. (Note that for the expanded analysis, the deflection criterion was changed from a ±5% increase from damaged-to-undamaged condition, to a ±15% increase.) The maximum delta deflection was 0.24 inches, occurring for Case 2. A review of these violations suggests nothing significant from a structural strength standpoint.

Table 7.5-8 Wing Nodal Deflection Violations per Case

Damage Case	Criterial Violations		Wing Ratios		LE Ratios	
	Total Wing	LE Only	Max	Min	Max	Min
1	26	4	1.23	0.79	1.22	1.20
2	9	8	1.22	1.16	1.22	1.20
3	0	0	0	0	0	0
4	0	0	0	0	0	0
5	0	0	0	0	0	0
6	21	0	1.31	0.79	0	0
7	0	0	0	0	0	0

Note that these results contain ratios that are lower than the initial damage case results shown in Table 7.5-6. This is due to damaged elements being included in the initial analysis results. For the expanded case, localized damage effects were screened out.

Illustrations of the case 1, 2 and 6 displacement violation nodes are shown in Figure 7.5-9. For case 1, the violations are located in the glove area and near the WLE spar. This is consistent with a loss of load path between glove area and Xo1040 spar. The change in magnitude from undamaged to damaged are relatively small (0.11 inches), however. For Case 2, displacement violations are located at the WLE, which is consistent where the damage was located. As previously stated, the maximum delta deflection was 0.24 inches. The load path between the Xo1040 bulkhead and glove area has been restored, resulting in no violations in the glove area. For case 6, displacement violations are located at the wing glove area, suggesting that the lower panels help provide structural rigidity to elements of the Xo1040 spar.

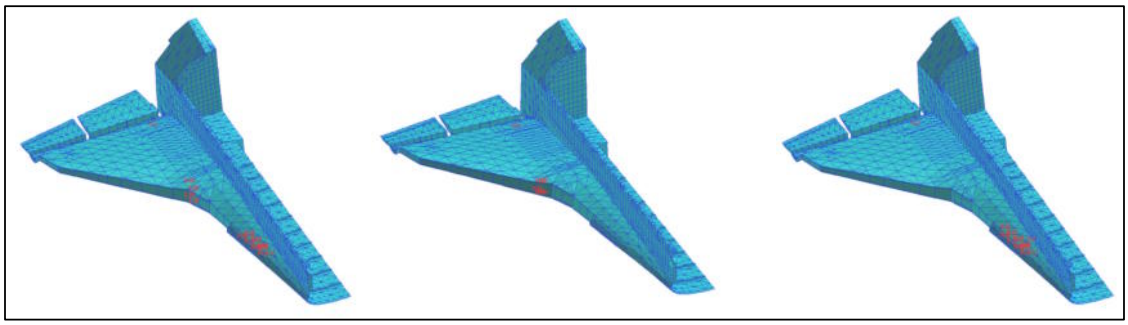

Figure 7.5-9 Node Displacement Violations

7.5.5.2.2 Wing-To-Fuselage Interface

As seen in Table 7.5-9, the results from the wing-to-fuselage comparison show no significant rise in loading from expanded damage conditions. The maximum load increase of 8% occurs for damage case 7. The location is at the X_O1040 upper wing-spar to fuselage interface. The maximum load increase along the lower wing interface is 7%, occurring at the X_O1191 wing-spar to fuselage interface. Note that the wing-carry-thru (WCT) interface reactions remain largely unchanged. This suggests that the main wing structure attaching the wing to the fuselage is not being compromised. The largest change for the lower wing interface is 7% at the X_O1191 lower spar interface.

Table 7.5-9 Wing-to-Fuselage Reaction Data

I/F Location	ELEM ID	Node ID	X_o	Y_o	Z_o	Case01	Case02	Case03	Case04	Case 05	Case06	Case 07	
Upper Wing	5070	5021	1040	105	342	1.04	1.00	1.01	1.02	1.00	0.97	1.00	
	5122	5023	1040	105	341	1.01	1.03	1.00	0.99	1.00	0.97	1.08	Max
	5035	5123	1090	105	339	0.97	0.97	0.95	0.95	0.99	1.00	0.97	
	5060	5194	1116	105	336	0.97	0.97	0.96	0.97	1.00	0.99	0.97	
	5124	5269	1191	105	325	0.99	0.99	0.99	1.00	1.00	0.97	1.00	Wing Carry Thru Locations
	5169	5054	1191	105	324	1.01	1.01	1.00	1.00	1.00	1.01	1.00	
	5133	5360	1249	105	317	1.02	1.01	1.01	1.01	1.00	1.03	1.00	
	5170	5059	1249	105	317	1.00	1.00	1.00	1.00	1.00	1.00	1.00	
	5141	5435	1307	105	308	0.99	0.99	0.99	1.00	1.00	0.97	1.00	
	5179	5435	1307	105	308	1.01	1.01	1.00	1.00	1.00	1.01	1.00	
	5160	5626	1365	112	300	1.02	1.02	1.01	1.01	1.00	1.04	1.00	
Lower Wing	5088	5018	1040	105	272	0.86	0.86	0.81	0.77	0.97	0.65	0.99	
	5123	5029	1040	105	273	0.85	0.85	0.80	0.77	0.97	0.60	0.99	
	5209	5265	1191	105	269	1.06	1.04	1.03	1.03	1.01	1.07	1.01	Wing Carry Thru Locations
	5220	5362	1249	105	267	1.01	1.01	1.00	1.01	1.00	1.01	1.00	
	5229	5437	1307	105	266	1.00	1.00	1.00	1.00	1.00	1.00	1.00	
	5240	5624	1365	112	267	0.98	0.98	1.00	0.99	1.00	0.99	1.00	

7.5.5.2.3 Stress & Force Results

Stress and force violations are summarized in Table 7.5-10. The most significant increases occur with cases 1, 6 and 7. Generally, the criteria violations are concentrated around the areas that have been damaged, with little impact to wing-to-fuselage interface, torque box or glove area.

Table 7.5-10 Stress and Force Violations

Damage Case	Element Type				Total Violations
	CTRIA3	CSHEAR	CROD	CQUAD4	
1	11	6	98	20	135
2	3	4	68	19	94
3	13	4	59	18	94
4	8	3	42	8	61
5	4	1	14	1	20
6	29	4	73	25	131
7	14	8	99	21	142

The stress violation dispersions illustrate load re-distributions within the wing. Dispersions for each of the cases are shown in Figure 7.5-10. Note that cases 2 & 7 show the widest area of dispersion. Case 2 load ratios are highly concentrated around the damaged WLE spar web, with some ratios scattered aft. Suggesting that there is not much load transfer moving toward the inboard wing structure. Case 7 also has high ratios around the damage area, but shows loads being distributed toward the wing-to-fuselage interface. Cases 4 & 5 show the least amount of dispersion, suggesting that the loads being routed around the wheel well is being more evenly distributed than with cases 2 & 7. Highly concentrated load

redistribution is observed for case 1, 3, & 6 around the area of damage. However, the dispersion does not move inward or outward.

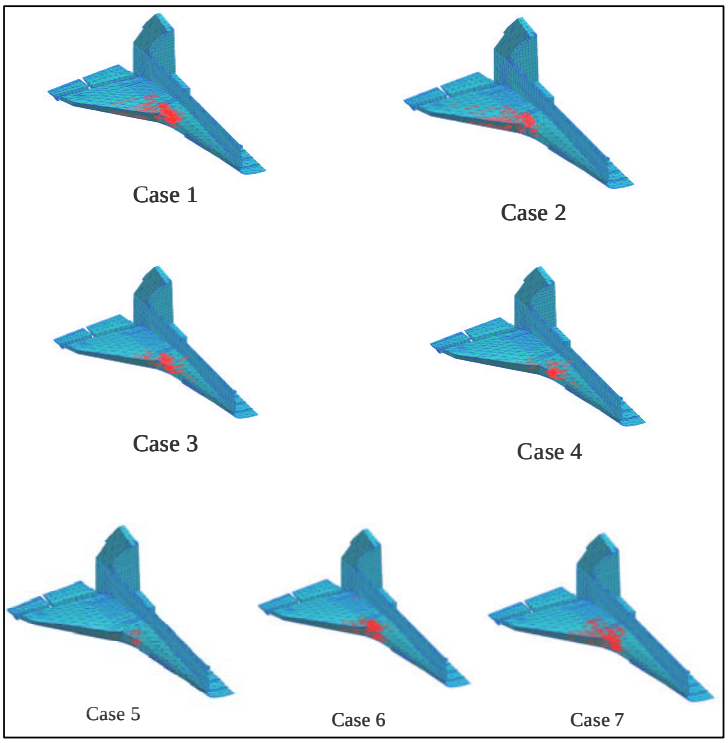

Figure 7.5-10 Stress/Force Violation Dispersions per Case

Table 7.5-11 shows the critical elements for each load case. The results show that, although load redistribution increases significantly with the expanded damage cases, the magnitudes were well within certification limits. The critical element for case 1, element 5515, was the closest to the certification load. This element is located in the Yo167 rib, near the main landing gear door forward hinge. The increase results from the damage WLE spar transferring the loads to the Xo1040 spar and Yo167 rib. The highest load shown in Table 7.5-11 is at element 5116, case 3. This element represents a beam in the Xo1040 spar. The load increase is to be expected since the element is close to the damaged area. Element 9053 represents a wing glove truss tube strut, located at the aft end of the glove at station Xo1010. Case 3 is the most critical for this element. This is due to the load path from the Xo1040 spar being lost and distributing an increased load forward.

Table 7.5-11 Critical Elements

Damage Case	Data	Type	Comp	ID	Damaged	Undamaged	Maximum Cert Load
1	Element Force	Crod	N (lb)	5515	820	51	967
2	Element Stress	Crod	Sx (psi)	5614	3542	204	10839
3	Element Stress	Crod	Sx (psi)	9053	-6774	-3853	-9886
4	Element Stress	Crod	Sx (psi)	5116	29731	11181	42877
5	Element Stress	Crod	Sx (psi)	5121	-3884	-1105	-10291
6	Element Stress	Ctria3	Sxy1 (psi)	51942	2699	1454	14111
7	Element Stress	Crod	Sx (psi)	5344	-4659	-1937	-14848

7.5.5.3 Refined Wing Stress Analysis

Structural analysis of a significantly damaged wing was requested to investigate potential sources of wing deformation. Correlation between the analytical results and the STS-107 measured aerodynamic data was the primary purpose of the analysis. Results were delivered to Aerodynamics group to study changes in aero coefficients seen during STS-107 descent.

The study was primarily focused on damage to the intermediate wing section. An attempt was made to model damage as closely as possible to the most probable failure scenario on STS-107, i.e., WLE spar breech at RCC panels 8 & 9. Three types of damage were applied to the FEM for this analysis. The first damage type was at areas where hot gas impingement was assumed to fail the structure. Susceptible structures were all the rib struts in the intermediate wing, the WLE spar behind RCC panels 8 & 9 and the top honeycomb panels just outboard of the wheel well wall. The modulus in these areas was set to 1% of their normal value. The second type of damage was concentrated on the upper and lower intermediate wing panels. The assumption was that the skin panels were affected by hot gas ingestion into the cavity, but not failed. The stiffness for these structures was reduced by a factor of two. The final type of damage was at the intermediate wing rib spars, Yo167 rib and the Xo1191 spar. Hot gas ingestion was assumed to lower the modulus of these locations by 30%. Refer to Figure 7.5-11 for the damage areas and modulus reduction values.

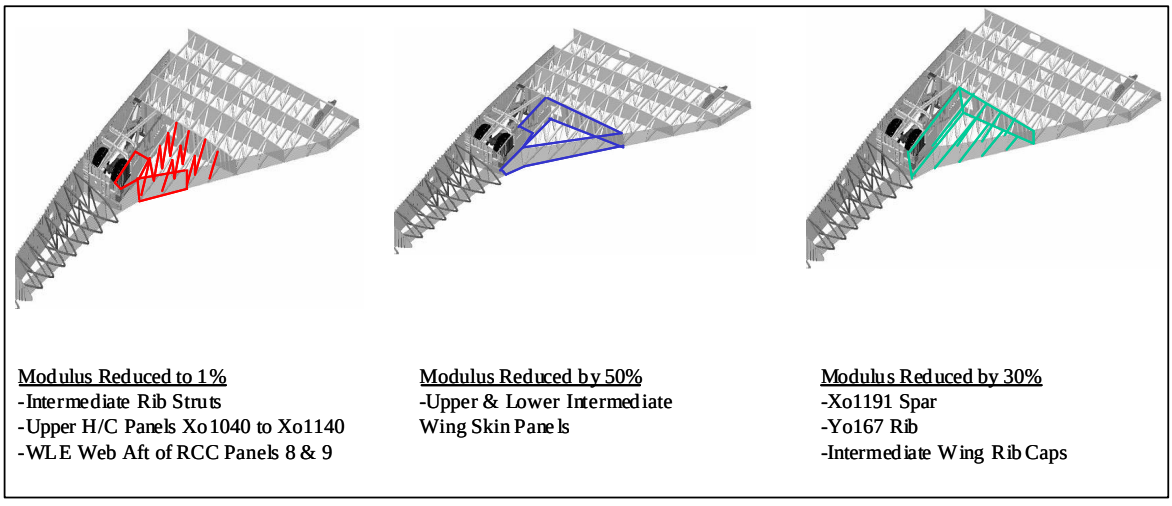

Figure 7.5-11 Refined Wing Damage Case

This linear FEM analysis was performed to show overall wing deformation, while hand calculations were done for local, non-linear effects on the lower wing skin. The FEM results show small deflections even with severe damage to the intermediate wing. The maximum delta deflection was 0.78 inch (Z), while the wing tip deflection increases to 0.25 inch. The wing tip deflection is nominally 1.1 inch. Maximum deflection results for the undamaged and damaged cases, as well as the difference between the two cases, are provided in Table 7.5-12.

Table 7.5-12 Refined Wing Damage, FEM Deflection Results

Condition	X (in)	Y (in)	Z (in)	RSS
Damaged Wing	0.1541 -0.1176	0.2298 -0.1334	1.3603 -0.0783	1.38817 0.19432
Undamaged Wing	0.0768 -0.1222	0.0681 -0.1236	1.0999 -0.0895	1.1047 0.19551
Delta Deflection	0.0774 -0.0195	0.2546 -0.1174	0.7822 -0.2561	-- --

Figure 7.5-12 shows the deflection of the wing with the refined damage. Significant distortion occurs around the intermediate wing just aft of RCC panels 8 & 9. Beyond this region, the wing deflections increase towards the wing tip. No significant deflections occur inboard of RCC panels 8 & 9. This is due to a denigrated load path from the outboard wing to the inboard wing.

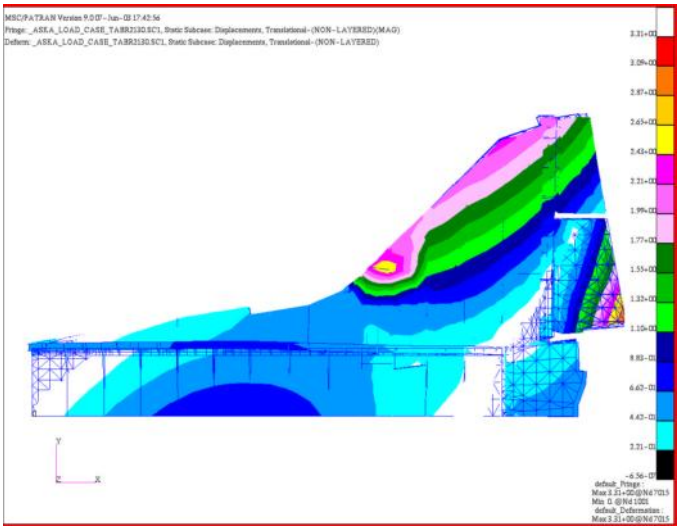

Figure 7.5-12 Refined Wing Damage, FEM Deformation Plot

Wind tunnel testing indicated that deflections of up to five inches are required to emulate the aerodynamic profile experienced during STS-107. These results show that the aerodynamic load at Mach 18 was not able to achieve overall wing deflections of this level, even with severe damage.

Hand analyses were performed to determine the maximum deflections that could occur on the lower wing skin panels. Three components were considered to cause the deflections. The first was a differential pressure across the panels. The difference in the free stream flow and the heated intermediate wing compartment was calculated to be 0.25 psi. This delta pressure was based on a pressure coefficient (Cp) of 1.0 and a dynamic pressure of 70 psf. The external pressure was approximately 0.5 psi with an

internal pressure of 0.25 psi, post breach. Potential loss of rib capability was considered as part of the analysis. As the loss of a rib can effectively double the width of the analysis panel, this can have a significant effect on the deflections calculated. For example, deflection increases as the fourth power of panel width based on this uniform pressure loading. To account for the partial effectivity of the rib cap, after the rib struts are lost, a factor (Leff Factor in Table 7.5-14) was assumed to produce an effectively shorter panel. The loss of the Yo198 rib is somewhat less effective based on the presence of the MLG door hinge backup structure found between panels 4,5, and 6. The effect of the loss of the rib between panel 8 and 9 is also less, because the rib is relatively short.

Two thermal scenarios were considered in addition to the pressure deflection: a thermal gradient across the honeycomb panel face sheets and a de-bonding of the inner face sheet. The deflection due to thermal gradient is a function of temperature differential from the inner to outer face sheet. This deflection increases as square of the panel width. The loss of the inner face sheet assumes a new stable configuration occurring when the tile gaps (.045 inch design; 0.050 inch assumed) are closed. Once the de-bonding occurs and the stable configuration has been reached, it was assumed that the outer face sheet acts as a membrane. This deflection is also a function of the square of panel width. The de-bond deflection is additive with delta pressure, but not thermal gradient deflection.

The hand analyses show that larger deflections are possible if a face sheet de-bond occurs. Note that this local, non-linear deflection scenario was not modeled in the FEM. The hand analysis results are shown in Table 7.5-13 and Table 7.5-14, with the wing panel layout shown in Figure 7.5-13. The results indicate that deflections are still relatively small without the loss of any ribs. Expanding the analysis to include damaged ribs, however, indicates that deflections of up to 5” are possible with the loss of three ribs and debond of the inner facesheet.

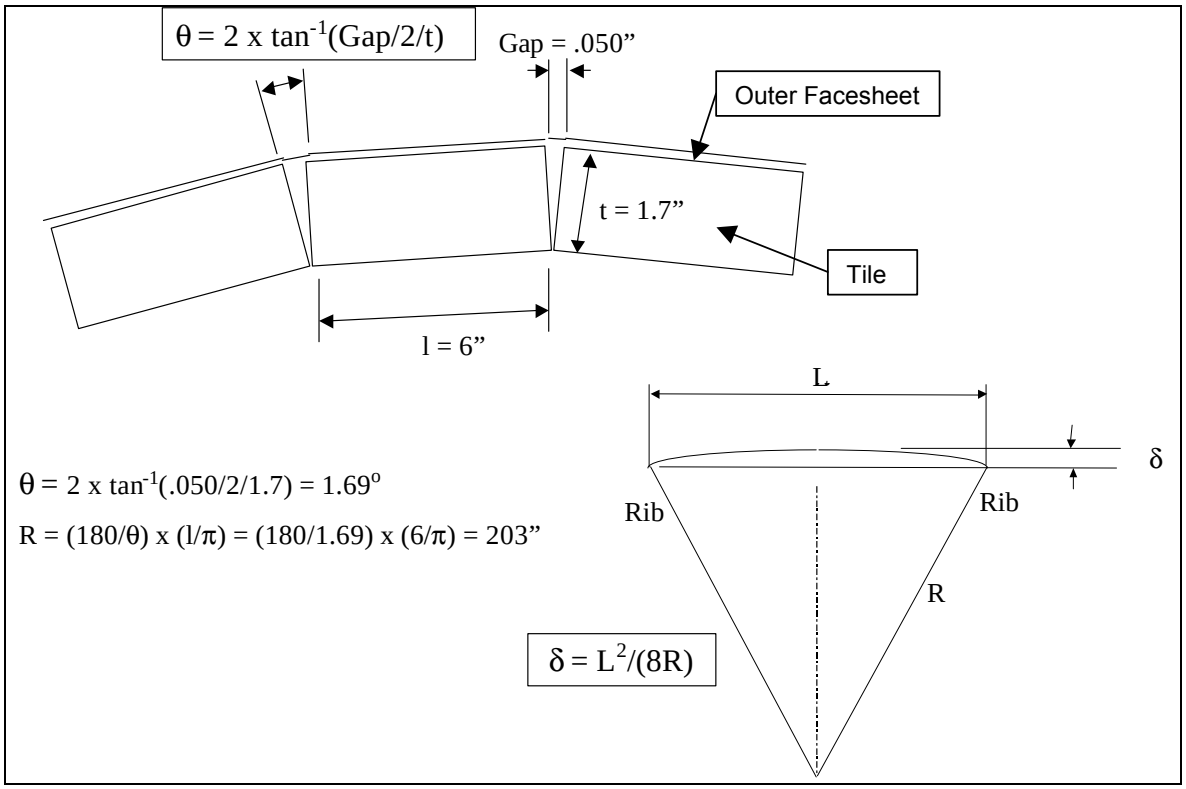

Figure 7.5-13 Calculations for Outer Facesheet and Tile Deflection

Table 7.5-13 Refined Wing Damage, Panel Deflection Results

Single Panel (Ribs Intact)									
Panel ID	Length	Leff Factor	Leff	Deflection for DP	Tile Gap	Deflection	Total Deflection	Yinbd	Youtbd
4	31	1	31	0.015	0.05	0.61	0.63	167	198
5	31	1	31	0.022	0.05	0.61	0.63	167	198
6	31	1	31	0.017	0.05	0.61	0.63	167	198
7	28	1	28	0.027	0.05	0.50	0.53	198	225
8	28	1	28	0.035	0.05	0.50	0.54	225	254
9	28	1	28	0.035	0.05	0.50	0.54	254	282

Table 7.5-14 Refined Wing Damage, Multi-Panel Deflection Results

Multiple Panel										
Panel ID	Length	Leff Factor	Leff	Deflection	Tile Gap	Deflection	Total Defl	Yinbd	Youtbd	Condition
4,5,6,7	59	0.8	47	0.13	0.05	1.42	1.56	167	225	1 rib lost
7,8	56	0.9	50	0.31	0.05	1.62	1.93	198	254	1 rib lost
4,5,6,7,8	87	0.7	61	0.67	0.05	2.37	3.04	167	254	2 ribs lost
4,5,6,7,8,9	115	0.65	75	1.52	0.05	3.56	5.09	167	254	3 ribs lost

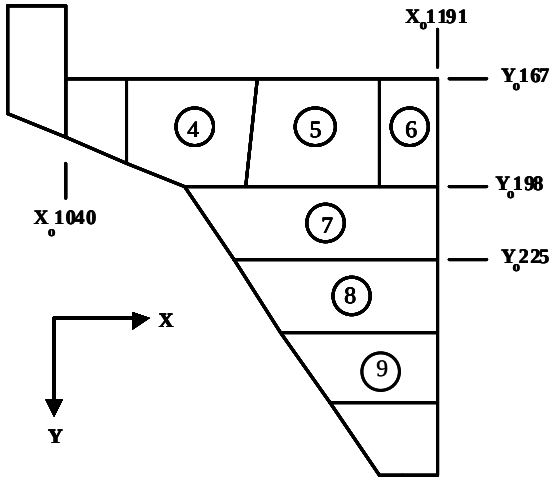

Figure 7.5-14 Lower Wing Panel Layout

7.5.6 Conclusions

Three distinct phases of analysis were performed on the OV-102 wing in order to help determine the most probable cause of the vehicle breakup. The “initial” analysis phase was performed to assess gross wing failure possibilities due to localized weakening of wing structural members. Results from this analysis showed that, although localized load increases do occur, the possibility of a gross wing failure or further damage propagation due to localized damage is highly remote. The “extended” analytical phase expanded the damage to larger areas of the forward and intermediate wing sections. These analyses attempted to quantify the effects of losing major portions of the intermediate wing structure. For this analysis, complete bottom to top “cuts” were made at critical structural locations around the main landing gear door wheel well, the wing leading edge spar and the honeycomb skin panels on the top and bottom wing surfaces. Results showed significant load redistribution throughout the wing; however, no structural members were shown to fail. The “refined” phase changed the investigative focus to a damage case that reflected the probable scenario occurring prior to the breakup. This analysis was initiated at the request of the Orbiter Aerodynamics groups in order to support an integrated analysis of the wing deformation. A combination of FEM analyses and hand analyses were used for this phase. The FEM results showed a change in overall wing panel deflections of approximately ¾”. However, hand analyses were able to show up to 5” inch deflections of the wing lower surface with de-bonded inner wing skin facesheets and loss of the intermediate wing ribs outboard of Yo167.

7.6 Stress Appendix

Appendix for Section 7.2

Table 7.6-1 FEM Summary Table of Results

		Temperatures									Results		
Case	Description	Default	Spar Web	Upper Skin	Lower Skin	Upper Spar Cap	Lower Spar Cap	Obd/Aft Upper Skin	Other (see notes)		Stress	Microstrain	Notes
4A	Calibration Case	70	70	70	70	70	70	70	-	Upper Cap (5073)	0	0	
										Lower Cap (5090)	0	0	
4B	Equal heating of spar web, upper and lower skins	70	180	180	180	70	70	70	-	Upper Cap (5073)	3749	354	
										Lower Cap (5090)	4445	419	
4C	Heating of only outboard, aft upper skin	70	70	70	70	70	70	400	-	Upper Cap (5073)	6668	629	
										Lower Cap (5090)	451	43	Nodes 73, 84, 95, 104, 103, 116, 141, 129
4D	Heat spar web, upper & lower skins, and outboard aft upper skin	70	180	180	180	70	70	400	-	Upper Cap (5073)	10416	983	
										Lower Cap (5090)	4896	462	
4E	Unequal heating of spar web, upper and lower skins	70	110	180	180	70	70	70	-	Upper Cap (5073)	3025	285	
										Lower Cap (5090)	2935	277	
4F	Heat lower skin near spar only	70	70	70	180	70	70	70	-	Upper Cap (5073)	-171	-16	
										Lower Cap (5090)	2210	208	
4G	Heat WLE nodes near panels 8/9	70	70	70	70	70	70	70	400	Upper Cap (5073)	-276	-26	
										Lower Cap (5090)	-602	-57	Nodes at y226 to 400°F
4H	Heating of only outboard, aft lower skin	70	70	70	70	70	70	70	400	Upper Cap (5073)	-377	-36	
										Lower Cap (5090)	119	11	Outboard, aft lower skin
4I	Heat spar web nodes only	70	110	70	70	70	70	70	-	Upper Cap (5073)	413	39	
										Lower Cap (5090)	863	81	Compare to 4E
4J	Heat sections of y167 Rib	70	70	70	70	70	70	70	200	Upper Cap (5073)	1	0	
										Lower Cap (5090)	5	0	167 Rib Web Nodes to 200°F
4K	Heating of only outboard, aft upper skin (see 4C)	70	70	70	70	70	70	200	-	Upper Cap (5073)	2627	248	
										Lower Cap (5090)	178	17	Compare to 4C
4L	Heating of only upper spar cap nodes	70	70	70	70	150	70	70	-	Upper Cap (5073)	-5474	-516	
										Lower Cap (5090)	-343	-32	
4M	Heating of only aft upper skin (wheel well)	70	70	70	70	70	70	70	200	Upper Cap (5073)	1273	120	Heating of aft upper skin in MLGD compartment
										Lower Cap (5090)	-108	-10	
4N	Heating of only aft upper skin (wheel well)	70	70	70	70	70	70	70	200	Upper Cap (5073)	3951	373	
										Lower Cap (5090)	-184	-17	4M plus nodes 73,95,103,116,129
M1	Mechanical load case TABR 2130 No Damage	-	-	-	-	-	-	-	-	Upper Cap (5073)	-1472	-139	
										Lower Cap (5090)	5868	554	
M2	Mechanical load case TABR 2130 Removed outboard aft upper skin	-	-	-	-	-	-	-	-	Upper Cap (5073)	-1432	-135	
										Lower Cap (5090)	5802	547	
A1	Combined heating	70	110	110	110	110	70	145	-	Upper Cap (5073)	141	13	
										Lower Cap (5090)	1549	146	
A2	Combined heating II	70	145	145	145	145	75	-	190	Upper Cap (5073)	-116	-11	Lose outboard aft upper skin (set to 70) Heat nodes 73,95,103,116,129 only
										Lower Cap (5090)	2388	225	
A3	Combined heating III	70	175	175	175	175	80	-	215	Upper Cap (5073)	777	73	
										Lower Cap (5090)	3082	291	Heat aft upper skin (wheel well) to 215
A4	Combined heating IV	70	175	175	175	175	90	-	260	Upper Cap (5073)	2122	200	
										Lower Cap (5090)	2513	237	Heat aft upper skin (wheel well) to 260

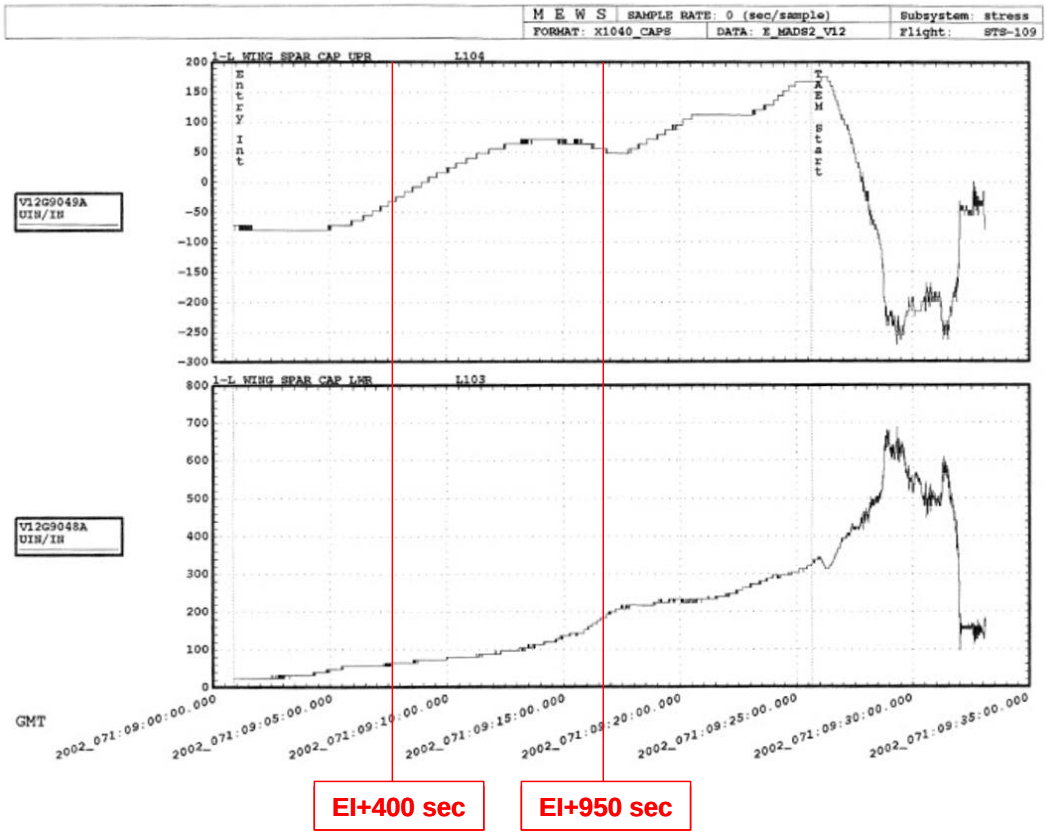

Figure 7.6-1 STS-109 Nominal Entry Strains

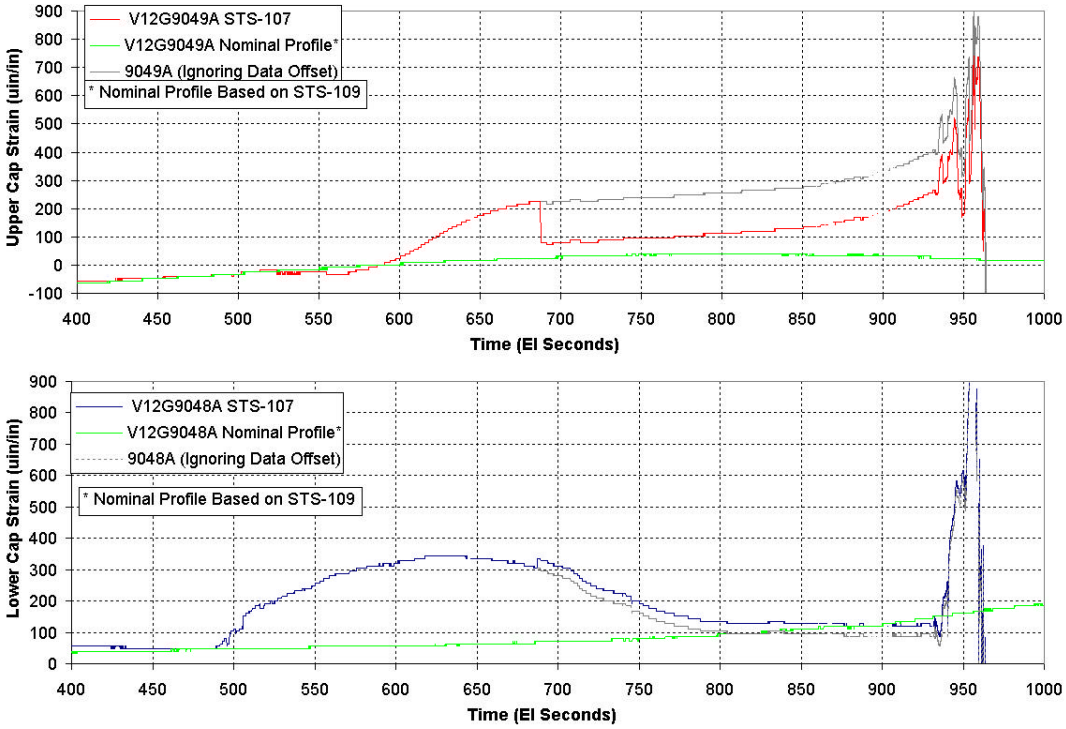

Figure 7.6-2 STS-107 Full Data Reconstruction

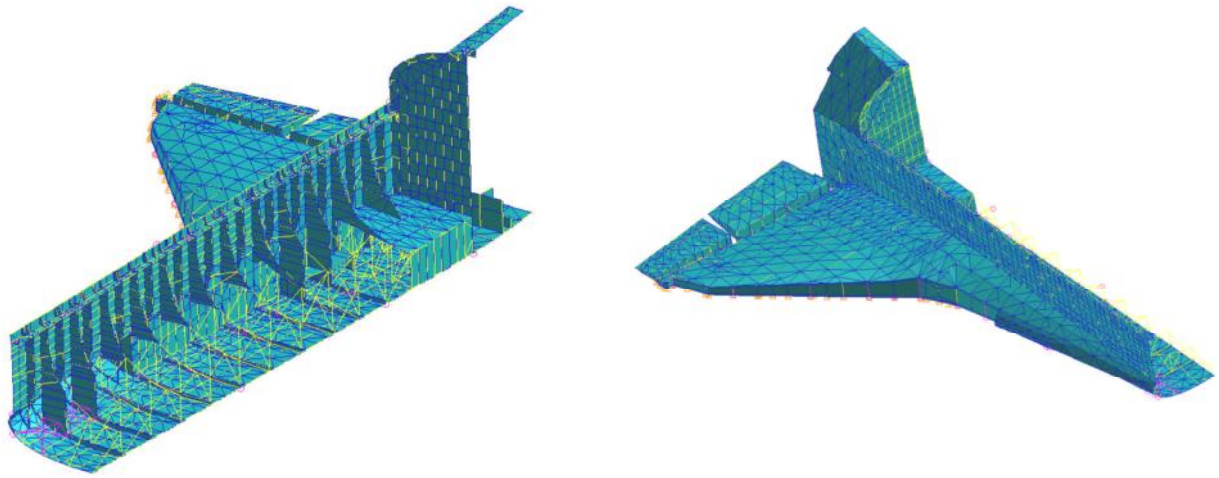

Figure 7.6-3 Complete FEM Model Illustration

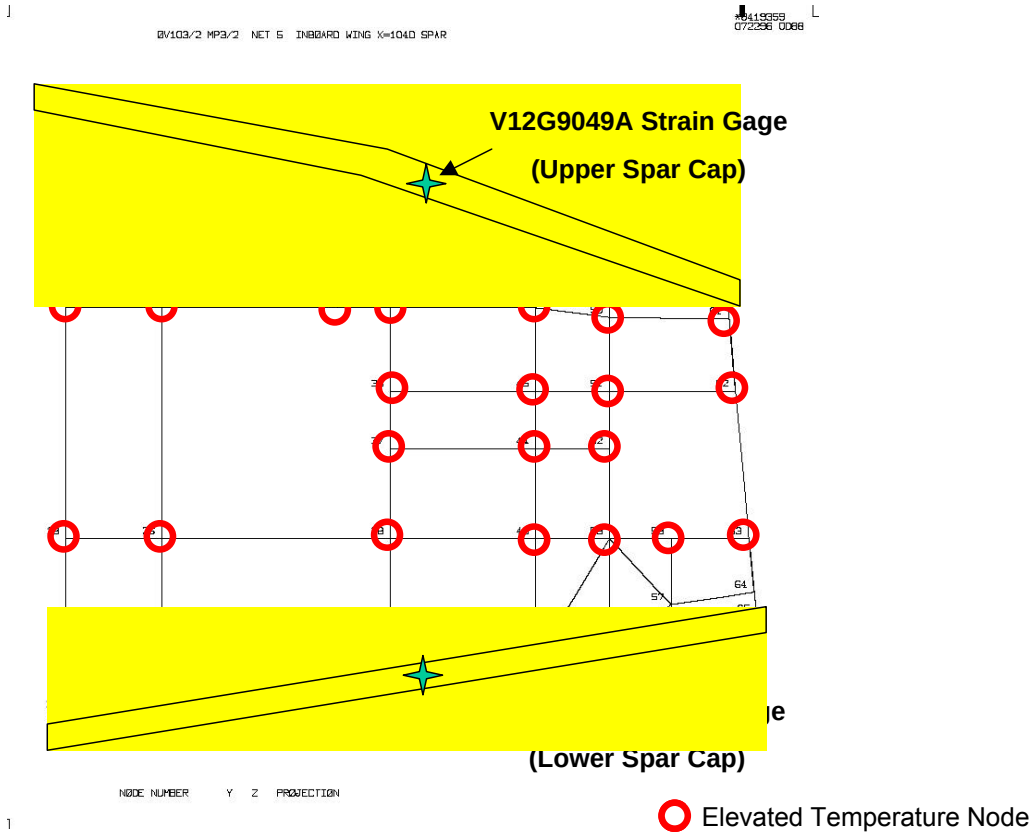

Figure 7.6-4 FEM Illustration, Xo1040 Spar Nodes

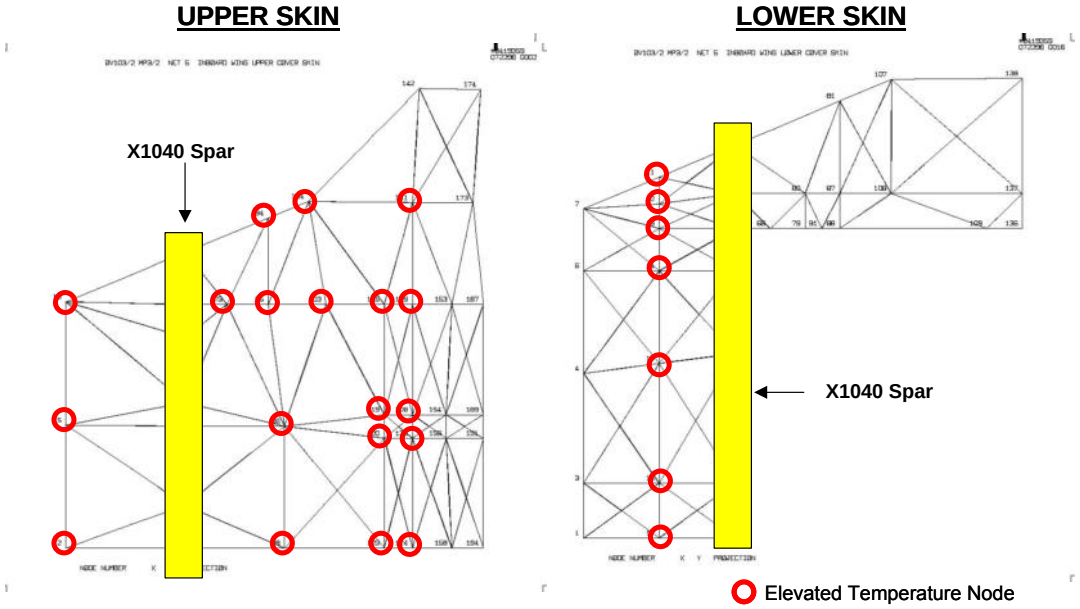

Figure 7.6-5 FEM Illustration, Nearby Skin Nodes

Appendix for Section 7.3

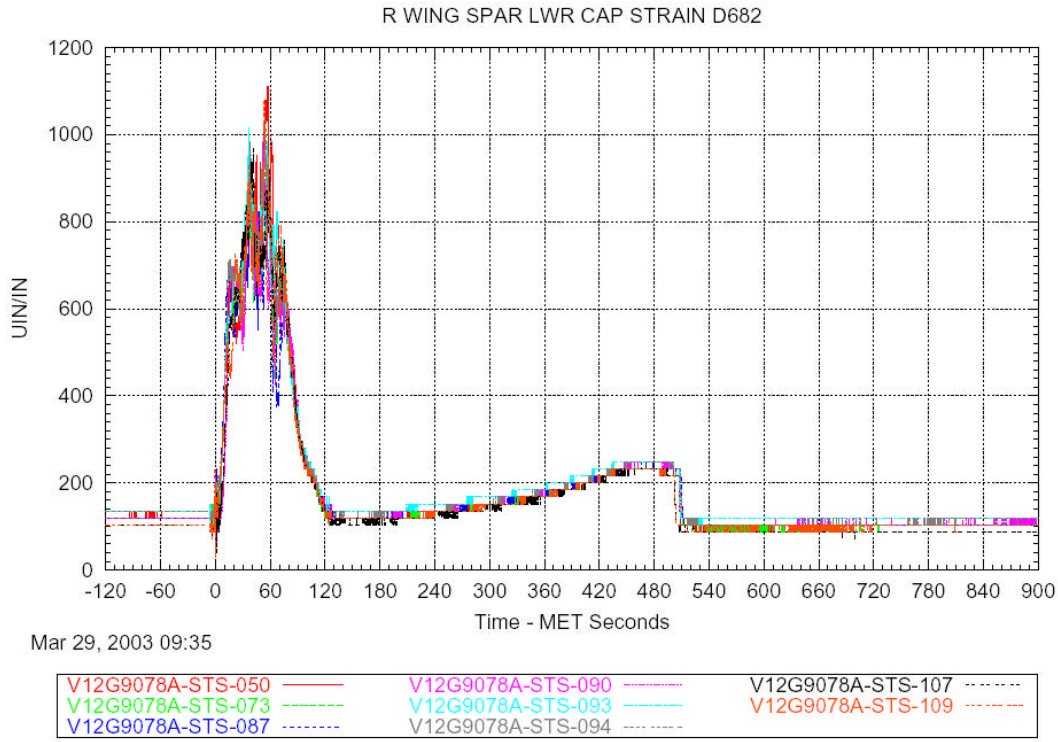

Figure 7.6-6 Typical Ascent Response

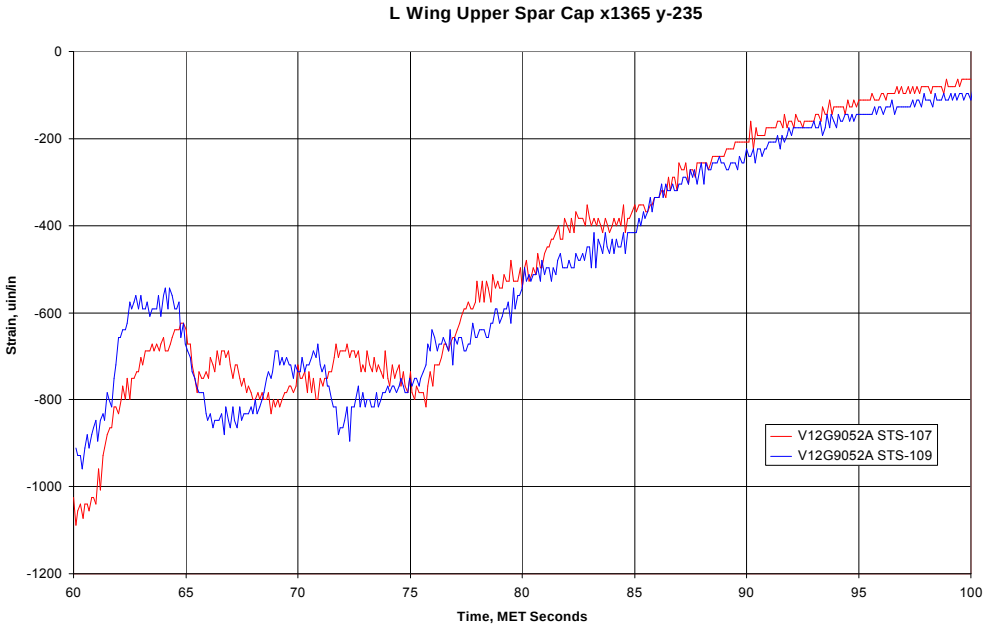

Figure 7.6-7 Interesting Signature Near Suspect Debris Impact Event

642

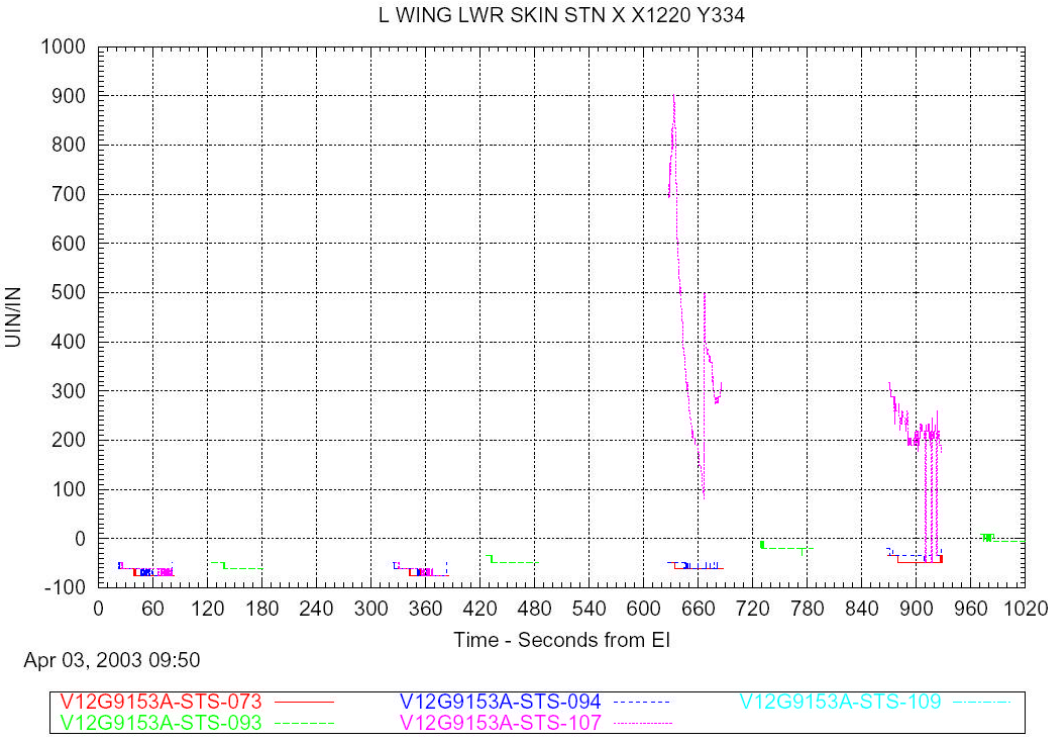

Figure 7.6-8 Typical PCM3 Entry Response

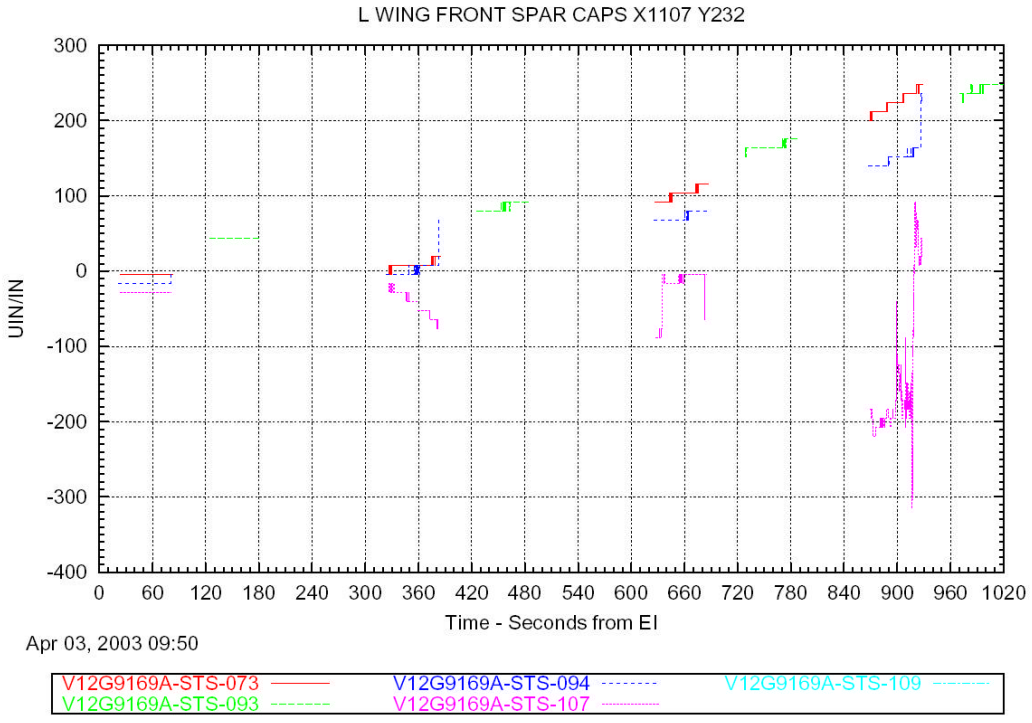

Figure 7.6-9 PCM3 Entry Response With Suspected Off-Nominal Trend

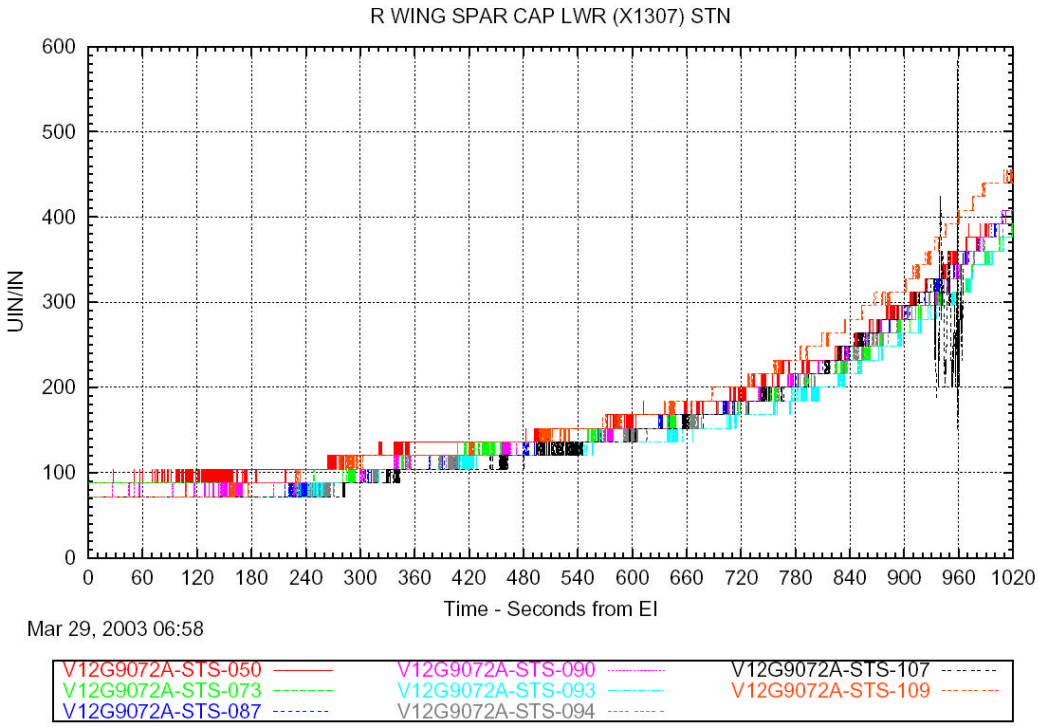

Figure 7.6-10 Typical, Nominal Right Wing Entry Response

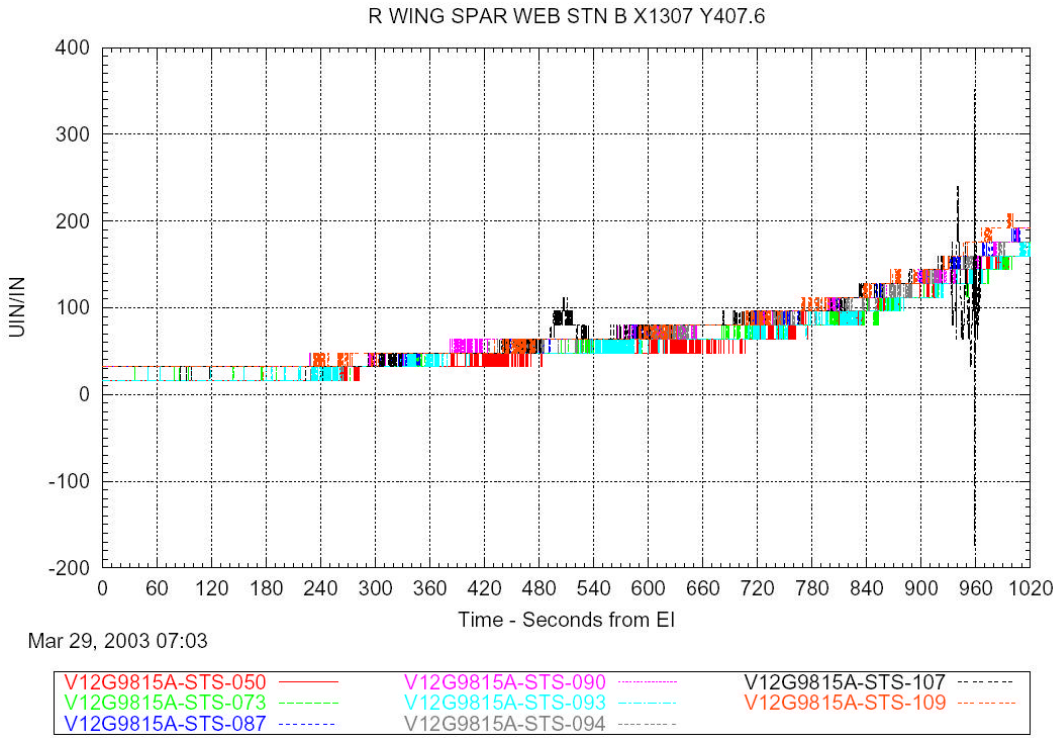

Figure 7.6-11 Right Wing Entry Brief Off-Nominal Response With Subsequent Return to Nominal

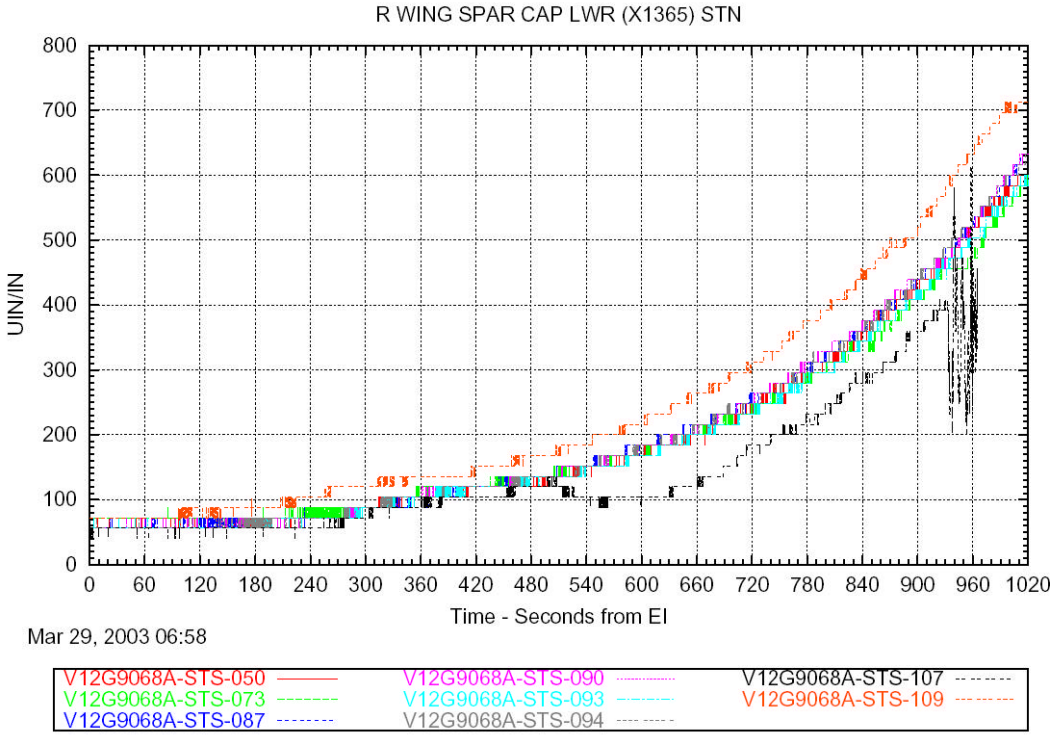

Figure 7.6-12 Right Wing Entry Off-Nominal Response With Subsequent Data Offset

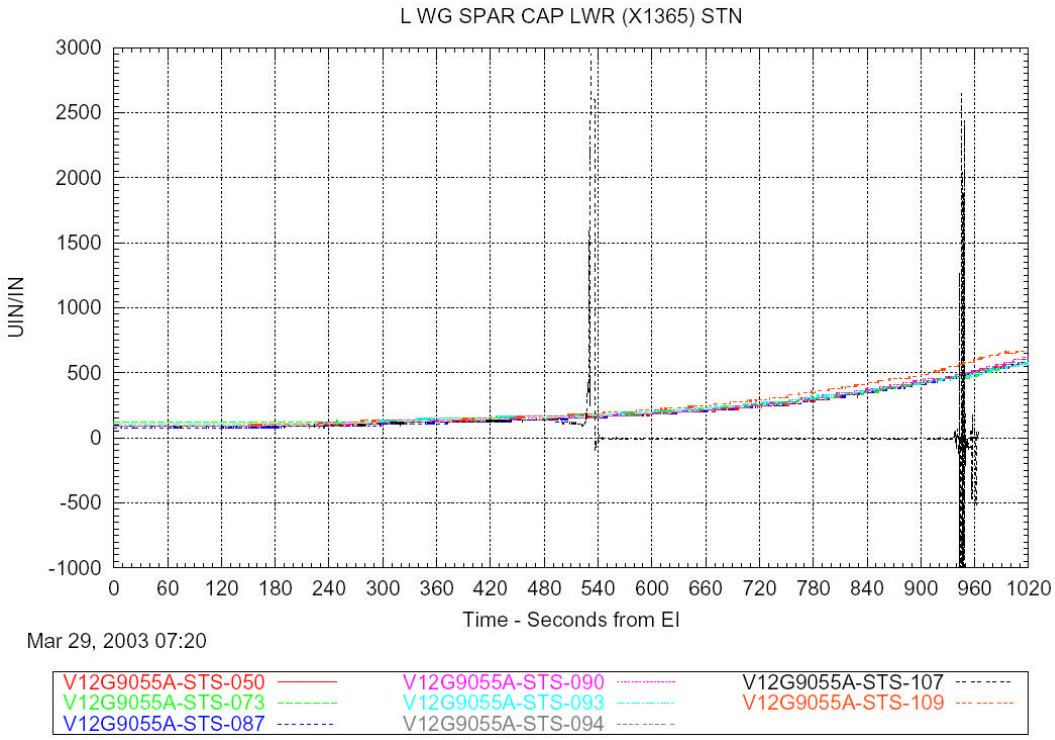

Figure 7.6-13 Typical Left Wing Entry Gage Failure

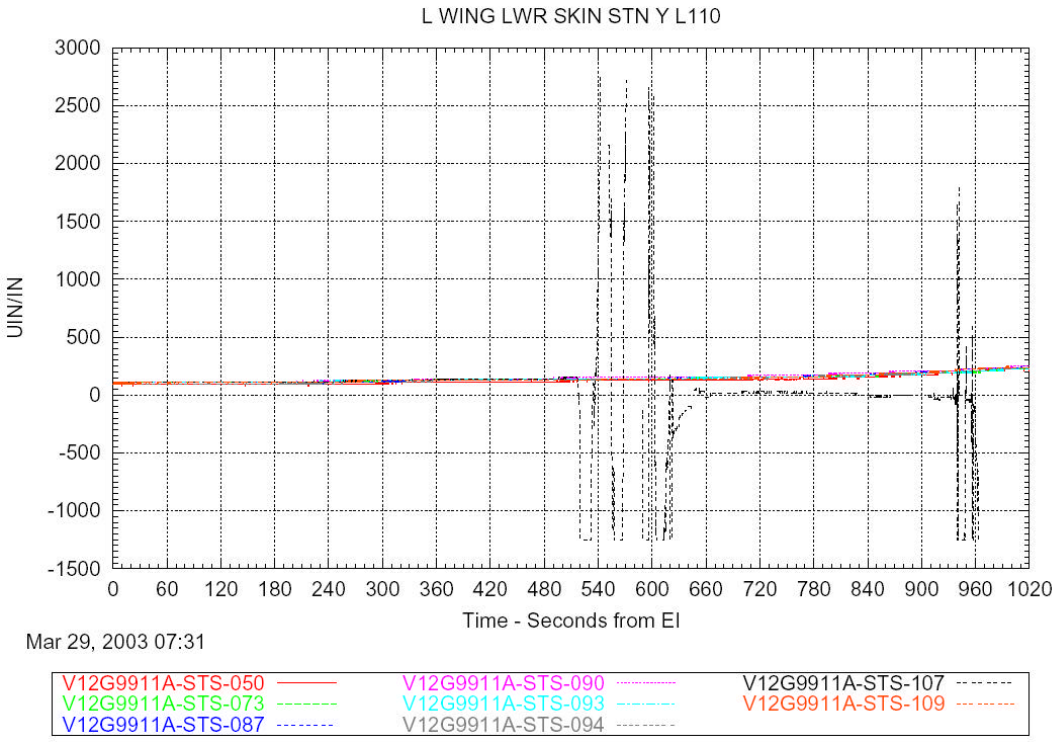

Figure 7.6-14 Left Wing Entry Gage Failure With Multiple Off-Scale Oscillations

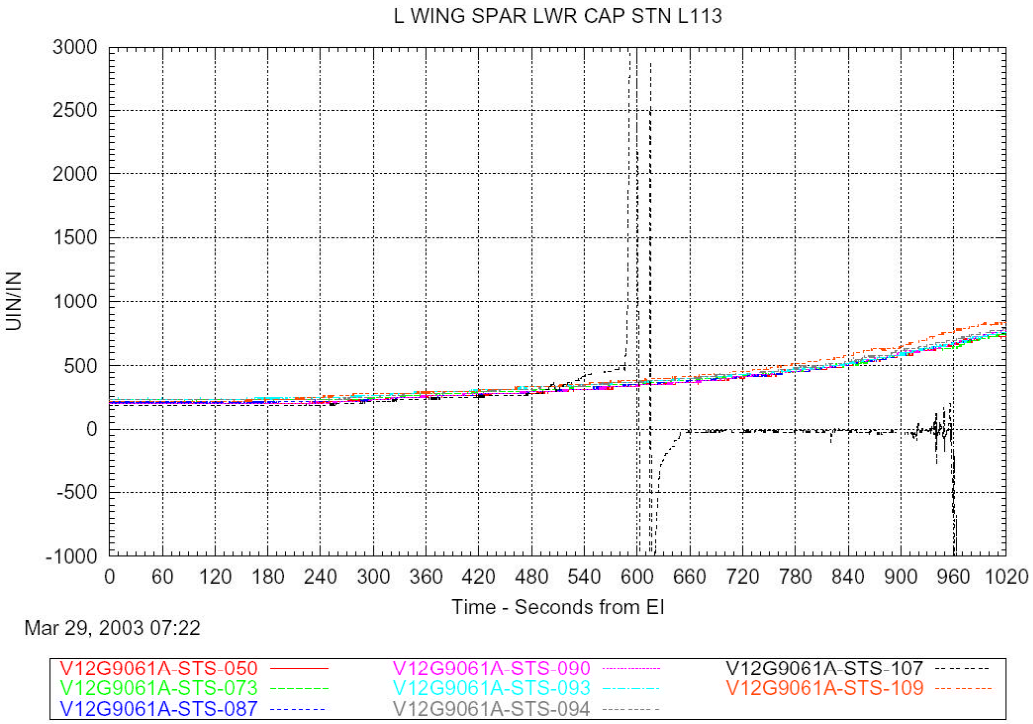

Figure 7.6-15 Left Wing Entry Gage Failure With Preceding Off-Nominal Inflection

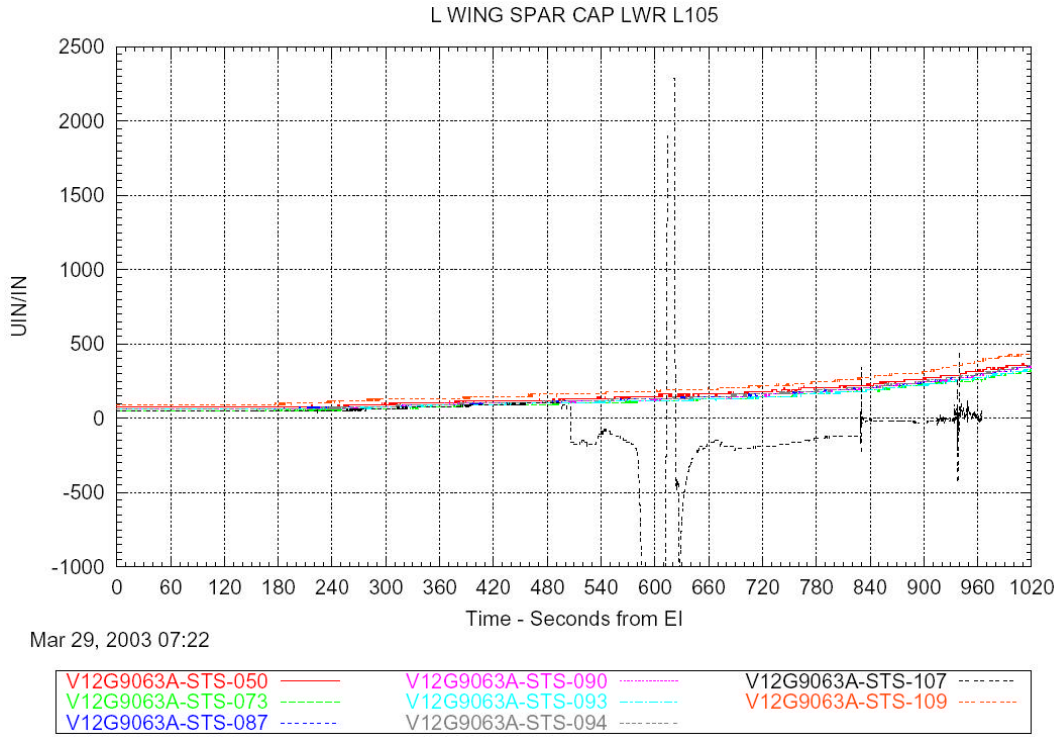

Figure 7.6-16 Left Wing Entry Gage Failure With Subsequent Nonzero Response

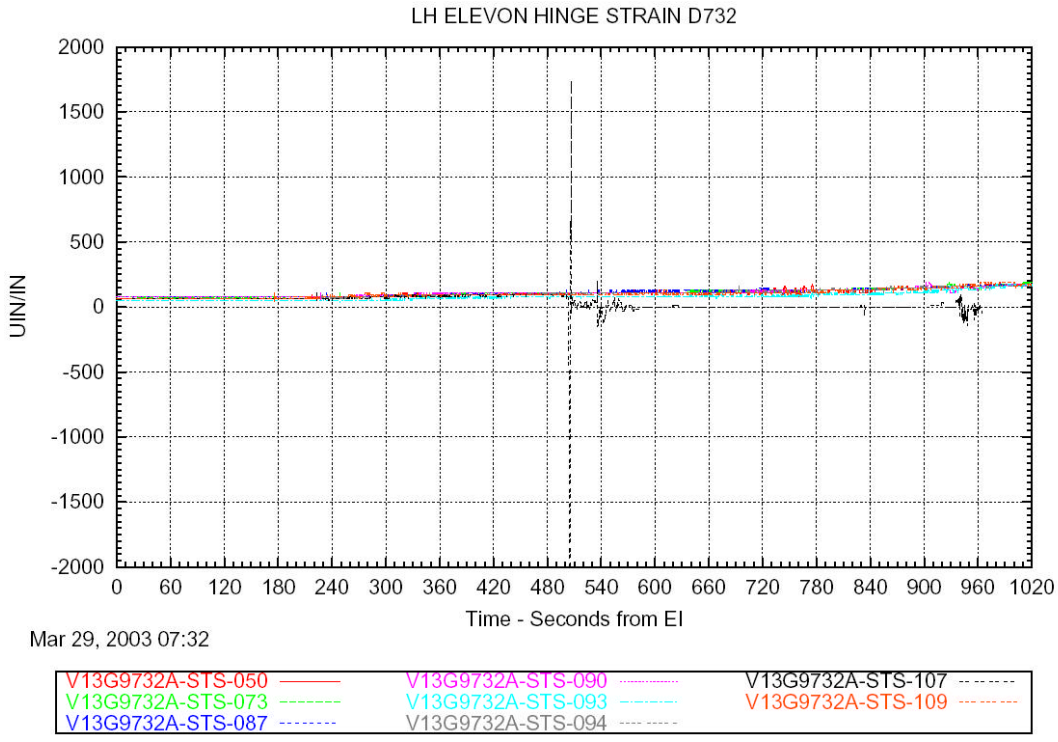

Figure 7.6-17 Typical Left Wing Elevon Entry Gage Failure

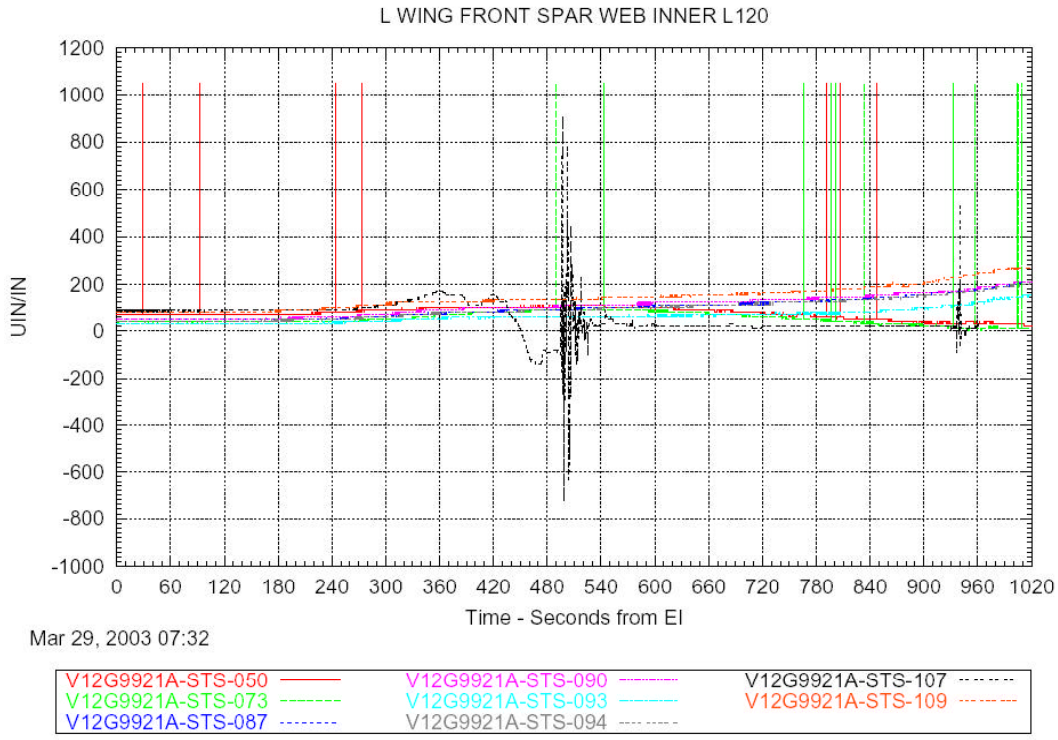

Figure 7.6-18 V12G9921A Entry Response

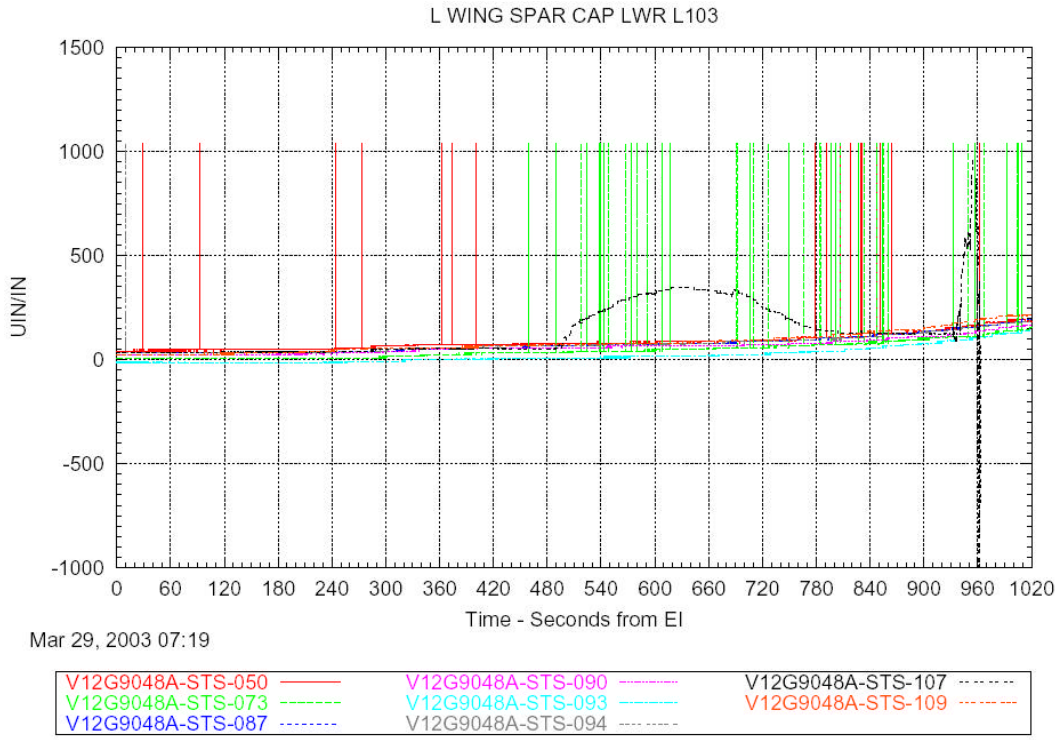

Figure 7.6-19 V12G9048A Entry Response

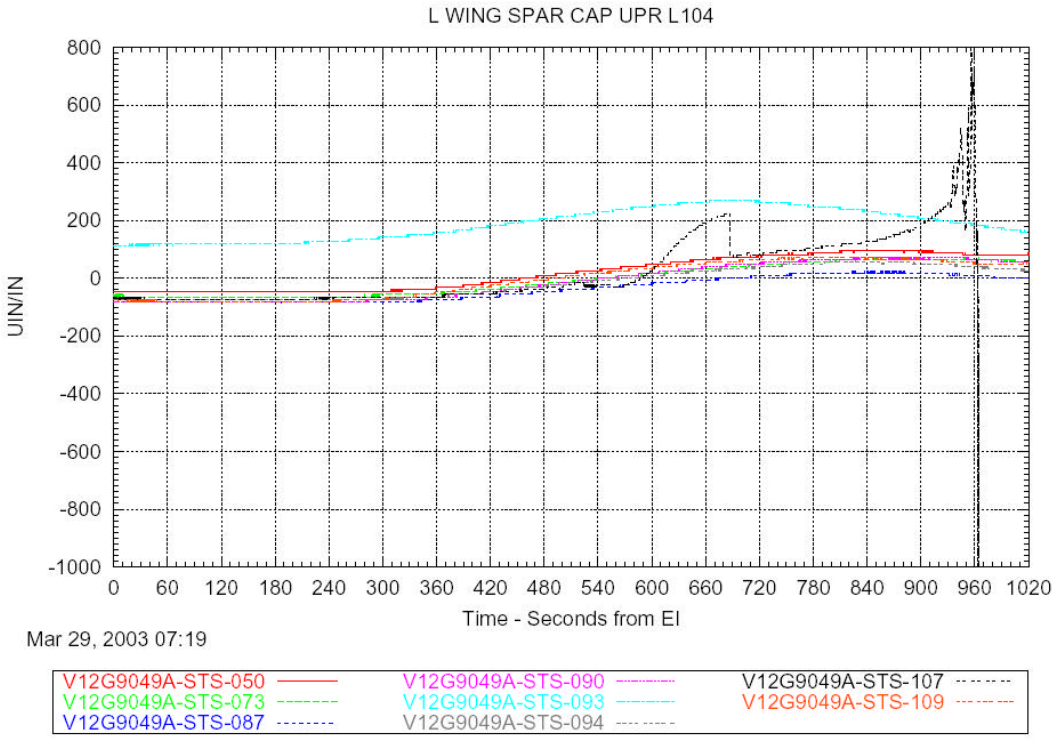

Figure 7.6-20 V12G9049A Entry Response

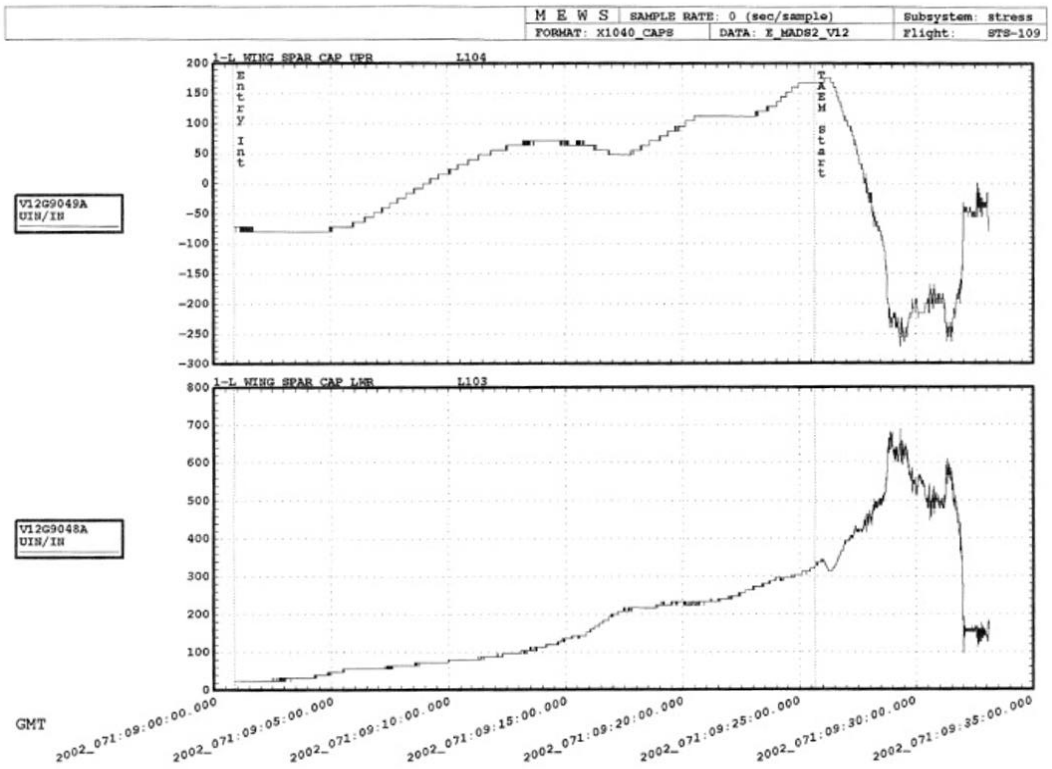

Figure 7.6-21 Xo1040 Spar Caps Nominal Entry (STS-109)

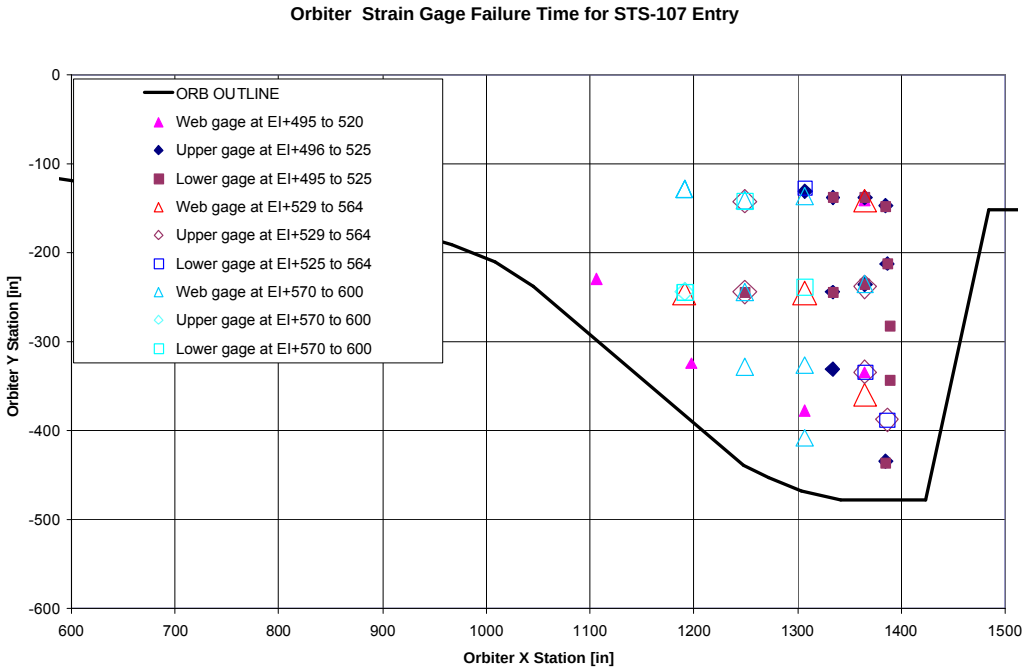

Figure 7.6-22 Left Wing Strain Gage Failure Times

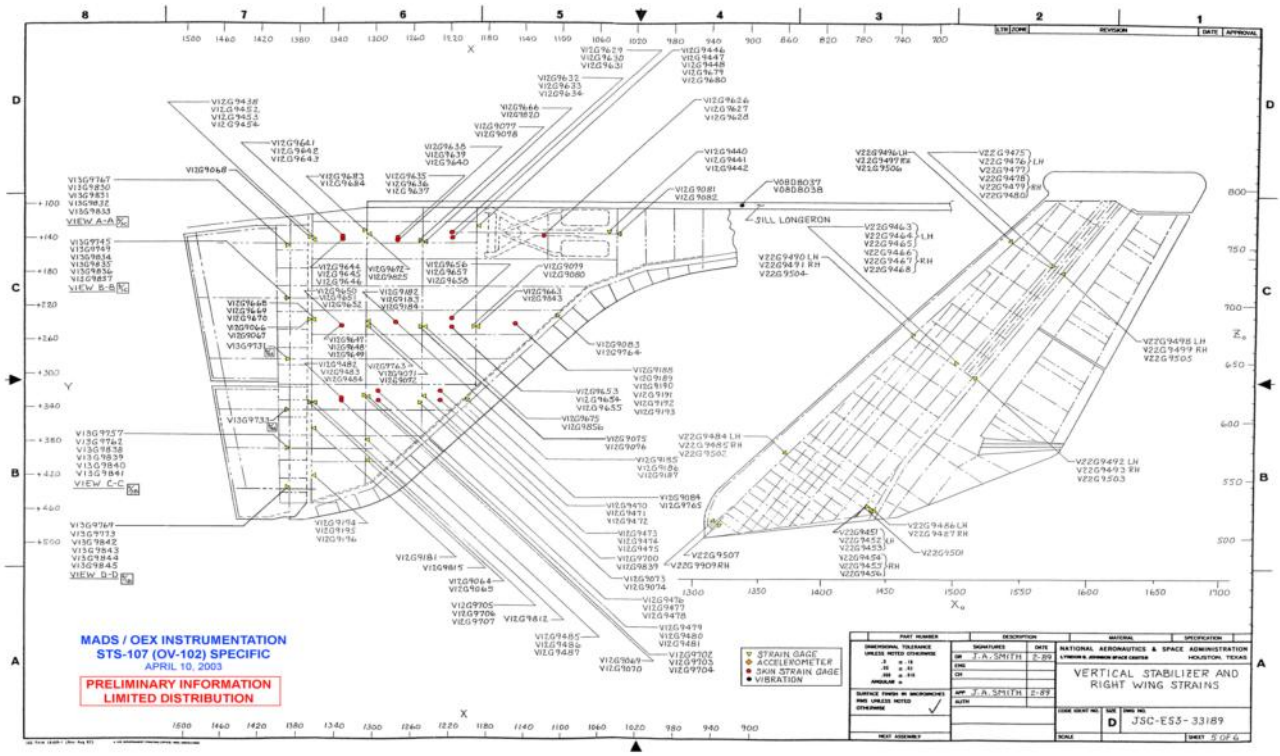

Figure 7.6-23 Right Wing Strain Gage Locations

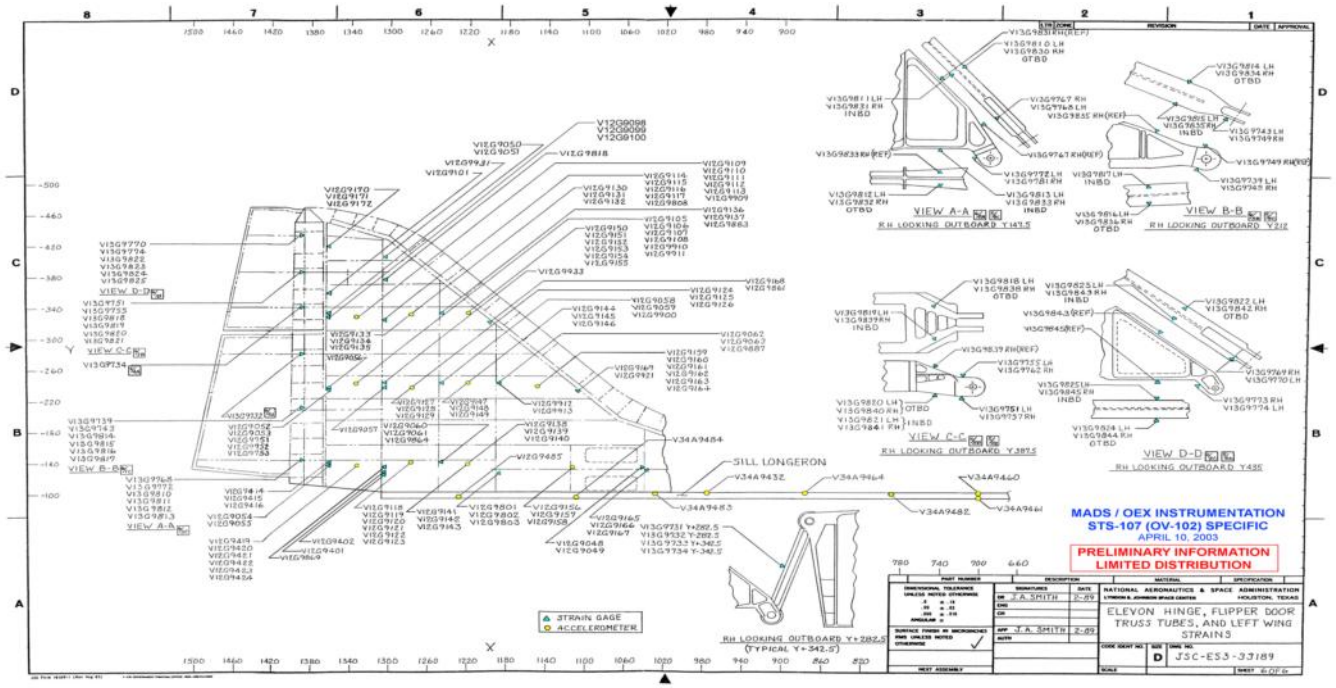

Figure 7.6-24 Left Wing Strain Gage Locations

7.7 Reference – MADS PCM Installation Drawings

Installation drawings for MADS PCM strain gages are as follows:

M072-754119
M072-754120
M072-755107
M072-756106
MC621-0004
V070-784102
V070-786117
VR70-754001

The appropriate drawing for a given strain gage installation may be determined from reference to document number JSC 23560, “OV-102 Modular Auxiliary Data System Measurement Locations”. All relevant installation drawings are included for reference in the data CD that accompanies this report.

8 CONCLUSIONS

The Aerodynamic/Aerothermodynamic/Thermal/Structures Team has completed analyses to support the Columbia Accident Investigation. The completion of this activity has resulted in the formulation of a most probable initial damage and damage progression scenario that can be used with results of other teams to identify the root cause of the Columbia accident.

The culmination of multiple analyses and tests suggest the following entry damage scenario:

Entry Interface to spar burn through:

Columbia began entry with damage to the wing leading edge reinforced-carbon-carbon (RCC) most likely in panels 7 or 8.

Hot gas was ingested into the cavity behind the RCC panels from the beginning of the entry profile. Internal aerothermodynamic and venting analyses show that the flow of hot gas into the RCC cavity was vectored outboard down the RCC cavity and up and aft toward the top of the wing leading edge spar. The hot gas impinged on the RCC panel rib and spanner beam insulation resulting in very high localized heating.

The panel 9 spar strain gage registered the first off-nominal indications at approximately 270 seconds from EI. Stress analysis shows that the panel 9 spar strain gage readings are consistent with shear strain associated with a temperature gradient that developed as the top of the spar is heated by the ingestion of hot gas.

Panel 9 clevis temperature began an off-nominal temperature increase at approximately 290 seconds from EI due to heating from conduction through the insulation and heating from convection due to sneak flow between the insulation and the clevis. Thermal analysis suggests that this response is consistent with flow entering an aperture with an area consistent with a ten inch diameter hole.

CFD analysis and wind tunnel test results modeling increased flow out of thermally degraded/expanded vents located at the top of the RCC cavity suggest that disturbed flow on the leeside of the vehicle can displace the strake and canopy vortices and temporarily reduce localized heating to the left sidewall and left OMS pod.

The damage magnitude is consistent with negligible aerodynamic increments experienced during this period.

Spar burn through to off-nominal increase in sidewall and OMS pod temperatures:

Spar burn through occurred by approximately 487 seconds from EI. This time is supported by:

Wing Spar Strain analysis	-> 420 - 470 sec
1040 Spar Strain analysis	-> 488 sec
Leading Edge Spar wire harness failure	-> 487 sec
Bit flip in wheel well measurement	-> 488 sec
Panel 8/9 thermal analysis	-> 490 sec

Analyses of spar burn through times suggest that the initial damage was consistent with a breach in the lower portion of RCC panel 8 with an area consistent with a six to ten inch diameter hole.

CFD analysis suggests that the transverse momentum of the flow of hot gas entering the RCC cavity is redirected as the flow impinges on RCC ribs and spanner beam hardware and insulation. As a result, the local pressure is increased and the plume entering the intermediate wing is directed normal from the spar toward the main landing gear compartment wall.

Thermal analysis of plume heating on wire bundles and the wheel well wall supports the location of the breach on the panel 8 spar.

Thermal analysis of measured temperature profiles for components in the wheel well show that convective heating is required to produce the measured results. This is consistent with the modeled burn through of the main landing gear compartment wall at approximately EI+601 seconds.

Increased heating of the left sidewall and OMS pod can be explained by redirection of the wing leading edge windward flow to the leeside through either a severely damaged and/or missing upper RCC carrier panel(s), severely damaged or missing full RCC panel (e.g. panel 9), or damaged upper wing just aft of the wing leading edge. Test and analyses of these damage conditions yields aerodynamic increments consistent with flight extracted aero between EI+500 to EI+600 seconds.

Evaluation of final aerodynamic increments:

Damage in the left wing cavity continued to progress until loss of signal. This damage resulted in a significant depression forming on the lower surface of the left wing due to burn though of intermediate wing truss tubes and compromised structural strength associated with heating internal to the wing. The depression in the lower wing resulted in external flow patterns that effectively increased the lift and drag on the left wing resulting in the large positive rolling moment and large negative yawing moment just prior to loss of signal.

As a final comment on the damaged configuration test and analysis results, it must be pointed out again that the nature of this analysis and the conclusions to be drawn from them should be limited to a proper engineering perspective. The test and analysis conducted for the investigation were performed on representative geometries. The representative geometries that have been assessed were chosen in a very dynamic investigation environment as engineers interpreted the latest results from wind tunnel testing, CFD analysis, flight measurement evaluation, recovered hardware forensics, etc. The fact that these geometries were chosen for investigation purposes should not be misconstrued as exactly reproducing the damaged configuration encountered in flight. These representative damaged configurations, however, do provide an insight into the nature and level of damage necessary to result in the loss of Columbia and her STS-107 crew.

9 CREDITS

The authors wish to recognize the outstanding efforts of the many personnel that directly or indirectly supported the AATS team. Numerous personnel from various organizations provided data, products or services in support of AATS team activities. Personnel supporting the accident investigation primarily through the AATS team are listed in Appendix B of this report. Many others, however, provided support through other teams and therefore are not individually credited here. The following teams are recognized for providing essential support to the AATS team:

Timeline Team
Vehicle Data Mapping Team
Integrated Entry Environments Team
Hardware Forensics Team
Scenario Team

In addition, many AATS team members did not author parts of this final report even though they were key contributors on the team, mostly due to reassignment to other activities later in the investigation. These individuals provide invaluable expertise, especially during the initial phase of the investigation. These team members are listed below:

Aerodynamics
Gary Bourland, NASA Johnson Space Center
James Brown, NASA Ames Research Center
Joe Gamble, NASA Johnson Space Center
Jim Greathouse, NASA Johnson Space Center
Gerald LeBeau, NASA Johnson Space Center
Chris Madsen, NASA Johnson Space Center
Charles Miller, NASA Langley Research Center
Phil Stuart, NASA Johnson Space Center

Aerothermodynamics
Ed Alexander, Boeing Houston
Maria Barnwell, Boeing Houston
Basil Hassan Ph. D., Sandia National Laboratories
Ron Merski, Ph. D., NASA Langley Research Center
Charles Miller, NASA Langley Research Center
Habib Sharifzadeh, Boeing Huntington Beach
Carl Peterson, Sandia National Laboratories
Richard Wheless, NASA Langley Research Center

Thermal
Stan Bouslog, Lockheed
Kevin Bowcutt, Boeing Huntington Beach
Doug Cline, Boeing Houston
Dianna Coronado, Boeing Houston
Don Curry, NASA Johnson Space Center
Fred Ghayasi, Boeing Huntington Beach
Andy Hong, NASA Johnson Space Center
John Kowal, NASA Johnson Space Center
Ronald K. Lewis, NASA Johnson Space Center
Jim Milhoan, Lockheed
Don Picetti, Boeing Huntington Beach
Steve Rickman, NASA Johnson Space Center
Dave Russell, Boeing Houston
Habib Sharifzadeh, Boeing Huntington Beach
John Sharp, NASA Marshall Space Flight Center
Lung-Chen Wong, Boeing Houston

Stress
Tony Chi, Boeing Huntington Beach
Scott Foust, Boeing Huntington Beach
Bill Novak, Boeing Huntington Beach
Dave Okino, Boeing Huntington Beach
Steve Scotti, NASA Langley Research Center

10 Acknowledgements

The work presented in this document is but a small demonstration of the total efforts of more than one hundred dedicated engineers and scientists across the country in support of the aerodynamic, aerothermodynamic, thermal, and structural analysis portion of this investigation. Those efforts are not only applicable to understanding Columbia's fate, but will also be used to improve future human space flight vehicle designs. Regardless of how outstanding our efforts, they merely shadow the tragic loss of Columbia and her crew. We dedicate these efforts and the immediate sacrifices of our families and loved ones since the morning of February 1, 2003, to Columbia, her crew, and the lifelong sacrifices of the crew's families and loved ones.

We would also like to recognize the devotion to space flight on the part of the Orbiter program engineers and flight controllers, as well as the dedication of the Space Shuttle and Orbiter program managers. The extreme energies put forth by the manned space flight community during this investigation must be acknowledged, for without their incredible insight, experience and focused drive, the understanding of Columbia's final flight would not have been possible within the allotted time frame. The passion exhibited by this team is the same unyielding dedication that keeps us moving forward, pursuing the vision of manned space flight.

Finally, we dedicate these results, the methods developed and the understanding acquired, to the future of manned space flight and all future crews. By pushing our limitations with each ensuing flight, we utilize the wisdom of the many sacrifices of the past in conjunction with our curiosity, to learn more and continue to follow the better path in mankind's quest for the stars.

References

1. NSTS-37376 Data Review and Timeline Reconstruction Team Final Report in support of the Columbia Accident Investigation

2. NSTS-37382 Integrated Entry Environment (IEE) Team Final Report in support of the Columbia Accident Investigation

3. NSTS-37383 Vehicle Data Mapping Final Report in support of the Columbia Accident Investigation

4. NSTS-37385 Hardware Forensics Team Final Report in support of Columbia Accident Investigation

5. NSTS-37386 Materials and Processes Failure Analysis Team Final Report in support of Columbia Accident Investigation

6. NSTS-37397 Vehicle Reconstruction Team Final Report in support of the Columbia Accident Investigation

7. NSTS-60502 Columbia Working Scenario Final Report

APPENDICES

Appendix A - Acronyms and Abbreviations

AATS	**Aerodynamic/Aerothermodynamic/Thermal/Structures**
ABLT	**Asymmetric Boundary Layer Transition**
ADTA	**Air Data Transducer Assembly**
aero	**Aerodynamic**
AFB	**Air Force Base**
Al	**Aluminum**
APU	**Auxiliary Power Unit**
ARC	**Ames Research Center**
ASA	**Reacting Flow Environments (Branch)**
BC	**Boundary Condition**
BFS	**Backup Flight System**
BHB	**Boeing Huntington Beach**
BL	**Boundary Layer**
BP	**Body Point**
B-RKDN	**Boeing Rocketdyne**
BTU	**British Thermal Unit**
CAD	**Computer-Aided Design**
CAIB	**Columbia Accident Investigation Board**
CART3D	**Cartesian Three Dimensional**
CF4	**Carbon Tetra-Flouride**
CFD	**Computational Fluid Dynamics**
CG	**Center of Gravity**
Comm	**Communication**
DAC	**DSCM Analysis Code**
DAO	**Data Assimilation Office**
DSMC	**Direct Simulation Monte Carlo**
EI	**Entry Interface**
ENV	**Environment**
EOM	**End of Mission**
FC	**Flight Control**
FCS	**Flight Control System**
FEM	**Finite Element Model**
FFT	**Fast Fourier Tranform**
FRSI	**Flexible Reusable Surface Insulation**
ft	**Feet**
FWD	**Forward**
GMT	**Greenwich Mean Time**
GN&C	**Guidance, Navigation and Control**
GNC	**Guidance, Navigation and Control**
GPS	**Global Positioning Satellite**
GRAM	**Global Reference Atmosphere Model**
GSFC	**Goddard Space Flight Center**
Hyd	**Hydraulic**
IEE	**Integrated Entry Environment**
IML	**Inner Mold Line**
IMU	**Inertial Measurement Unit**
INBD	**Inboard**
IR	**Infrared**
JSC	**Johnson Space Center**
Kn	**Knudsen Number**
KSC	**Kennedy Space Center**
LaRC	**Langley Research Center**
LE	**Leading Edge**
LESS	**Leading Edge Subsystem**

LG	**Landing Gear**
LH	**Left Hand**
LHIB	**Left hand Inboard**
LMG	**Left Main Gear**
LMSC	**Lockheed Management Sevices Company**
Ln	**Line**
LOS	**Loss of Signal**
LT	**Left**
M	**Mach**
MADS	**Measurement Acquisition Data System**
MEDS	**Multifunction Electronic Display Subsystem**
MET	**Mission Elapsed Time**
MLG	**Main Landing Gear**
MLGD	**Main Landing Gear Door**
MMOD	**Micro Meteoroid Orbital Debris**
MPH	**Miles per hour**
MPS	**Main Propulsion System**
MSFC	**Marshall Space Flight Center**
MSID	**Measurement Stimulus Identification**
NAIT	**NASA Accident Investigation Team**
NASA	**National Aeronautics and Space Administration**
NAV	**Navigation**
NLG	**Nose Landing Gear**
NSTS	**National Space Transportation System**
OADB	**Operational Aerodynamic Data Book**
OARE	**Orbital Acceleration Research Experiment**
OB	**Outboard**
ODRC	**Orbiter Data Reduction Complex**
OEX	**Orbiter Experimentation**
OFT	**Operational Flight Test**
OI	**Operational Instrumentation**
OML	**Outer Mold Line**
OMS	**Orbital Maneuvering System**
OSH	**Off Scale High**
OSL	**Off Scale Low**
OUTBD	**Outboard**
OVE	**Orbiter Vehicle Engineering**
OVEWG	**Orbiter Vehicle Engineering Working Group**
PCM	**Pulse Code Modulation**
PCM	**Pulse Code Modulation**
PDSS	**PRACA Data Support System**
PIC	**Pyro Initiator Controller**
PRACA	**Problem Resolution And Corrective Action**
Press	**Pressure**
PRSD	**Power Reactant Storage and Distribution**
PRT	**Prevention / Resolution Team**
PSD	**Power Spectral Density**
psf	**Pounds per square foot**
RCC	**Reinforced Carbon-Carbon**
RCG	**Reaction Cured Glass**
RCS	**Reaction Control System**
RMS	**Root mean square**
RTD	**Resistant Temperature Devise**
RTV	**Room Temperature Vulcanizing**
SABER	**Sounding of the Atmosphere using Broadband Emission Radiometry**
sec	**second**
SES	**Shuttle Engineering Simulator**
SGS	**Simple Geometric Shapes**
SiC	**Silicon Carbide**

SILTS	**Shuttle Infrared Leeside Temperature Sensing**
SLA	**Stereolithography**
SNL	**Sandia National Laboratories**
SOFI	**Spray On Foam Insulation**
SPR	**Suspect Problem Report**
SR&QA	**Safety, Reliability & Quality Assurance**
SSVEO	**Space Shuttle Vehicle Engineering Office**
STS	**Shuttle Transportation System**
Surf	**Surface**
Sw	**Switch**
Sys	**System**
TAEM	**Terminal Area Energy Management**
TAS	**True Air Speed**
TC	**Thermocouple**
Temp	**Temperature**
TEOS	**Tetraethyl Orthosilicate**
TIM	**Technical Interchange Meeting**
TIMED	**Thermosphere Ionosphere Mesosphere Energetics and Dynamics**
TMM	**Thermal Math Model**
TPS	**Thermal Protection System**
Unlk	**Unlock**
Uplk	**Uplock**
USA	**Unified Solution Algorithm**
USA	**United Space Alliance**
VGM	**Volume Grid Manipulator**
Vlv	**Valve**
VT	**Vertical Tail**
WBS	**Work Breakdown Structure**
WCT	**Wing Carry Through**
WLE	**Wing Leading Edge**
WSTF	**White Sands Test Facility**
WT	**Wind Tunnel**
WTT	**Wind Tunnel Test**

Appendix B - Team Member List & Biographies

Team Lead Biographies

Pam Madera
Ms. Madera has twenty years of experience in the Space Shuttle Program. Her current position is Subsystem Area Manager for Orbiter Vehicle and Systems Analysis for United Space Alliance in support of the NASA JSC Orbiter Vehicle Engineering Office. She provides oversight of analysis activities associated with the flight readiness, mission support as well as design changes.

Steven Labbe – Aerodynamics Team
Mr. Steven G. Labbe is a 1984 graduate of the University of Cincinnati with a Bachelor of Science Degree in Aerospace Engineering. He has been employed by NASA since 1981, beginning as a cooperative education student at the Lewis (now Glenn) Research Center. He transferred to the Johnson Space Center as a coop and accepted a full-time position in 1984. He currently serves as the Chief of the Applied Aeroscience and Computational Fluid Dynamics Branch. Previous positions at NASA include: Aeroscience Branch Engineer responsible for the development and analysis of Shuttle aerodynamic characteristics; Professional Development Program (PDP) participation via rotational assignment at NASA Ames Research Center in the Applied CFD Analysis Branch; Space Shuttle Ascent Aerodynamic Sub System Manager; Aeroscience Branch Aerodynamics Group Leader; X-38 Project, Aeroscience and Flight Mechanics, Division Chief Engineer/Flight Dynamics Team Lead; X-38 Aerodynamics Lead; and Deputy Chief, Applied Aeroscience & CFD Branch.

Joe Caram – Aerothermodynamics Team
Mr. Caram is an aerospace engineer employed at NASA Johnson Space Center since 1989 working in the Aeroscience and Flight Mechanics Division of the Engineering Directorate. He received his Bachelor of Science and Masters of Science degrees from Texas A&M University in 1986 and 1989, respectively. Until recently he was serving as chief engineer for the feasibility studies of the Orbital Space Plane on Expendable Launch Vehicles (08/02 – 01/03) and X-38 Project EG Division Chief Engineer / Flight Dynamics Lead (03/96 – 07/03). Previous positions at NASA include: Aeroscience Branch engineer responsible for development and analysis of aerothermodynamic environments of various configurations including the Space Shuttle Orbiter. In that position Mr. Caram was responsible for developing math models of the shock-shock interaction heating to the wing leading edge of the Orbiter (9/89 – 3/91) and lead a team investigating Orbiter early/asymmetric hypersonic boundary layer transition (6/92 – 12/95). Other activities during the 1991 to 1995 time frame included being aerothermodynamics team lead in support of advanced projects such as Assured Crew Return Vehicle, First Lunar Outpost, Single Launch Core Station, and Liquid FlyBack Booster. Mr. Caram is an Associate Fellow of AIAA and author or co-author of 20 publications including AIAA conference papers and journal articles, NASA TM's and Symposia.

Charles Campbell – External Aerothermodyanamic Environment Sub-team Lead
Chuck Campbell has been a member of the Applied Aeroscience and CFD Branch at NASA Johnson Space Center since 1990 and has had extensive experience in the application of CFD and wind tunnel testing to manned spacecraft design. Significant activities he has been involved with include the Orbiter Boundary Layer Transition Working Group in the mid-1990's, and hypersonic aerodynamic and aerothermodynamic design for the X-38 Crew Return Vehicle. He holds an Bachelor of Science from the University of Minnesota (1990) in Aerospace Engineering and Mechanics, and a Master of Science from the University of Houston (1998) in Mechanical Engineering.

Team Lead Biographies, Concluded

Steve Fitzgerald – Internal Aerothermodyanamic Environment Sub-team Lead
Steve Fitzgerald joined the Applied Aeroscience and CFD Branch of the Johnson Space Center as a cooperative education student in 1984. Since that time, he has worked a wide range of fluid dynamic fields ranging from numerical simulation of arcjet flows and re-entry flows to rarefied gas dynamics and on-orbit plume impingement flows. As the JSC plume lead, he was a principal author of the Orbiter plume impingement enviromnents and served as a principal investigator for two space flight experiments. In his role as X-38/Crew Return Vehicle aerothermal lead, he oversaw the development of the complete aerothermal database for the X-38, integrating CFD efforts from three separate agencies, and hypersonic wind tunnel testing results from both U.S. and European facilities. Steve holds Bachelors (1986) and Masters (1988) degrees from Texas A&M University in Aerospace Engineering. He presently serves as deputy chief for the GN&C Design and Analysis Branch.

Chris Madden – Thermal Team Lead
Mr. Christopher B. Madden is a 1987 graduate of the University of Texas at Austin with a Bachelor of Science Degree in Aerospace, Aeronautical and Astronautics. He completed his Master of Mechanical Engineering at the University of Houston in 1993. He has been employed by NASA/Johnson Space Center since 1984 where he began as a cooperative student in the Thermal Analysis Section. Mr. Madden is currently serving as the Deputy Chief of the Thermal Design Branch. His previous duties included performing thermal analysis of reentry spacecraft thermal protection systems including the Space Shuttle and other advanced spacecraft; investigation of Space Shuttle thermal anomalies; design and planning of arc-jet tests in support of thermal protection system design and analysis; conducting simulations of orbital debris reentry, and lead engineer for the X-38 structures team including the composite aeroshell and thermal protection system.

Mike Dunham – Stress Team Lead
Mike Dunham is currently is the Boeing Subsystem Manager for Orbiter Stress, Loads and Dynamics. He has worked on Shuttle Orbiter program for 21 years and has a Masters in Civil Engineering Structures from the University of Missouri-Columbia.

Aerodynamics Sub-Team

NASA Johnson Space Center

Rick Barton
Jerry Borrer
Gary Bourland
Kevin Dries
Joe Gamble
Reynaldo Gomez
Jim Greathouse
Mark Hammerschmidt
Steve Labbe
Gerald LeBeau
Randy Lillard
Forrest Lumpkin
Ricardo Machin
Chris Madsen
Fred Martin
Phil Robinson
Steven Robinson
Josh Schneider
Melanie Siloski
Phil Stuart
Tuan Truong
Darby Vicker

Ames Research Center

James Brown
Carol Carroll
David Kinney
James Reuther

Langley Research Center

Karen Bibb
Maria Bobskill
Greg Brauckmann
Pete Gnoffo
Bill Scallion
Charles Miller
Ramadas Prabhu
Bill Woods

Boeing - Houston

Olman Carvajal
Brandon Reddell
Georgi Ushev

Aerodynamics Sub-Team, Concluded

Boeing - Huntington Beach

Rick Burrows
Sergio Carrion
Ron Pelley
Karuna Rajagopal
Harry Sexton
Jeff Stone

Aerothermodynamics Sub-Team

NASA Johnson Space Center

Jerry Borrer
Katie Boyles
Chuck Campbell
Joe Caram
Steve Derry
Kevin Dries
Steve Fitzgerald
Gerald LeBeau
Chien Li, Ph. D.
Forrest Lumpkin, Ph. D.
Randy Lillard
Carl Scott, Ph. D.

NASA Johnson Space Center – White Sands Facility

Harold Beeson, Ph. D
Tim Gallus
Miguel Maes
Mike Shoffstall
Joel Stoltzfus
Bruce Wilson, Ph. D

Langley Research Center

Steve Alter
Kim Bey, Ph. D
Maria Bobskill, Ph. D
Kamran Daryabeigi
Joel Everhart, Ph. D
Chris Glass, Ph. D
Pete Gnoffo, Ph. D
Frank Greene
Harris Hamilton
Tom Horvath
William Kleb
Ron Merski, Ph. D
Charles Miller
Bob Nowak, Ph. D
Ricky Thompson
Bill Wood, Ph. D
William Wood??
Richard Wheless
Kay Wurster
Vince Zoby

Aerothermodynamics Sub-Team, Continued

Ames Research Center

James Brown, Ph. D
Dean Kontinos, Ph. D
Ryan McDaniel
Joe Olejniczak, Ph. D
James Reuther, Ph. D

Marshall Space Flight Center

Herb Bush
Mark Cousins
W. Dahm
Will Downs
Tim Karigan
Ken Kittredge
Al Mayers
David McDaniels
Stu Nelson
Richard Norman
Maurice Prendergast
Joe Ruf
Greg Schunk
John Sharp
Jim Sieja
Mickey White
Joe Wilson

Boeing - Houston

Ed Alexander
Maria Barnwell
Dennis Chao
Mark Fields
Ignacio Norman
K.C. Wang
Lung Wong

Boeing - Huntington Beach

Kevin Bowcutt, Ph. D
Michelle Chaffey
Dan Dominik
Fred Ghahyasi
Suk Kim, Ph. D.
Gerry Kinder
Todd Magee
Kurian K. Mani, Ph. D
Charles R. Olling , Ph. D
Don Picetti
Karuna Rajagopal, Ph. D
Leonel Serrano
Habbib Sharifzedah

Aerothermodynamics Sub-Team, Concluded

Boeing - Rocketdyne

Shashi Aithal
Edward Ascoli
Cliff Bampton
Steve Barson
Pai Chang
Willard Clever
Adon Delgado Jr.
John Fasheh
Scott Halloran
Yann-Fu Hsu
Zhining Liu
Michael Jacques
Dale Ota
S, V. Ramakrishnan
Touraj Sahely
Mark Stewart
Wallace Weider
Kaye Yun

Sandia National Laboratories

Tom Bickel, Ph. D
Michail Gallis, Ph. D
Basil Hassan, Ph. D
Roy Hogan, Ph. D
Dave Kuntz, Ph. D.
William Oberkamphf, Ph. D.
Jeff Payne
Carl Peterson, Ph. D
Ed Piekos, Ph. D.
Don Potter
Art Ratzel, Ph. D
Chris Roy, Ph. D.

AFRL

Susan Arnold
Peter Erbland
Roger Kimmel
James Miller
Richard Neumann

Lockheed Martin

Stan Bouslog
Jose Dobarco-Otero
Tom Paul
Bill Rochelle
Ries Smith

Thermal Sub-Team

NASA Johnson Space Center

Michael Baine
Stan Bouslog
Charlie Camarda
Chuck Campbell
Joe Caram
Joyce Carpenter
Harry Chang
Eric Christiansen
Don Curry
Horatio De La Fuente
Steven Del Papa
Steve Derry
Bonnie Dunbar
Steve Fitzgerald
Mike Fowler
Vadim Gandelsman
Andrew Hong
Eric Hurlbert
Justin Kerr
John Kowal
Gerald LeBeau
Ronald K. Lewis
Stan Love
Chris Madden
Robert Maraia
Tom Modlin
Dan Newswander
Tom Paul
Steve Rickman
Rodney Rocha
Alvaro Rodriguez
Stephanie Wilson

NASA Johnson Space Center – White Sands Facility

Joel Stoltzfus

Langley Research Center

Brian Hollis
Stephen Scotti

Ames Research Center

Scott Lawrence

Thermal Sub-Team, Continued

Marshall Space Flight Center
Joe Ruf
Greg Schunk
John Sharp

Boeing - Houston

Ed Alexander
Maria Barnwell
Shannon Belknap
John Blake
Scott Christensen
Doug Cline
Dennis Chao
Diana Coronado
Tim Davies
Stan Kennedy
Mohammed Nasrullah
Than Nguyen
David Norman
Ignacio Norman
Alfred Olaleye
Renee Rabke
Dave Russell
Steven Tidwell
John Tran
K.C. Wang
Lung-Chen Wong
Michael Zhang

Boeing - Huntington Beach

Kevin Bowcutt
Michelle Chaffey
Dan Dominik
Faustino Garcia
Fred Ghahyasi
Gerry Kinder
Kurian K. Mani
Charles R. Olling
Don Picetti
Karuna Rajagopal
Habbib Sharifzedah

Cimarron

James Smith

Thermal Sub-Team, Concluded

Boeing – Kennedy Space Center

Dan Bell

Boeing - Rocketdyne
Steve Barson
Scott Halloran

Sandia National Laboratories

Tom Bickel
Michail Gallis
Basil Hassan
Roy Hogan
David Kuntz
Jeff Payne
Carl Peterson
Ed Piekos
Don Potter
Art Ratzel

SAIC (Science Application International Corporation)
Omar Hatamleh
Mohamed Ishmael

AFRL
Peter Erbland
Roger Kimmel

Lockheed Martin
Stan Bouslog
Bill Rochelle
Jim Milhoan
Matthew Vogel

United Space Alliance
Pam Madera

Structures Sub-Team

NASA Johnson Space Center

Trevor Kott
Julie Kramer
Tom Modlin
Deneen Taylor

Langley Research Center

Max Blosser
Lynn Bowman
Roger Chen
Kamran Daryabeigi
Christapher Lang
Stephen Scotti

Boeing - Houston

Jason Adair
Bob Clark
Mike Dunham
Danny Le
Aaron Leinmiller
Gus (Constantine) Michalopolous
Darwin Moon
Paul Parker
Shawn Sorenson

Boeing - Huntington Beach

Tony Chi
Gary Collier
Ken Fiorelli
Scott Foust
Judy Goldish
George Hartnett
Mahesh Jain
Mike Koharchick
Jerry Lai
John McKinney
Bill Novak
Dave Okino
Charles Park
Al Richardson
Lou Swayne
Ed Tong
Jerry Warren